N 5 1979

Item 830-H-14

NAS 1.26: 3113

NASA Contractor Report 3113

ORIGINAL

COMPLETED

An Electronic Control for an Electrohydraulic Active Control Aircraft Landing Gear

MICROFILMED FROM
BEST AVAILABLE COPY

Irving Ross and Ralph Edson

CONTRACT NAS1-14459
APRIL 1979

NASA

170

NASA Contractor Report 3113

An Electronic Control for an Electrohydraulic Active Control Aircraft Landing Gear

Irving Ross and Ralph Edson
Hydraulic Research Textron
Valencia, California

Prepared for
Langley Research Center
under Contract NAS1-14459

NASA
National Aeronautics
and Space Administration

Scientific and Technical
Information Office

1979

Blank Page

CONTENTS

Page

SUMMARY 1

INTRODUCTION 1

SYMBOLS 3

ANALYSIS 8
  Nonlinear Math Model for Vertical Drops 8
    Equations of Motion 10
    Pressure, Flow, and Volume Relationship 14
    Servovalve Dynamics 16
  Linear Math Model for Vertical Drops 18
  Energy Considerations 27
  Stability Analysis 39

ANALYTICAL RESULTS 51
  Vertical Drop Cases 53
  Land and Roll Cases 53

CONTROLLER FUNCTIONAL DESCRIPTION 71
  Associated Equipment 71
  Interface 71
  Performance Characteristics 76
  Operating-Mode Determination 76
    Landing Mode 76
    Takeoff Mode 77
  Limit-Force Command Determination 78
  Control Law Implementation 78
  Controller Design 78
    Functional Sections 78

CONTENTS (Contd.)

Page

TEST 89

Test Fixture 89

Test Conditions 93

Test Results 93

CONCLUSIONS 114

APPENDIX

A Microprocessor Program Listing 115

B Electronic Controller Detailed Description 131

C Test Procedure 142

D Oscillograph Recordings 148

FIGURES

1 Illustration of variables used in nonlinear simulation of simplified vertical drop case 9

2 Free body diagram of airplane mass 11

3 Free body diagram of upper shock strut 11

4 Free body diagram of lower shock strut 11

5 Dynamic response of servovalve, ±10% input signal . . . 17

6 Illustration of "Equivalent" system for the linear math model. 22

7 Block diagram of linear math model 26

8 Comparison of linear model and nonlinear model results, open loop, no compensation, no position feedback 28

9 Various energy terms versus time, from the simplified nonlinear vertical drop simulation 33

10 Illustration of the variation of limit force versus time and the various phases of operation following impact . . . 35

11 Block diagram of linear system without compensation . . 40

CONTENTS (Contd.)

Page

FIGURES

12 Nyquist plot of F_{wg}/F_{lim} with force loop opened, no position feedback, no compensation 41

13 Electronic compensation network and its characteristics . . 42

14 Nyquist plot of F_{wg}/F_{lim} with force loop opened, no position feedback, with compensation 43

15 Nyquist plot of F_{wg}/F_{lim} with force loop opened, position loop closed, with compensation 45

16 Nyquist plot of X_s/X_c with position loop opened, force loop closed, with compensation 46

17 Frequency response of F_{wg}/F_{lim} with force and position loops closed, with compensation 47

18 Frequency response of X_s/X_c with force and position loops closed, with compensation 48

19 Nyquist plot of F_{wg}/F_{lim} with force loop opened, position loop closed, with compensation. 49

20 Nyquist plot of F_{wg}/F_{lim} with force loop opened, position loop closed, with compensation. 50

21 Wing/gear force transient, case A 54

22 Wing/gear force transient, case B 55

23 Strut position transient, case B 56

24 Wing/gear force transient, case 1 57

25 Strut pressures, case 1 58

26 Strut position transient, case 1 59

27 Wing/gear force transient, case 2 60

28 Strut position transient, case 2 61

29 Wing/gear force transient, case 3 63

30 Wing/gear force transient, case 4 64

31 Servovalve flow rate, case A 65

32 Servovalve flow rate, case B 66

CONTENTS (Contd.)

Page

FIGURES

33 Servovalve flow rate, case 1 67
34 Servovalve flow rate, case 2 68
35 Servovalve flow rate, case 3 69
36 Servovalve flow rate, case 4 70
37 Input/Output Signal Schematic 72
38 Control Law Functional Schematic 79
39 Controller Functional Schematic 81
40 Basic Functional Requirements 82
41 Software Flow Chart 84
42 Analog Section Schematic 85
43 Analog Section - Front Panel Inputs 87
44 Analog Section - Front Panel Outputs 88
45 S-1C Test Fixture, Landing Gear Installed (View 1) 90
46 S-1C Test Fixture, Landing Gear Installed (View 2) 91
47 Net Force, Conditions 1, 4 (From W/G Accel #1) 95
48 Net Force, Conditions 2, 5 (From W/G Accel #1) 96
49 Net Force, Conditions 3, 6 (From W/G Accel #1) 97
50 Net Force, Conditions 7, 10 (From W/G Accel #1) 98
51 Net Force, Conditions 8, 11 (From W/G Accel #1) 99
52 Net Force, Conditions 9, 12 (From W/G Accel #1) 100
53 Gear Hydraulic Pressure, Conditions 1, 4 101
54 Gear Hydraulic Pressure, Conditions 2, 5 102
55 Gear Hydraulic Pressure, Conditions 3, 6 103
56 Gear Hydraulic Pressure, Conditions 7, 10 104
57 Gear Hydraulic Pressure, Conditions 8, 11 105
58 Gear Hydraulic Pressure, Conditions 9, 12 106

CONTENTS (Contd.)

Page

FIGURES

59 Strut Deflection, Conditions 1, 4 107
60 Strut Deflection, Conditions 2, 5 108
61 Strut Deflection, Conditions 3, 6 109
62 Strut Deflection, Conditions 7, 10 110
63 Strut Deflection, Conditions 8, 11 111
64 Strut Deflection, Conditions 9, 12 112

TABLES

I SUMMARY OF ACTIVE CONTROL LANDING CASES SIMULATED ON THE COMPUTER 52
II PRIMARY INPUT SIGNAL SPECIFICATIONS 73
III SECONDARY INPUT SPECIFICATIONS 74
IV OUTPUT SPECIFICATIONS 75
V CONTROL LAW TRANSFER FUNCTIONS 80
VI PEAK FORCES AND PERCENTAGE REDUCTION 94

REFERENCES 161

SUMMARY

The electronic controller described in this report, together with an active control landing gear, are found to provide significant reductions in forces sustained by an aircraft during takeoff, landing impact and rollout. The degree of force reduction increases with the sink rate. These results were obtained analytically and confirmed experimentally by actual drop tests of a landing gear under active control.

The electronic controller continuously compares the kinetic energy of the aircraft with the work potential of the gear until the work potential exceeds the kinetic energy. The wing/gear interface force present at this condition becomes the command force to a servo loop which maintains the wing/gear interface force at this level by providing a signal to an electrohydraulic servovalve to port flow into or out of the landing gear.

INTRODUCTION

Hydraulic Research (HR) was retained under NASA Contract NAS 1-14459 to design, develop, fabricate and test an electronic controller for an electrohydraulic active control landing gear, as described in Reference 1. The primary function of the active control landing gear is to minimize the force to which the aircraft is subjected as a result of landing impact and rollout, takeoffs and taxi operations. As shown in Ref. 1, the resultant decrease in applied loads could be very beneficial in reducing structural fatigue design problems and increasing ride comfort for passengers and crew. The work was divided into two major phases: Phase 1 for the analytical development and design of the controller; and, Phase 2 for the fabrication and testing. This report summarizes the effort of both phases and provides the rationale for the controller design selected.

Phase 1 included the development and use of digital computer programs which simulated the dynamics of the landing gear/controller system. A nonlinear dynamic model and a simplified linear model for vertical drops were developed by HR and used extensively in the analysis. In addition, a computer program developed by NASA, which included aerodynamic simulation and landing gear dynamics, was supplied to HR in support of the program. The computer program was modified by HR to include the dynamics of the electrohydraulic servovalve and this program was incorporated into the study. The landing gear parameters, as described in the NASA computer program, were used as the basis for all analyses described herein. During this phase, the controller design was also developed. This design included analog circuitry for the control laws, compensation, summations and the signal to the servovalve driver while a digital microprocessor was used for the nonlinear computations and decision making.

During Phase 2, the controller, as defined in Phase 1, was fabricated and tested by actual drop tests of the gear.

SYMBOLS

A_o	area of orifice in shock strut orifice plate, 0.0000786 m^2 (0.1219 in^2)
A_1	shock strut hydraulic area (piston area), 0.00317 m^2 (4.909 in^2)
A_2	shock strut pneumatic area (cylinder area), 0.00535 m^2 (8.286 in^2)
A_3	annular area in shock strut between piston and cylinder walls, 0.00151 m^2 (2.34 in^2)
C_d	discharge coefficient for active control servovalve orifice, 0.62
C_{do}	discharge coefficient for shock strut orifice, 0.90
C_o	orifice coefficient for shock strut orifice = $C_{do} A_o \sqrt{2g_c/\rho}$, 3.45 (10^{-6}) $m^4\ sec^{-1} \cdot N^{-1/2}$ (17.51 $in^3/sec/\sqrt{lb/in^2}$)
CP	linearized orifice coefficient for active control servovalve $= -\partial Q_{sv}/\partial P_1$ = 3.16 (10^{-11}) $m^5 \cdot N^{-1} \cdot sec^{-1}$(0.01334 $in^3/sec/lb/in^2$)
CP_o	linearized orifice coefficient for shock strut orifice $= \partial Q_o/\partial P_1$ $= C_o/(2\sqrt{P_1-P_2})$, $m^5 \cdot N^{-1} \cdot sec^{-1}$ ($in^3/sec/lb/in^2$)
CQ	linearized orifice coefficient for active control servovalve $= \partial Q_{sv}/\partial X_{sv}$ $= C_{sv} \sqrt{(P_S + P_R)/2}$, 8.61 m^2/sec (13 340 · $in^3/sec/in$)
C_{sv}	orifice coefficient for active control servovalve $= C_d W_{sv} \sqrt{2g_c/\rho}$, 0.00268 $m^3 \cdot sec^{-1} \cdot lb^{-1/2}$ (344.4 $in^3/sec/\sqrt{lb/in^2}$)
f	Coulomb friction between shock strut piston and cylinder, N (lb)
F_a	vertical force exerted on shock strut by the runway surface, N (lb)
F_{li}	impact phase limit force, N (lb)
F_{lim}	limit force, N (lb)
F_s	shock strut force, N (lb)
F_{wg}	wing/gear interface force, N (lb)

SYMBOLS (Continued)

g	acceleration due to gravity, 9.80 $\mathrm{m/sec^2}$ (386 · $\mathrm{in/sec^2}$)
g_c	gravitational acceleration constant, 1 $\mathrm{kg \cdot m \cdot N^{-1} \cdot sec^{-2}}$ (12 $\mathrm{slug \cdot in \cdot lb^{-1} \cdot sec^{-2}}$)
i_1	input signal to electronic compensation networks, A
i_2	output signal from electronic compensation networks, or input signal to active control servovalve, A ($\pm$0.040 A maximum)
K_a	amplifier gain in active control loop, 0.000040 A/V
K_f	position feedback gain in strut position control loop, 196.9 V/m (5.0 V/in)
K_{FDGE}	fraction of total strut stroke assumed available when computing impact phase force from equation 37
K_{sv}	position gain of servovalve in active control loop, 0.0635 m/A (2.50 in/A)
K_t	effective spring rate of tire, 245 000 · N/m (1400 lb/in)
K_x	gain in strut position control loop, 1.0 m/m (1.0 in/in)
L	total life force, N (lb)
M	mass of airplane per gear, 1456 kg (99.8 slugs)
M_C	mass of upper portion of landing gear (cylinder plus orifice plate attachment, kg (slug)
M_L	mass of lower portion of landing gear (piston plus tire), 32.1 kg (2.20 slugs)
M_U	upper mass, 1456 kg (99.8 slugs)
PE_t	potential energy stored in tire due to compression, N·m (ft·lb)
P_S	hydraulic supply pressure, 2.07 (10^7) $\mathrm{N/m^2}$ (3000 $\mathrm{lb/in^2}$)
P_R	hydraulic return pressure, 0.0 $\mathrm{N/m^2}$ (0.0 $\mathrm{lb/in^2}$)

SYMBOLS (Continued)

PROM	programmable read only memory
P_1	hydraulic pressure in shock strut piston, N/m^2 (lb/in^2)
P_2	pneumatic pressure in shock strut cylinder, N/m^2 (lb/in^2)
P_3	pressure in volume between walls of shock strut piston and cylinder, N/m^2 (lb/in^2)
Q_O	flow rate through shock strut orifice from piston to cylinder, m^3/sec (in^3/sec)
Q_{sv}	flow rate from active control servovalve to shock strut piston, linear mode, m^3/sec (in^3/sec)
Q_{sv_1}	flow rate through active control servovalve from supply pressure to the shock strut piston, m^3/sec (in^3/sec)
Q_{sv_2}	flow rate through active control servovalve from shock strut piston to return pressure, m^3/sec (in^3/sec)
RAM	random access memory
R_s	the slope of the limit force with respect to time during transition phase, 137 900 N/sec (31 000 lb/sec)
s	LaPlace operator, sec^{-1}
t	time, sec
V	velocity
V_1	hydraulic volume in shock strut piston and lines up to the active control servovalve, 0.00426 m^3 (260.0 in^3) for fully extended strut
V_2	pneumatic volume, 0.000624 m^3 (38.1 in^3) for fully extended strut
V_3	volume between shock strut piston and cylinder, 0.0 m^3 (0.0 in^3) for fully extended strut
Wsv	window width of orifices on third stage spool of active control servovalve, 0.0884 m (3.48 in)

SYMBOLS (Continued)

X	displacement, m (in)
X_c	commanded position of shock strut, 0.1016 m (4.0 in)
β	bulk modulus of hydraulic fluid, 6.89 (10^8) N/m^2 $(1 \cdot 10^5$ lb/in$^2)$
γ	ratio of specific heat of gas at constant pressure to that at constant volume, 1.1
ρ	mass density of hydraulic fluid, 838 kg/m^3 (0.000941 slugs/in^3)
τ_f	time constant in strut position feedback loop, 0.10 sec
τ_1	time constant in electronic compensation network, 0.0281 sec
τ_2	time constant in electronic compensation network, 0.0141 sec
τ_3	time constant in electronic compensation network, 0.0010 sec
τ_4	time constant in electronic compensation network, 0.0001 sec
ω_c	corner frequency in active control servovalve transfer function, 1263 sec^{-1}
ω_{sv}	natural frequency in active control servovalve transfer function, 655.5 sec^{-1}
ω_1	natural frequency in electronic compensation network, 251.3 sec^{-1}
ζ_{sv}	damping coefficient in active control servovalve transfer function, 0.436
ζ_1	damping coefficient in electronic compensation network, 5.10
ζ_2	damping coefficient in electronic compensation network, 0.10

SYMBOLS (Continued)

Subscripts:

a	lower mass of shock strut or axle
g	ground
i	initial conditions before impact
im	impact phase
L	lower mass
max	maximum value
min	minimum value
r	rollout phase
s	shock strut relative motion of the lower mass (piston) with respect to the upper mass (cylinder)
sv	servovalve
tr	transition phase
U	upper mass
wg	wing/gear interface

Miscellaneous:

$d(\ )$	indicates the differential of a variable
$\Delta(\ )$	indicates difference or change in a variable
$(\dot{\ }),(\ddot{\ }),(\dddot{\ })$	dots indicate differentiation with respect to time

ANALYSIS

Nonlinear Math Model for Vertical Drops

A simplified nonlinear dynamic model of an active control landing gear for vertical drops without aerodynamics and airplane dynamics was developed. The airplane mass is represented simply as a point mass located on top of the landing gear. This model proved to be of great value in this project for various reasons. First, it enhanced understanding of the basic equations of motion of the landing gear and the dynamic characteristics. This was very useful in the further development of an even more simplified linearized dynamic model, which was used extensively in the development of the electronic compensation networks that are required for stability. The linear model and its application are discussed in later sections. Secondly, it often was desirable to study the dynamic operation of the system without the complicating influences of the airplane dynamics, and the simplified nonlinear model provided a good tool to do this. Also, by neglecting airplane dynamics, the size of the computer simulation is greatly reduced and runs can be made in less computational time. Finally, the simplified model was used as a check with the more general computer program supplied by NASA, which required many programming changes in its application to this study.

Figure 1 shows a schematic of the simplified vertical drop case along with some of the variables used in modeling the system. The system basically consists of (1) an upper mass M_U, which is the mass M (per gear) of the airplane plus the mass M_C of the upper portion of the landing gear (i. e., the cylinder plus the orifice plate attachment), (2) a lower mass M_L, which consists of the tire mass plus the mass of the lower portion of the landing gear (i. e., the piston), (3) a three-way servovalve that ports fluid in the piston chamber to either supply or return pressure, and (4) an electronic controller. Note that the tire dynamics are simulated as a mass and linear

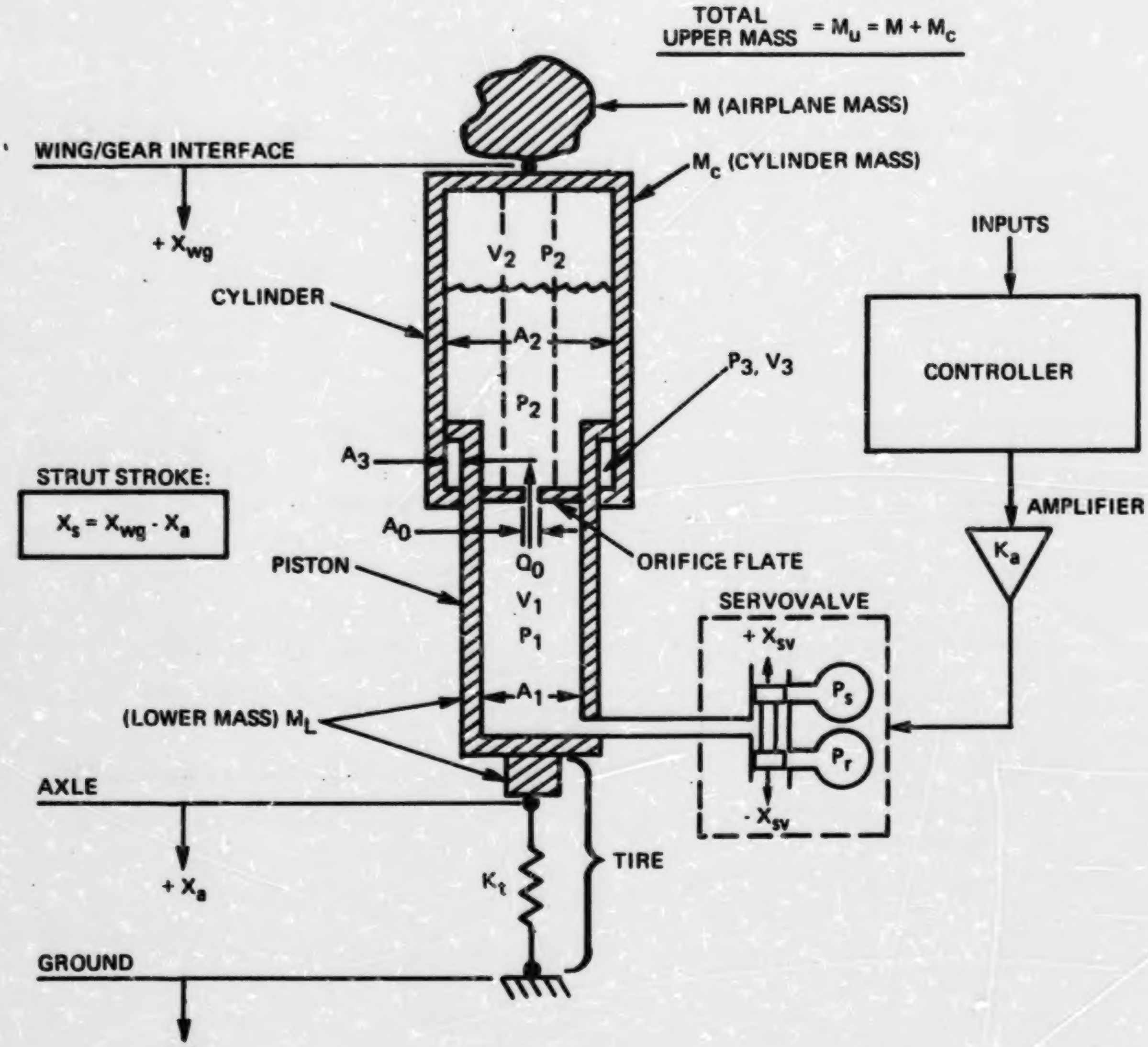
TOTAL UPPER MASS = M_u = M + M_c
M (AIRPLANE MASS)
WING/GEAR INTERFACE
M_c (CYLINDER MASS)
+ X_{wg}
INPUTS
V_2
P_2
CYLINDER
A_2
P_3, V_3
CONTROLLER
P_2
A_3
STRUT STROKE:
$X_s = X_{wg} - X_a$
AMPLIFIER
A_0
K_a
ORIFICE FLATE
PISTON
Q_0
SERVOVALVE
V_1
P_1
+ X_{sv}
P_s
A_1
(LOWER MASS) M_L
P_r
AXLE
- X_{sv}
TIRE
+ X_a
K_t
GROUND
+ X_g

Figure 1. - Illustration of variables used in nonlinear simulation of simplified vertical drop case.

spring K_t. The controller dynamics are presented later and will not be repeated here. Suffice it to say that at each instant in time the controller processes the input signals to provide a current to the servovalve.

Equations of Motion

The equations of motion of the landing gear in the vertical direction will now be derived, with down being defined as the positive direction. The two independent masses M_U and M_L give rise to two degrees of freedom, X_{wg} and X_a (See Figure 1). The final results, however, will be expressed in terms of the displacement variables X_{wg} and X_s, where X_s is the shock strut stroke, which ranges from zero for a fully extended strut to the maximum value for a fully contracted strut. The variable X_s is equal to $(X_{wg}-X_a)$.

Referring to Figure 2, a force balance on the airplane mass gives

$$M\ddot{X}_{wg} = Mg - L - F_s = -F_{wg} \qquad \ldots (1)$$

where F_s is the "shock strut force" and F_{wg} is the "wing gear interface force".

Referring to Figure 3, a force balance on the upper portion of the shock strut, which is assumed to be rigidly connected to the airplane mass, gives

$$M_c \ddot{X}_{wg} = M_c g + F_s - P_2A_2 + P_2(A_1-A_o) - P_1(A_1-A_o) + P_3A_3 \mp f$$

or

$$F_s = M_c \ddot{X}_{wg} - M_c g + (P_1-P_2)(A_1-A_o) + P_2A_2 - P_3A_3 \pm f \qquad \ldots (2)$$

Referring to Figure 4, a force balance on the lower portion of the shock strut, which includes the wheel and tire mass, gives

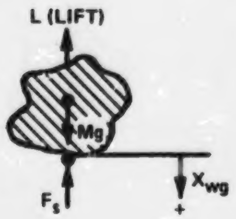
L (LIFT)
Mg
F_s
X_{wg}
+

Figure 2. - Free body diagram of airplane mass

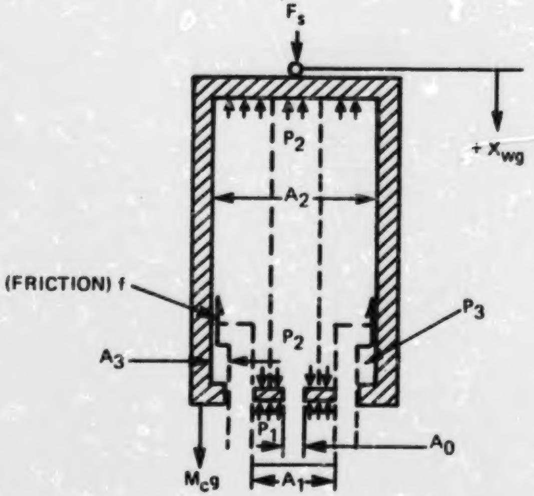
F_s
P_2
$+X_{wg}$
A_2
(FRICTION) f
P_3
P_2
A_3
P_1
A_0
M_cg
A_1

Figure 3. - Free body diagram of upper shock strut

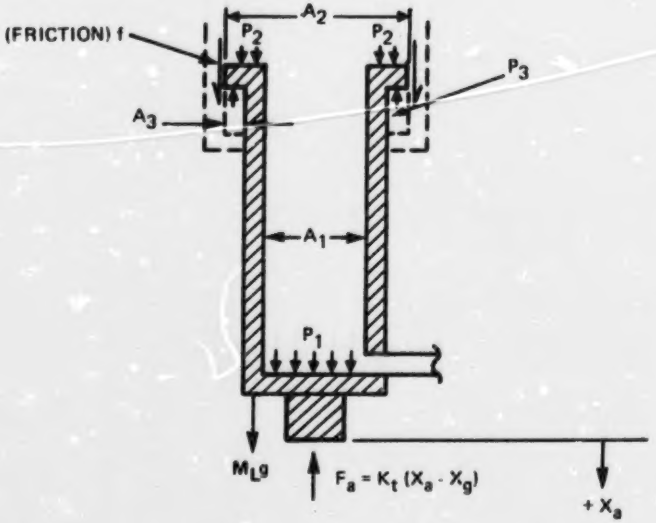
A_2
(FRICTION) f
P_2
P_2
P_3
A_3
A_1
P_1
M_Lg
$F_a = K_t (X_a - X_g)$
$+X_a$

Figure 4. - Free body diagram of lower shock strut

$$M_L\ddot{X}_a = M_Lg + P_2(A_2-A_1) + P_1A_1 - P_3A_3 - F_a \pm f \qquad \ldots (3)$$

substituting $(X_{wg}-X_s)$ for X_a

$$\left.\begin{aligned} M_L(\ddot{X}_{wg} - \ddot{X}_s) &= M_Lg + (P_1-P_2)A_1 + P_2A_2 - P_3A_3 - F_a \pm f \\ \text{where } F_a &= \begin{cases} K_t(X_{wg} - X_s - X_g) & \text{for } X_{wg} - X_s > X_g \\ 0 & \text{for } X_{wg} - X_s \leq X_g \end{cases} \end{aligned}\right\} \ldots (4)$$

Note that the tire force F_a is zero when the tire is not in contact with the runway surface.

Equations were developed for: (1) the case where the piston is in motion relative to the cylinder, or $V_s \neq 0$; and (2) the case where the piston is not in motion relative to the cylinder due to Coulomb stiction between the two, or $V_s = 0$. For the first case, the Coulomb friction f is simply the value of running friction that exists. But for the second case, the Coulomb friction is actually a stiction force that can vary over a range of absolute values from zero up to the breakaway friction value. Transition from case 1 to case 2 will occur whenever the relative velocity is zero or passes through zero throughout the digital integration process. Transition from case 2 to case 1 will occur whenever the absolute value of the friction force f exceeds the known breakaway friction value. The following equations express these relationships.

First, for the case when $V_s \neq 0$, equations 1 and 2 are combined to eliminate F_s.

$$M_u\ddot{X}_{wg} = M_ug - L - (P_1-P_2)(A_1-A_o) - P_2A_2 + P_3A_3 \mp f \qquad \ldots (5)$$

Substituting equation 5 for $\ddot{X}_{wg}$ into equation 4

$$\frac{M_L}{M_u}\left[M_u g - L - (P_1-P_2)(A_1-A_o) - P_2A_2 + P_3A_3 \mp f\right] - M_L\ddot{X}_s$$

$$= M_L g + (P_1-P_2)A_1 + P_2A_2 - P_3A_3 - F_a \pm f$$

Solving for $\ddot{X}_s$

$$M_L\ddot{X}_s = \frac{M_L}{M_u}\left[(M_u + M_L)\,g - L\right] + \left(1 + \frac{M_L}{M_u}\right)\left[-M_L g - (P_1-P_2)\,A_1 - P_2A_2 + P_3A_3\right]$$

$$+ \frac{M_L}{M_u}(P_1 - P_2)\,A_o + F_a \mp \left(1 + \frac{M_L}{M_u}\right) f$$

or

$$M_L\ddot{X}_s = \left(1 + \frac{M_L}{M_u}\right)\left[\text{FORCE} \mp f\right] \qquad \ldots(6)$$

$$\text{FORCE} = \frac{\frac{M_L}{M_u}\left[(M_u + M_L)\,g - L\right] + \left(1 + \frac{M_L}{M_u}\right)\left[-M_L g - (P_1 - P_2)\,A_1 - P_2A_2 + P_3A_3\right] + \frac{M_L}{M_u}(P_1 - P_2)A_o + F_a}{1 + \frac{M_L}{M_u}}$$

Equations 5 and 6 constitute the two inertial equations of motion when $V_s \neq 0$.

Next, for the case when $V_s = 0$, equations 4 and 5 are totaled to get

$$(M_u + M_L)\,\ddot{X}_{wg} = (M_u + M_L)\,g - L + (P_1 - P_2)\,A_o - F_a \qquad \ldots(7)$$

$$\ddot{X}_s = 0 \qquad \ldots(8)$$

Equations 7 and 8 are the two inertial equations of motion when $V_s = 0$. However, an expression must be derived to tell when the two masses break away from one another; i.e., when the break away stiction will be overcome causing relative motion between them. This required solving for the variable friction force f. Substituting equation 5 for $\ddot{X}_{wg}$ into equation 4

$$\frac{M_L}{M_u} [M_u g - L - (P_1 - P_2)(A_1 - A_o) - P_2A_2 + P_3A_3 \mp f]$$

$$= M_Lg + (P_1 - P_2) A_1 + P_2A_2 - P_3A_3 - F_a \pm f$$

Solving for f, gives

$$\pm f = \frac{\frac{M_L}{M_u} [(M_u + M_L) g - L] + (1 + \frac{M_L}{M_u})[- M_Lg - (P_1 - P_2) A_1 - P_2A_2 + P_3A_3] + \frac{M_L}{M_u} (P_1 - P_2) A_o + F_a}{1 + \frac{M_L}{M_u}} \qquad \ldots(9)$$

If the value of f as calculated by equation 9 exceeds the breakaway stiction, then relative motion will result.

Pressure, Flow, and Volume Relationship

Referring to Figure 1, conservation of mass applied to the hydraulic fluid in volume V_1 gives

$$\frac{V_1}{\beta} \dot{P}_1 = A_1 \dot{X}_s - Q_o + Q_{sv1} - Q_{sv2} \qquad \ldots(10)$$

where

$$Q_o = \begin{cases} A_o C_{do} \sqrt{\dfrac{2 g_c}{\rho} (P_1 - P_2)} & \text{for } P_1 > P_2 \\ -A_o C_{do} \sqrt{\dfrac{2 g_c}{\rho} (P_2 - P_1)} & \text{for } P_2 > P_1 \end{cases}$$

$$V_1 = V_{1_i} - A_1 X_s$$

The parameters Q_{sv1} and Q_{sv2} are the servovalve flows from supply pressure to P_1 and from P_1 to return pressure, respectively, and are a function of the spool displacement and valve geometry. These flows are calculated in a subroutine titled FLOZE2 in the nonlinear simulations. Note also that equation 10 considers the effect of fluid compressibility, which gives rise to the first derivative of pressure term.

The pressure/volume relationship for the pneumatic volume V_2 is

$$P_2 = P_{2_i} \left(\frac{V_{2_i}}{V_2}\right)^{\gamma} \qquad \text{...(11)}$$

where

$$V_2 = V_{2_i} - (A_2 - A_1) X_s - V_{cum} + (V_3 - V_{3_i})$$

$V_{cum} = \Sigma (Q_o \Delta t) =$ the cumulative fluid flow through the orifice from V_1 to V_2

$$V_3 = V_{3_i} + A_3 X_s$$

The initial values of the pressure and volume variables referred to in the above equations are for the fully extended strut just prior to impact.

Servovalve Dynamics

The dynamic characteristics of the NASA-selected three-stage high response servovalve were supplied to HR by NASA. A mathematical representation of the servovalve dynamics was derived by the following procedure. The small signal frequency response characteristics obtained from NASA are shown reproduced in Figure 5 for reference. Amplitude and phase angle data at several discrete frequencies over the range of interest were taken from these curves and input to an HR-developed computer program that solves for an approximate linear transfer function by the method of least squares. The resultant transfer function is

$$\frac{X_{sv}}{i_2} = \frac{K_{sv}}{\left(\frac{s^2}{\omega^2_{sv}} + \frac{2\zeta_{sv}}{\omega_{sv}} s + 1\right)\left(\frac{s}{\omega_c} + 1\right)} \qquad \ldots(12)$$

where the values of the constants K_{sv}, ω_{sv}, ω_c, and ζ_{sv} are given in the SYMBOLS section and i_2 is input current and X_{sv} is output displacement of the third stage spool. For the nonlinear simulation this transfer function is represented in differential equation form as follows:

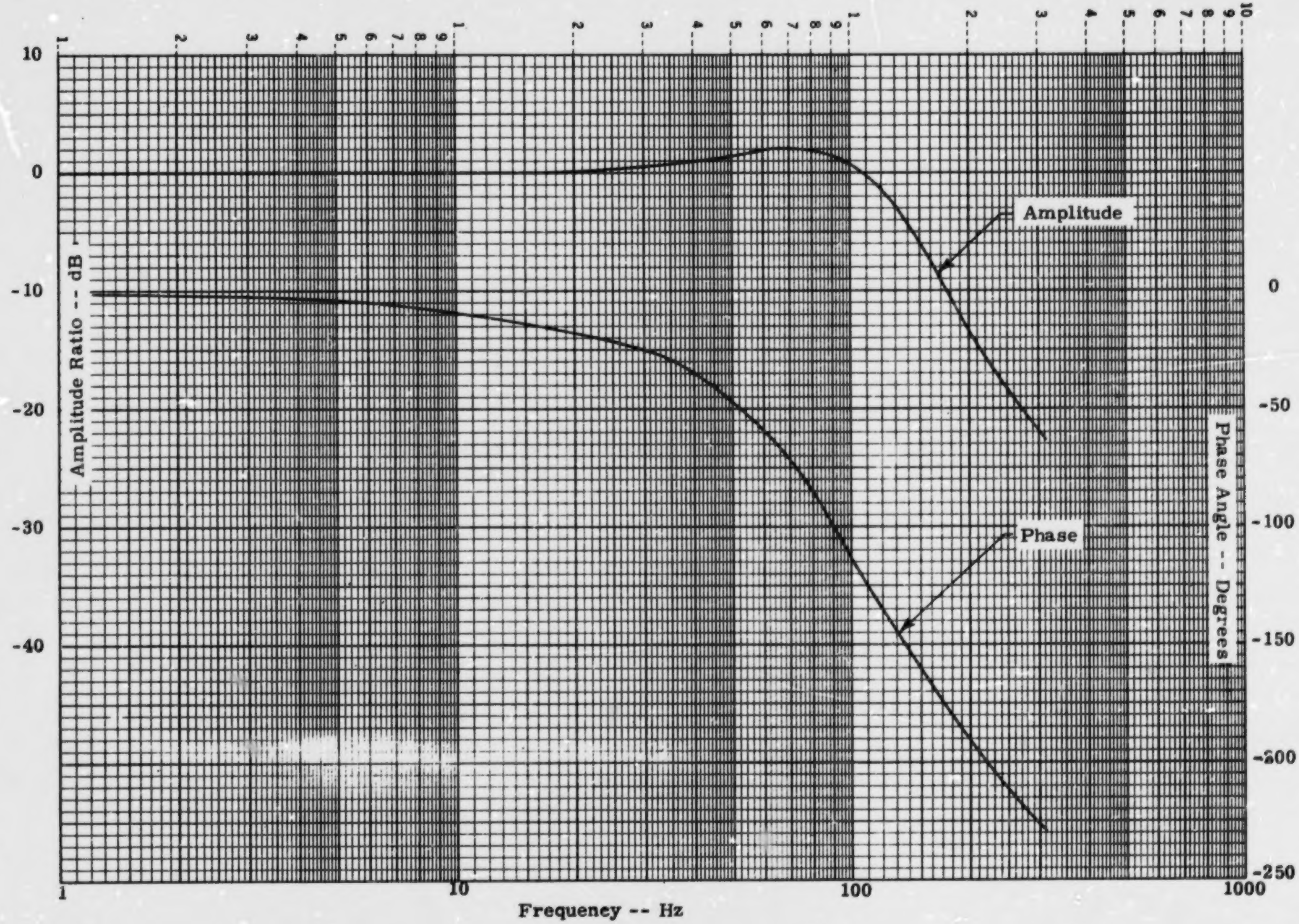

Figure 5. - Dynamic response of servovalve, ±10% input signal.

$$\left(\frac{1}{\omega^2_{sv}\,\omega_c}\right)\dddot{X}_{sv} + \left(\frac{1}{\omega^2_{sv}} + \frac{2\,\zeta_{sv}}{\omega_{sv}\,\omega_c}\right)\ddot{X}_{sv} + \left(\frac{2\,\zeta_{sv}}{\omega_{sv}} + \frac{1}{\omega_c}\right)\dot{X}_{sv} + X_{sv} = K_{sv}\,i_2 \qquad \ldots(13)$$

Saturations in the various stages are treated as follows. Third stage spool saturation obviously places a limit on X_{sv} equal to $\pm X_{sv}$ max. Second stage saturation is assumed to place a limit on $d(X_{sv})/dt$ equal to $\pm$ (QSV2/ASV3), where QSV2 is the second stage saturation flow and ASV3 is the effective cross sectional area of the third stage spool connected to the lines from the second stage. First stage flapper saturation is assumed to place a limit on $d^2(X_{sv})/dt^2$ equal to $\pm (QSV1 \cdot CQ_2)/(ASV2 \cdot ASV3)$, where QSV1 is the first stage saturation flow, CQ_2 is the linearized flow gain of the second stage spool (flow rate per unit displacement of spool), ASV2 is the effective cross sectional area of the second stage spool connected to the flow lines from the first stage, and ASV3 is as already described.

Linear Math Model for Vertical Drops

This section describes the development of an approximate linear model of an active control landing gear for vertical drops, exclusive of aerodynamics and airplane dynamics. The linear model is a valuable tool since the effect of system modifications can be ascertained very rapidly. The study of system stability and the development of the electronic compensation networks, discussed in the following section, relied very heavily on the linear model. The results were then supported by analysis using the complete nonlinear model.

The equations for the actual landing gear and controller are inherently nonlinear, so some assumptions and simplifications must be made. The following list summarizes the assumptions that were made in the linearization process.

(1) The coulomb friction f between the piston and the cylinder is neglected.

(2) The pneumatic pressure P_2 is assumed constant.

(3) The pressure P_3 is identical to the pressure P_2.

(4) The lift and gravitational forces are constant.

(5) The cross sectional area of the piston wall is negligible with respect to the overall piston area.

(6) The area of the fixed orifice is negligible with respect to the overall piston area.

(7) The inertia of the upper part of the shock strut mass is negligible with respect to the airplane mass.

(8) Servovalve nonlinearities are neglected (i.e., constant flow gain and pressure gain partial derivative values are assumed).

The equations given in the previous section for the nonlinear math model can now be simplified as follows. Equations 5 and 6 become

$$M_u \ddot{X}_{wg} \approx M_u g - L - P_1 A_1$$

$$M_L \ddot{X}_s \approx \frac{M_L}{M_u} \left[(M_u + M_L)\, g - L \right] + \left(1 + \frac{M_L}{M_u}\right) \left[- M_L g - P_1 A_1 \right] + K_t \left(X_{wg} - X_s \right)$$

If we let the variables X'_{wg}, X'_a, X'_s, and P'_1 represent the perturbation variables of X_{wg}, X_a, X_s, and P_1, (that is, they represent changes in those variables about some mean condition), then these two equations can be written

$$M_u \ddot{X}'_{wg} = -P'_1 A_1$$

$$M_L \ddot{X}'_s = (1 + \frac{M_L}{M_u})(-P'_1 A_1) + K_t (X'_{wg} - X'_s)$$

where the lift and gravitational terms have dropped out because they are assumed constant. Making use of the identity $X_s = X_{wg} - X_a$, these two equations can be solved for X_{wg} and X_a. Dropping the primes for simplicity, the results in LaPlace transform notation are

$$X_{wg} = -\frac{A_1 P_1}{M_u s^2} \qquad \ldots(14)$$

$$X_a = \frac{A_1 P_1}{M_L s^2 + K_t} \qquad \ldots(15)$$

Also, note from equations 1 and 2 that

$$F_{wg} = F_s \approx P_1 A_1 \qquad \ldots(16)$$

It is instructive to note that equations 14 and 15 are the linearized equations of motion that would result from a mass and piston driving into a sleeve connected to ground by a spring, with an orifice in the piston connecting the internal pressure P_1 with a constant pressure P_2 on the other side. This is illustrated schematically in Figure 6, along with a servovalve for active control. A force balance on the masses M_U and M_L will result exactly in equations 14 and 15.

A linearized expression for the pressure P_1 will now be derived. Referring to Figure 6, conservation of mass applied to the hydraulic fluid in volume V_1 gives

$$dQ_{sv} - dQ_o + A_1 \dot{X}_s = \frac{V_1}{\beta} \dot{P}_1 \qquad \ldots(17)$$

The flow from the servovalve is

$$Q_{sv} = \begin{cases} C_{sv} X_{sv} \sqrt{P_S - P_1} & \text{for } X_{sv} \geq 0 \\ C_{sv} X_{sv} \sqrt{P_1 - P_R} & \text{for } X_{sv} < 0 \end{cases}$$

Differentiating this, gives

$$dQ_{sv} = \begin{cases} C_{sv} \sqrt{P_S - P_1}\, dX_{sv} - \left(\dfrac{C_{sv} X_{sv}}{2 \sqrt{P_S - P_1}} \right) dP_1 & \text{for } X_{sv} \geq 0 \\ \\ C_{sv} \sqrt{P_1 - P_R}\, dX_{sv} + \left(\dfrac{C_{sv} X_{sv}}{2 \sqrt{P_1 - P_R}} \right) dP_1 & \text{for } X_{sv} < 0 \end{cases}$$

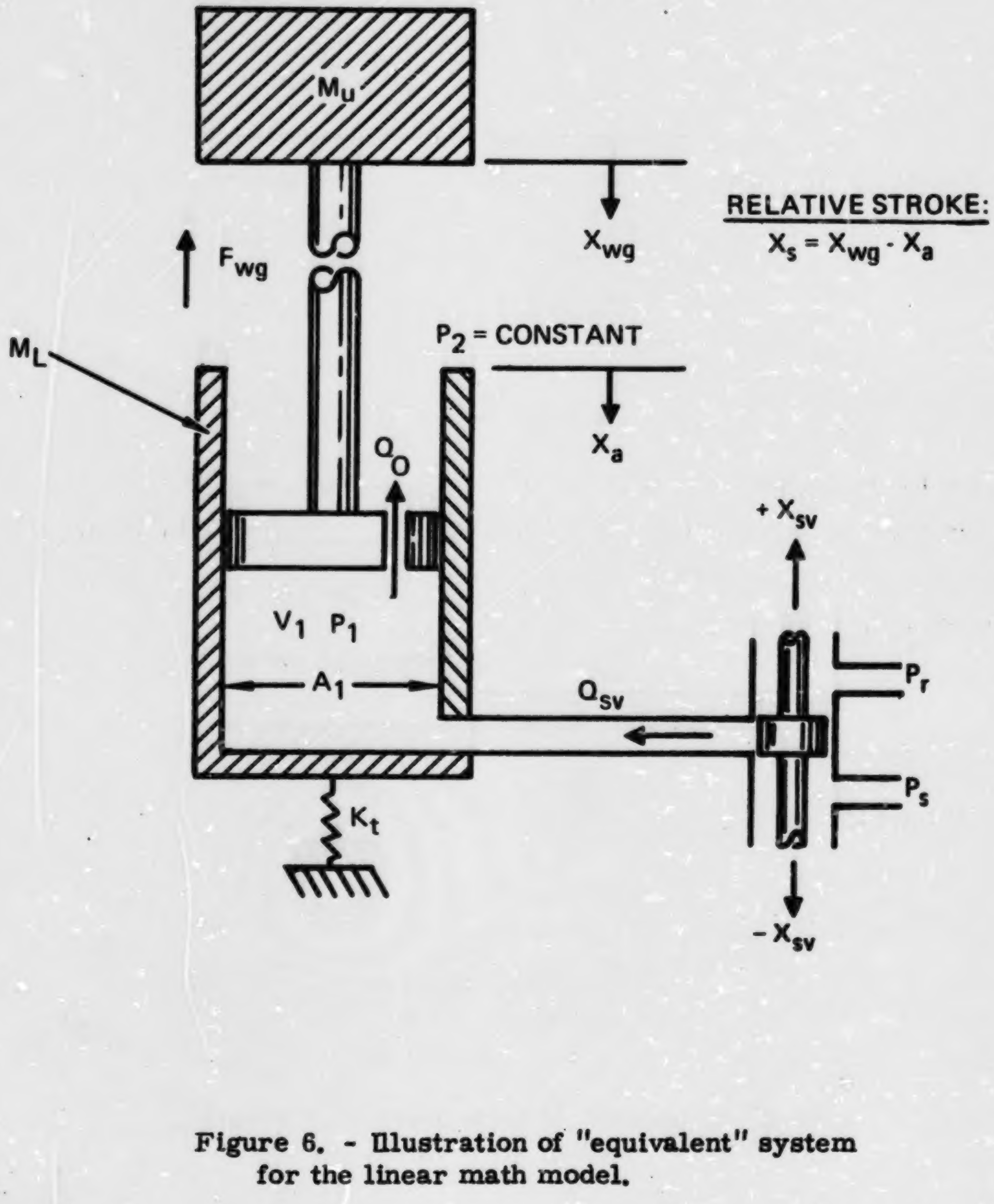
M_u
F_wg
X_wg
RELATIVE STROKE:
X_s = X_wg - X_a
M_L
P_2 = CONSTANT
X_a
Q_O
+X_sv
V_1 P_1
A_1
Q_sv
P_r
P_s
K_t
-X_sv

Figure 6. - Illustration of "equivalent" system for the linear math model.

Letting the mean value of the pressure P_1 equal $(P_S + P_R)/2$, and assuming small perturbations about this mean condition, the above relationships can be expressed as

$$dQ_{sv} = CQ \cdot dX_{sv} - CP \cdot dP_1 \qquad \text{...(18)}$$

where

$$CQ = \frac{\partial Q_{sv}}{\partial X_{sv}} = C_{sv} \sqrt{(P_S + P_R)/2}$$

$$CP = -\frac{\partial Q_{sv}}{\partial P_1} = -CQ/PG$$

and where PG is the pressure gain of the spool in terms of pressure per spool displacement, at constant flow. In the linearized model the values of CQ and CP are assume constant.

The flow through the fixed orifice is

$$Q_o = K_o \sqrt{P_1 - P_2}$$

Differentiating this gives

$$dQ_o = \left(\frac{K_o}{2 \sqrt{P_1 - P_2}} \right) dP_1 = CP_o \, dP_1 \qquad \text{...(19)}$$

However, note that at the mean condition P_1 equals P_2, so the coefficient CP_o is undefined. In actuality, CP_o is a function of excitation amplitude and frequency. It is important to keep this fact in mind when applying the linearized model. The approach taken in this study was to vary CP_o over a reasonable range to determine its influence on the dynamic response of the system, and to proceed accordingly.

Substituting equations 18 and 19 into equation 17, solving for P_1, and expressing it in LaPlace transform notation gives

$$P_1 = \frac{CQ \cdot X_{sv} + A_1 s X_s}{\frac{V_1}{\beta} s + (CP_o + CP)} \qquad \ldots(20)$$

The transfer function of the servovalve dynamics in terms of output displacement of the third stage spool for input current was derived in the preceding section (equation 12) and is

$$\frac{X_{sv}}{i_2} = \frac{K_{sv}}{\left(\frac{s^2}{\omega^2_{sv}} + \frac{2\zeta_{sv}}{\omega_{sv}} s + 1\right)\left(\frac{s}{\omega_c} + 1\right)}$$

The transfer function for the electronic compensation network, which is derived in the next section, is

$$\frac{i_2}{i_1} = \left(\frac{s^2 + 2\zeta_2 \omega_1 s + \omega_1{}^2}{s^2 + 2\zeta_1 \omega_1 s + \omega_1{}^2}\right)\left(\frac{\tau_1 s + 1}{\tau_2 s + 1}\right)\left(\frac{\tau_3 s + 1}{\tau_4 s + 1}\right) \qquad \ldots(21)$$

The relationship describing the force feedback and the position loop feedback is

$$i_1 = K_a (F_{lim} - F_{wg}) - K_a \left(\frac{K_f}{\tau_f s + 1}\right)(X_c - K_x X_s) \qquad \ldots (22)$$

Equations 14, 15, 16, 20, 12, 21 and 22 make up the complete linarized model, and Figure 7 is a block diagram arrangement of these equations. The algebraic solution of transfer functions from this set of equations would be very tedious, so this practice was avoided. The following approach was taken. First, working from the block diagram, the system of equations is expressed in matrix form, where each element of the matrix is in general a polynomial in "s". A computer program is then used to solve for the coefficients of the numerator and denominator of the desired transfer function using Cramer's Rule. Frequency response characteristics are then calculated from the transfer function. Also, the roots of the numerator and denominator polynominals are easily determined using standard computer techniques. The linear model gives very rapid results, and thus is ideal for evaluating the effect of varying different parameters and for developing electronic compensation networks for stability.

The validity of the linear model was evaluated by comparing the open loop frequency response with results obtained from the nonlinear vertical drop model described in the preceding section. The loop was opened at the point of wing gear force (F_{wg}) feedback, and position feedback was not included. The conditions were for zero lift with the shock strut at a mean stroke equal to that required to balance the weight of the airplane, which was 67 percent of maximum stroke for this case. Also, no electronic compensation was used.

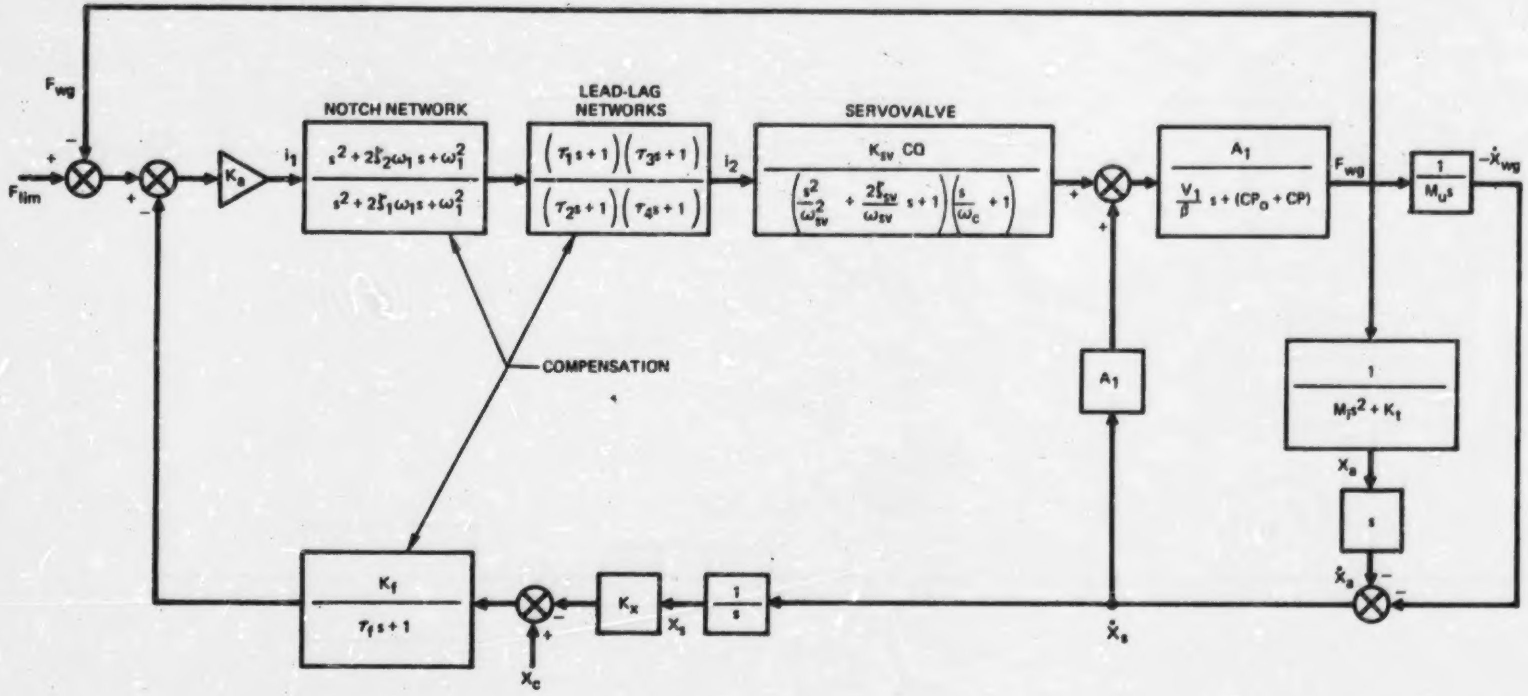

F_{wg}
F_{lim}
+
−
+
−
K_a
i_1
NOTCH NETWORK
$\frac{s^2 + 2\zeta_2\omega_1 s + \omega_1^2}{s^2 + 2\zeta_1\omega_1 s + \omega_1^2}$
LEAD-LAG NETWORKS
$\frac{(\tau_1 s + 1)(\tau_3 s + 1)}{(\tau_2 s + 1)(\tau_4 s + 1)}$
i_2
SERVOVALVE
$\frac{K_{sv}\ CQ}{\left(\frac{s^2}{\omega_{sv}^2} + \frac{2\zeta_{sv}}{\omega_{sv}} s + 1\right)\left(\frac{s}{\omega_c} + 1\right)}$
+
+
$\frac{A_1}{\frac{V_1}{\beta} s + (CP_0 + CP)}$
F_{wg}
$\frac{1}{M_u s}$
$-\dot{X}_{wg}$
COMPENSATION
A_1
$\frac{1}{M_j s^2 + K_t}$
X_a
s
$\dot{X}_a$
−
−
$\frac{K_f}{\tau_f s + 1}$
−
+
X_c
K_x
X_s
$\frac{1}{s}$
$\dot{X}_s$

Figure 7. - Block diagram of linear math model

The comparison of results is shown in Figure 8. Input is commanded limit force and output is wing gear force. Linear model results are shown for both a low and a high value of the fixed orifice parameter CP_o. The results for the low value of CP_o match the nonlinear results closest at low frequencies while the results for the high value of CP_o match closest at high frequencies. The basic trends are predicted reasonably well and it is concluded that the linear model is a valid tool for performing initial design and stability studies.

Energy Considerations

The primary function of the landing gear control system is to control the wing gear force at some commanded level. A secondary but necessary function of the controller is to set this commanded level such that the strut will not fully collapse, precluding structural damage. In order to do this, the controller must be able to monitor the energies present in the system during impact, and then set the limit force accordingly so that the work potential of the shock strut will be sufficient to absorb these energies. In order to study the feasibility of the controller performing this function, it is worthwhile to undergo an analytical development of the various energies present in the system and relate them to the work performed by the shock strut — the subject of this section. The equations will be developed from the equations of motion of the simplified vertical drop case, presented earlier; however, the results are almost directly applicable to the more general cases.

Equations 3 and 5 are the inertial equations of motion corresponding to the two independent masses M_U and M_L. These equations are rewritten in a form where each term represents the differential of an energy or work. This is done by multiplying equation 5 by dX_{wg} and equation 3 by dX_a, resulting in

$$M_u V_{wg} dV_{wg} = [M_u g - L - (P_1 - P_2)(A_1 - A_0) - P_2 A_2 + P_3 A_3 \mp f]\, dX_{wg} \qquad \ldots (23)$$

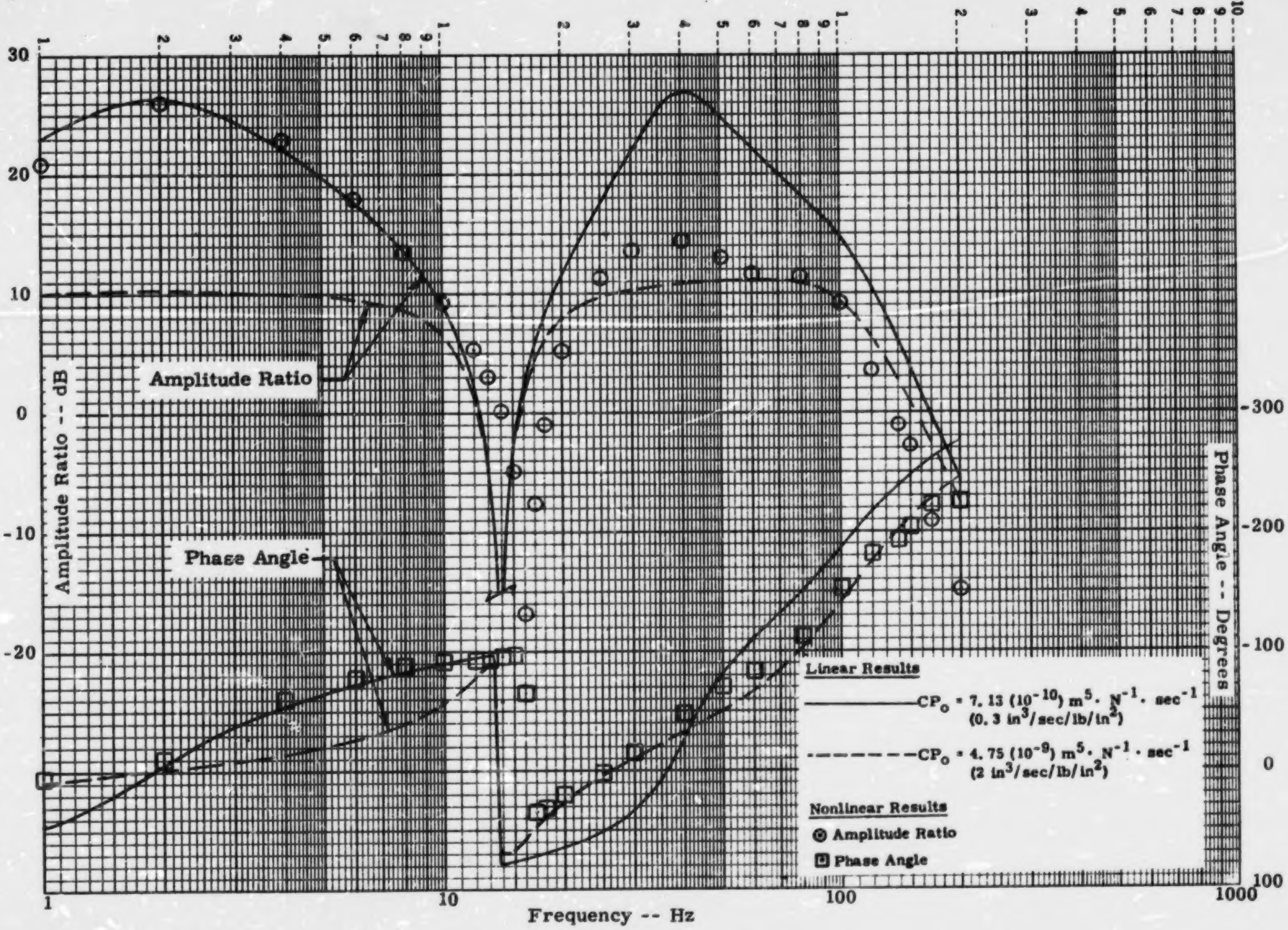

Figure 8. - Comparison of linear model and nonlinear model results, open loop, no compensation, no position feedback.

$$M_L V_a \, dV_a = [M_L g + P_2 (A_2 - A_1) + P_1 A_1 - P_3 A_3 - F_a \pm f] \, dX_a \qquad \ldots(24)$$

Note that if these equations are integrated from some initial condition to a final condition they express changes in energy that occur over that time interval. For example, the integral of the terms on the left side of the equations express the total change in kinetic energy of each mass. It is desired now to write an equation expressing the total change in kinetic energy of the system, which is assumed to consist entirely of the two masses M_U and M_L, as a function of the various other energy and work terms. This is done by adding equations 23 and 24, resulting in

$$\overbrace{M_u V_{wg} \, dV_{wg}}^{1} + \overbrace{M_L V_a \, dV_a}^{2} + \overbrace{[-M_u g}^{3} + \overbrace{L}^{4} \overbrace{-(P_1 - P_2) A_o}^{5}] \, dX_{wg}$$

$$+ \overbrace{[-M_L g}^{6} + \overbrace{F_a}^{7}] \, dX_a + \overbrace{[(P_1 - P_2) A_1}^{8} + \overbrace{P_2 A_2 - P_3 A_3}^{9} \overbrace{\pm f}^{10}] \, dX_s = 0 \qquad \ldots(25)$$

Equation 25 can be thought of as a statement of conservation of energy, since it essentially says that the sums of all changes in energy and work done in the system equals zero. Some of the terms in equation 25 are easily recognizable as to the type of energy they represent. For example, terms 1 and 2 represent changes in kinetic energy. Terms 3 and 6 represent changes in potential energy of the upper and lower masses due to height changes. Term 7 represents changes in potential energy stored in the tire spring. Term 10 represents energy dissipation due to Coulomb friction. Energy dissipation due to flow across the shock strut orifice also occurs, although this is not directly identifiable in equation 25 because of the complicating effects of fluid compressibility and flow to and from the active-control servovalve.

Equation 25 must be simplified to the point where it becomes a useful tool to the controller for monitoring the energies present in the system in terms of the available input signals; e.g., accelerometers, transducers, etc. First, term 5 was found to be negligible and can be immediately eliminated. Next, the combination of terms in the third bracket (terms 8, 9 and 10) are approximately equivalent to the shock strut force F_s. This can be seen by referring back to equation 2, neglecting the inertia and gravity forces on the shock strut portion of the upper mass, and neglecting the orifice area with respect to the piston area. With these simplifications, equation 25 is rewritten as

$$M_U V_{wg} dV_{wg} + M_L V_a dV_a + (-M_U g + L)\, dX_{wg} + (-M_L g + F_a)\, dX_a + F_s dX_s = 0 \qquad \ldots (26)$$

Note that the quantity $F_s dX_s$ represents the differential of the work performed by the shock strut. Integration of this equation over a given interval will thus yield an expression showing the net work performed by the shock strut as a function of the various other energy changes. The task of the controller is to monitor these energies and make sure that the remaining work potential of the shock strut is sufficient to dissipate them.

At this point, it is worthwhile summarizing the instrumentation that is available to the controller as originally proposed.

(1) Wing/gear acceleromters - measures $\ddot{X}_{wg}$
(2) Hub accelerometer - measures $\ddot{X}_a$
(3) LVDT on shock struct - measures X_s
(4) Upper cylinder pressure transducer - measures P_2 (pneumatic)
(5) Lower piston pressure transducer - measures P_1 (hydraulic).

With this instrumentation, it is not possible to apply equation 26 to the task at hand, because there is no way to monitor the lift L or the shock strut force F_s (note that by knowing one of these, the other may be obtained equation 1). It is therefore necessary to make further simplifications. Assuming that the total airplane weight equals the lift throughout impact, and neglecting the $M_L g$ term, then equation 26 becomes

$$M_U V_{wg} dV_{wg} + M_L V_a dV_a + F_a dX_a + F_s dX_s = 0 \qquad \ldots(27)$$

With the weight-equals-lift assumption, all of the parameters in equation 27 may be obtained. From equation 1,

$$F_s = -M_U \ddot{X}_{wg} \qquad \ldots(28)$$

It is possible to solve for F_a by first noting that equation 3 may be expressed as

$$M_L \ddot{X}_a \approx -F_a + F_s \qquad \ldots(29)$$

Substituting equation 28 for F_s into equation 29,

$$F_a \approx - M_U \ddot{X}_{wg} - M_L \ddot{X}_a \qquad \ldots(30)$$

The individual terms in equation 27 were integrated with respect to time throughout a typical vertical drop simulation using the simplified nonlinear vertical drop model described in a previous section to determine if the equation is indeed a valid representation of all the major energy changes that take place. The lift was set equal to the weight throughout the simulation, so this test case will say nothing regarding the validity of the "weight-equals-lift" simplification. The validity of that will be demonstrated later using actual land and roll simulations. The integrated variables are shown plotted in Figure 9. The sum of all the integrated variables is also shown, representing the total energy plus work done by the system. This should remain constant from the conservation of energy principle. It is indeed relatively constant, thus supporting the validity of equation 27, at least for vertical drop cases where weight equals lift. Note that the kinetic energy of the lower mass is negligible. Also, the potential energy stored in the tire, although not completely negligible, is a minor part of the total energy of the system. This raises the question whether it is worth the added complexity of including this term in the energy computations of the controller. The approach taken here is to neglect it and incorporate any errors into an empirical correction factor, if necessary. As a result, the only terms considered in the energy computations of the controller are the kinetic energy of the upper mass and the work of the shock strut.

The next step is to derive relationships that the controller can apply in setting the commanded limit force to a level such that bottoming of the strut will be prevented. There are various approximations or simplifications that can be made, some of which have already been mentioned in the preceding paragraph, which will introduce errors in the final result. In the interest of completeness and for reference, the more general derivation will be presented first, followed by the simplifications. The procedure is to integrate equation 27 from a time t_1 (controller initiation) to the end of transition; i.e., the start of rollout. The following assumptions are made.

(1) The actual wing/gear force is identical to the commanded limit force throughout the impact and transition phases.

(2) The velocity of the masses is zero at the end of transition (this also is the criterion used in calculating the wing/gear velocity at which transition begins).

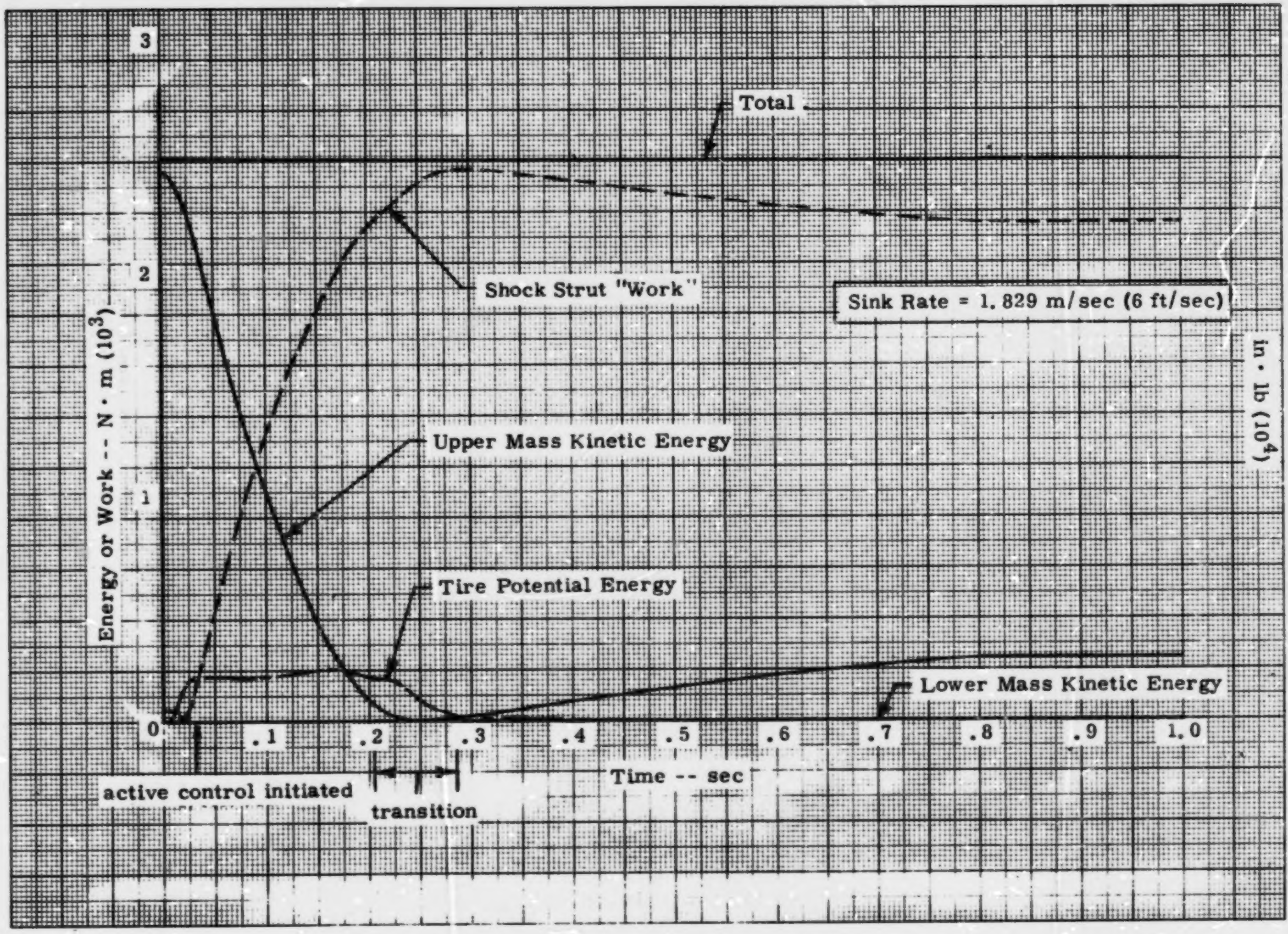

Figure 9. - Various energy terms versus time, from the simplified nonlinear vertical drop simulation.

(3) The commanded limit force is constant throughout the impact phase and linearly decreases during transition to zero limit force at the beginning of rollout. The slope in the transition phase is a known quantity.

A sketch of the variation of wing/gear force versus time for the above conditions is shown in Figure 10. Integration of equation 27 from t_1 to the start of transition t_{tr} gives

$$1/2\ M_u\,(V^2_{u_{tr}} - V^2_u) + 1/2\ M_L\,(V^2_{L_{tr}} - V^2_L) + \int_{t_1}^{t_{tr}} F_a\, dX_a + F_{li}\,\Delta X_{s_{im}} = 0$$

Integration from the start of transition t_{tr} to the end of transition t_r gives

$$1/2\ M_u\,(\cancelto{0}{V^2_{u_r}} - V^2_{u_{tr}}) + 1/2\ M_L\,(\cancelto{0}{V^2_{L_r}} - V^2_{L_{t_r}}) + \int_{t_{tr}}^{t_r} F_a\, dX_a + \frac{F_{li}}{2}\,\Delta X_{s_{tr}} = 0$$

The quantities $\Delta X_{s_{im}}$ and $\Delta X_{s_{tr}}$ represent the shock strut stroke used in the impact and transition phases, respectively. The sum of these should be equal to or less than the total remaining available stroke, to prevent bottoming. Solving for ΔX_{s_i} and $\Delta X_{s_{tr}}$ in these equations and adding them together gives

$$\Delta X_s = \frac{1/2\ M_u(V^2_u - V^2_{u_{tr}}) + 1/2\ M_L\, V^2_{L_{tr}} - \int_{t_1}^{t_{tr}} F_a\, dX_a}{F_{li}} + \frac{1/2\ M_u\, V^2_{u_{tr}} + 1/2\ M_L\, V^2_{L_{tr}} - \int_{t_{tr}}^{t_r} F_a\, dX_a}{F_{li}/2} \qquad \ldots(31)$$

Referring back to Figure 9, it is shown that any potential energy changes in the tire during the impact phase may be neglected. This is true because F_a and X_a remain relatively constant throughout this phase. Also, since the final

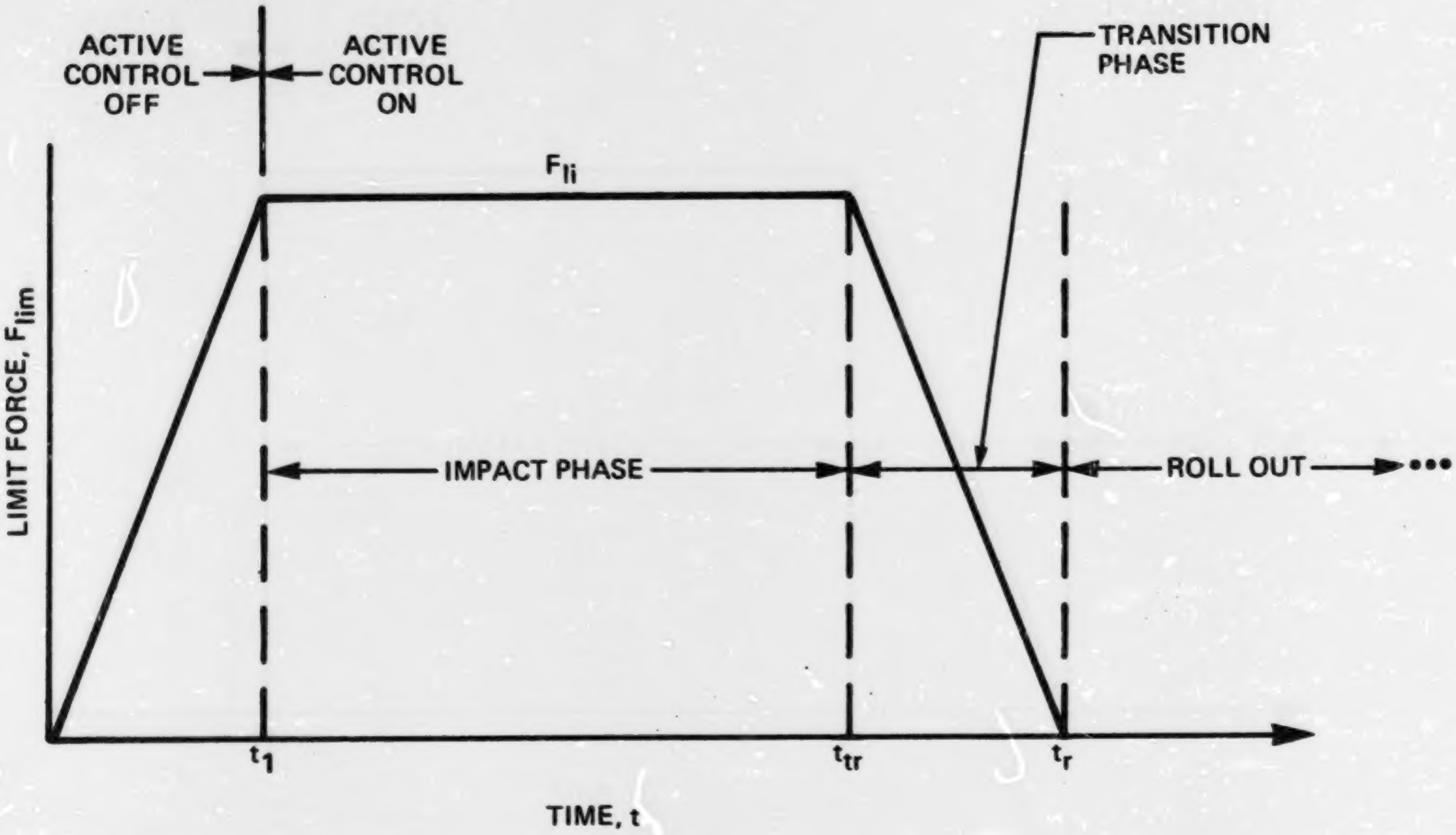
ACTIVE CONTROL OFF
ACTIVE CONTROL ON
TRANSITION PHASE
F_{li}
LIMIT FORCE, F_{lim}
IMPACT PHASE
ROLL OUT
t_1
t_{tr}
t_r
TIME, t

Figure 10. - Illustration of the variation of limit force versus time and the various phases of operation following impact.

rollout limit force is zero, F_a at that point will be approximately zero; and hence, roughly stated, that during transition the potential energy of the tire will go from its initial impact phase state to a zero energy state. This fact can be seen in Figure 9. Thus, in equation 31, the integral of $F_a dX_a$ over the interval t_1 to t_{tr} is approximately zero and the integral of $F_a dX_a$ over the interval t_{tr} to t_r is approximately equal to the negative of the potential energy stored in the tire at time t_1, the start of the integration interval. Signifying this energy level by the symbol PE_t, and neglecting the kinetic energy of the lower mass, equation 31 reduces to

$$F_{li} \Delta X_s = 1/2\, M_u V_u^2 + 1/2\, M_u (V_{u_{tr}})^2 + 2 \cdot PE_t \qquad \ldots(32)$$

The upper mass velocity at the start of transition can be determined by equating the impulse to the change in momentum for the transition phase, resulting in

$$V_{u_{tr}} = \frac{F_{li}^2}{2 \cdot M_u \cdot R_s} \qquad \ldots(33)$$

where R_s is the slope of the limit force with respect to time during transition.

The application of equation 32 to the controller could be as follows: when the gear first impacts the runway surface the controller is in a passive mode; that is, no command is being initiated to the servovalve. Immediately after impact, at discrete intervals, the controller will compute the strut work ($F_{li} \Delta X_s$) required to absorb the energy using equations 32 and 33. In equation 33, the transition velocity is calculated using the current value of wing/gear interface force as the impact limit force (i.e., F_{li} is set equal to F_{wg}).

This calculated value of required strut work is continually compared to a signal representing the actual strut work currently available if the controller were to go into active control at that instant. This actual strut work is simply the current value of the wing gear force times the remaining shock strut stroke. When comparison of these signals indicates that the available shock strut work exceeds the value calculated by equation 32, then active control to the servovalve is initiated and the commanded impact phase limit force is set equal to that current value of wing gear force. The velocity of transition is also then set to the value computed from equation 33.

It may be desirable to further monitor the energy situation through the remainder of the impact phase to ensure that the strut will not bottom due to additional energy inputs. If so, equations 32 and 33 could be used to compute F_{1i} from the known remaining strut stroke (ΔX_s), and if the computed F_{1i} ever exceeded the original F_{1i} value, the controller would update F_{1i} to the newly-computed value; however, this would require the solution of a quartic equation.

A simplification in equation 32 can be made by neglecting the transition region. In other words, assume that in Figure 10 the constant impact limit force is continued throughout the transition region, and at the end of transition it drops abruptly to the rollout limit force of zero. It should also be stressed that it is not being proposed that the actual limit force commanded by the controller follow this pattern; this is only for the purpose of simplifying the energy relationships. Integration of equation 27 will then result in

$$1/2\ M_u\,(V^2_{u_r} - V^2_u) + 1/2\ M_L\,(V^2_{L_r} - V^2_L) + \int_{t_1}^{t_r} F_a\,dX_a + F_{li}\,\Delta X_s = 0 \qquad \ldots(34)$$

Again, the integral of $F_a dX_a$ from t_1 to t_r is approximately equal to the negative of the potential energy stored in the tire at time t_1. Neglecting the kinetic energy of the lower mass, equation 34 becomes

$$F_{li}\,\Delta X_s = 1/2\, M_u V_u^2 + PE_t \qquad \text{...(35)}$$

with equation 33 still applying for the velocity of transition. The use of equations 35 and 33 in the controller would be similar to that already described for equations 32 and 33.

A still further simplification, in addition to those already made, is to neglect the potential energy in the tire. Equation 35 then reduces to

$$F_{li}\,\Delta X_s = 1/2\, M_u\, V_u^2 \qquad \text{...(36)}$$

with equation 33 still applying for the velocity of transition. This last approach is the one taken in the current design, and is the one programmed into the computer simulations.

To extend the use of equation 36 to actual land and roll cases, $\Delta X_s \cos\theta$ is substituted in place of ΔX_s, where θ is the angle the shock strut axis makes with the vertical (gravitational) direction. The angle θ is equal to the pitch angle of the airplane fuselage plus the angle of the wing with respect to the airplane fuselage. Also, the velocity and force in equation 36 are now the components in the vertical, or gravitational direction. The energy relationship used for land and roll cases is then

$$F_{li}\,\Delta X_s \cos\theta = 1/2\, M_u\, V^2{}_u \qquad \text{...(37)}$$

For land and roll cases, the question of the validity of the "weight-equals-lift" simplication is raised. Whether or not this is valid is demonstrated by computer simulation of the actual landing roll cases provided by NASA. The simulation results are presented in the ANALYTICAL RESULTS section. Of interest to the present discussion, however, is the maximum resultant stroke that occurs in each case when the limit force is set according to equation 37 and the aforementioned procedure. Table I, presented in a later section, summarizes this information. As can be seen, the method is reasonably successful in setting the limit force so that a maximum amount of strut stroke is used in absorbing the impact energy.

Stability Analysis

The linear model discussed earlier was used to evaluate the frequency response and stability of the system. System parameters used were basically those given under SYMBOLS. The linearized orifice coefficient CP_O was given a value of 7.13 (10^{-7}) $m^3/sec/kPa$ (0.3 $in^3/sec/lb/in^2$) for frequencies less than 14 Hz and a value of 4.75 (10^{-6}) $m^3/sec/kPa$ (2.0 $in^3/sec/lb/in^2$) for frequencies greater than 14 Hz, providing a reasonable match with frequency responses generated with the nonlinear model.

Based on results from the nonlinear vertical drop model, it was determined that a force loop bandwidth of 10 Hz would be adequate to achieve desired performance. Using the uncompensated linear model shown in Figure 11, the Nyquist plot of Figure 12 was generated. The uncompensated system was unstable at a frequency (140 Hz) related to the servovalve dynamics and could not be stabilized by simply lowering loop gain without violating the 10-Hz bandwidth goal. It was evident that signal shaping was required.

Analysis of various forms of forward path electronic compensation ultimately yielded the filter configuration shown in Figure 13. It consists of a second-order notch and two lead lags. The resulting Nyquist plot is shown in Figure 14; and, it can be seen that stability margins are adequate.

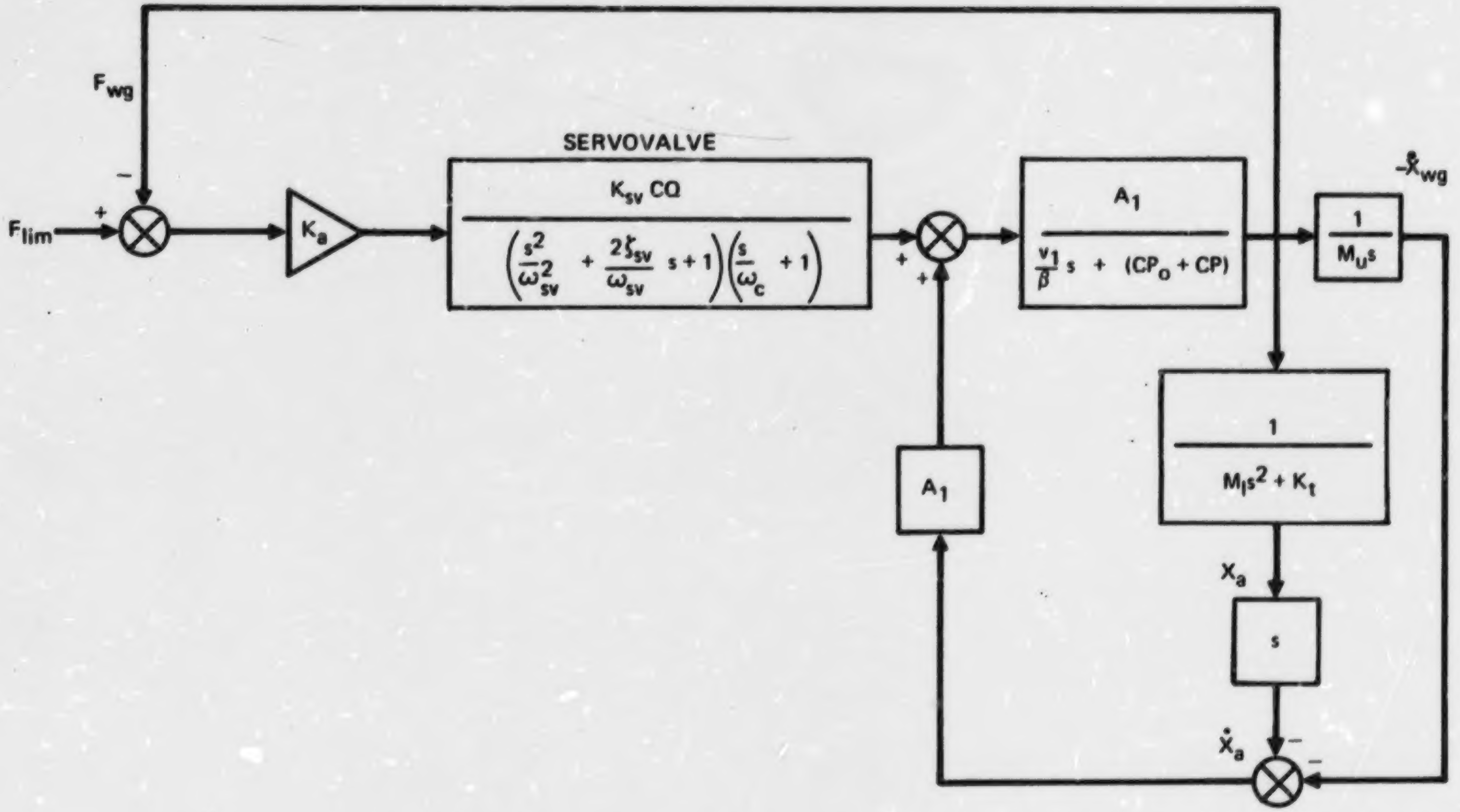
F_{wg}
−
+
F_{lim}
K_a
SERVOVALVE
$\dfrac{K_{sv}\,CQ}{\left(\dfrac{s^2}{\omega_{sv}^2} + \dfrac{2\zeta_{sv}}{\omega_{sv}} s + 1\right)\left(\dfrac{s}{\omega_c} + 1\right)}$
+
+
$\dfrac{A_1}{\dfrac{v_1}{\beta} s + (CP_o + CP)}$
$\dfrac{1}{M_u s}$
$-\dot{X}_{wg}$
A_1
$\dfrac{1}{M_l s^2 + K_t}$
X_a
s
$\dot{X}_a$
−
−

Figure 11. - Block diagram of linear system without compensation.

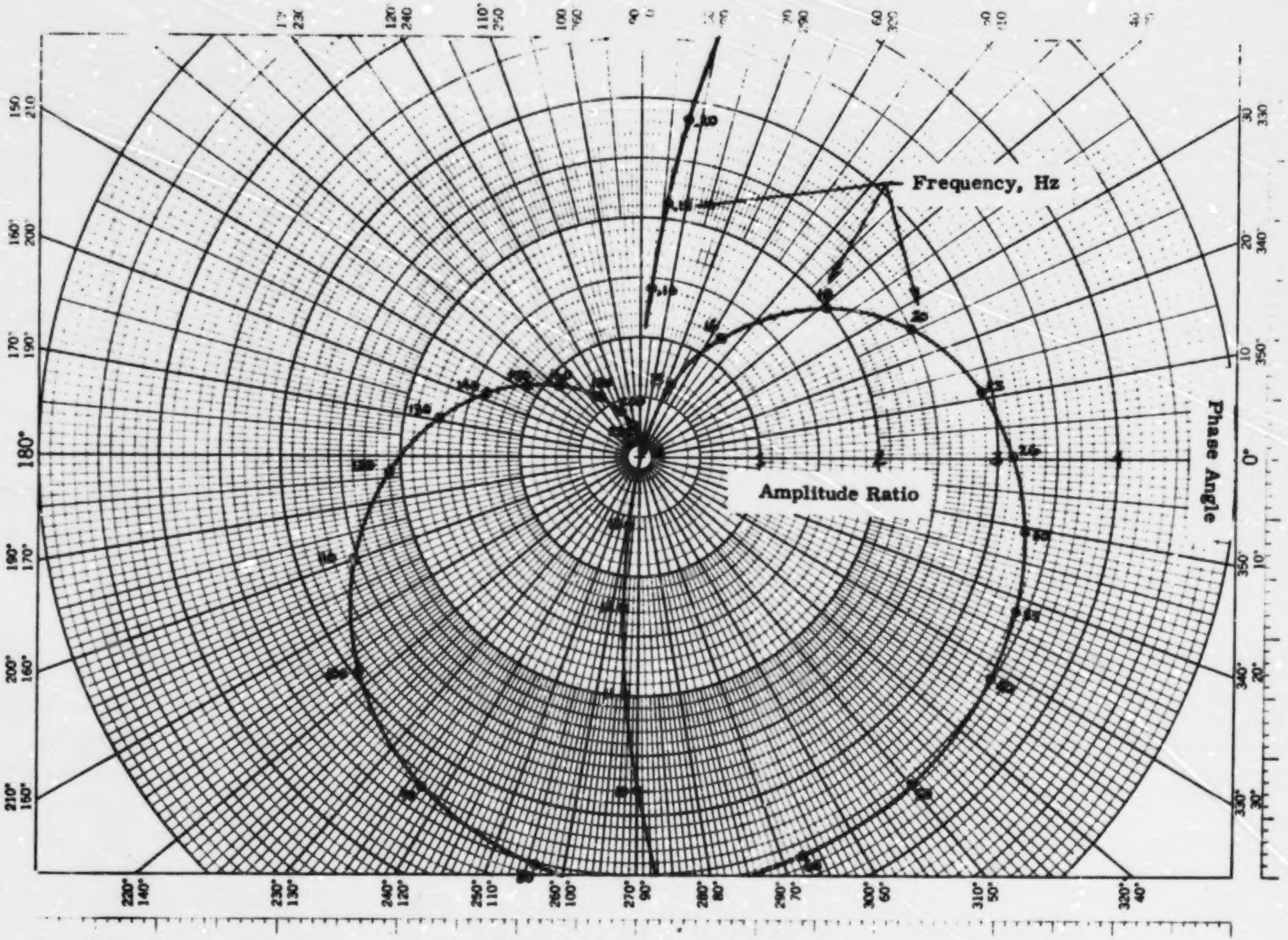

Figure 12. - Nyquist plot of F_{wg}/F_{lim} with force loop opened, no position feedback, no compensation.

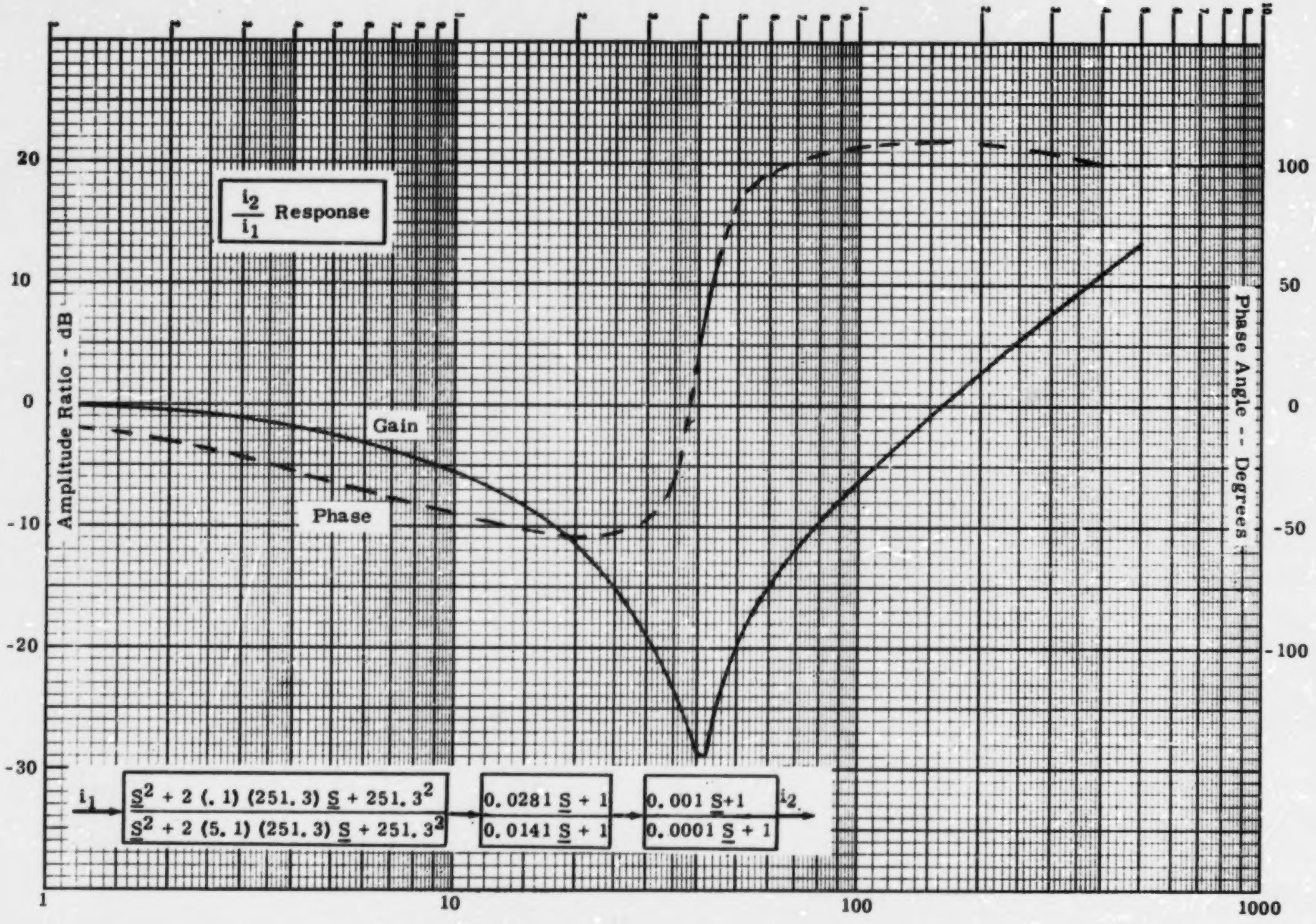

Figure 13. - Electronic compensation network and its characteristics.

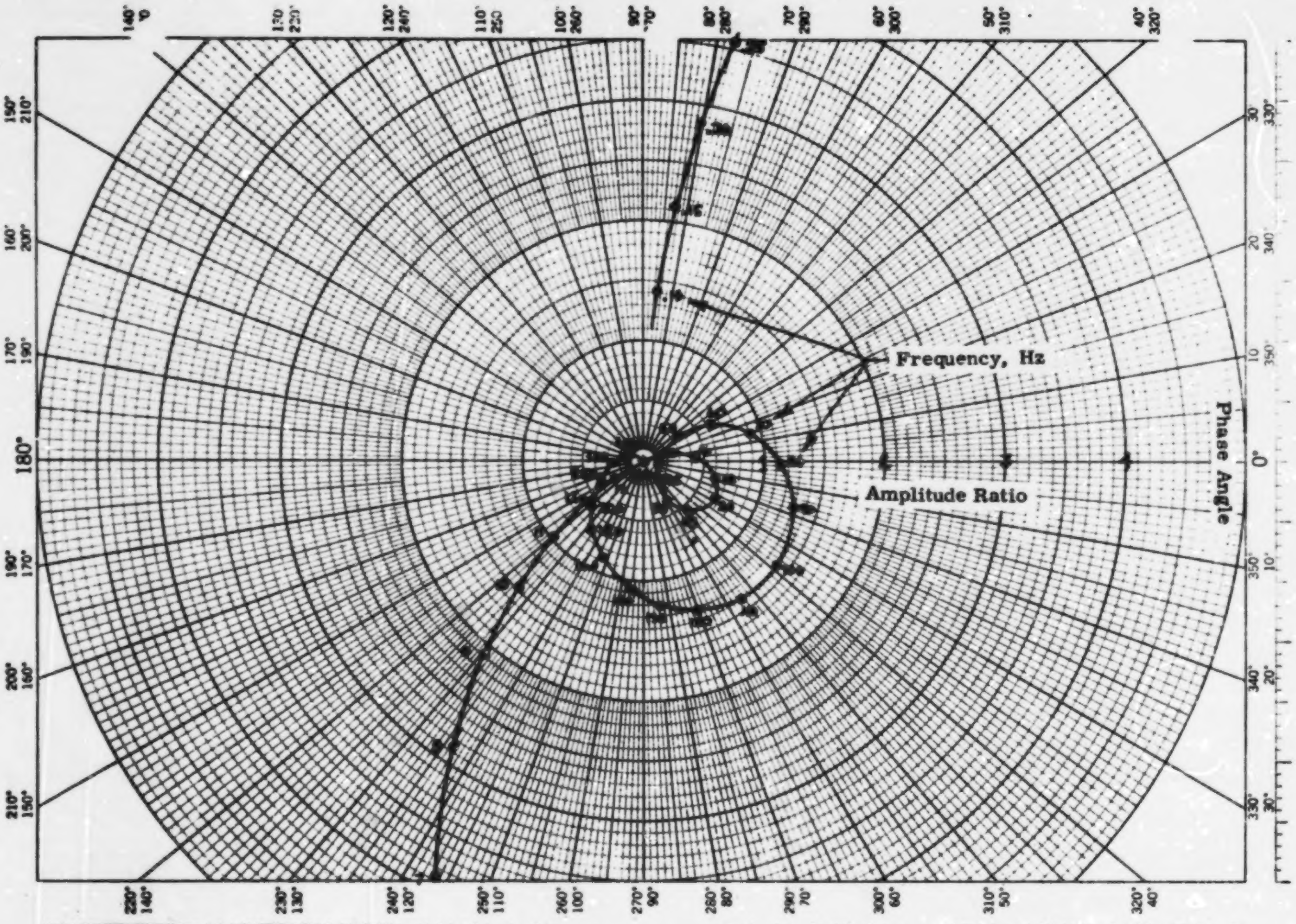

Figure 14. - Nyquist plot of F_{wg}/F_{lim} with force loop opened, no position feedback, with compensation.

The strut position feedback was next incorporated into the models. Its purpose is to ensure the return of the strut to its neutral position after landing impact. With no specific requirements on the time to return to neutral, it was assumed that a relatively gradual (approximately 10-sec) return would be acceptable. This assumption allowed a low bandwidth position loop which is essentially decoupled from the force loop. The resulting benefit is that the position loop can be continually active at all times during impact, transition, and rollout without degrading the performance of the force loop. A first-order lag in the position loop forward path yielded the desired results. The block diagram for the complete linearized system with position and force loops and compensation is shown in Figure 7.

Figure 15 shows the Nyquist plot of the F_{wg}/F_{lim} response for the complete system with the force loop opened and the position loop closed. Figure 16 shows the Nyquist plot of the X_s/X_c response with the position loop open and the force loop closed. Adequate stability margins are exhibited in these plots.

Figures 17 and 18 show the frequency response characteristics of the complete linearized system with the force and position loops closed, for F_{wg}/F_{lim} and X_s/X_c responses, respectively. Note that the bandwidth of the F_{wg}/F_{lim} response is about one hundred times greater than that for the X_s/X_c response.

The sensitivity of the system to hydraulic fluid compressibility was investigated because the effective bulk modulus of the air/oil mixture within the strut is relatively unknown. Throughout this study, a nominal bulk modulus of $6.89 (10^5)$ kPa (100 000 lb/in^2) was used based on past experience with hydraulic systems. Nyquist plots indicating system stability with bulk modulus values of $3.45 (10^5)$ kPa (50 000 lb/in^2) and $1.38 (10^6)$ kPa (200 000 lb/in^2) are shown in Figures 19 and 20. A linearized orifice coefficient of $7.13 (10^{-7})$ $\text{m}^3/\text{sec/kPa}$ (0.3 $\text{in}^3/\text{sec/lb/in}^2$) was used at all frequencies for these cases. A high bulk modulus is destabilizing in the 200-Hz range and a

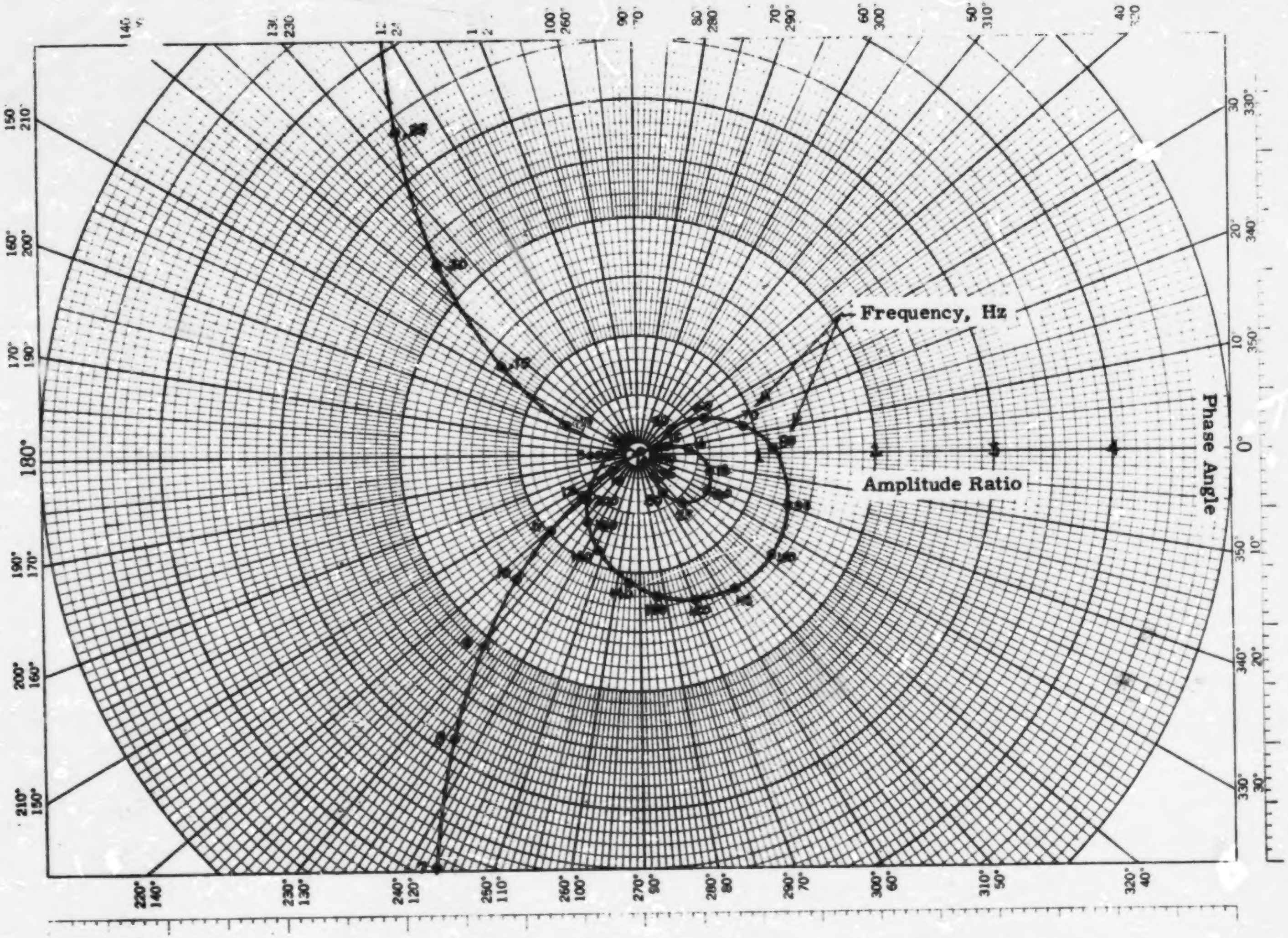

Figure 15. - Nyquist plot of F_{wg}/F_{lim} with force loop opened, position loop closed, with compensation.

45

BLANK PAGE

BLANK PAGE

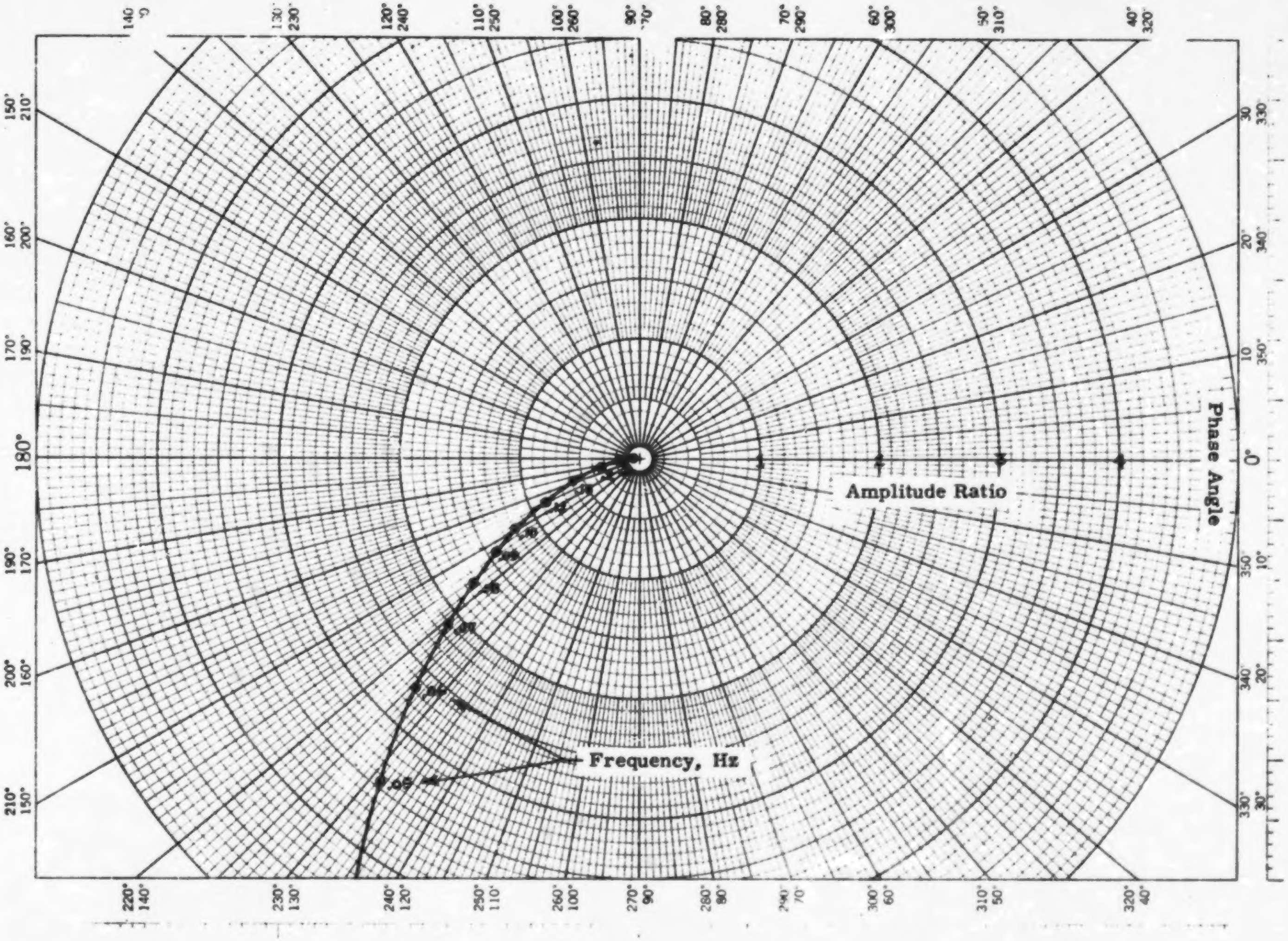

Figure 16. - Nyquist plot of X_s/X_c with position loop opened, force loop closed, with compensation.

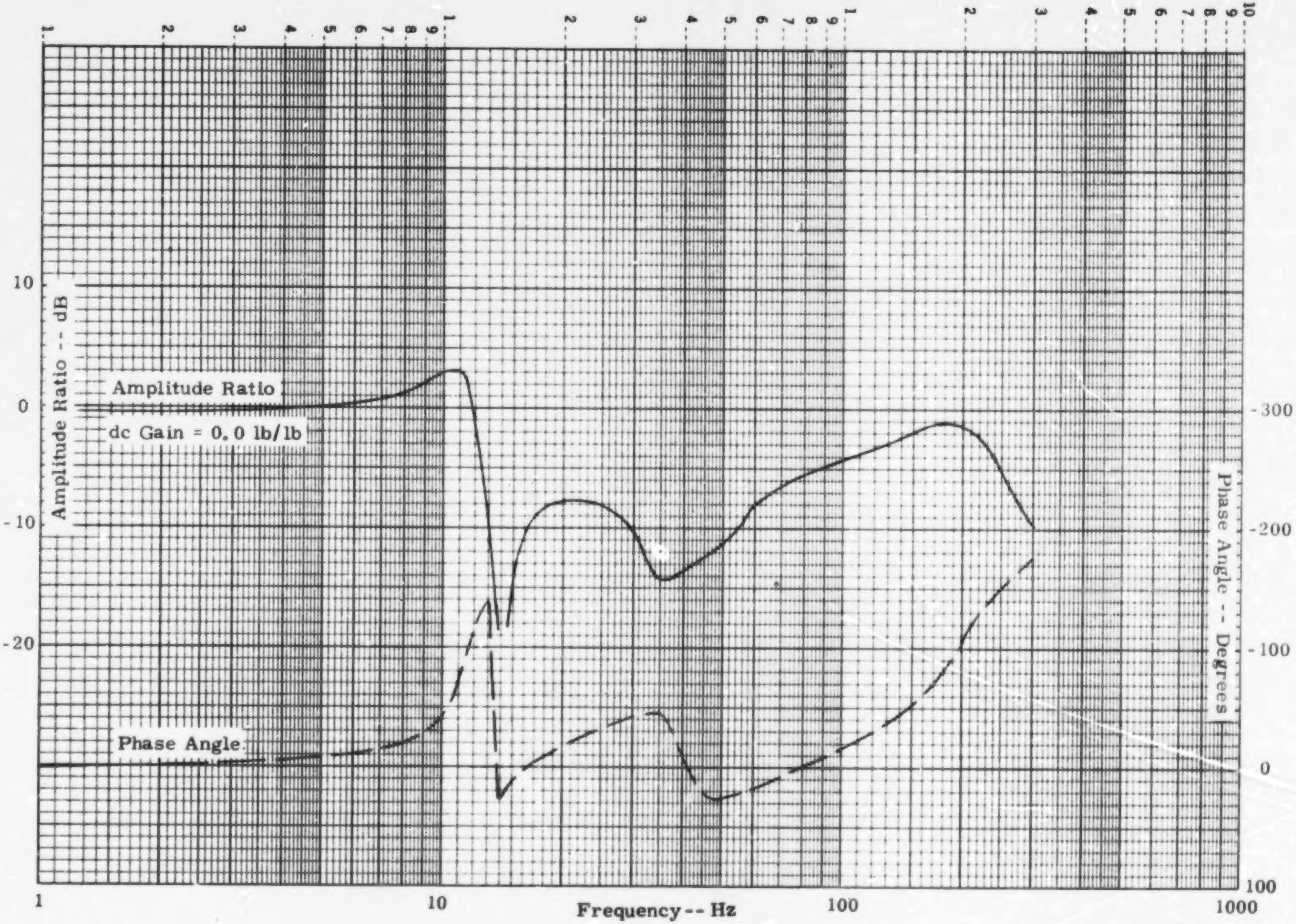

Figure 17. - Frequency response of F_{wg}/F_{lim} with force and position loops closed, with compensation.

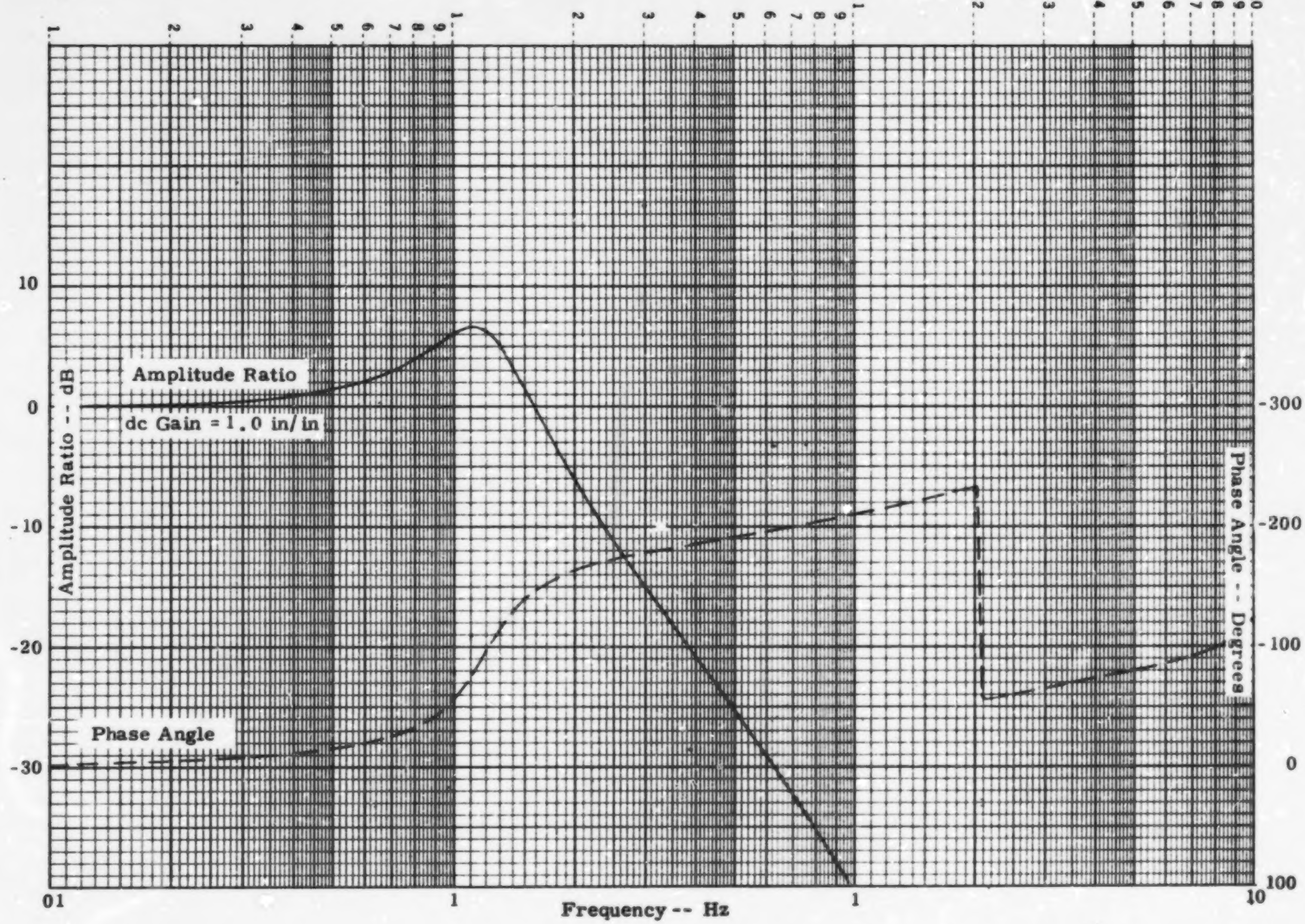

Figure 18. - Frequency response of X_s/X_c with force and position loops closed, with compensation.

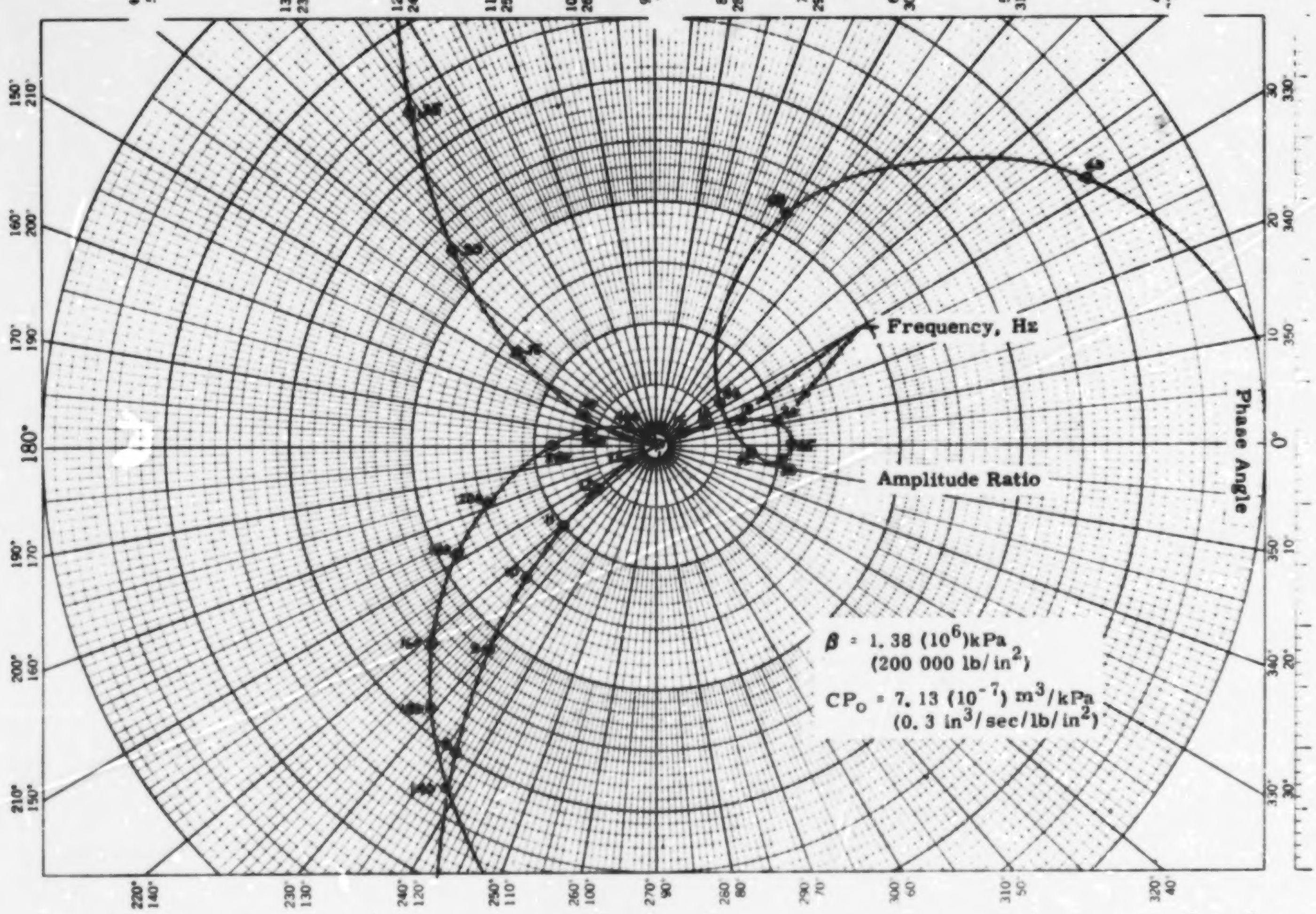

Figure 19. Nyquist plot of F_{wg}/F_{lim} with force loop opened, position loop closed, with compensation.

49

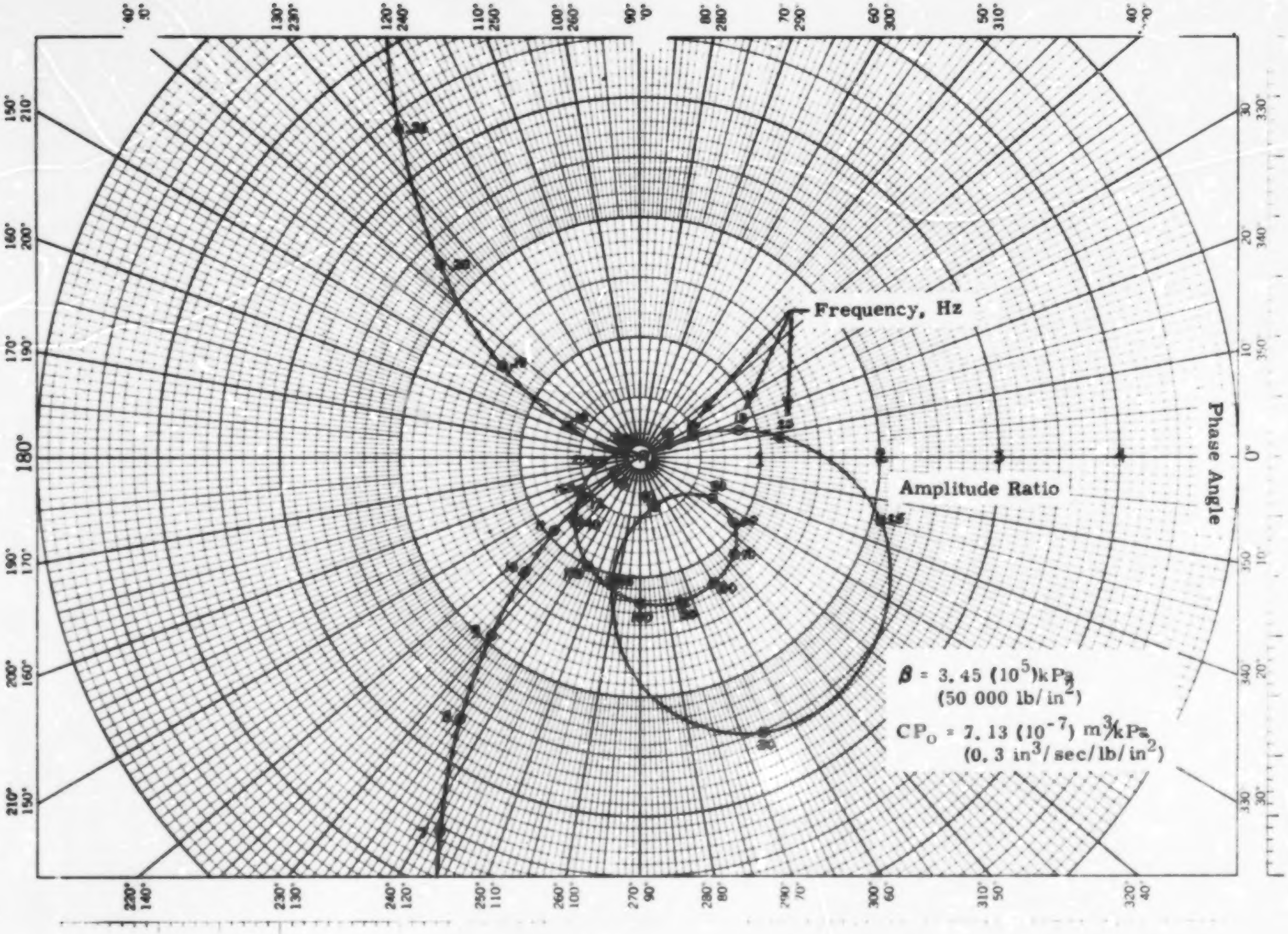

Figure 20. - Nyquist plot of F_{wg}/F_{lim} with force loop opened, position loop closed, with compensation.

low bulk modulus is destabilizing in the 100-Hz range. While these results show some sensitivity to bulk modulus, they are thought to be conservative in light of the model being used. It is expected that the bulk modulus in the actual strut will lie somewhere between 3.45 (10^5) and 1.38 (10^6) m^3/sec/kPa (50 000 and 200 000 lb/in^2), and that the system, as configured, will exhibit the desired performance.

ANALYTICAL RESULTS

In this section, transient response results obtained from digital computer simulations are presented for: (1) vertical drop cases using the simplified nonlinear vertical drop model presented earlier, and (2) actual land and roll cases provided by NASA using a NASA-supplied computer program which was modified by HR for incorporation into this study. The purpose of these simulations is to demonstrate that the landing gear controller is developed and described in the previous sections performs the desired functions satisfactorily.

The NASA computer program includes detailed simulation of the aerodynamic and aircraft dynamics in two dimensions, as opposed to the one dimension for the simplified vertical drop model. However, the NASA program as supplied to HR did not contain control system and servovalve dynamics and did not include the effect of fluid compressibility. Therefore, it was modified to include all these items.

Table I lists all the cases which were simulated and reported in this section, along with a brief description of each. Cases will be referred to by the case number shown in the left column. For each case, two simulations were run — one using an active control landing gear and one using a passive gear — so that the performance of the active gear in reducing wing forces could be evaluated.

TABLE I
SUMMARY OF ACTIVE CONTROL LANDING CASES SIMULATED ON THE COMPUTER

Case No.	Type	Sink Rate m/sec(in/sec)	Forward Speed m/sec(in/sec)	Miscellaneous Comments	Peak Strut Stroke	Reduction in Peak F_{wg} due to Active Control
A*	Vertical Drop	1.83 (72)	0	Lift=Weight	95%	28%
B*		1.83 (72)	0	Lift=Weight initially, linearly decreased by 50% over 0.4 sec interval	97%	23%
1	Land and Roll	1.83 (72)	42.7 (1680)	Sinusoidal runway (3Hz, ±0.0254 m (1 in)	91%	11%
2		1.83 (72)	42.7 (1680)	Flat runway, no braking	99%	23%
3		1.22 (48)	42.7 (1680)	Sinusoidal runway (.5 Hz, ±0.0254 m (1 in)	92%	18%
4		1.22 (48)	42.7 (1680)	Flat runway	83%	17%

* K_{FDGE} = 0.9 All other Cases K_{FDGE} = 1.0

Vertical Drop Cases

Figure 21 shows the commanded and actual wing gear forces occurring during the initial impact and transition phases for Case A. The total lift force is set equal to the total weight throughout this transient; and, as a consequence, the landing gear eventually lifts off the ground (or rebounds) after 0.754 seconds. At that time, the gear is fully extended and the system has some finite upward velocity which it continues to maintain as long as the lift stays equal to the weight. Figure 21 also shows the forces for the passive gear case. A 28% reduction in peak wing/gear force is obtained when using active control.

Figure 22 shows the forces for Case B. This is the same as Case A, except that starting from the instant of impact the lift force is linearly reduced to one half of its initial value. This reduction occurs over a time interval of 0.4 seconds. The gear does not leave the ground for this case. A 23% reduction in peak wing gear force from the passive gear case is obtained. The response of the strut stroke is shown in Figure 23. As the impact transients subside, the strut approaches the value commanded by the strut positioning loop.

Land and Roll Cases

Figure 24 shows the commanded and actual wing/gear forces occurring during the initial impact and transition phases for Case 1, which uses a 3-Hz, 0.0254 m (1-inch) amplitude sinusoidal runway for the first 3.083 seconds, then a flat runway. For this case, an 11% reduction in peak wing/gear force is obtained when using active control. Figure 25 shows the pressures in the strut as a function of time. Figure 26 shows the strut stroke transient. At a time of 1.86 seconds, the strut hits the stops in the fully extended position and remains there until 2.01 seconds. Figures 27 and 28 show the wing gear force

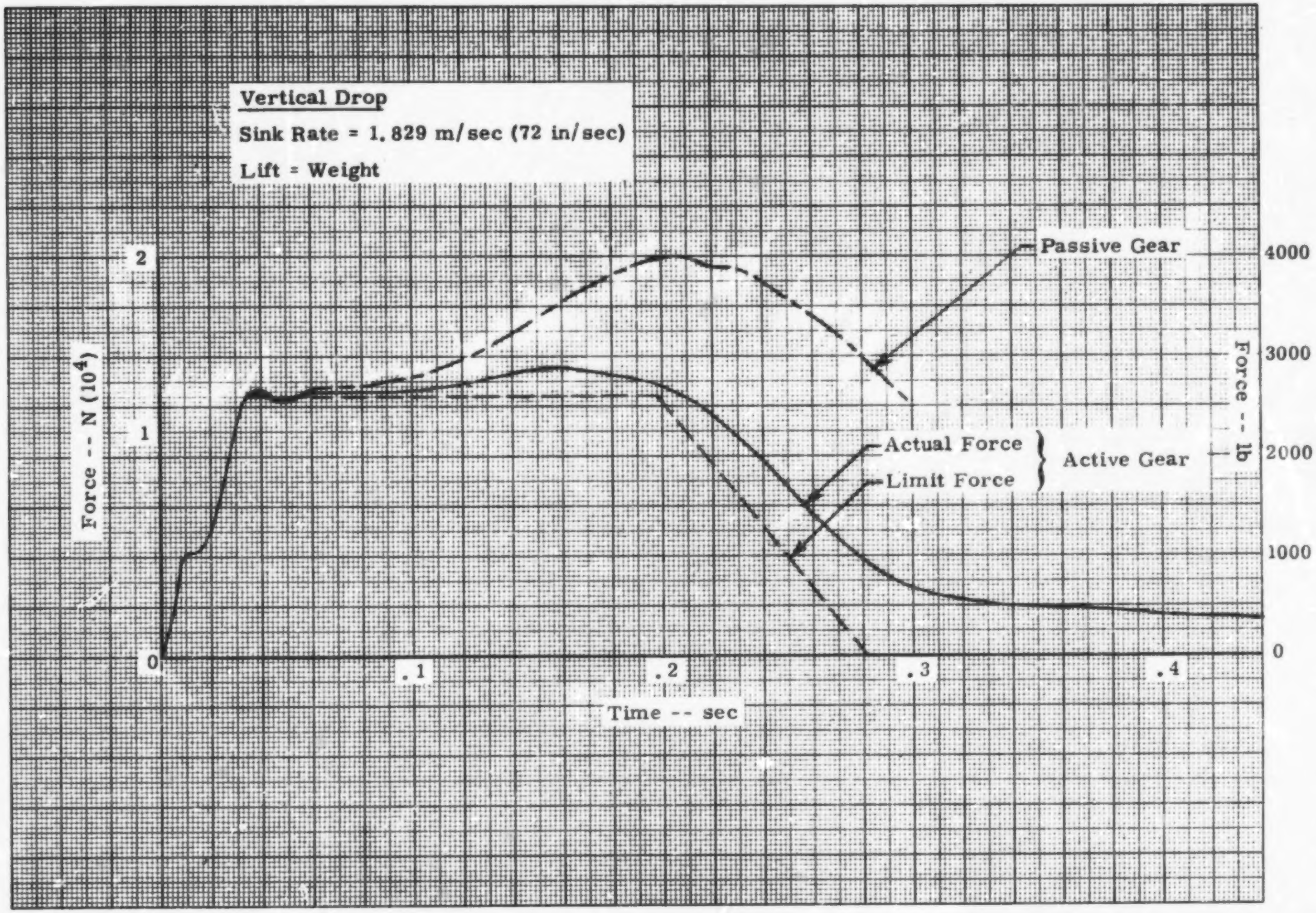

Figure 21. - Wing/gear force transient, case A.

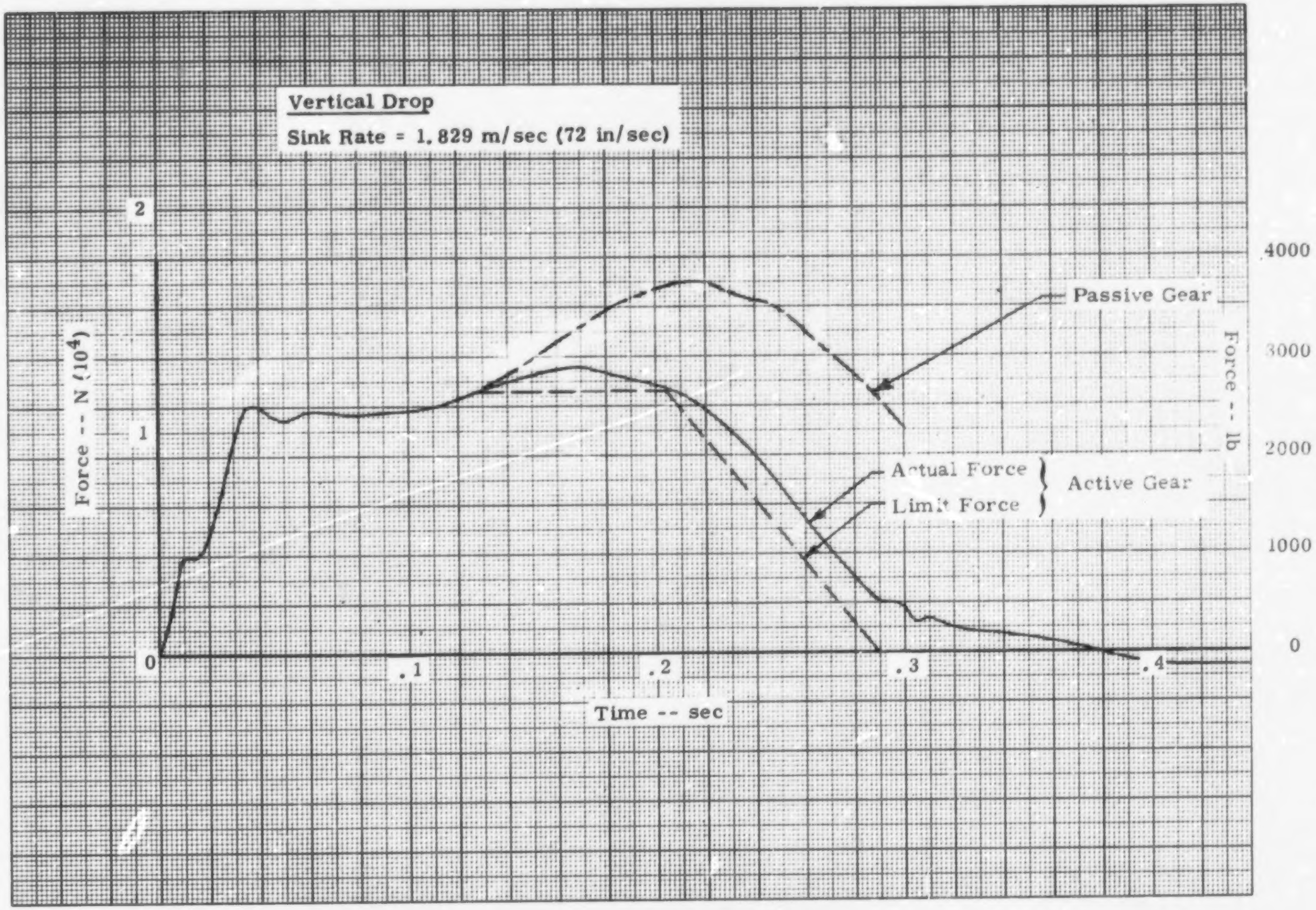

Figure 22. - Wing/gear force transient, case B.

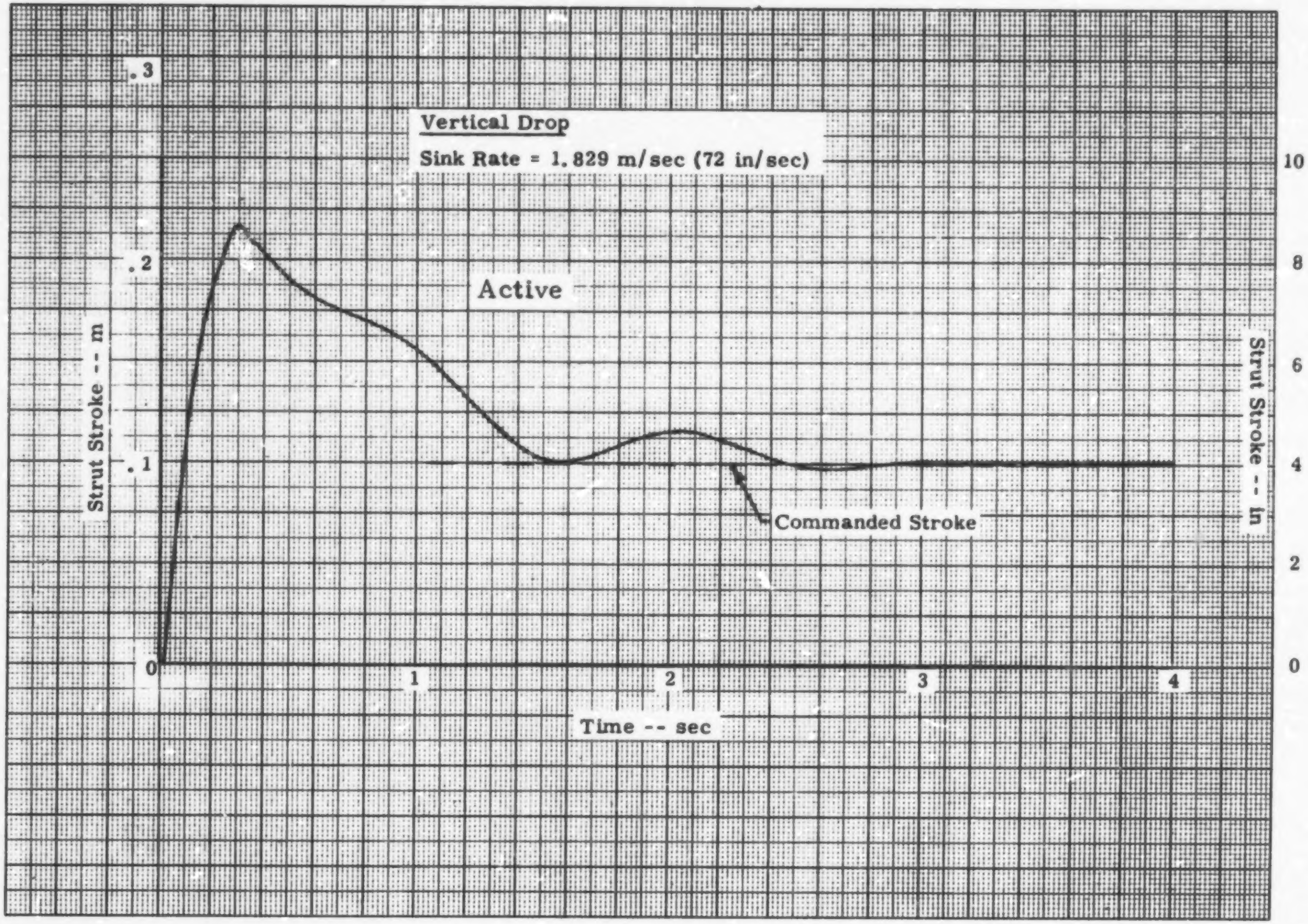

Figure 23. - Strut position transient, case B.

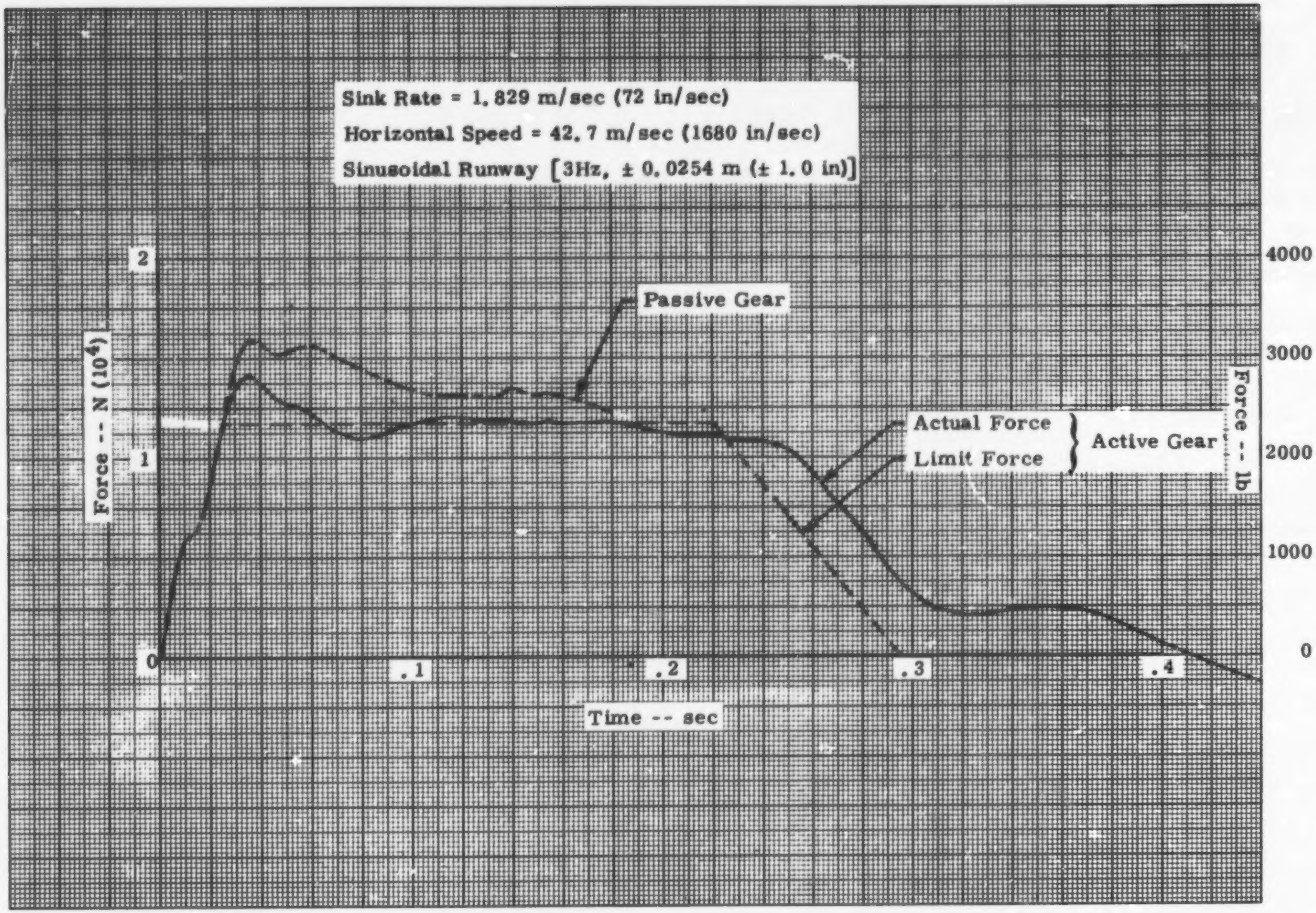

Figure 24. - Wing/gear force transient, case 1.

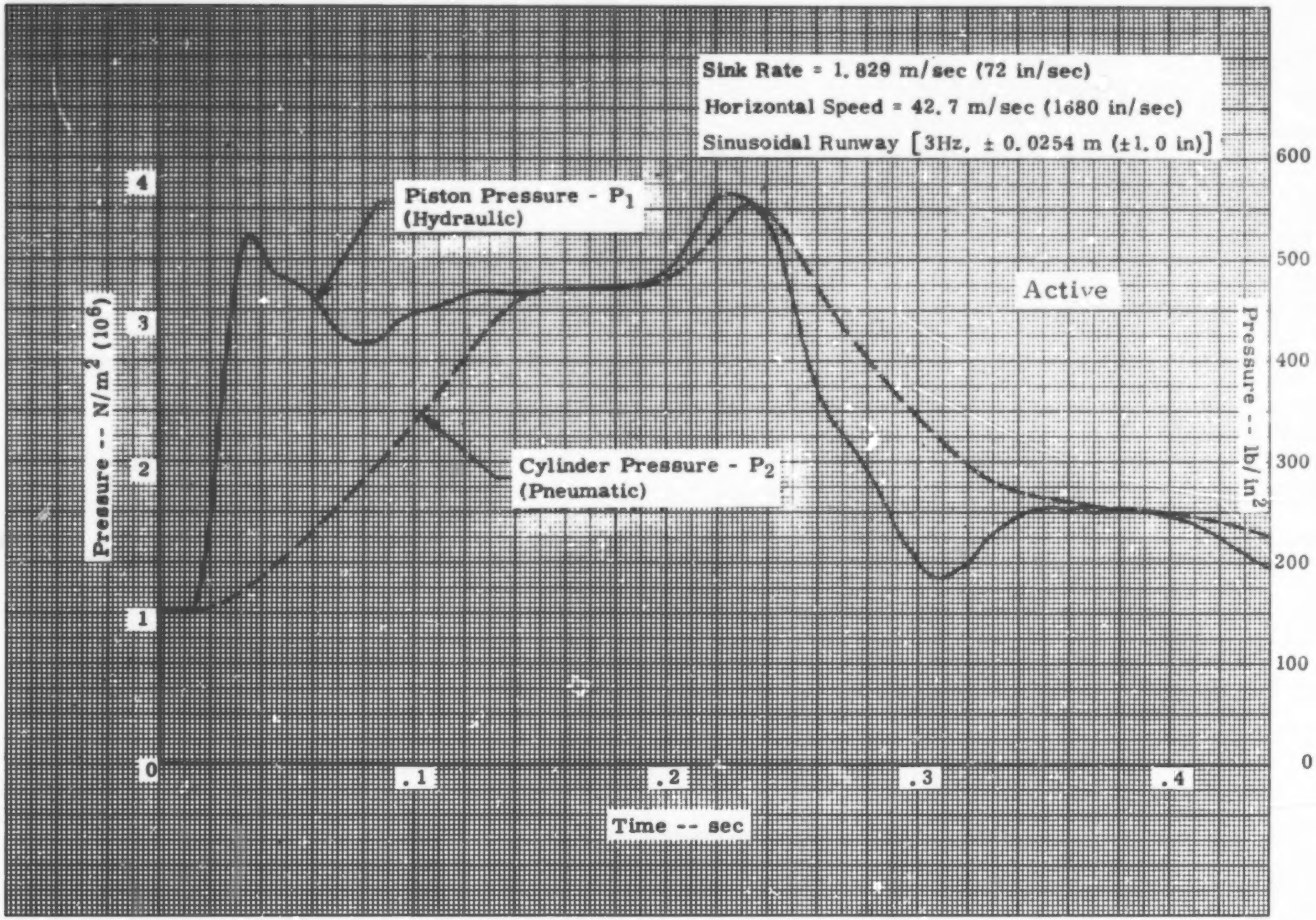

Figure 25. - Strut pressures, case 1.

58

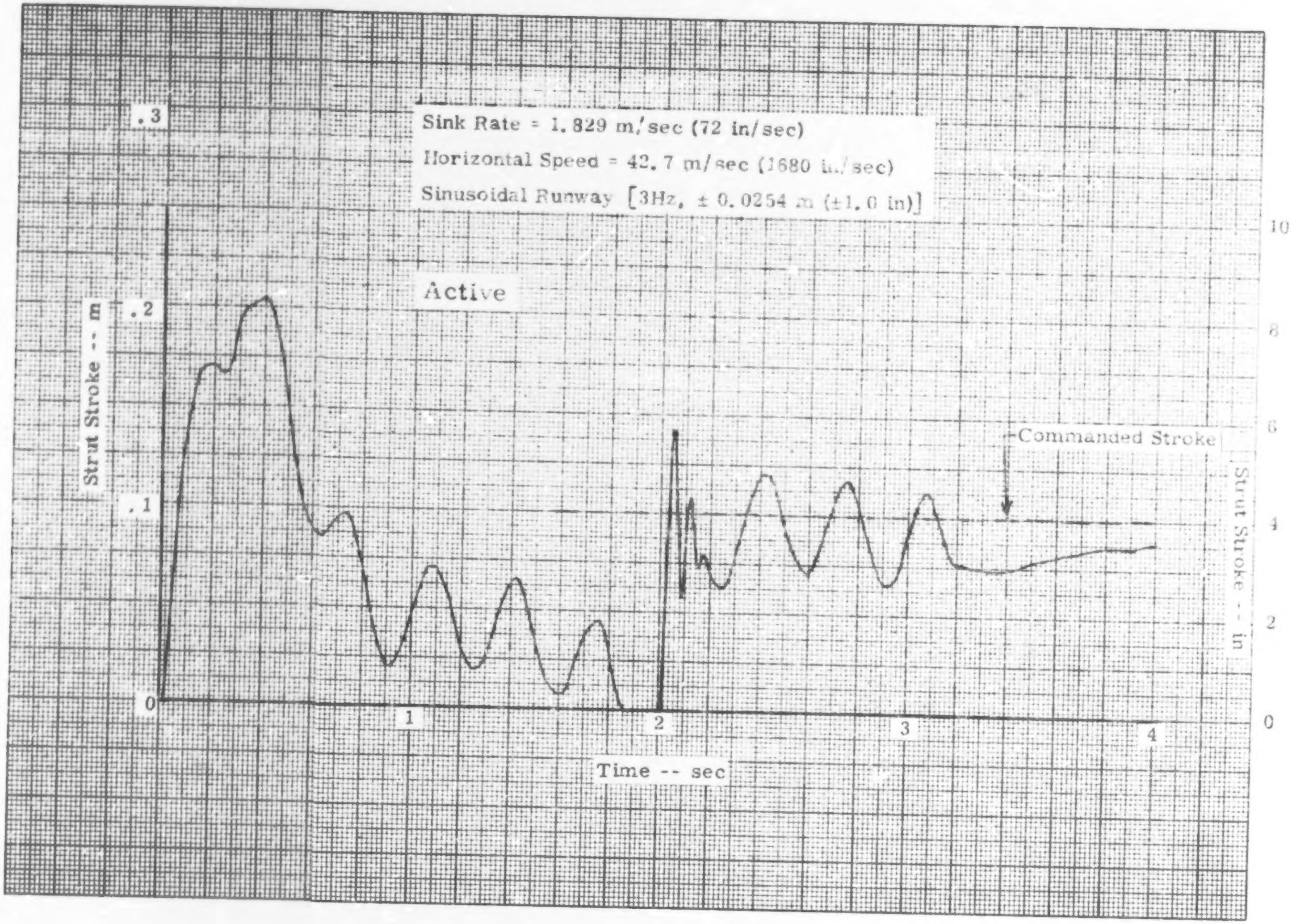

Figure 26. - Strut position transient, case 1.

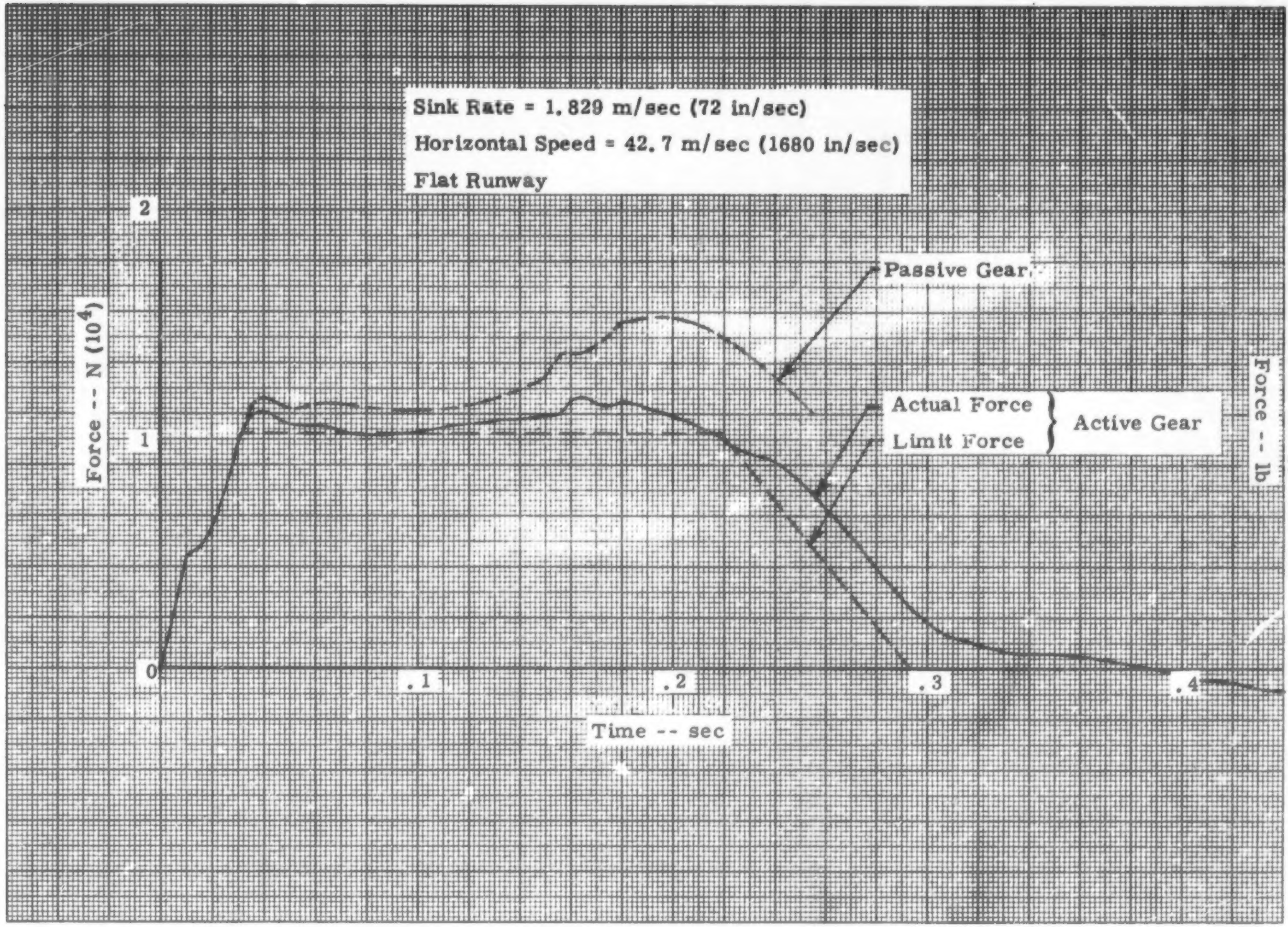

Figure 27. - Wing/gear force transient, case 2.

CONTENTS

Page

SUMMARY 1 1/A14

INTRODUCTION 1 1/A14

SYMBOLS 3 1/B2

ANALYSIS 8 1/B7
- Nonlinear Math Model for Vertical Drops 8 1/B7
  - Equations of Motion 10 1/B9
  - Pressure, Flow, and Volume Relationship 14 1/B14
  - Servovalve Dynamics 16 1/C2
- Linear Math Model for Vertical Drops 18 1/C5
- Energy Considerations 27 1/D1
- Stability Analysis 39 1/E2

ANALYTICAL RESULTS 51 1/F11
- Vertical Drop Cases 53 1/F14
- Land and Roll Cases 53 1/F14

CONTROLLER FUNCTIONAL DESCRIPTION 71 2/B11
- Associated Equipment 71 2/B11
- Interface 71 2/B11
- Performance Characteristics 76 2/C7
- Operating-Mode Determination 76 2/C7
  - Landing Mode 76 2/C7
  - Takeoff Mode 77 2/C8
- Limit-Force Command Determination 78 2/C9
- Control Law Implementation 78 2/C9
- Controller Design 78 2/C9
  - Functional Sections 78 2/C9

CONTENTS (Contd.)

Page

TEST . . . 89 2/E1
Test Fixture . . . 89 2/E1
Test Conditions . . . 93 2/E6
Test Results . . . 93 2/E6

CONCLUSIONS . . . 114 3/A9

APPENDIX

A Microprocessor Program Listing . . . 115 3/A10
B Electronic Controller Detailed Description . . . 131 3/B12
C Test Procedure . . . 142 3/C11
D Oscillograph Recordings . . . 148 3/D4

FIGURES

1 Illustration of variables used in nonlinear simulation of simplified vertical drop case . . . 9 1/B8
2 Free body diagram of airplane mass . . . 11 1/B10
3 Free body diagram of upper shock strut . . . 11 1/B10
4 Free body diagram of lower shock strut . . . 11 1/B10
5 Dynamic response of servovalve, ±10% input signal . . . 17 1/C3
6 Illustration of "Equivalent" system for the linear math model . . . 22 1/C9
7 Block diagram of linear math model . . . 26 1/C13
8 Comparison of linear model and nonlinear model results, open loop, no compensation, no position feedback . . . 28 1/D2
9 Various energy terms versus time, from the simplified nonlinear vertical drop simulation . . . 33 1/D8
10 Illustration of the variation of limit force versus time and the various phases of operation following impact . . . 35 1/D11
11 Block diagram of linear system without compensation . . . 40 1/E3

CONTENTS (Contd.)

Page

FIGURES

12 Nyquist plot of F_{wg}/F_{lim} with force loop opened, no position feedback, no compensation 41 1/E5

13 Electronic compensation network and its characteristics . . 42 1/E7

14 Nyquist plot of F_{wg}/F_{lim} with force loop opened, no position feedback, with compensation 43 1/E9

15 Nyquist plot of F_{wg}/F_{lim} with force loop opened, position loop closed, with compensation 45 1/E12

16 Nyquist plot of X_s/X_c with position loop opened, force loop closed, with compensation 46 1/F1

17 Frequency response of F_{wg}/F_{lim} with force and position loops closed, with compensation 47 1/F3

18 Frequency response of X_s/X_c with force and position loops closed, with compensation 48 1/F5

19 Nyquist plot of F_{wg}/F_{lim} with force loop opened, position loop closed, with compensation. 49 1/F7

20 Nyquist plot of F_{wg}/F_{lim} with force loop opened, position loop closed, with compensation. 50 1/F9

21 Wing/gear force transient, case A 54 1/G1

22 Wing/gear force transient, case B 55 1/G3

23 Strut position transient, case B 56 1/G5

24 Wing/gear force transient, case 1 . . . . 57 1/G7

25 Strut pressures, case 1 . . . . 58 1/G9

26 Strut position transient, case 1 . . . . 59 1/G11

27 Wing/gear force transient, case 2 . . . . 60 1/G13

28 Strut position transient, case 2 . . . . 61 2/A6

29 Wing/gear force transient, case 3 . . . . 63 2/A9

30 Wing/gear force transient, case 4 . . . . 64 2/A11

31 Servovalve flow rate, case A 65 2/A13

32 Servovalve flow rate, case B 66 2/B1

CONTENTS (Contd.)

Page

FIGURES

33 Servovalve flow rate, case 1 . . . . 67 2/B3
34 Servovalve flow rate, case 2 . . . . 68 2/B5
35 Servovalve flow rate, case 3 . . . . 69 2/B7
36 Servovalve flow rate, case 4 . . . . 70 2/B9
37 Input/Output Signal Schematic 72 2/B10
38 Control Law Functional Schematic 79 2/C10
39 Controller Functional Schematic 81 2/D1
40 Basic Functional Requirements 82 2/D3
41 Software Flow Chart 84 2/D6
42 Analog Section Schematic 85 2/D8
43 Analog Section - Front Panel Inputs 87 2/D11
44 Analog Section - Front Panel Outputs 88 2/D13
45 S-1C Test Fixture, Landing Gear Installed (View 1) . . . 90 2/E2
46 S-1C Test Fixture, Landing Gear Installed (View 2) . . . 91 2/E3
47 Net Force, Conditions 1, 4 (From W/G Accel #1) 95 2/E9
48 Net Force, Conditions 2, 5 (From W/G Accel #1) 96 2/E11
49 Net Force, Conditions 3, 6 (From W/G Accel #1) 97 2/E13
50 Net Force, Conditions 7, 10 (From W/G Accel #1) 98 2/F1
51 Net Force, Conditions 8, 11 (From W/G Accel #1) 99 2/F3
52 Net Force, Conditions 9, 12 (From W/G Accel #1) 100 2/F5
53 Gear Hydraulic Pressure, Conditions 1, 4 . . . . 101 2/F7
54 Gear Hydraulic Pressure, Conditions 2, 5 . . . . 102 2/F9
55 Gear Hydraulic Pressure, Conditions 3, 6 . . . . 103 2/F11
56 Gear Hydraulic Pressure, Conditions 7, 10 . . . . . . 104 2/F12
57 Gear Hydraulic Pressure, Conditions 8, 11 . . . . . . 105 2/G1
58 Gear Hydraulic Pressure, Conditions 9, 12 . . . . . . 106 2/G3

CONTENTS (Contd.)

Page

FIGURES

59 Strut Deflection, Conditions 1, 4 . . . . 107 2/G5

60 Strut Deflection, Conditions 2, 5 . . . . 108 2/G7

61 Strut Deflection, Conditions 3, 6 . . . . 109 2/G9

62 Strut Deflection, Conditions 7, 10 . . . . 110 2/G11

63 Strut Deflection, Conditions 8, 11 . . . . 111 2/G13

64 Strut Deflection, Conditions 9, 12 . . . . 112 3/A6

TABLES

I SUMMARY OF ACTIVE CONTROL LANDING CASES SIMULATED ON THE COMPUTER 52 1/F12

II PRIMARY INPUT SIGNAL SPECIFICATIONS 73 2/C1

III SECONDARY INPUT SPECIFICATIONS 74 2/C3

IV OUTPUT SPECIFICATIONS 75 2/C5

V CONTROL LAW TRANSFER FUNCTIONS. 80 2/C12

VI PEAK FORCES AND PERCENTAGE REDUCTION. 94 2/E7

REFERENCES. 161 3/F1

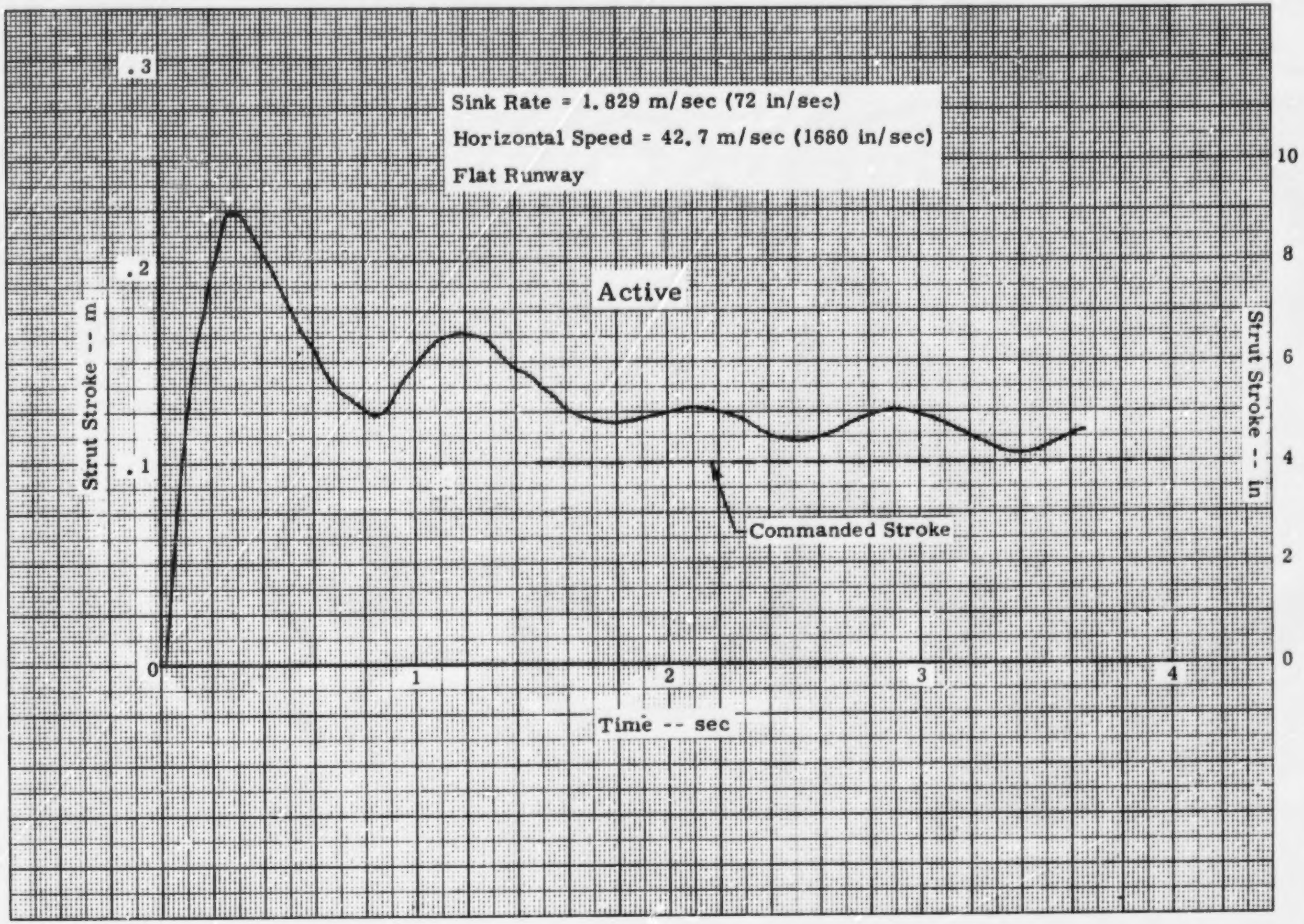

Figure 28. - Strut position transient, case 2.

and strut stroke transients for Case 2, which is the same as Case 1 except it uses a flat runway and has no wheel braking, while Figures 29 and 30 show the wing/gear force transients for Cases 3 and 4.

The flow rate through the servovalve of the active control landing gear during landing impacts is also of interest. Figures 31 through 36 show the time histories of the servovalve flow rates for each of the landings simulated herein. Positive flow is flow from supply to the piston chamber and negative flow is flow from the piston chamber to return.

Table I summarizes the amount of wing gear force reduction that was obtained from using active control for each of the cases reported in this section. From inspection of the force transients it appears that the reduction for some cases could be improved by increasing the bandwidth of the controller, which is presently about 10 Hz. This would reduce the magnitude of the initial overshoot. However, increasing the bandwidth would likely require more complex electronic compensation than that presently being used. In the absence of specific requirements, the results presented herein are judged satisfactory. The analyses indicate that the basic concept is workable.

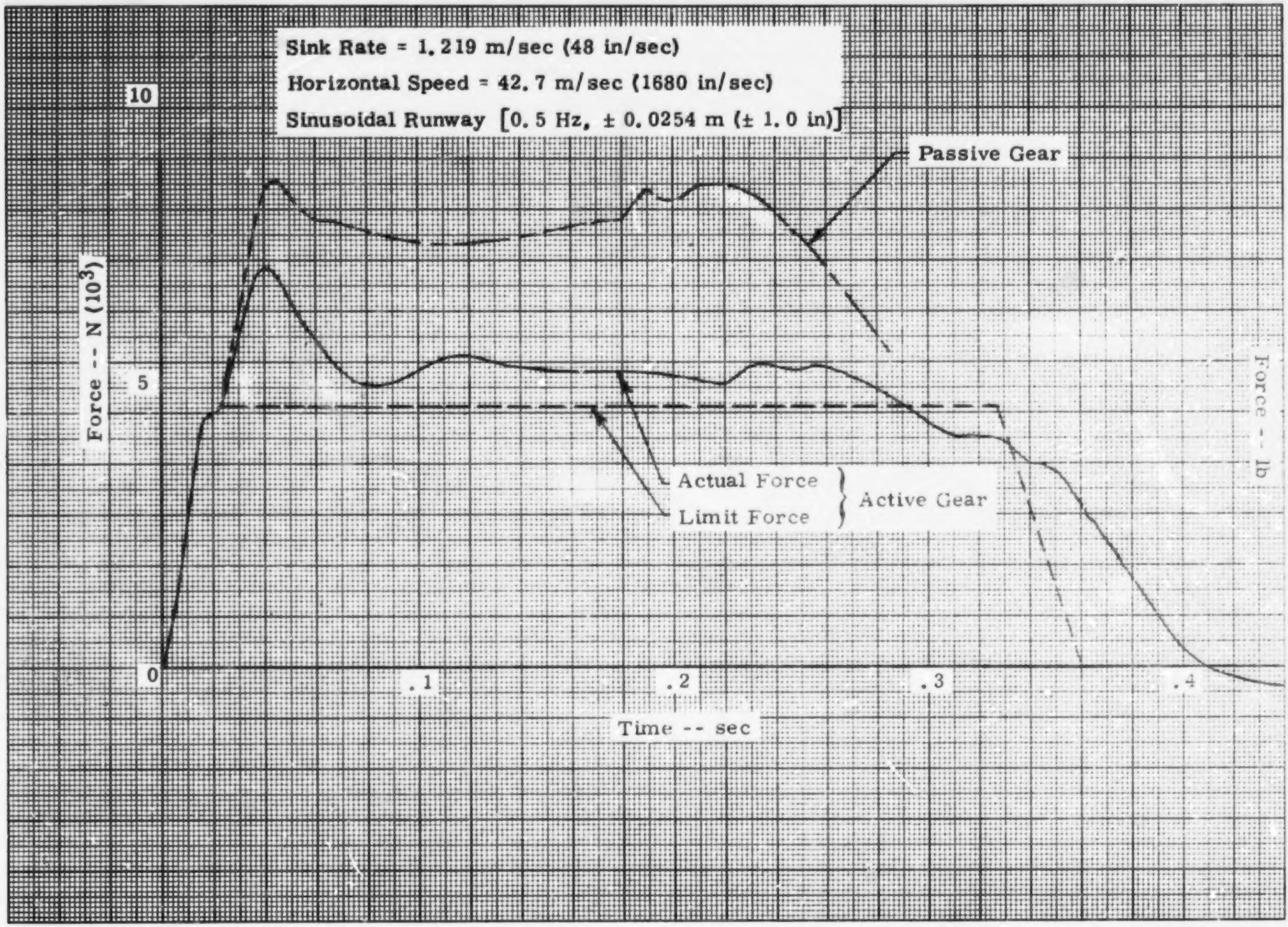

Figure 29. - Wing/gear force transient, case 3.

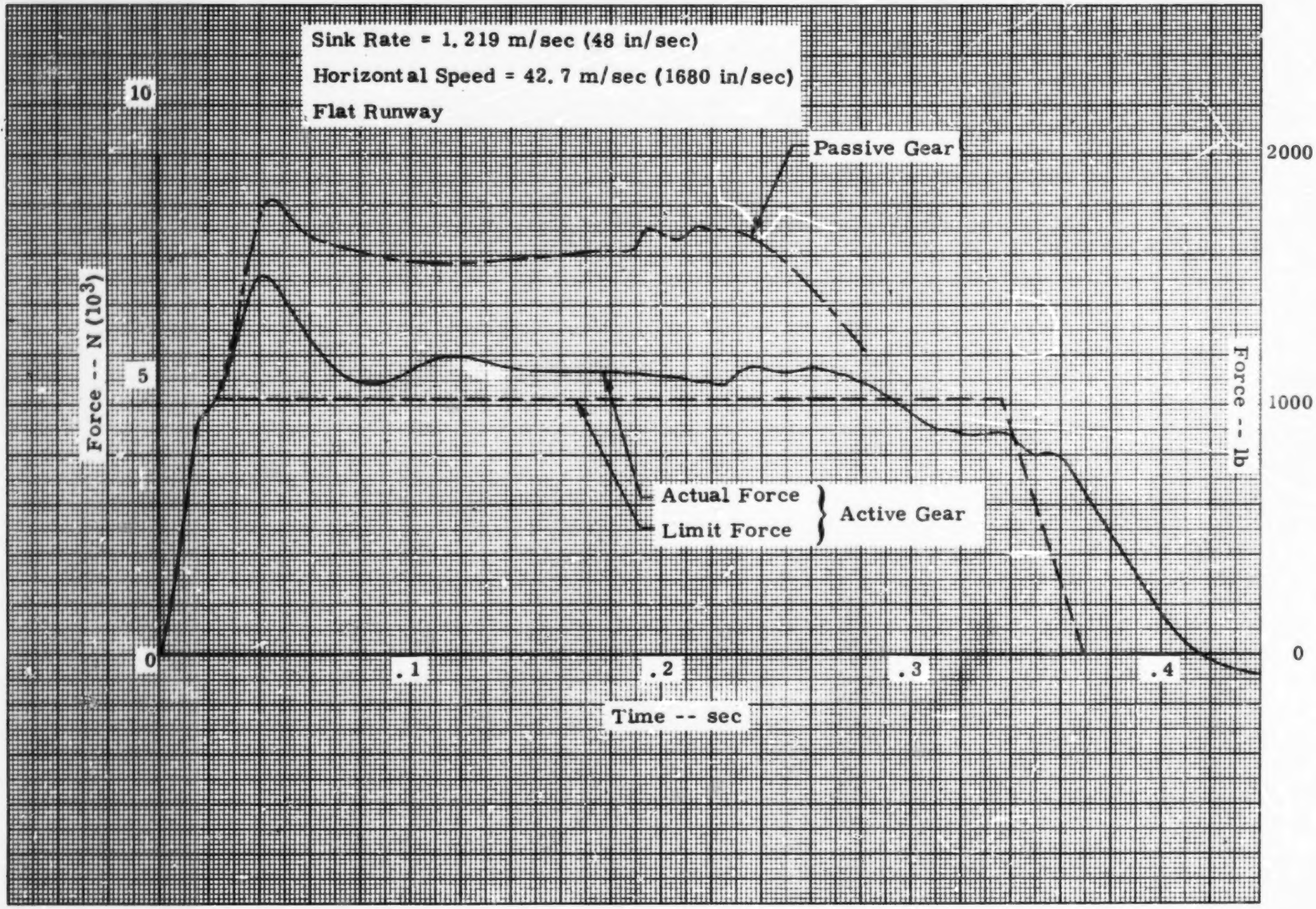

Figure 30. - Wing/gear force transient, case 4.

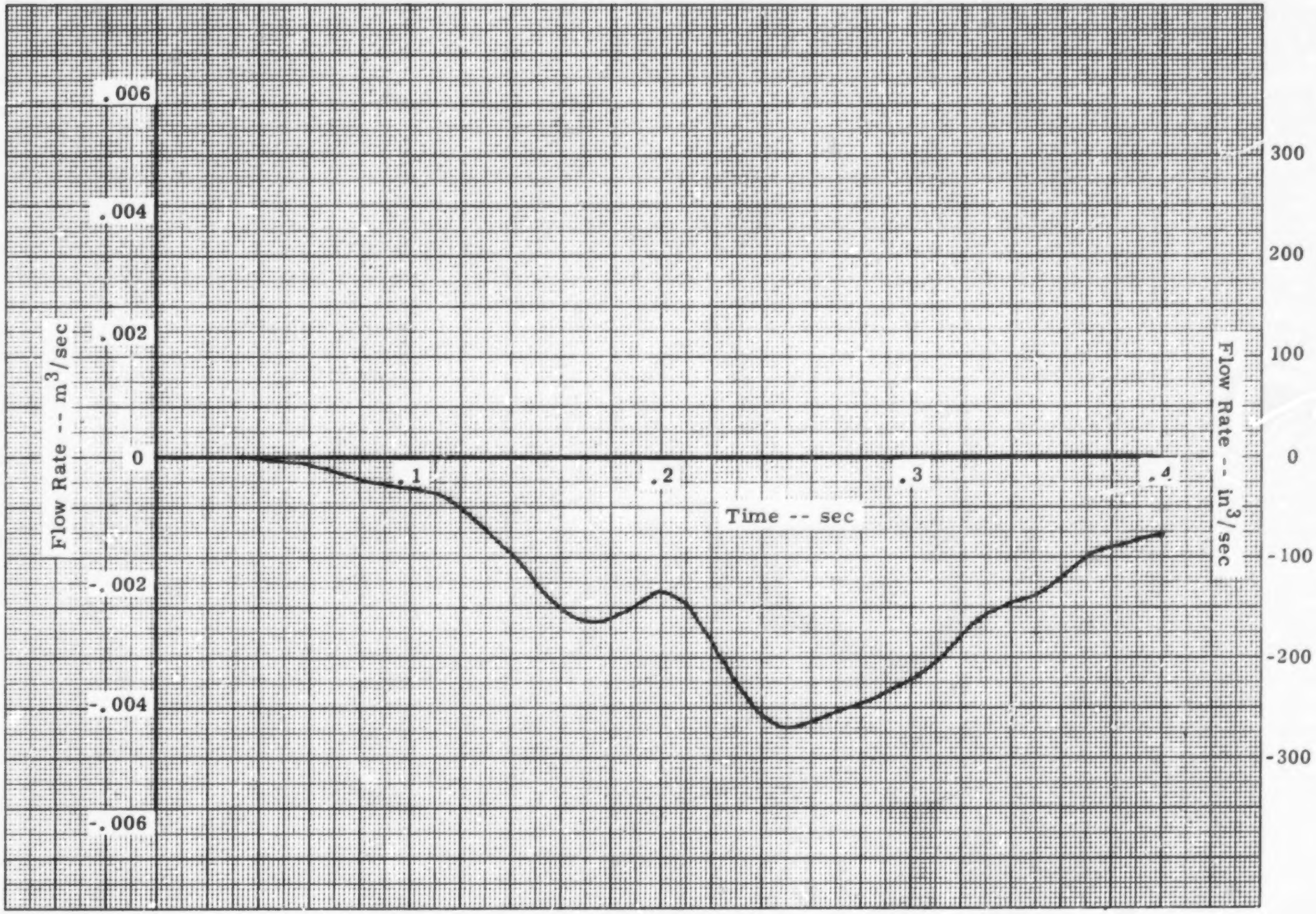

Figure 31. - Servovalve flow rate, case A.

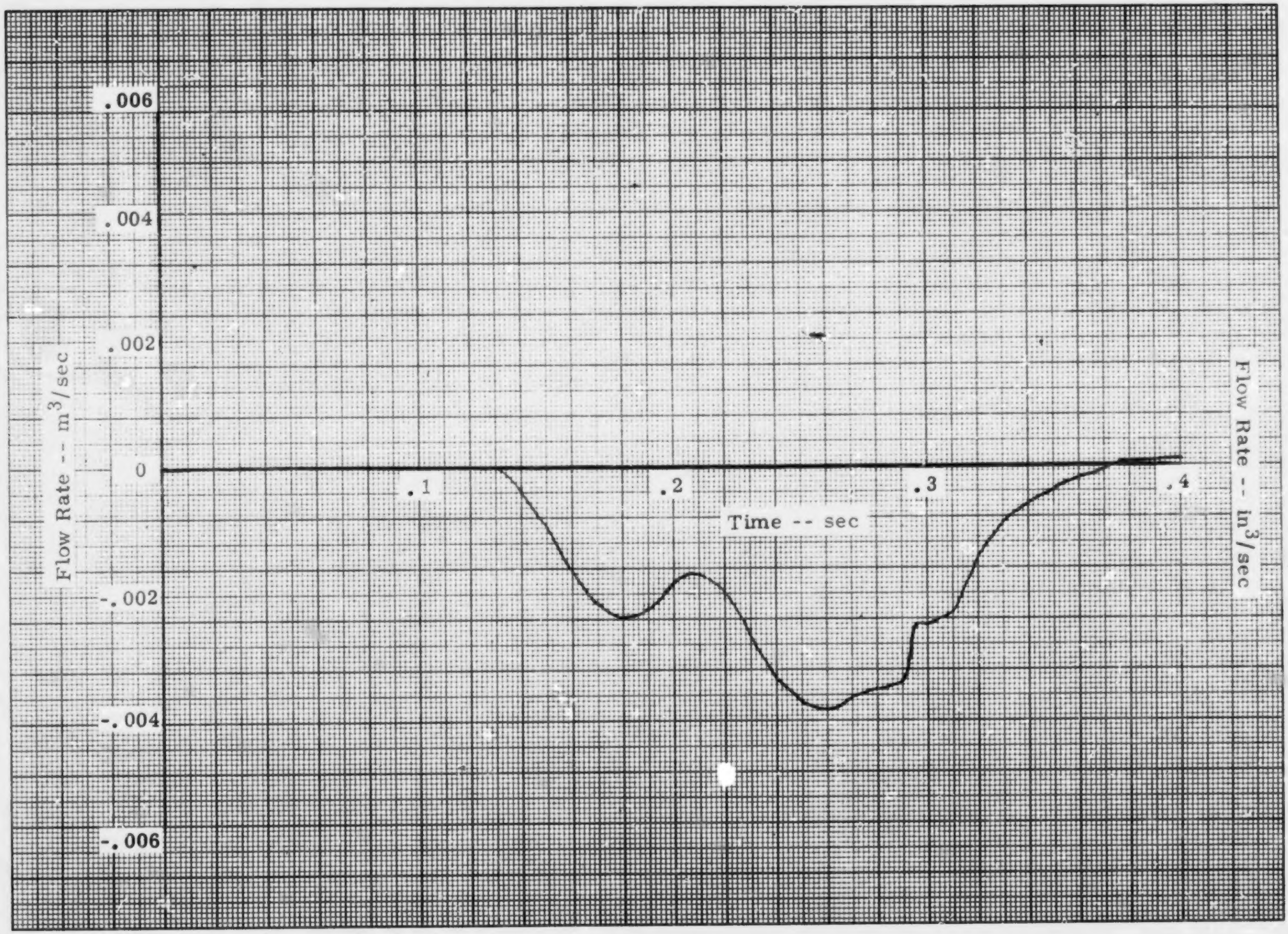

Figure 32. - Servovalve flow rate, case B.

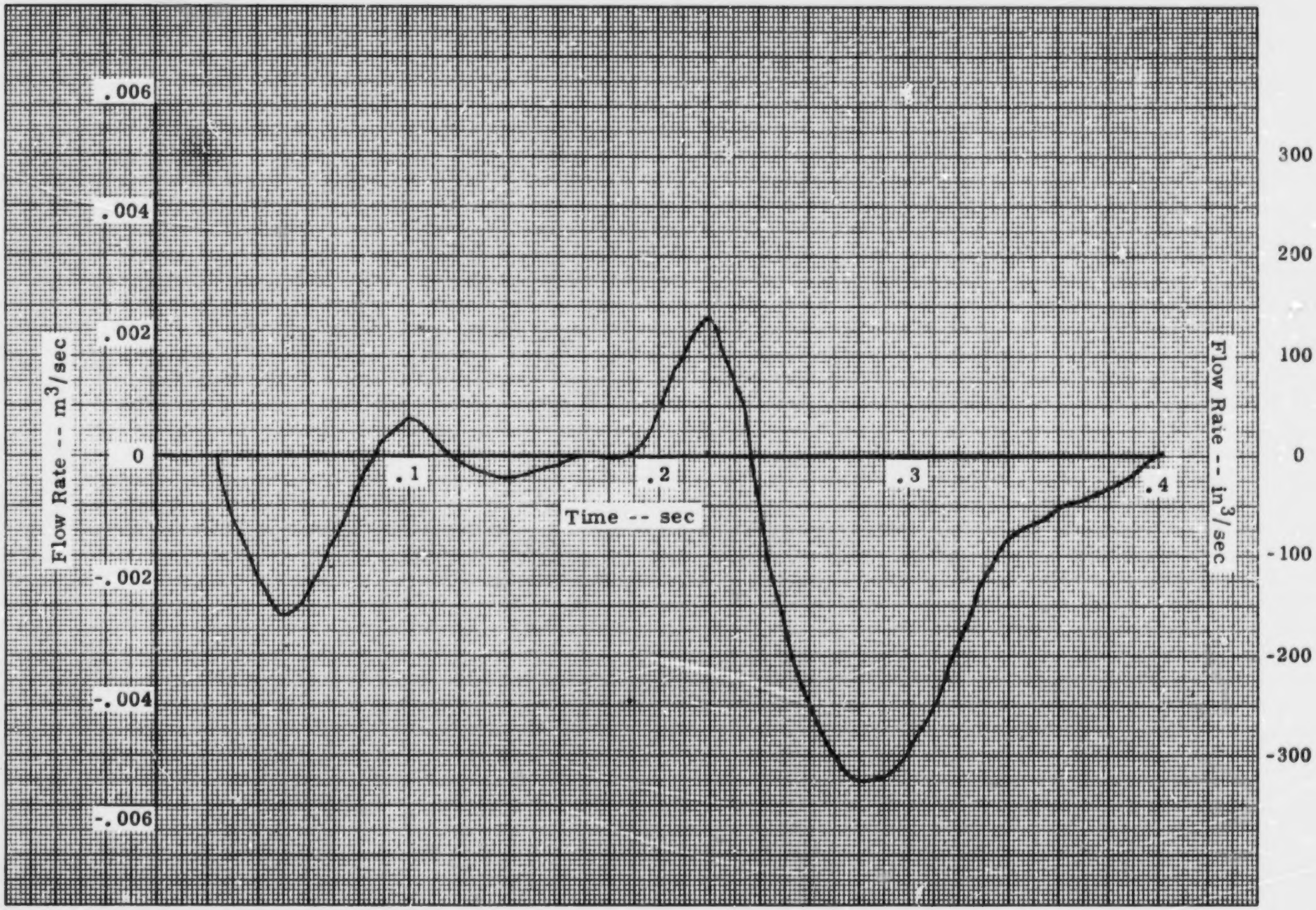

Figure 33. - Servovalve flow rate, case 1.

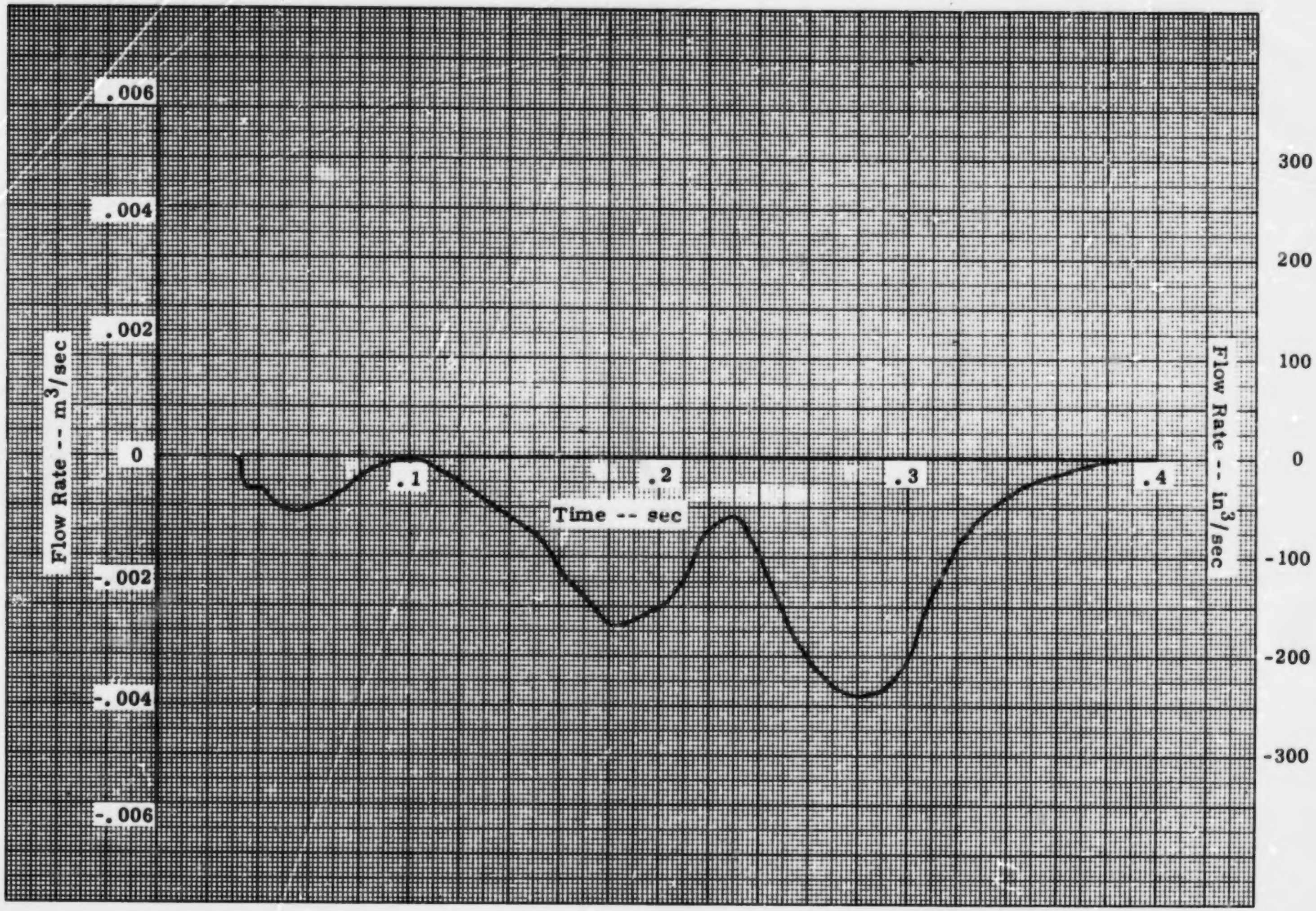

Figure 34. - Servovalve flow rate, case 2.

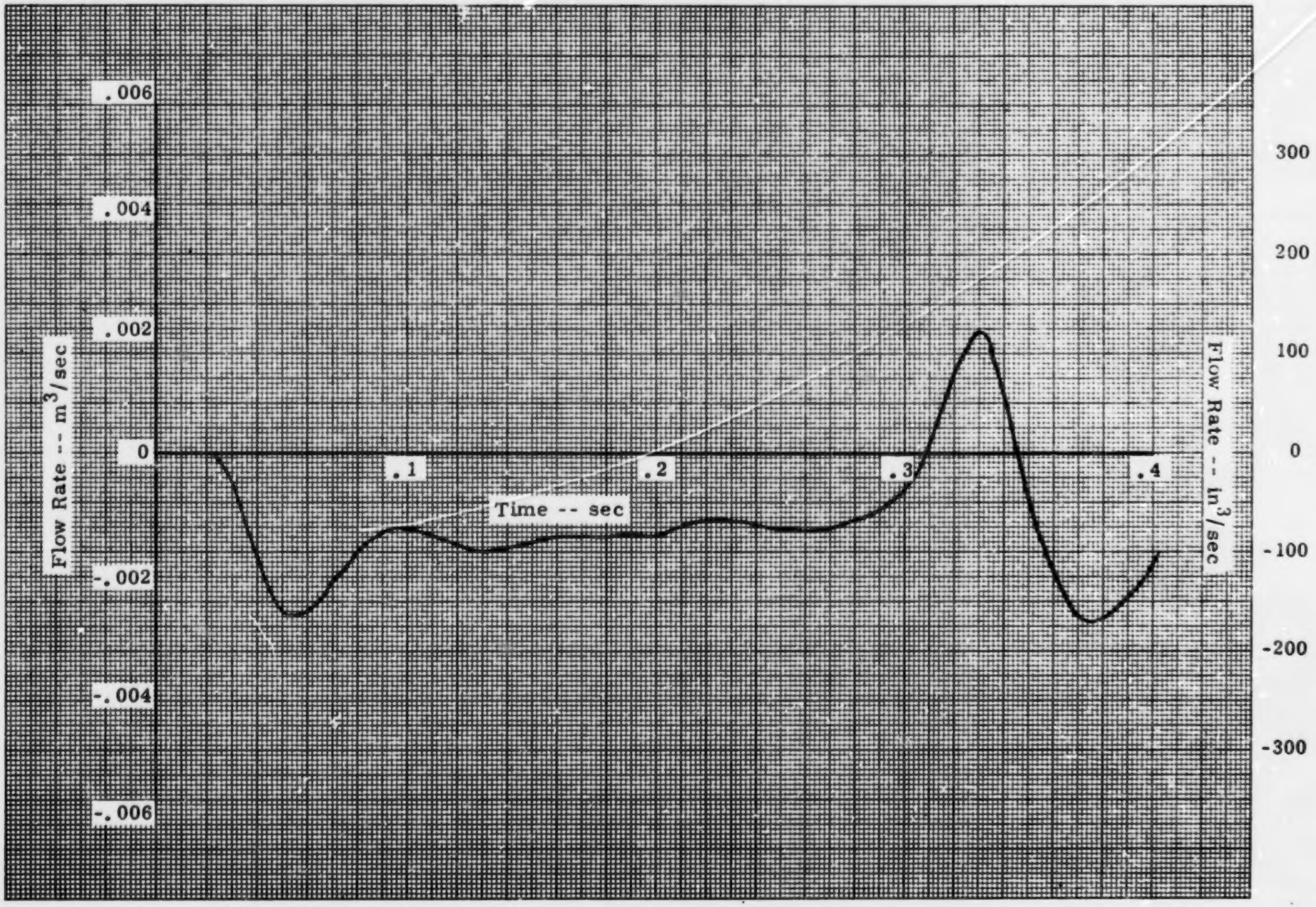

Figure 35. - Servovalve flow rate, case 3.

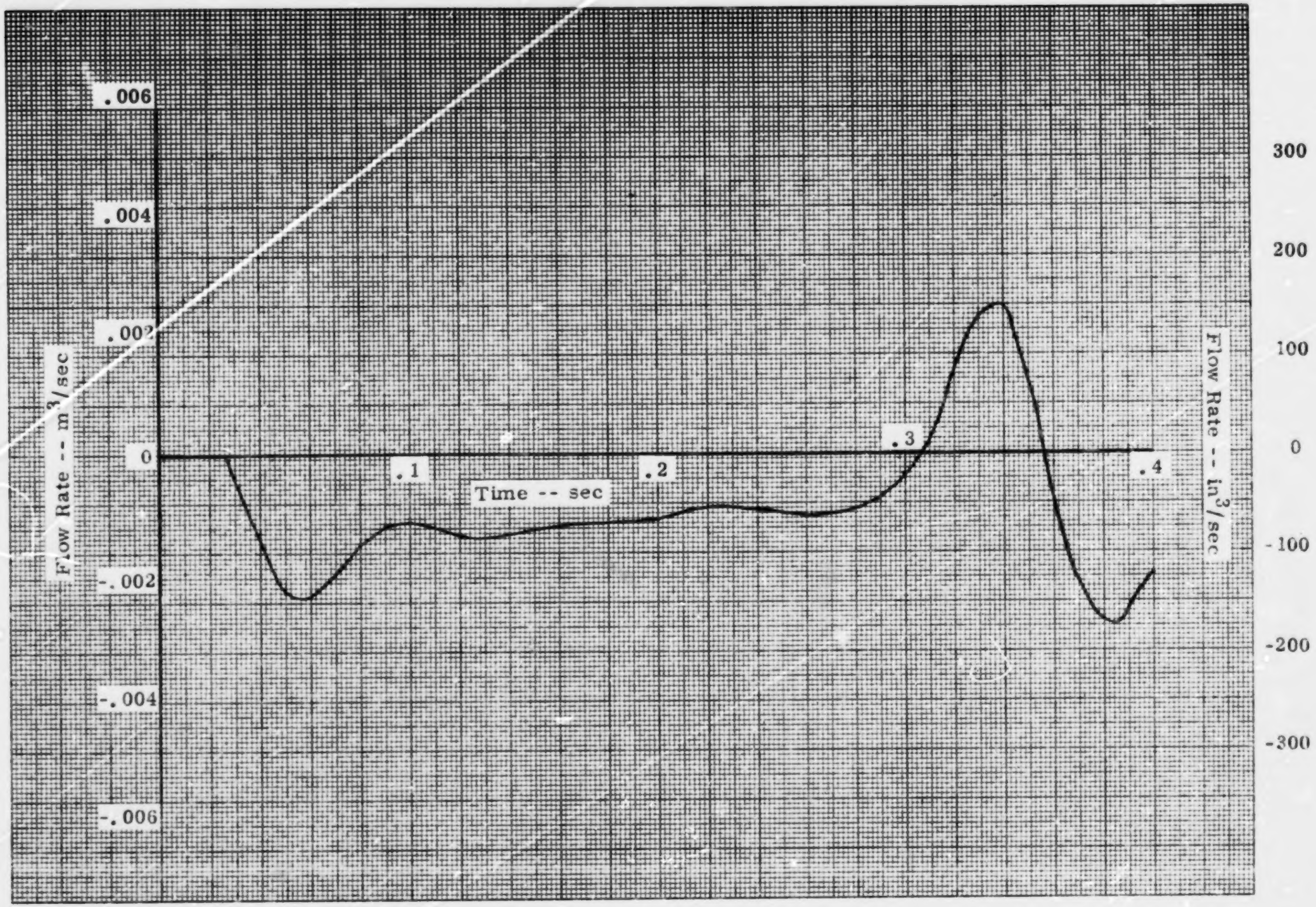

Figure 36. - Servovalve flow rate, case 4.

Associated Equipment

The following NASA-supplied equipment is used in conjunction with the electronic controller.

(1) Accelerometer - range ± 3 g's, measures wing/gear interface force.

(2) Accelerometer - range ± 25 g's, measures hub acceleration.

(3) Potentiometer - range 0-0.305 m (0-12 in.), measures strut deflection.

(4) Pressure transducer hydraulic - range 0-3.45 (10^4) kPa (0-5000 lb/in^2), measures the gear hydraulic pressure.

(5) Pressure transducer, pneumatic - range 0-1.38 (10^4) kPa (0-2000 lb/in^2), measures the gear pneumatic pressure.

(6) Servovalve - max. flow 0.757 m^3/min @ 6895 kPa (200 gal/min. @ 1000 lb/in^2).

(7) Servovalve Electronic controller - provides the signal to drive the servovalve.

(8) Hydraulic power unit.

(9) Modified landing gear.

Interface

The interface of input/output signals is shown schematically in Figure 37. Primary inputs and outputs are those required by the controller to perform its function. Secondary inputs and outputs are provided for testing, status indication and parameter monitoring, but play no part in the basic function of the controller. The primary inputs are shown in Table II, secondary inputs in Table III and the outputs are in Table IV.

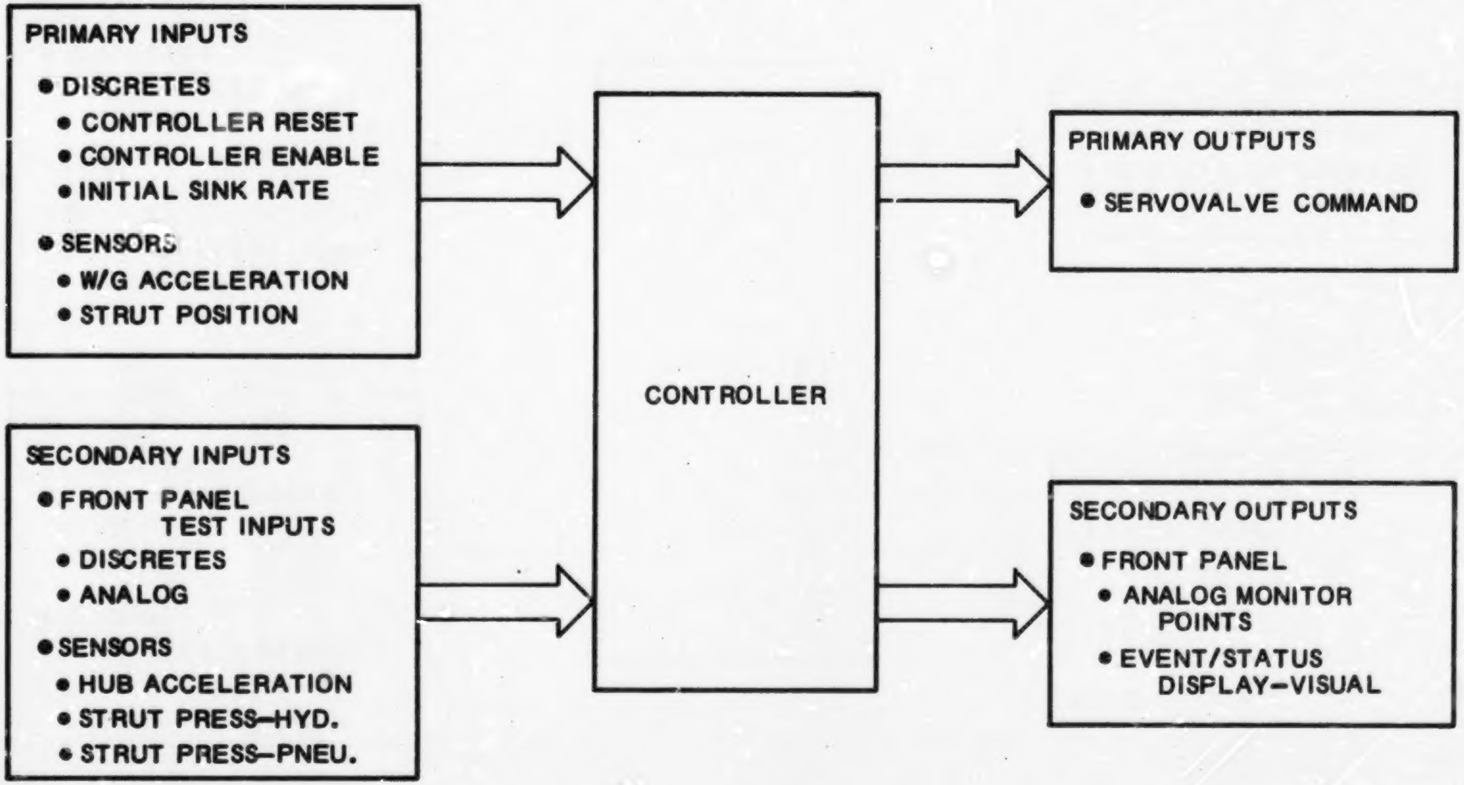
PRIMARY INPUTS
• DISCRETES
• CONTROLLER RESET
• CONTROLLER ENABLE
• INITIAL SINK RATE
• SENSORS
• W/G ACCELERATION
• STRUT POSITION
SECONDARY INPUTS
• FRONT PANEL TEST INPUTS
• DISCRETES
• ANALOG
• SENSORS
• HUB ACCELERATION
• STRUT PRESS–HYD.
• STRUT PRESS–PNEU.
CONTROLLER
PRIMARY OUTPUTS
• SERVOVALVE COMMAND
SECONDARY OUTPUTS
• FRONT PANEL
• ANALOG MONITOR POINTS
• EVENT/STATUS DISPLAY–VISUAL

Figure 37. - Input/Output Signal Schematic.

BLANK PAGE

BLANK PAGE

TABLE II. - PRIMARY INPUT SIGNAL SPECIFICATIONS

PARAMETER	UNITS	TYPE	SIGNAL RANGE
Wing/Gear Acceleration	g's	Analog	± 3g
Strut Position	m (in)	Analog	0 to 0.229 m (0 to 9 in)
Initial Sink Rate	m/sec (in/sec)	Digital	0 to 2.54 m/sec (0 to 100 in/sec)
Controller Reset	V	Logic Level	(*)
Controller Enable	V	Logic Level	(*)

(*) Logic 1 = 0 ± 0.5 V.
Logic 0 = 2.4 to 5V.

TABLE III. - SECONDARY INPUT SPECIFICATIONS

PARAMETER	UNITS	TYPE	SIGNAL RANGE	SCALE FACTOR
Hub Acceleration	g's	Analog	± 25 g	0.2 V/g
Strut Pressure - Hydraulic	kPa (lb/in^2)	Analog	0 to 2.07 (10^4) kPa (0 to 3000 lb/in^2)	6.418 (10^{-4}) m V/kPa (0.004425 mV/lb/in^2)
Strut Pressure - Pneumatic	kPa (lb/in^2)	Analog	0 to 1.384 (10^4) kPa (0 to 2000 lb/in^2)	6.418 (10^{-4}) m V/kPa (0.004425 mV/lb/in^2)
Limit Force Command	N (lb)	Analog	± 7.94 (10^4) N (± 17 860 lb)	1.26 (10^{-4}) V/N (0.00056 V/lb)
Wing/Gear Acceleration	g's	Analog	± 3 g	1.8 g
Wing/Gear Velocity	m/sec (in/sec)	Analog	0 to 2.54 m/sec (0 to 100 in/sec)	0.0393 V/m/sec (0.1 V/in/sec)
Strut Position	m (in)	Analog	0 to 0.229 m (0 to 9 in)	39.37 V/m (1 V/in)
Servoloop Enable	V	Logic Level	(*)	--
Integrator Enable	V	Logic Level	(*)	--

(*) Logic 1 = 0 ± 0.5 V.
Logic 0 = +2.4 to +5 V.

TABLE IV. - OUTPUT SPECIFICATIONS

PARAMETER	UNITS	TYPE	FRONT PANEL SOURCE		SIGNAL RANGE	SCALE FACTOR
			Jack	Visual Display		
Servovalve Command	V	Analog	X		± 10 V	1.0 V/(V Force Error)
Wing/Gear Acceleration	g's	Analog	X		± 3 g	1.8 V/g
Hub Acceleration	g's	Analog	X		± 25 g	0.2 V/g
Strut Position		Analog	X		0 to 22.9 cm (0 to 9 in)	39.37 V/m (1.0 V/in)
Strut Position Error		Analog	X		0 to 22.9 cm (0 to 9 in)	39.37 V/m (1.0 V/in)
Strut Pressure-Hydraulic	kPa (lb/in^2)	Analog	X		0 to 2.07 (10^{4}) kPa (0 to 3000 lb/in^2)	6.48 (10^{-4}) mV/kPa (0.004425 mV/lb/in^2)
Strut Pressure-Pneumatic	kPa (lb/in^2)	Analog	X		0 to 1.38 (10^{4}) kPa (0 to 2000 lb/in^2)	6.48 (10^{-4}) mV/kPa (0.004425 mV/lb/in^2)
Force Error	N (lb)	Analog	X		± 79.4 kN (± 17 860 lb)	1.26 (10^{-4}) V/N (0.00056 V/lb)
Limit Force Command	N (lb)	Analog	X		± 79.4 kN (± 17 860 lb)	1.26 (10^{-4}) V/N (0.00056 V/lb)
Wing/Gear Velocity	m/sec (in/sec)	Analog Logic	X		0 to 2.54 m/sec (0 to 100 in/sec)	0.03937 V/m/sec (0.1 V/in/sec)
Servoloop Enable	--	Logic Level	X		--	--
Integrator Enable	--	Logic Level	X		--	--
Controller Reset	--	Visual		X	--	--
Controller Enable	--	Visual		X	--	--
Takeoff Mode	--	Visual		X	--	--
Landing Mode	--	Visual		X	--	--

Performance Characteristics

The controller monitors the sensor data; and then, by performing computations of energy relationships and signal conditioning, provides an output signal which is the input command to the servovalve.

The controller has three basic functions which are: (1) operating-mode determination, (2) limit-force command determination, and (3) control-law implementation.

Operating-Mode Determination

When the controller is enabled, it automatically determines the operating mode — landing or takeoff.

Landing Mode

The controller selects the landing mode if the controller-enable signal has been received and the strut position signal indicates full extension. The landing mode is divided into several phases, each imposing a different functional command on the controller. These are: (1) pre-touchdown, (2) active control initiation, (3) transition, and (4) rollout.

Pre-touchdown. - During the pre-touchdown phase, the controller provides a bias signal to the servovalve to maintain the strut hydraulic pressure equal to the design charging pressure. This is accomplished by a pressure control loop in which the hydraulic pressure is the feedback signal. It also receives a signal from an external source which is representative of the aircraft sink rate prior to touchdown. In addition, it monitors the strut deflection. The servoloop is not enabled and the gear remains in a passive state.

Active Control Initiation. - Active control is initiated when the energy relationships indicate that the work potential of the strut exceeds the kinetic energy of the aircraft. Upon such occurrence, the controller causes the following to occur.

(1) The servoloop is enabled.

(2) An output is generated to the servovalve controller proportional to the force error as modified by the control laws.

(3) Energy computations are discontinued.

(4) A constant limit force is maintained.

(5) The strut pressure loop is opened.

(6) The servovalve bias is removed.

(7) The transition velocity is computed and continuously compared to the actual wing gear velocity to determine the start of transition.

Transition. - Transition to the rollout phase commences when the wing gear velocity equals the transition velocity. During transition, the controller linearly decreases the limit force command to zero and maintains active control.

Rollout. - The rollout phase commences when the limit force command during transition reaches zero. Active control is maintained and the controller remains in this mode until receipt of a reset signal (push button on the front panel).

Takeoff Mode

The controller selects the takeoff mode when: (1) a controller-enable signal has been received, and (2) the strut potentiometer signal indicates that the strut is at 0.005 m (0.2 in) less-than-full extension. At takeoff, the controller status is the same as in the rollout phase of the landing mode.

Limit-Force Command Determination

During the period prior to control initiation, the limit force is zero. (Since the servoloop is disabled during this time, the limit-force command has no effect). During the active control phase, the limit-force command is equal to the wing gear force which was present at the instant when active control was initiated. As indicated above, the limit-force command is linearly decreased to zero during the transition phase and maintained at zero throughout the rollout phase.

Control Law Implementation

The controller implements the control laws as shown in Figure 38. The transfer functions are listed in Table V.

Controller Design

Functional Sections

The controller consists of a digital section, an analog section and a power supply section as shown in Figure 39.

Digital Section. - The digital section includes a general-purpose stored-program digital computer (microprocessor) and its associated input/output devices as shown in Figure 40. The digital section accepts three analog and three discrete inputs and provides one analog and two discrete outputs. The analog inputs are applied through an analog multiplexer and A/D converter. The multiplexer is controlled by the computer software. The operating range of all inputs is 0 to +10 V.

The controller reset input is generated by a push button switch on the front panel. This input is normally in a logic "0" state. Depression of the

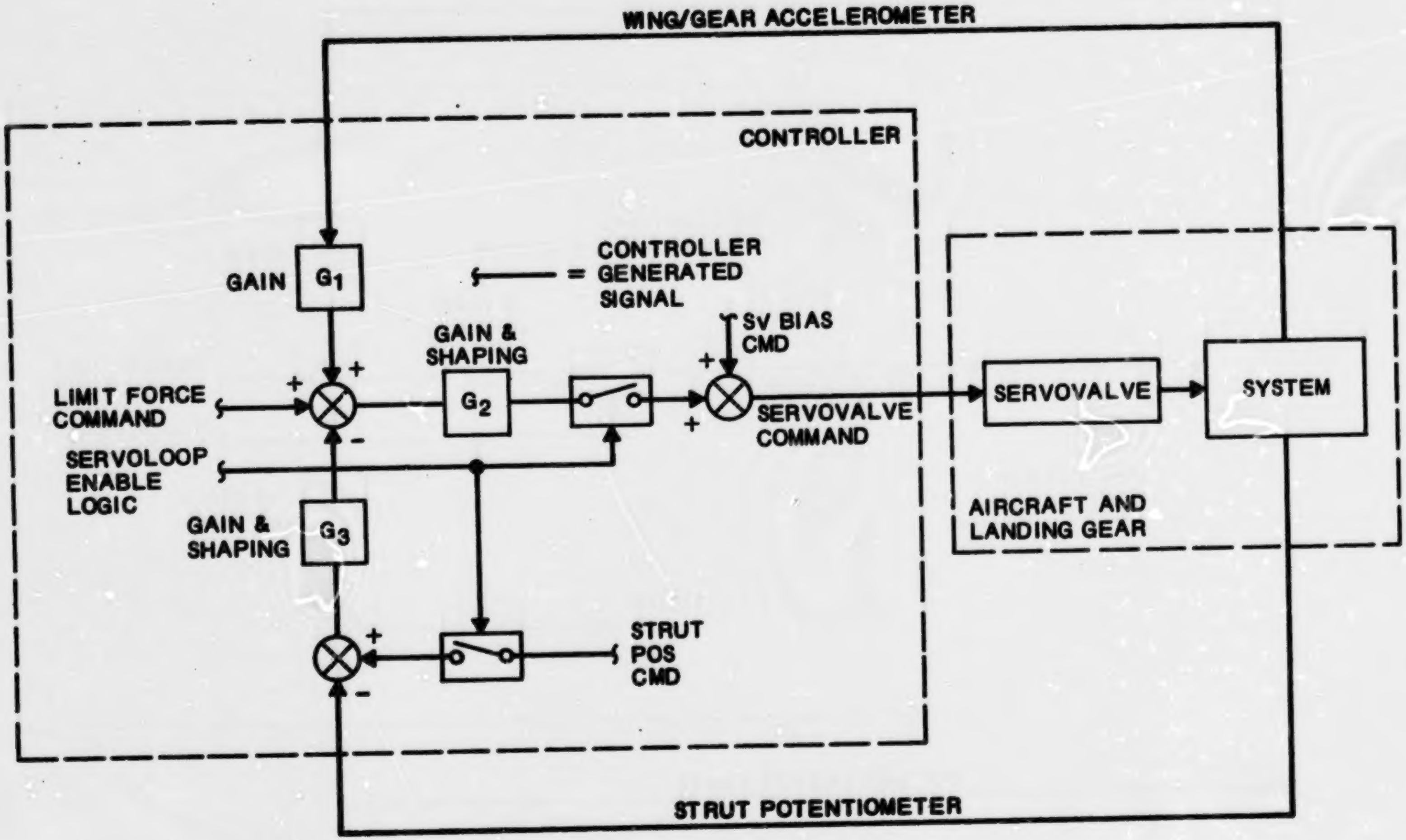
WING/GEAR ACCELEROMETER
CONTROLLER
GAIN
G_1
CONTROLLER GENERATED SIGNAL
GAIN & SHAPING
G_2
SV BIAS CMD
+
+
+
-
+
LIMIT FORCE COMMAND
SERVOVALVE COMMAND
SERVOLOOP ENABLE LOGIC
SERVOVALVE
SYSTEM
GAIN & SHAPING
G_3
AIRCRAFT AND LANDING GEAR
STRUT POS CMD
+
-
STRUT POTENTIOMETER

Figure 38. - Control Law Functional Schematic

TABLE V. - CONTROL LAW TRANSFER FUNCTIONS

SYMBOL (REF. FIGURE 3.2-6)	TRANSFER FUNCTION	PARAMETER VALUES
G_1	K_{WG}	K_{WG} = 1.0 V/V
G_2	$\frac{(S^2 + 2\zeta_2\omega_1 S + \omega_1^2)(T_1S + 1)(T_3S + 1)K_A}{(S^2 + 2\zeta_1 \omega_1 S + \omega_1^2)(T_2S+1)(T_4S + 1)}$	T_1 = 0.0281 sec T_2 = 0.0141 sec T_3 = 0.001 sec T_4 = 0.0001 sec ω_1 = 251.3 rad/sec ζ_2 = 0.1 ζ_1 = 5.1 K_A = 1.0 V/V nominal (variable from 50% to 200% of nominal)
G_3	$\frac{K_F}{T_FS + 1}$	K_F = 196.9V/M (5.0V/in.) T_F = 0.1 sec

BLANK PAGE

BLANK PAGE

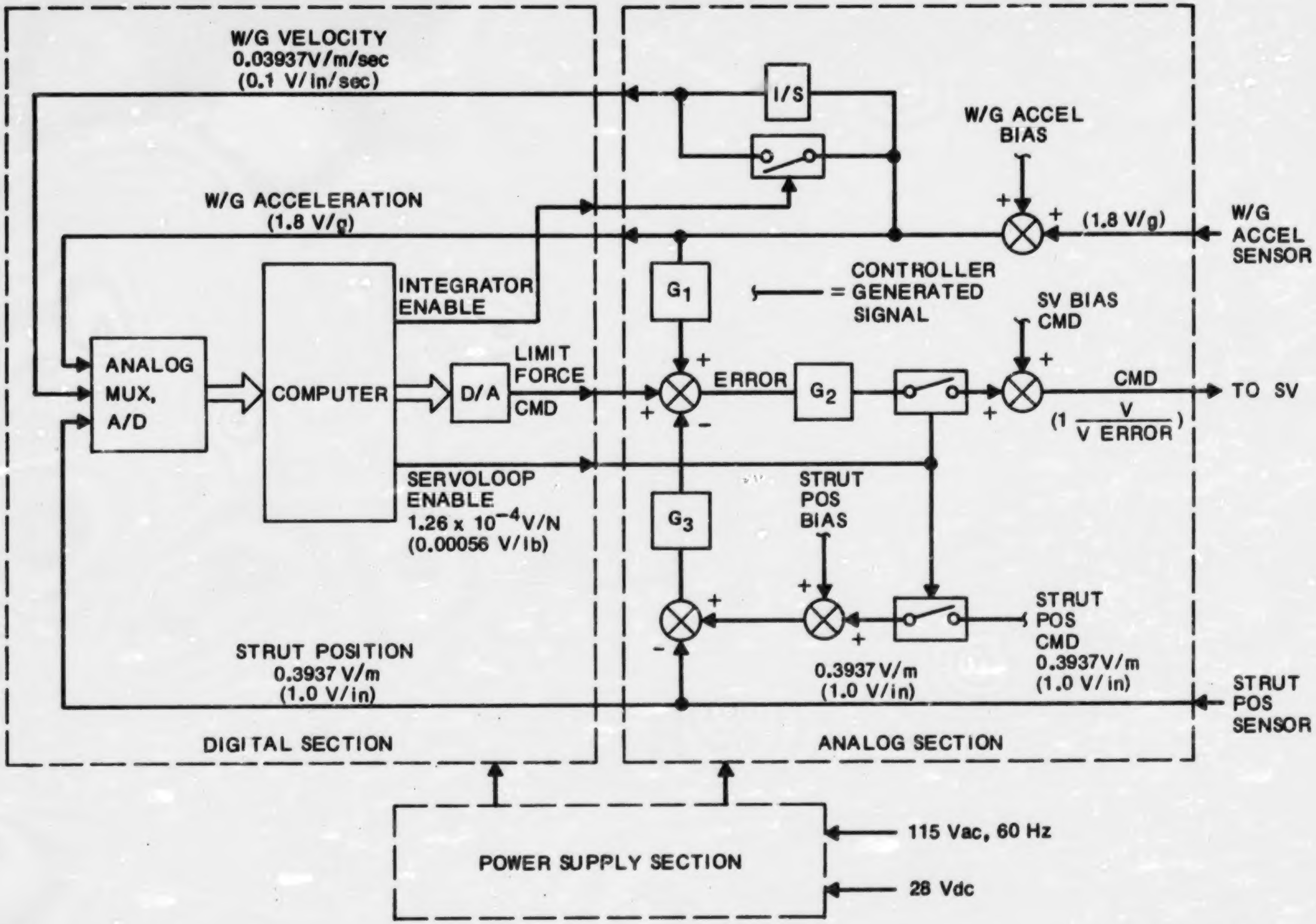
W/G VELOCITY
0.03937V/m/sec
(0.1 V/in/sec)
I/S
W/G ACCEL
BIAS
W/G ACCELERATION
(1.8 V/g)
(1.8 V/g)
W/G
ACCEL
SENSOR
CONTROLLER
= GENERATED
SIGNAL
G1
INTEGRATOR
ENABLE
SV BIAS
CMD
ANALOG
MUX,
A/D
COMPUTER
D/A
LIMIT
FORCE
CMD
ERROR
G2
CMD
TO SV
(1 V / V ERROR)
SERVOLOOP
ENABLE
1.26 x 10^-4 V/N
(0.00056 V/lb)
STRUT
POS
BIAS
G3
STRUT
POS
CMD
0.3937V/m
(1.0 V/in)
STRUT POSITION
0.3937 V/m
(1.0 V/in)
0.3937 V/m
(1.0 V/in)
STRUT
POS
SENSOR
DIGITAL SECTION
ANALOG SECTION
POWER SUPPLY SECTION
115 Vac, 60 Hz
28 Vdc

Figure 39. - Controller Functional Schematic

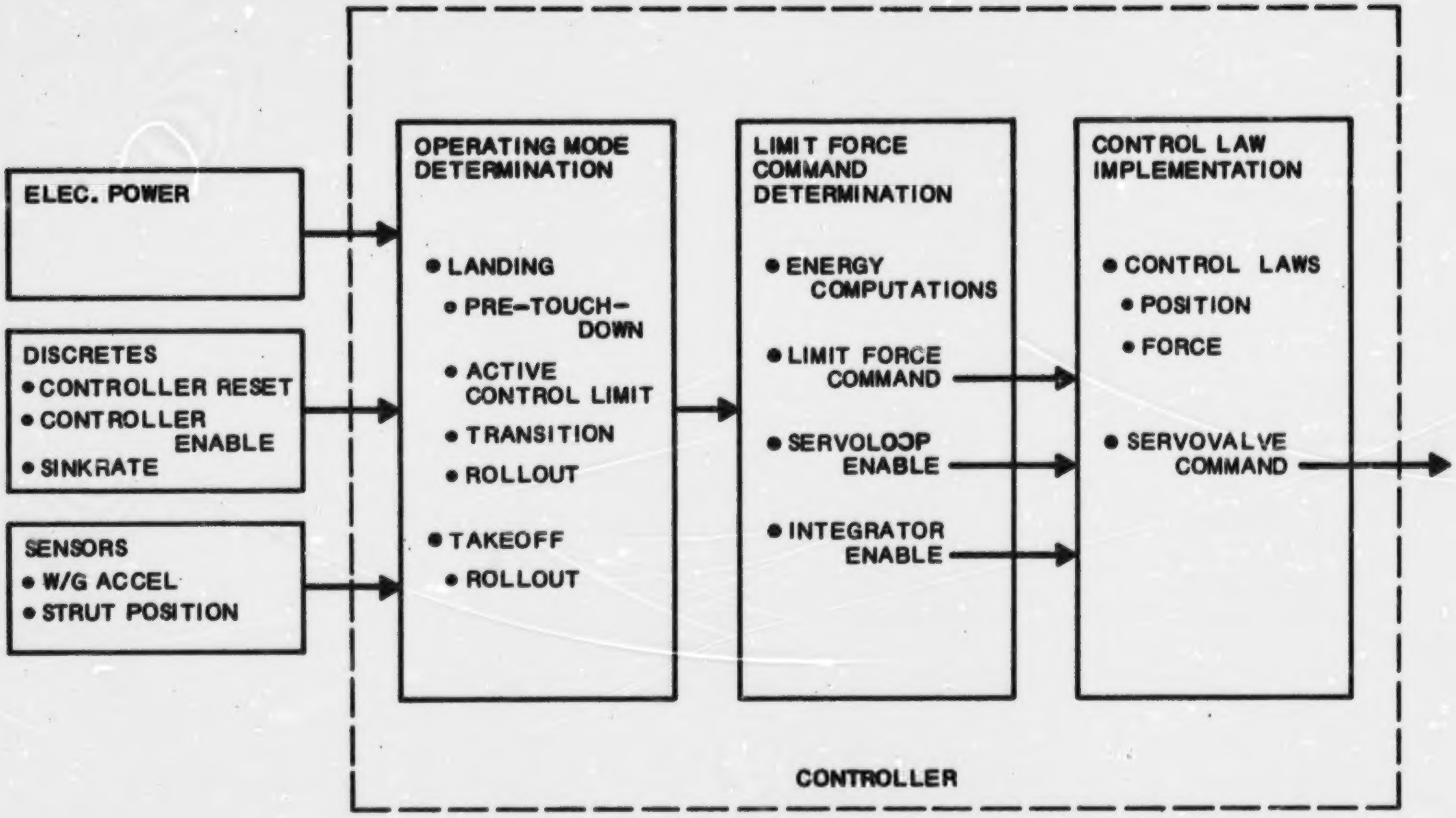
ELEC. POWER
DISCRETES
• CONTROLLER RESET
• CONTROLLER ENABLE
• SINKRATE
SENSORS
• W/G ACCEL
• STRUT POSITION
OPERATING MODE DETERMINATION
• LANDING
• PRE-TOUCH-DOWN
• ACTIVE CONTROL LIMIT
• TRANSITION
• ROLLOUT
• TAKEOFF
• ROLLOUT
LIMIT FORCE COMMAND DETERMINATION
• ENERGY COMPUTATIONS
• LIMIT FORCE COMMAND
• SERVOLOOP ENABLE
• INTEGRATOR ENABLE
CONTROL LAW IMPLEMENTATION
• CONTROL LAWS
• POSITION
• FORCE
• SERVOVALVE COMMAND
CONTROLLER

Figure 40. - Basic Functional Requirements

button changes the state to "1" which causes the controller to reset the computer. (The computer goes to step 0000 of memory).

The controller is enabled by a logic level input. Provision is made so that this input can be generated by a panel-mounted push button switch or a microswitch mounted on the gear. Both switches are connected in series. Therefore, if the controller is to be enabled by the panel switch only, then the microswitch input should be short-circuited. In any event, this signal is normally in a "0" state, and upon actuation the state becomes "1" which causes the computer to enable the controller.

Initial sink rate is an additional analog input to the multiplexer. This input is generated by an external source which is a velocity sensor or a d c signal which simulates the sink rate.

The outputs from the controller are the limit-force command (analog) signal, servoloop-enable (discrete) signal, and integrator-enable (discrete) signal.

The limit-force command is an output from the digital section by means of a digital-to-analog converter. The servoloop-enable signal is a logic level signal. A logic level "1" causes a switch to close and completes the path between the limit-force command and the output to the servovalve controller. The integrator-enable signal is also a logic-level signal. A level "0" causes a switch which is connected across the integrator, to open, thus allowing integration to occur. The integrator is used to generate wing/gear velocity from wing/gear acceleration and the input sink rate.

The computer software is illustrated in flow diagram form in Figure 41 and a detailed listing is provided as Appendix A.

Analog Section. - The function of the analog section is shown schematically in Figure 42. A detailed schematic drawing, wiring diagrams and assembly drawings, as well as a complete functional description can be found in Appendix B. The analog section accepts the primary and secondary

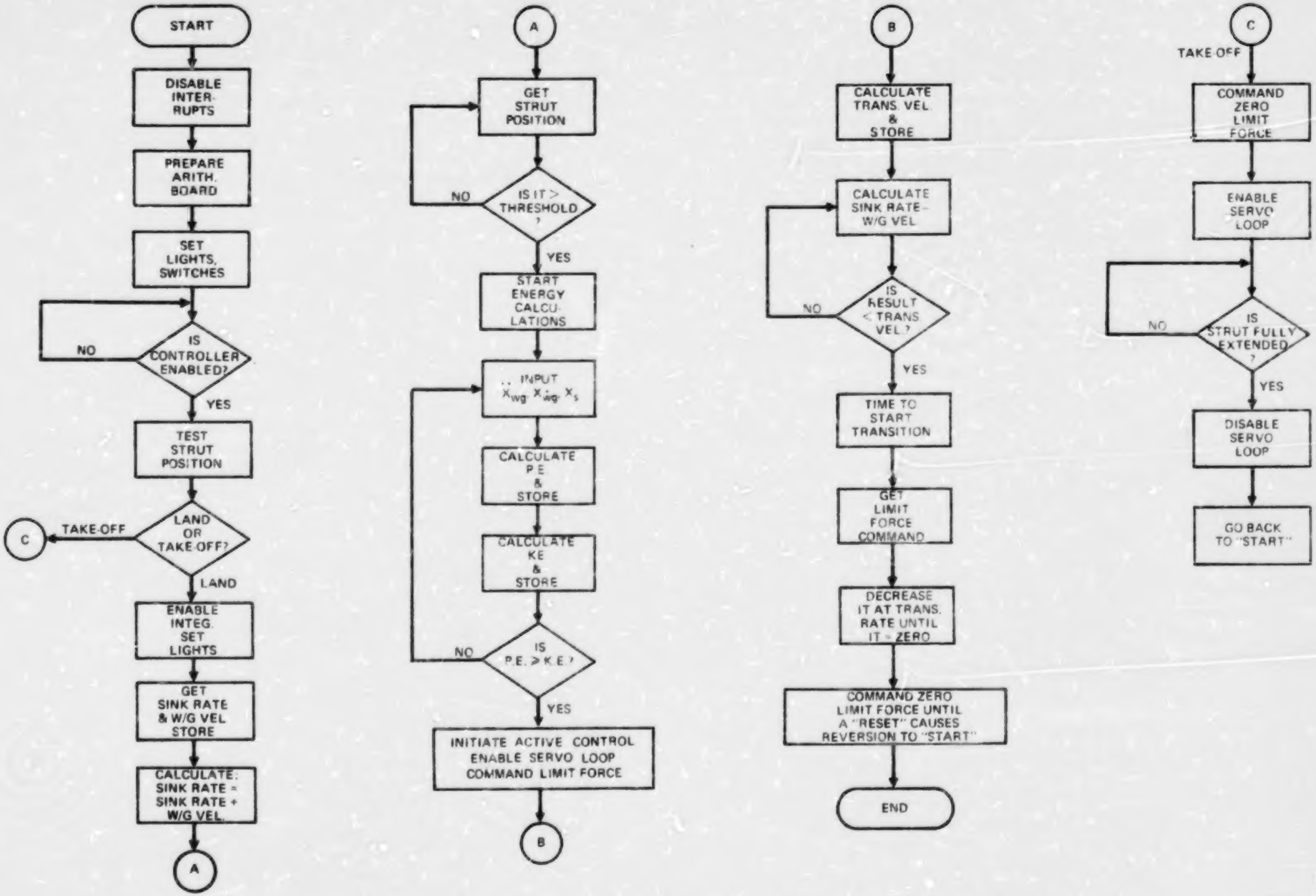
START
DISABLE INTER-RUPTS
PREPARE ARITH. BOARD
SET LIGHTS, SWITCHES
IS CONTROLLER ENABLED?
NO
YES
TEST STRUT POSITION
LAND OR TAKE-OFF?
TAKE-OFF
C
LAND
ENABLE INTEG. SET LIGHTS
GET SINK RATE & W/G VEL STORE
CALCULATE: SINK RATE = SINK RATE + W/G VEL.
A
A
GET STRUT POSITION
IS IT > THRESHOLD ?
NO
YES
START ENERGY CALCU-LATIONS
INPUT $\ddot{X}_{wg}, \dot{X}_{wg}, X_s$
CALCULATE P.E. & STORE
CALCULATE K.E. & STORE
IS P.E. ≥ K.E.?
NO
YES
INITIATE ACTIVE CONTROL ENABLE SERVO LOOP COMMAND LIMIT FORCE
B
B
CALCULATE TRANS. VEL. & STORE
CALCULATE SINK RATE – W/G VEL
IS RESULT < TRANS VEL.?
NO
YES
TIME TO START TRANSITION
GET LIMIT FORCE COMMAND
DECREASE IT AT TRANS. RATE UNTIL IT = ZERO
COMMAND ZERO LIMIT FORCE UNTIL A "RESET" CAUSES REVERSION TO "START"
END
C
TAKE-OFF
COMMAND ZERO LIMIT FORCE
ENABLE SERVO LOOP
IS STRUT FULLY EXTENDED ?
NO
YES
DISABLE SERVO LOOP
GO BACK TO "START"

Figure 41. - Software Flow Chart

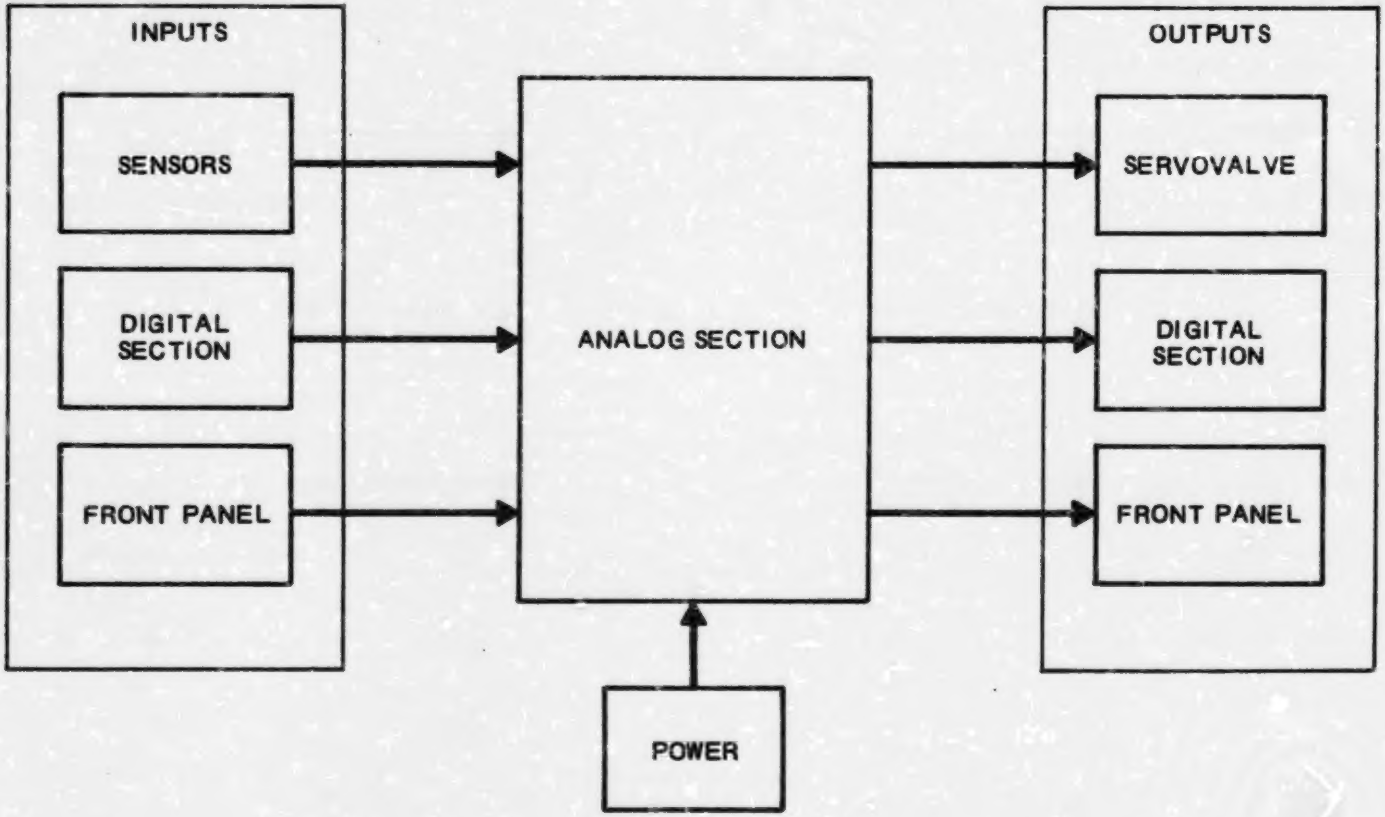
INPUTS
SENSORS
DIGITAL SECTION
FRONT PANEL
ANALOG SECTION
OUTPUTS
SERVOVALVE
DIGITAL SECTION
FRONT PANEL
POWER

Figure 42. - Analog Section Schematic

inputs, implements the required control laws and provides the output signal to the servovalve controller. It accepts signals from, and supplies signals to, the digital section.

Provisions are included to apply test signals to the controller by means of jacks on the front panel. These are shown in Figure 43. Buffered outputs are also provided on the front panel so that signals of interest can be monitored or recorded. These are shown in Figure 44.

The inputs to the analog section from the digital section are the limit-force command, servoloop-enable and integrator-enable signals, while the outputs from the analog section to the digital section are the wing/gear velocity, wing/gear acceleration and strut position signals. As previously stated, the wing/gear velocity is derived by integrating the wing/gear acceleration.

In addition, the analog section accepts inputs from the following sensors.

(1) Wing/gear accelerometer.

(2) Hub accelerometer.

(3) Strut position potentiometer.

(4) Strut hydraulic pressure transducer.

(5) Strut pneumatic pressure transducer.

These signals are applied by means of connectors on the rear panel.

Several other signals are applied to the analog section by means of controls on the front panel. These are:

(1) Servovalve bias command - to determine the static operating level of the servovalve.

(2) Strut position command - to determine static strut extension.

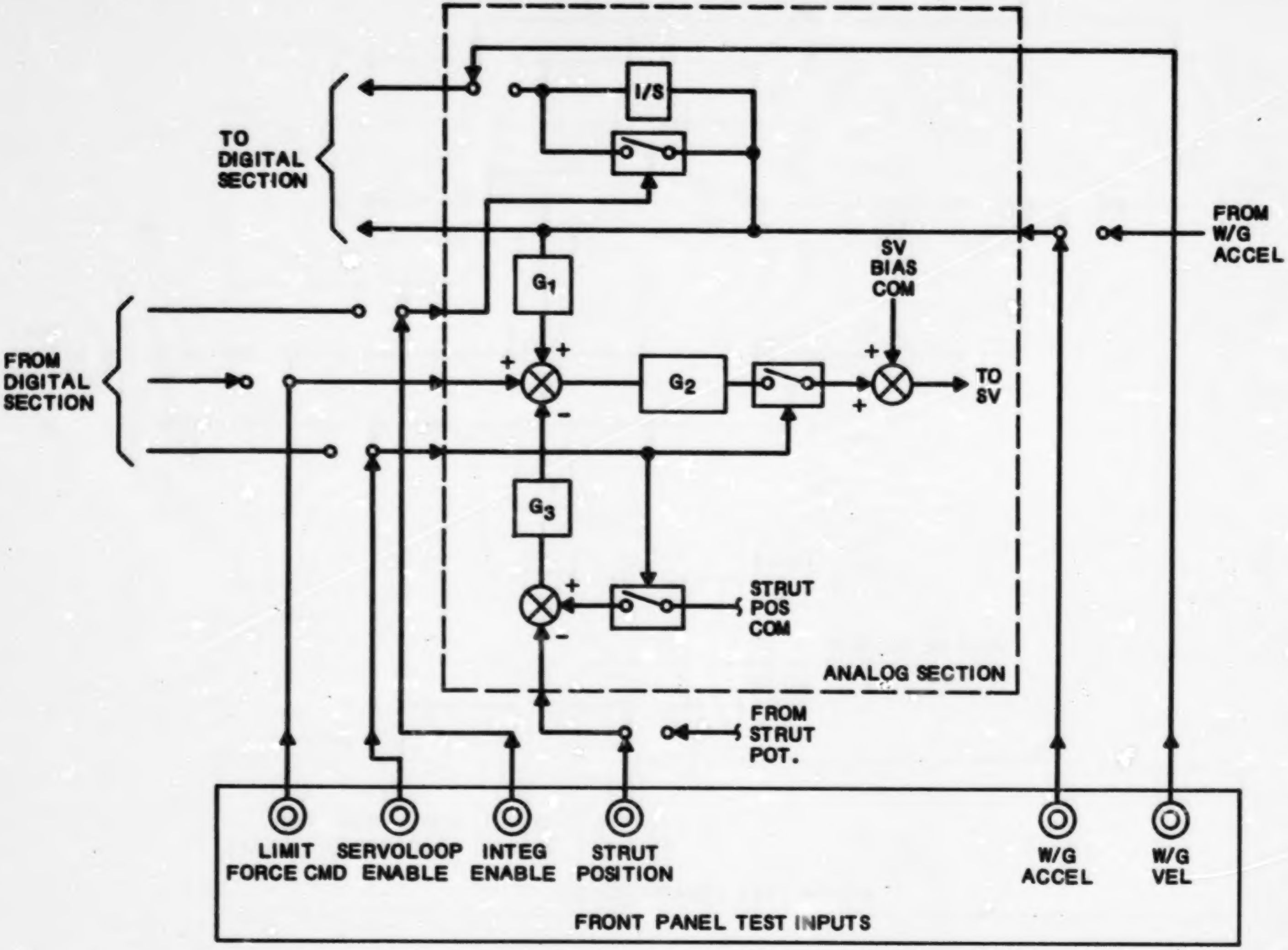
TO
DIGITAL
SECTION
I/S
FROM
W/G
ACCEL
SV
BIAS
COM
G1
FROM
DIGITAL
SECTION
+
+
+
-
G2
+
+
TO
SV
G3
+
-
STRUT
POS
COM
ANALOG SECTION
FROM
STRUT
POT.
LIMIT
FORCE CMD
SERVOLOOP
ENABLE
INTEG
ENABLE
STRUT
POSITION
W/G
ACCEL
W/G
VEL
FRONT PANEL TEST INPUTS

Figure 43. - Analog Section - Front Panel Inputs

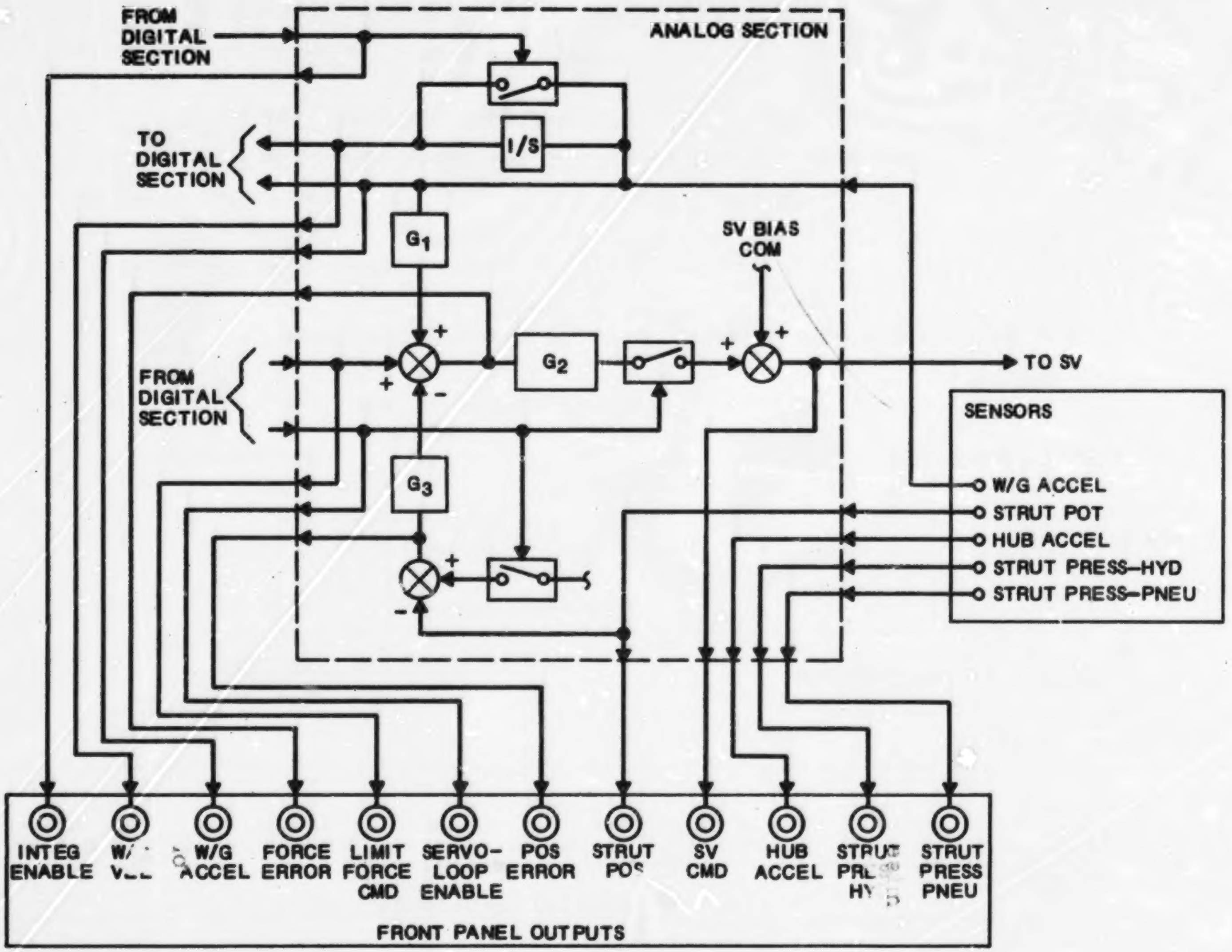
FROM DIGITAL SECTION
ANALOG SECTION
TO DIGITAL SECTION
I/S
G1
SV BIAS COM
FROM DIGITAL SECTION
G2
TO SV
G3
SENSORS
W/G ACCEL
STRUT POT
HUB ACCEL
STRUT PRESS-HYD
STRUT PRESS-PNEU
INTEG ENABLE
W/ V
W/G ACCEL
FORCE ERROR
LIMIT FORCE CMD
SERVO-LOOP ENABLE
POS ERROR
STRUT PO
SV CMD
HUB ACCEL
STRUT PR HY
STRUT PRESS PNEU
FRONT PANEL OUTPUTS

Figure 44. - Analog Section - Front Panel Outputs

TEST

Test Fixture

The test fixture used for the ACLG is a pivoted, variable-inertia beam originally designed to test the S-1C main engine vectoring servoactuators. The fixture is shown in Figures 45 and 46. Configured for the ACLG test program, the beam, added weights, landing gear, associated mounting components and miscellaneous hardware, represents a total calculated rotational inertia of 1426 kg - m^2 (1050 slug-ft^2). The landing gear is rigidly attached at a distance of 1.02 m (3.33 ft) from the beam pivot which produces a vertical translational inertia equivalent to a mass of 1388 kg (3060 lb). This value is about 5% below the targeted simulation value of 1458 kg (3215 lb) in order to allow for the weight of components which were added (hoses, fittings, instrumentation, etc.).

Motion is imparted to the beam by means of a hydraulic cylinder attached (through a load cell) to the beam at a distance of 0.305 m (1 ft) from the beam pivot and on the opposite side of the pivot from the landing gear. The cylinder is controlled by a 0.00189-m^3/sec (30-gal/min) electrohydraulic servovalve and its associated electronics. An LVDT is used for position indication and position loop closure.

Since the gear is rigidly mounted to the beam, it traverses the same angle as the beam. The angle of the gear at touchdown is about 4° forward of vertical. After touchdown, it passes through vertical and reaches an extreme of approximately 11° aft of vertical, depending on the test condition. These angles were chosen on the basis of gear geometry and the gear forces and deflections predicted by the analytical simulation. They represent an optimum mounting configuration, the basis of which is to make the strut frictional forces the same percentage of the total axial force on the gear at both touchdown and maximum force condition.

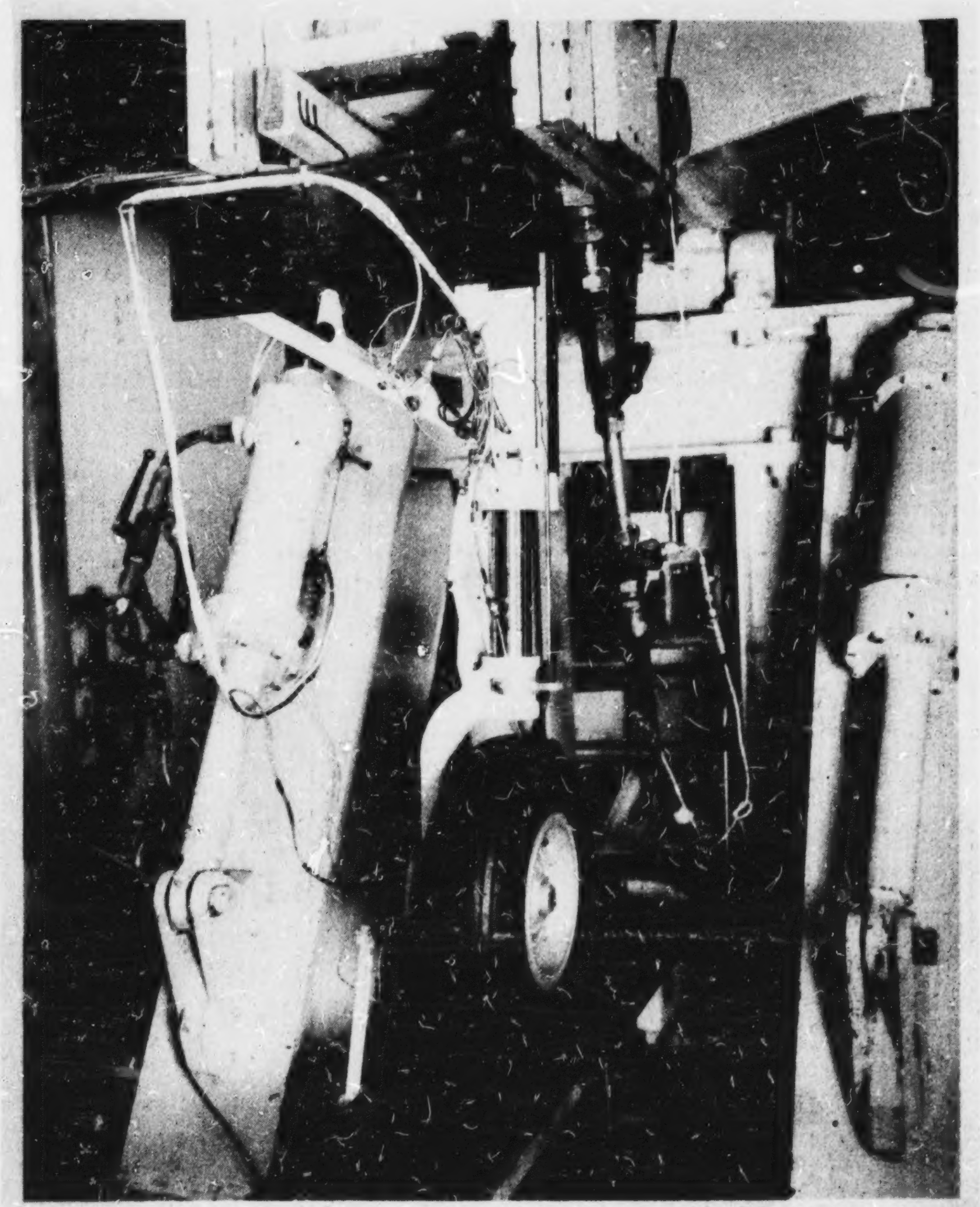

Figure 45. - S-1C Test Fixture, Landing Gear Installed (View 1)

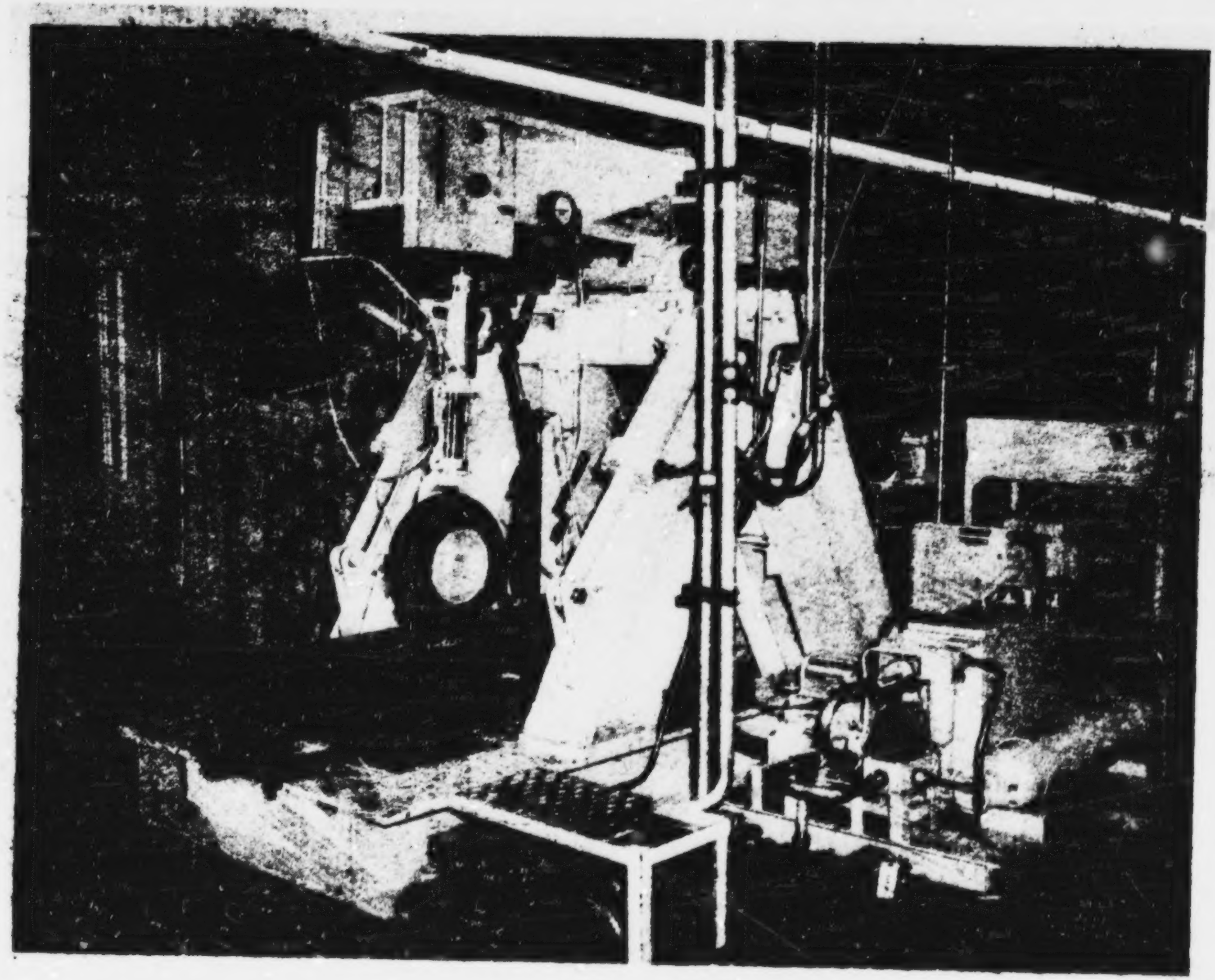

Figure 46. - S-1C Test Fixture, Landing Gear Installed (View 2)

The loading system operates in three modes as follows:

(1) Pre-test gear positioning: The cylinder is in a closed position loop, using the LVDT for feedback to "cock" the beam and gear to a pre-test position as determined by a command potentiometer.

(2) Sink speed generation: The LVDT is disconnected so that the cylinder is an open-loop configuration. A preset velocity potentiometer then provides a signal to the servovalve, thereby commanding a flow rate from the cylinder corresponding to the required sink speed.

(3) Programmed force: At touchdown, a microswitch is activated which connects the load cell and places the cylinder in a closed force loop to control the force during the interval from touchdown to the end of the test. The force program is provided by a ramp generator which begins with a 4315 N (970 lb) upward force at the gear [14 370 N (3230 lb) of tension at the load cylinder] which cancels the beam unbalance of 4315 N (970 lb) and simulates the condition of lift = weight. After 0.4 sec, the force ramps linearly to provide a downward force on the gear of 2180 N (490 lb) [7250 N (1630 lb) of compression at the load cylinder] which adds to the beam unbalance at this point of 4982 N (1120 lb) (due to the fact that the beam c.g. is above its pivot point) to produce a total downward force of 7161 N (1610 lb), which is equivalent to half of the aircraft weight per gear. The force is then held constant at this level throughout the remainder of the test.

Test Conditions

Tests were conducted under the following conditions.

Condition	Sink Speed m/sec (ft/sec)	Fully-extended Gear Pressure kPa (lb/in^2)	Mode
1.	0.305 (1)	1048 (152)	Passive
2.	0.914 (3)	1048 (152)	Passive
3.	1.524 (5)	1048 (152)	Passive
4.	0.305 (1)	1048 (152)	Active
5.	0.914 (3)	1048 (152)	Active
6.	1.524 (5)	1048 (152)	Active
7.	0.305 (1)	1931 (280)	Passive
8.	0.914 (3)	1931 (280)	Passive
9.	1.524 (5)	1931 (280)	Passive
10.	0.305 (1)	1931 (280)	Active
11.	0.914 (3)	1931 (280)	Active
12.	1.524 (5)	1931 (280)	Active

Test Procedure

The procedure for conducting the drop tests is given in Appendix C.

Test Results

The peak forces produced and percentage reduction due to active control are presented in Table VI. Comparative plots of force, strut deflection, and pressure are shown in Figures 47 through 64. The oscillograph recordings from which those plots were constructed are included as Appendix D.

TABLE VI. - PEAK FORCES AND PERCENTAGE REDUCTION

Condition No.	Sink Speed m/sec (ft/sec)	Static Strut Pressure kPa (lb/in^2)	Force at first peak N (lb)		% Reduction	Force at second peak or at 0.1 sec after touchdown N (lb)		% Reduction
			Passive	Active		Passive	Active	
1, 4	0.305 (1)	1048 (152)	4 226 (950)	4 226 (950)	0	5 004 (1125)	4 448 (1000)	11.1
2, 5	0.914 (3)	1048 (152)	8 674 (1950)	7 784 (1750)	10.3	8 007 (1800)	6 005 (1350)	25.0
3, 6	1.524 (5)	1048 (152)	11 120 (2500)	9 564 (2150)	14.0	10 900 (2450)	10 900 (2450)	0
7, 10	0.305 (1)	1931 (280)	1 335 (300)	445 (100)	66.7	4 893 (1100)	4 448 (1000)	9.1
8, 11	0.914 (3)	1931 (280)	11 340 (2550)	10 450 (2350)	7.8	11 570 (2600)	8 007 (1800)	30.8
9,12	1.524 (5)	1931 (280)	16 240 (3650)	16 240 (3650)	0	16 680 (3750)	11 790 (2650)	29.3

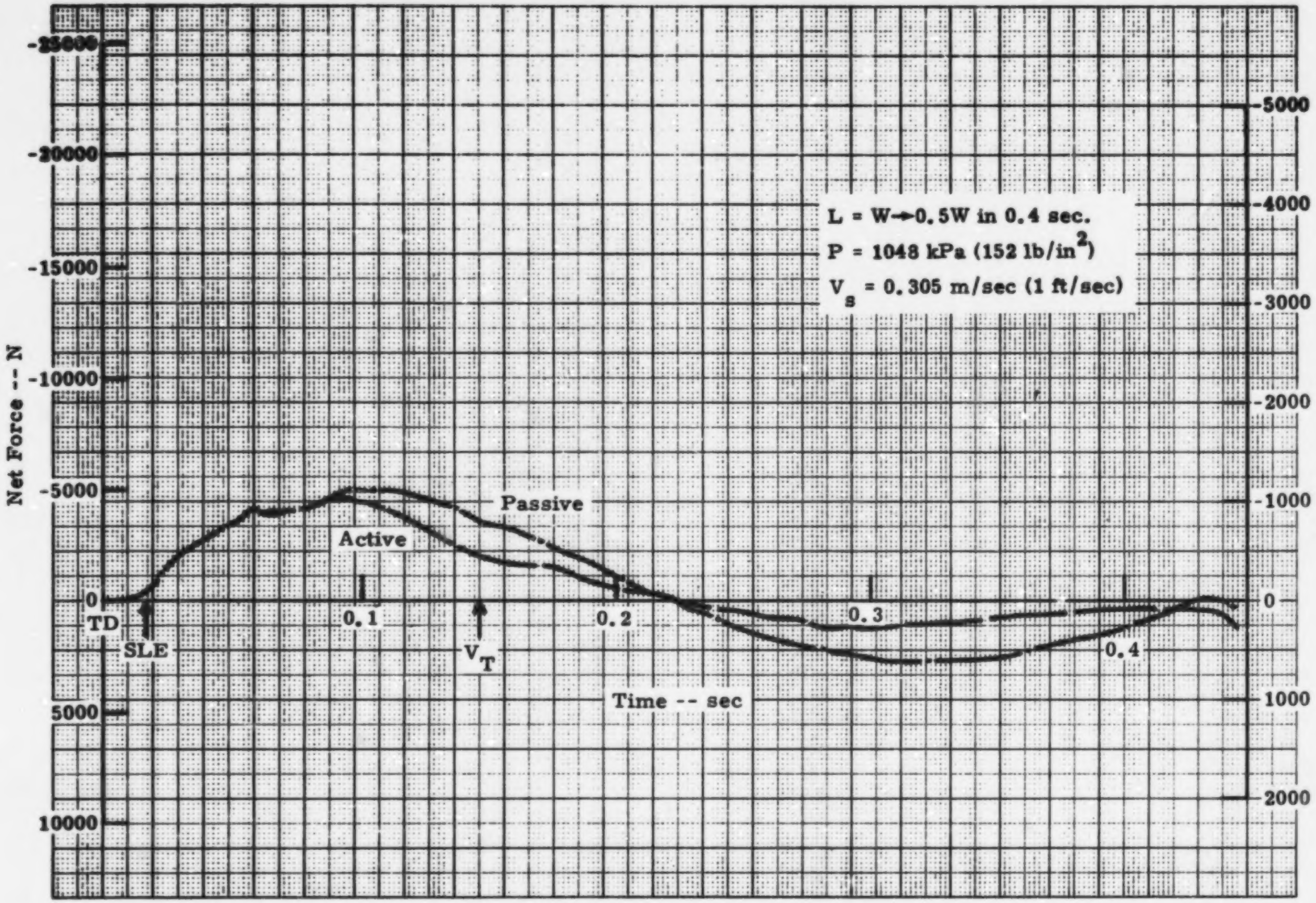

Figure 47. Net Force, Conditions 1, 4
(From W/G Accel #1)

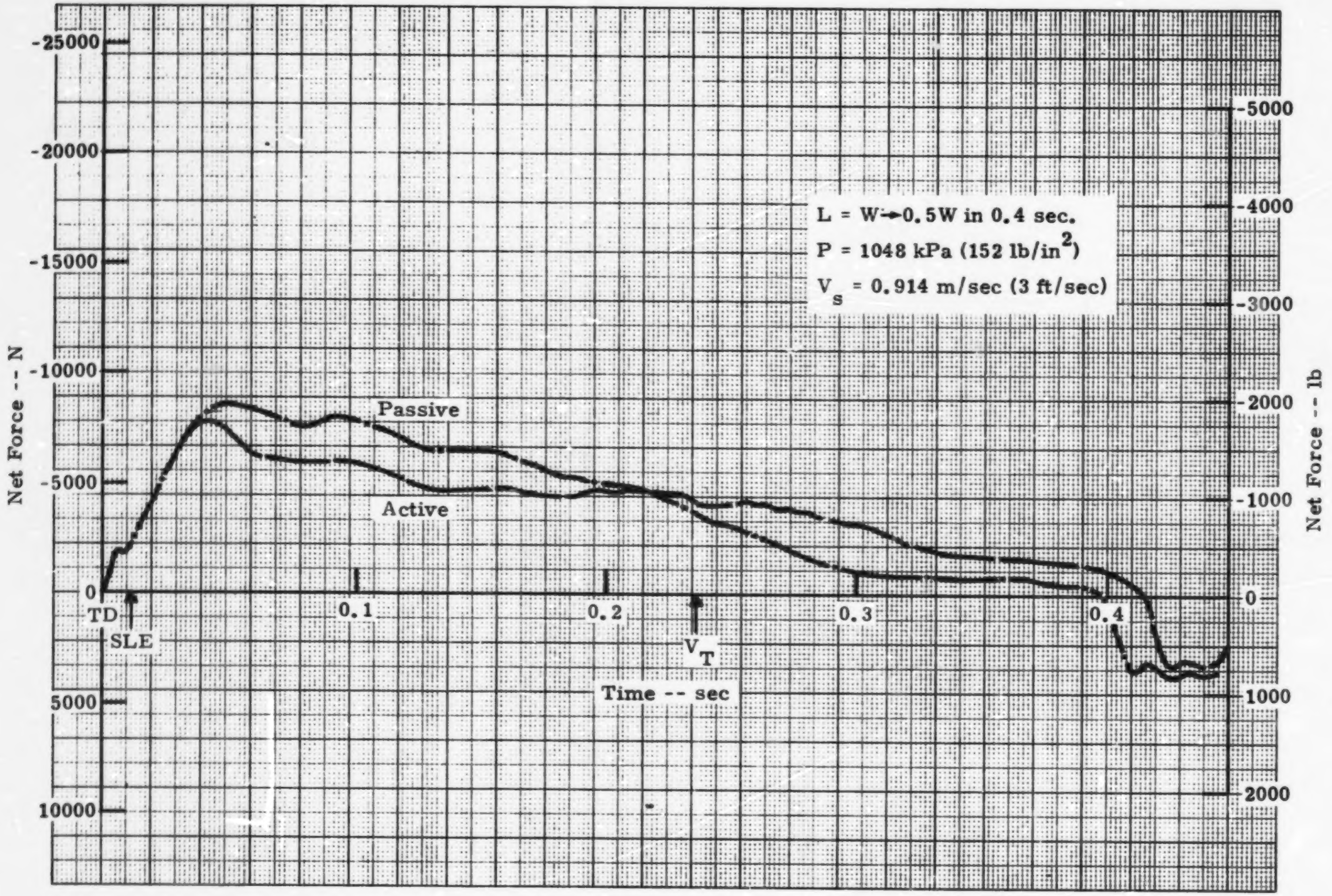

Figure 48. Net Force, Conditions 2, 5
(From W/G Accel #1)

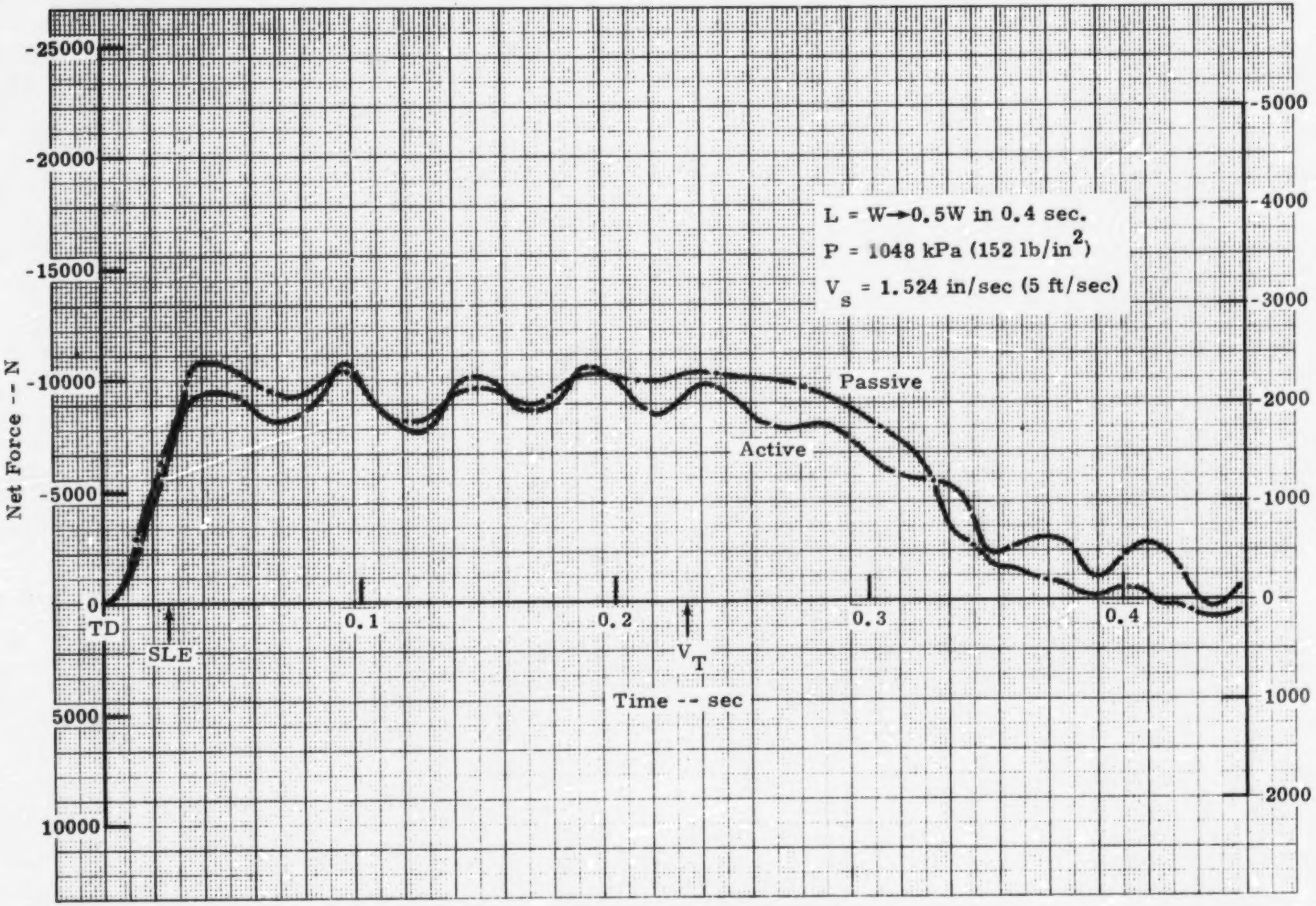

Figure 49. Net Force, Conditions 3, 6
(From W/G Accel #1)

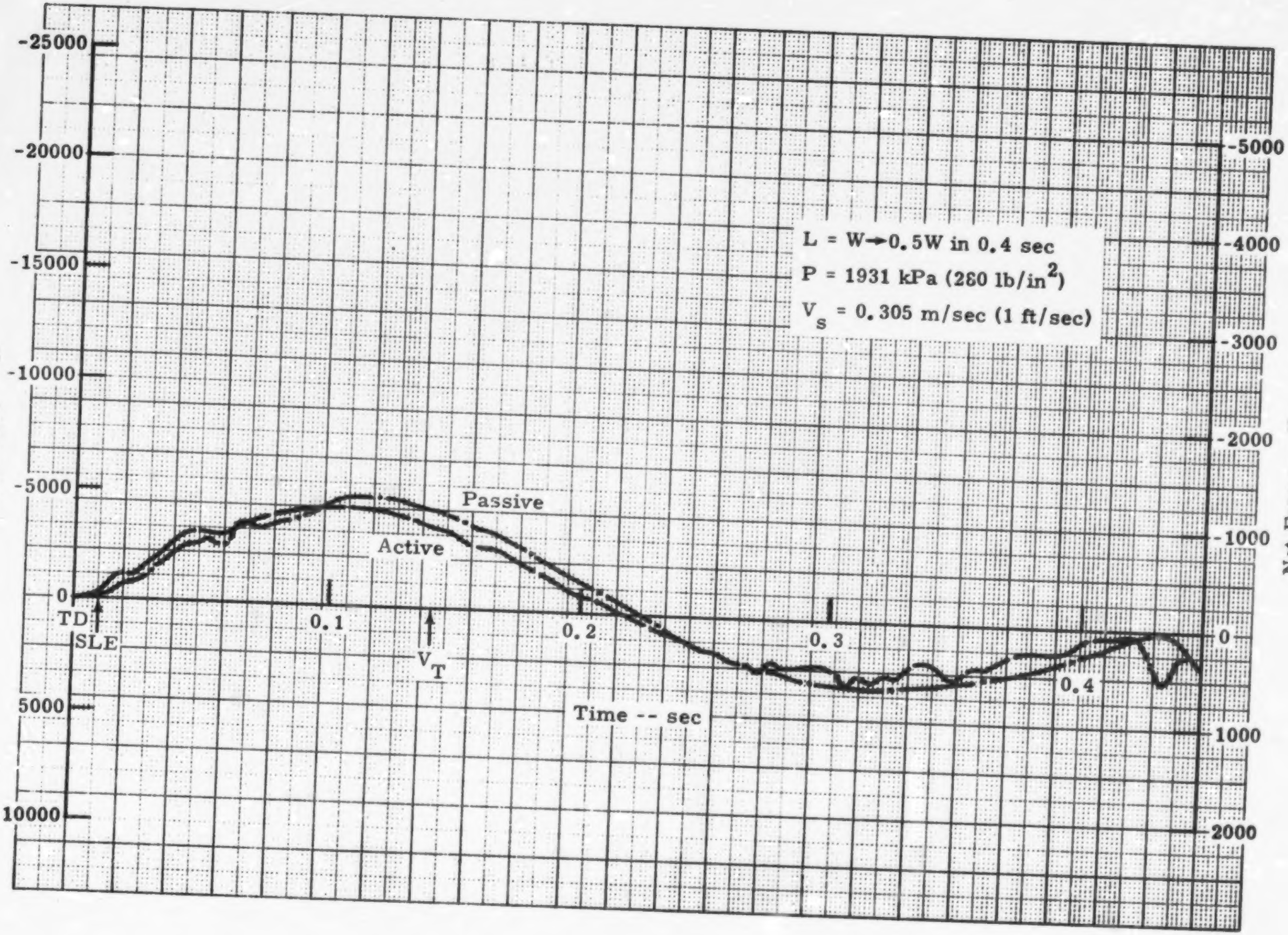

Figure 50. Net Force, Conditions 7, 10
(From W/G Accel #1)

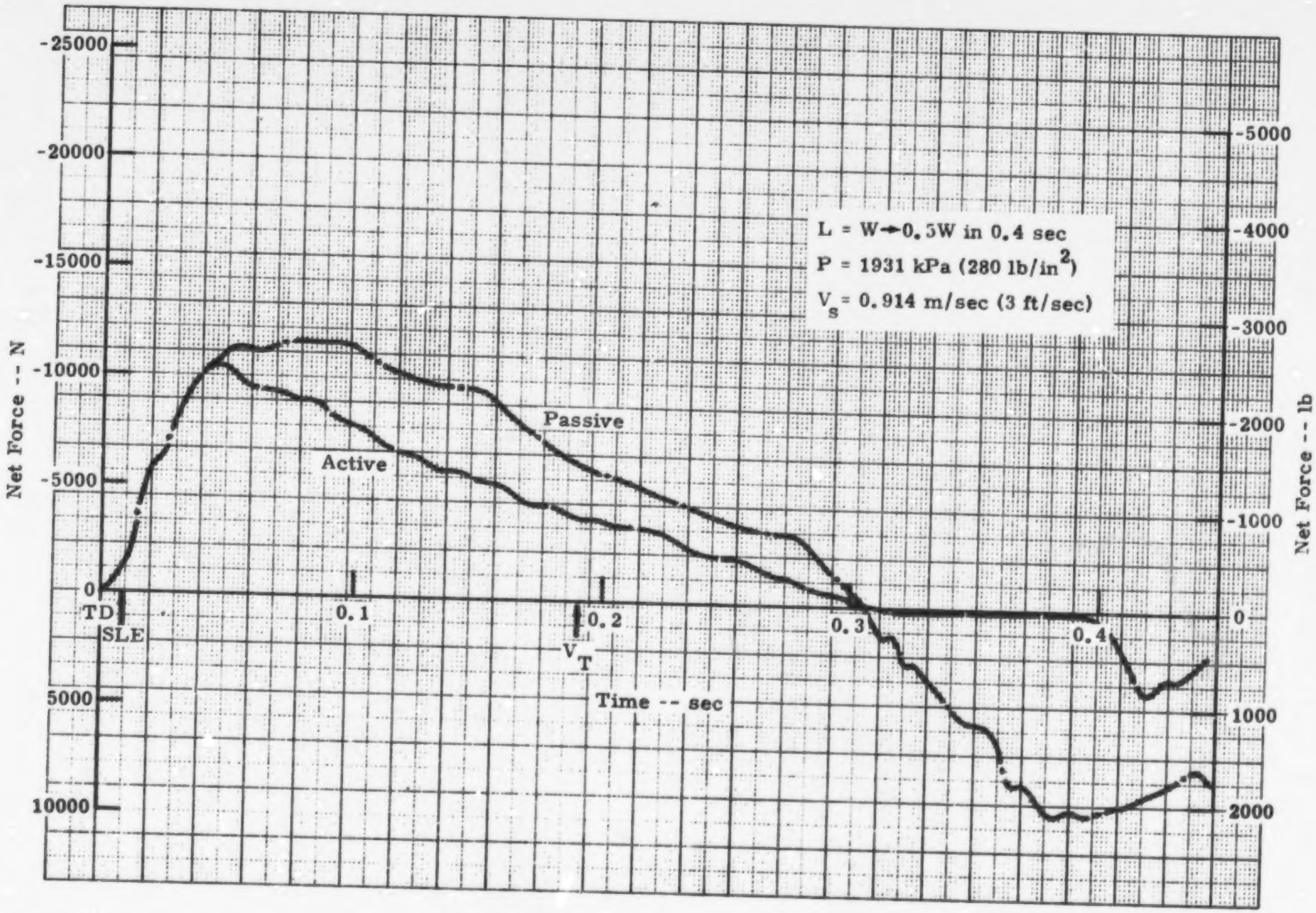

Figure 51. Net Force, Conditions 8, 11
(From W/G Accel #1)

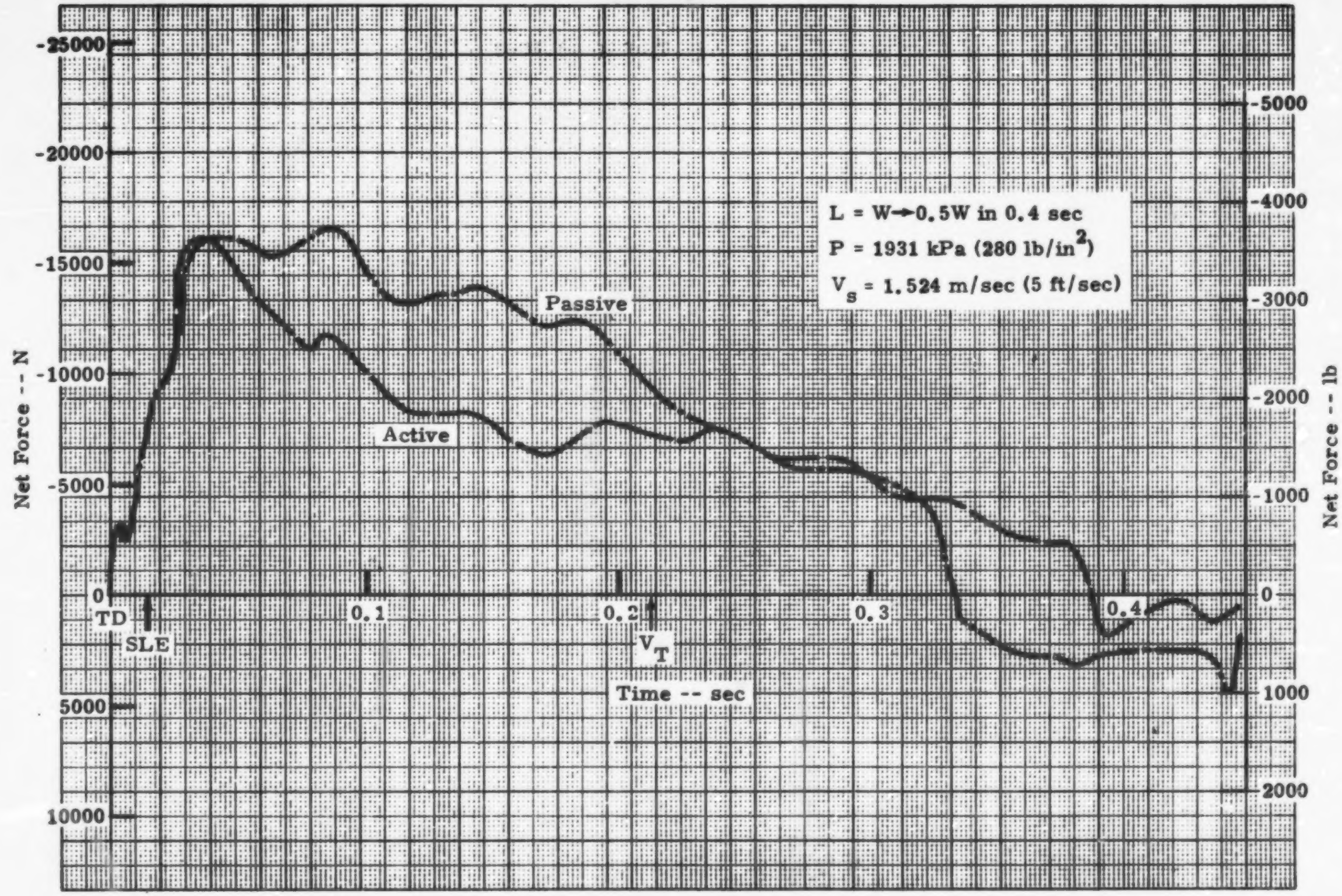

Figure 52. Net Force, Conditions 9, 12
(From W/G Accel #1)

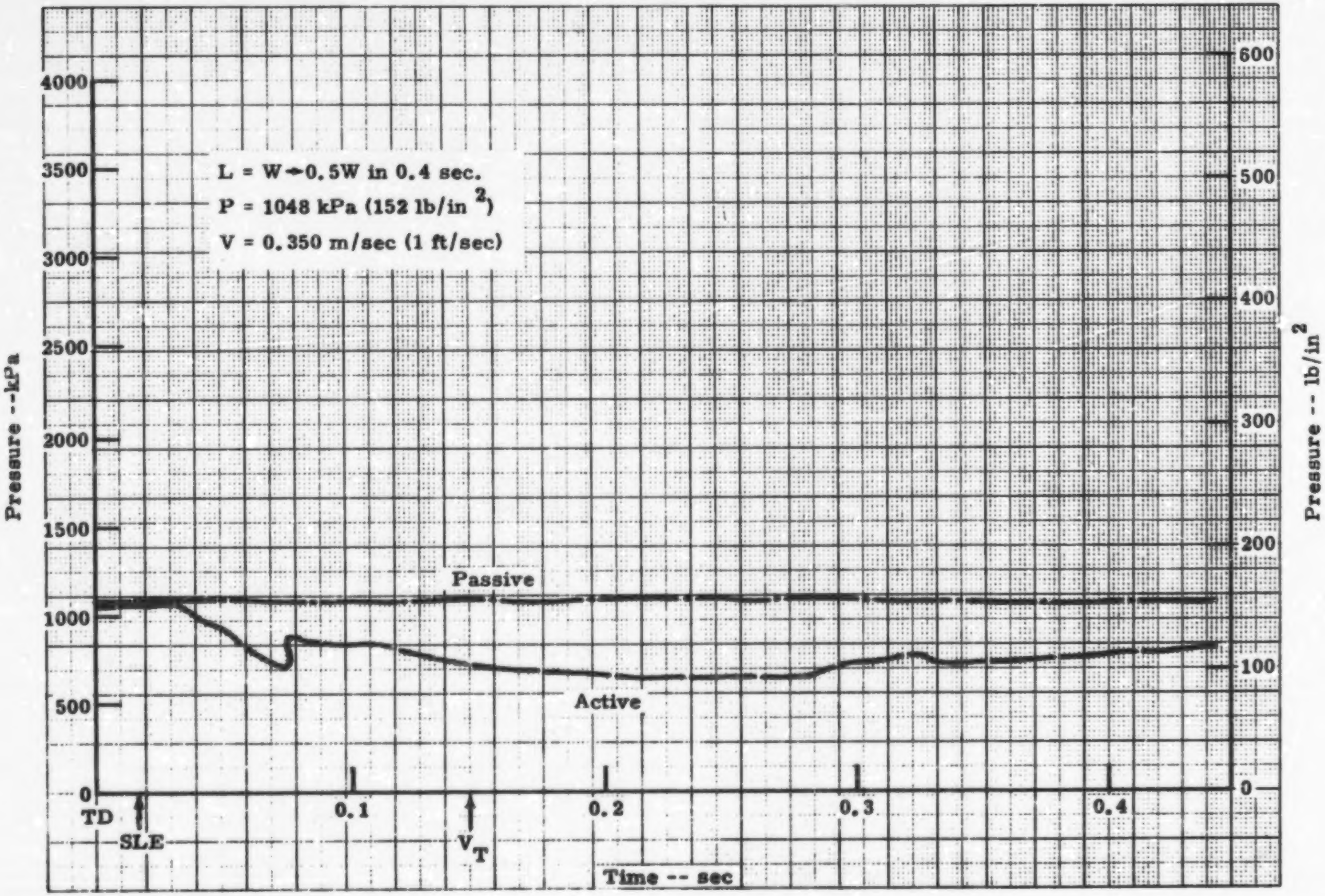

Figure 53. Gear Hydraulic Pressure, Conditions 1, 4

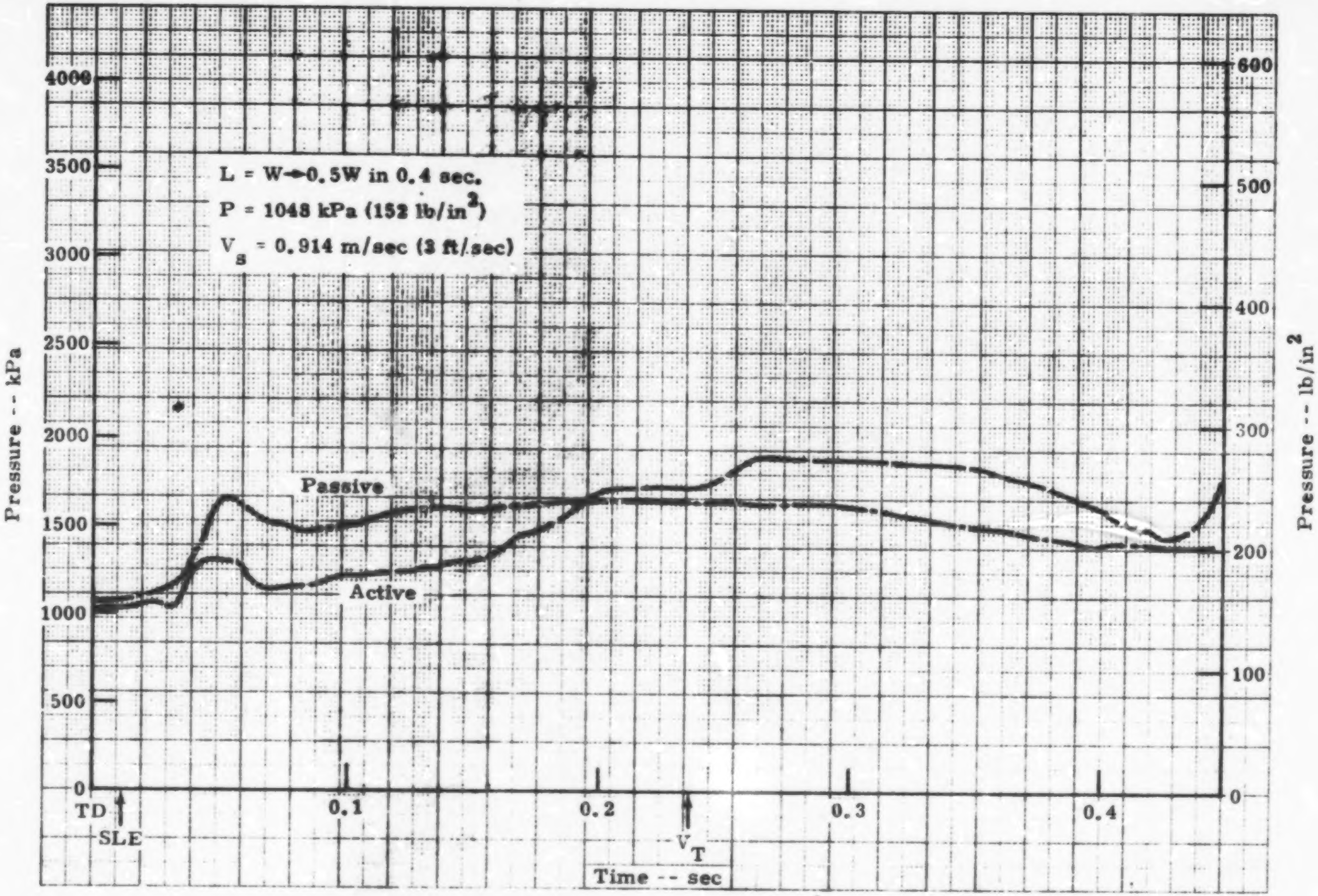

Figure 54. Gear Hydraulic Pressure, Conditions 2, 5

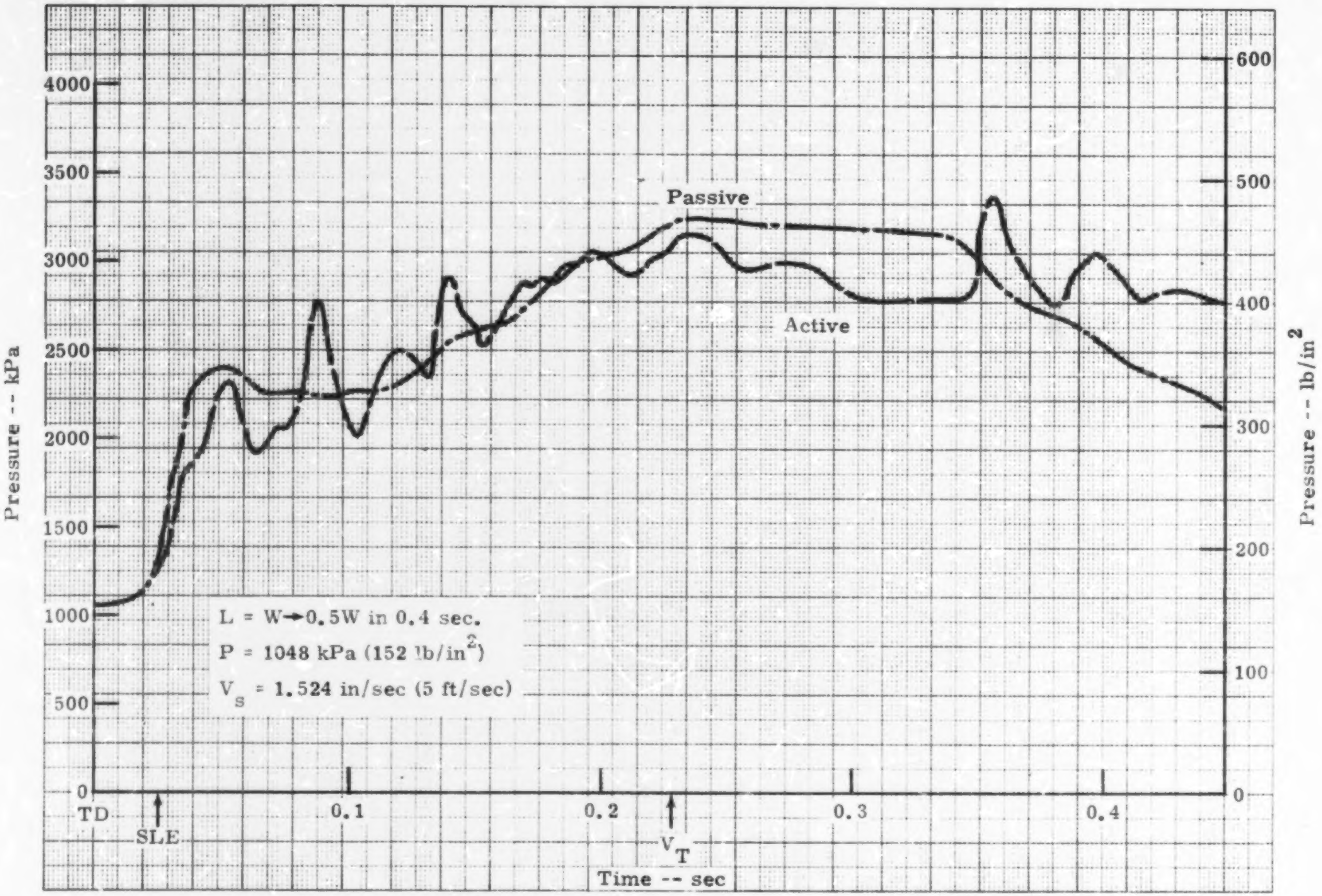

Figure 55. Gear Hydraulic Pressure, Conditions 3, 6

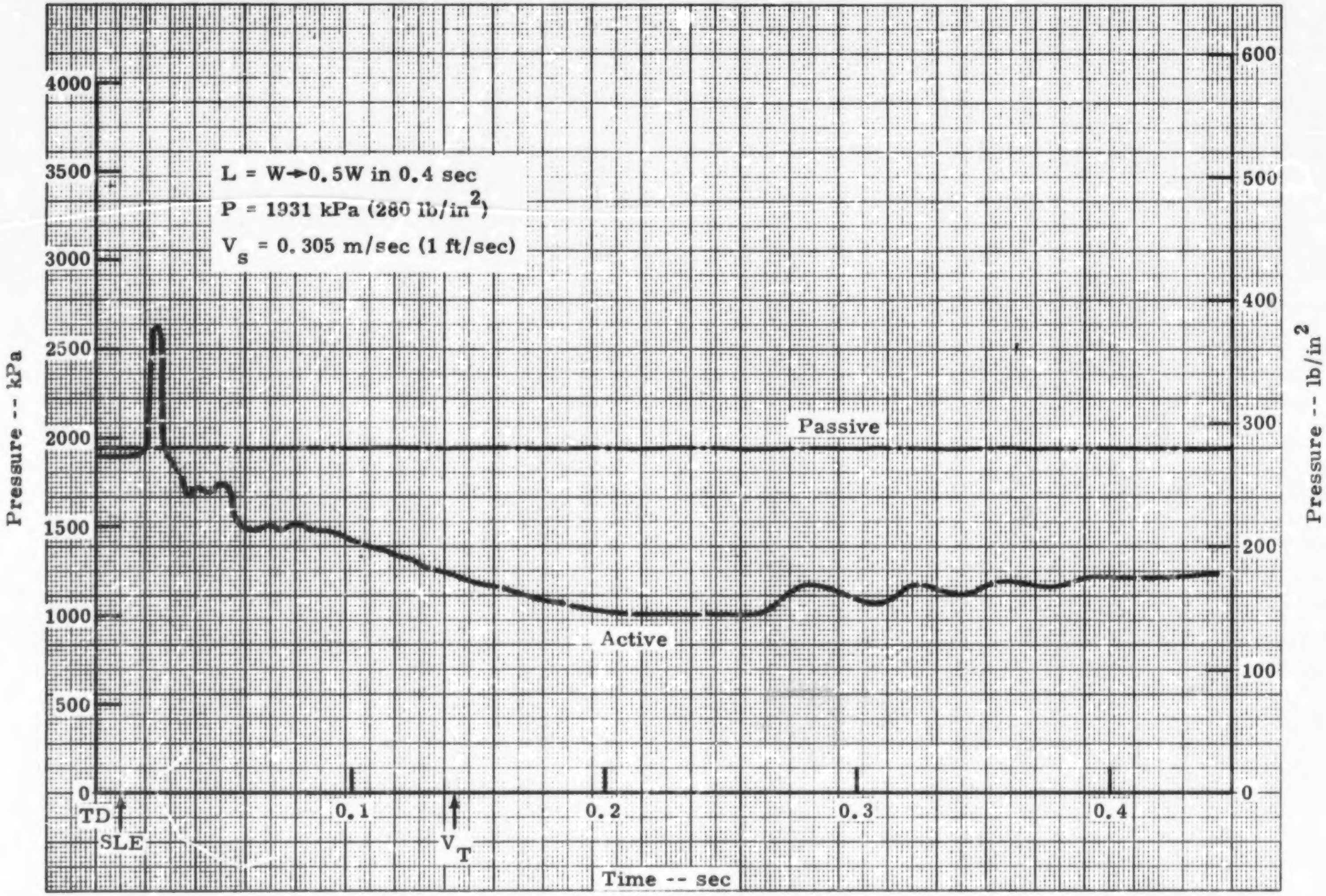

Figure 56. Gear Hydraulic Pressure, Conditions 7, 10

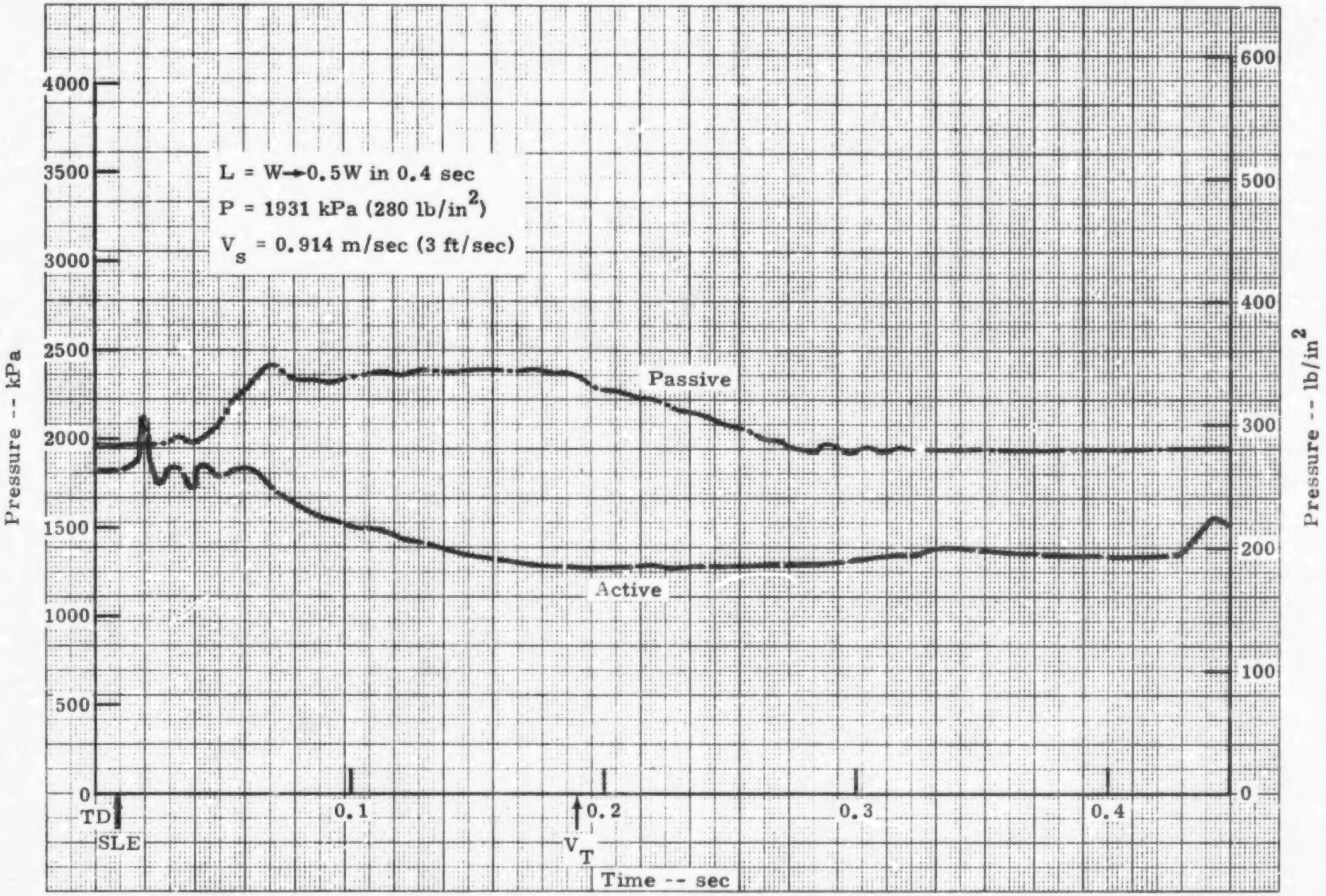

Figure 57. Gear Hydraulic Pressure, Conditions 8, 11

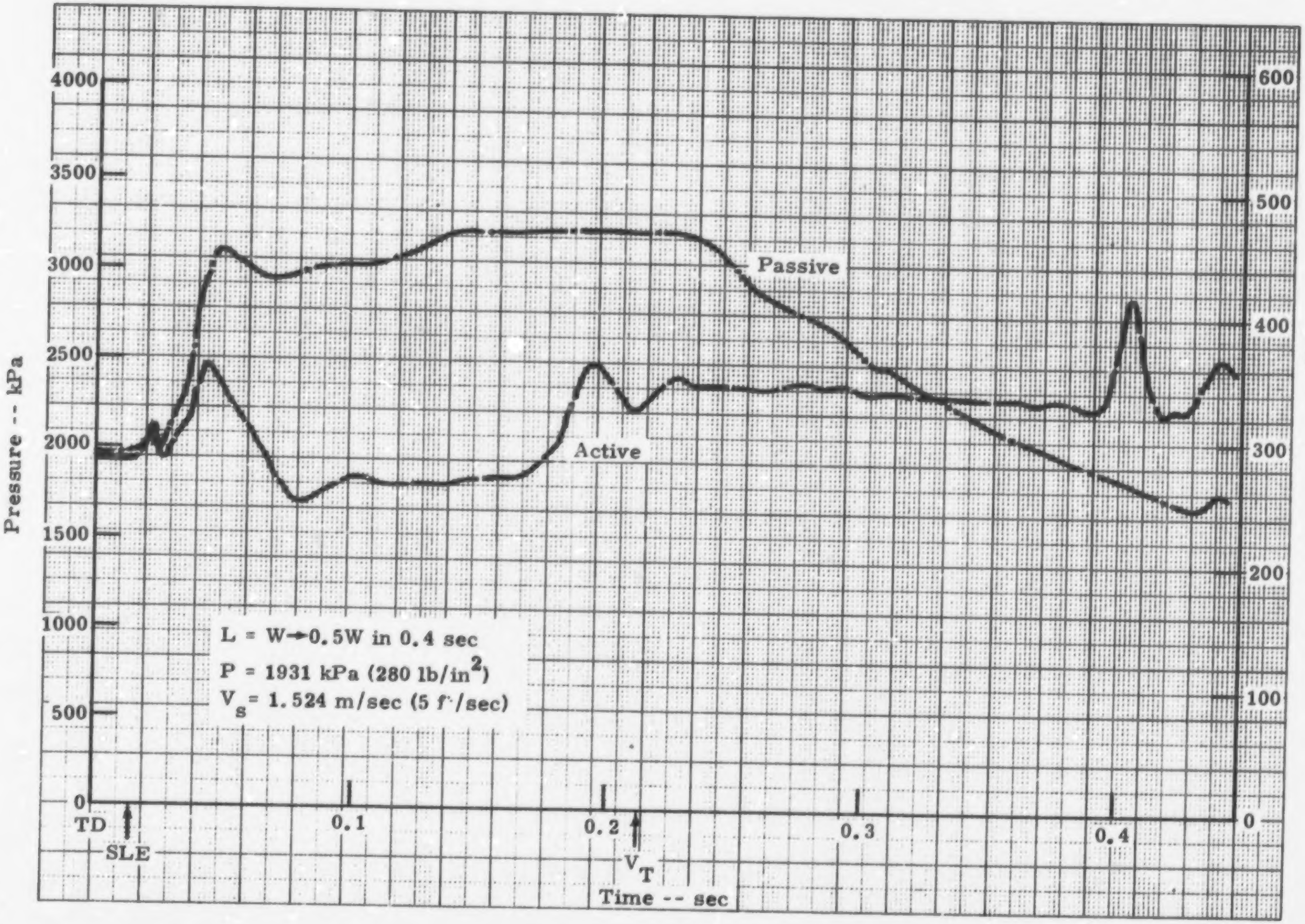

Figure 58. Gear Hydraulic Pressure, Conditions 9, 12

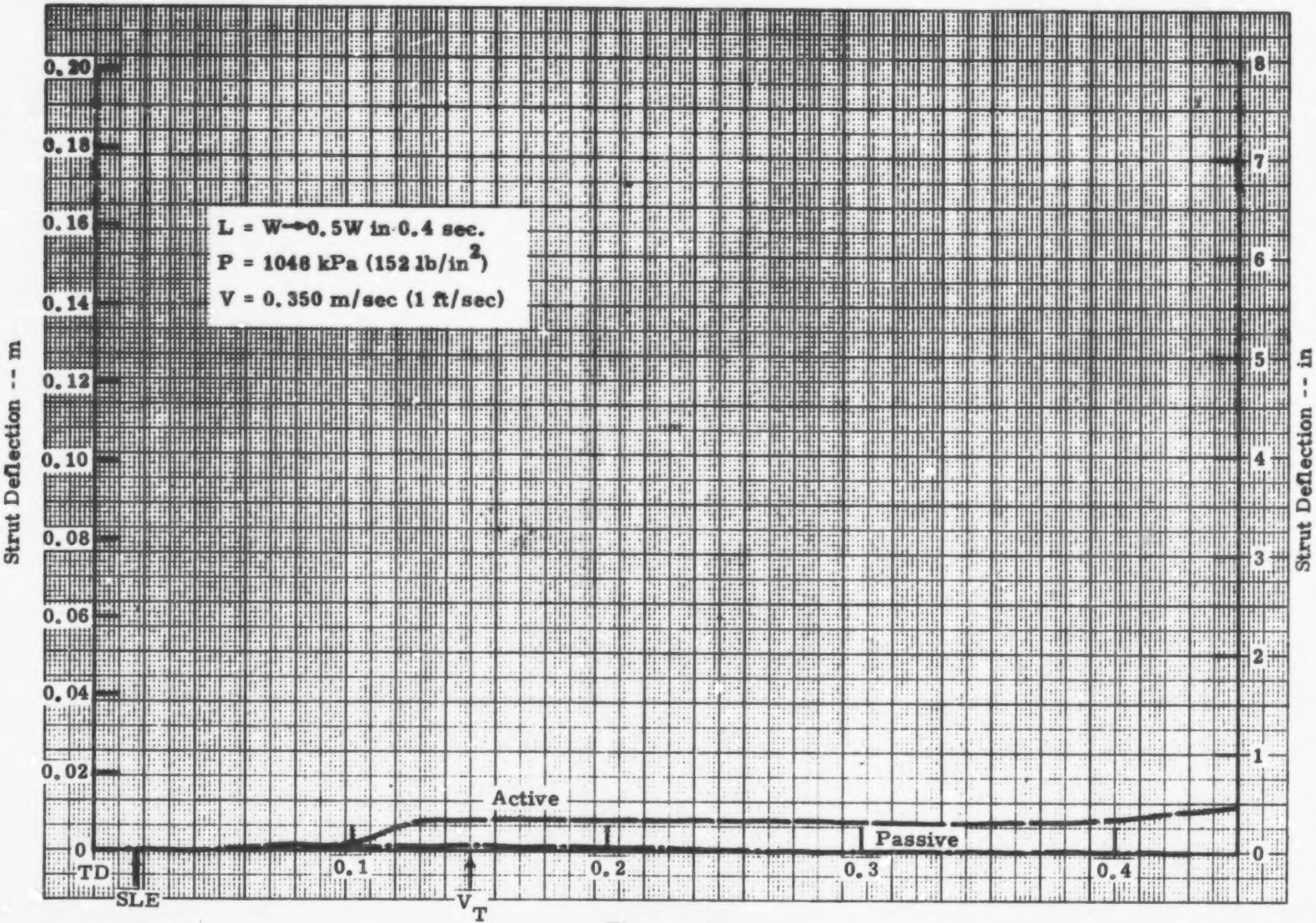

Figure 59. Strut Deflection, Conditions 1, 4

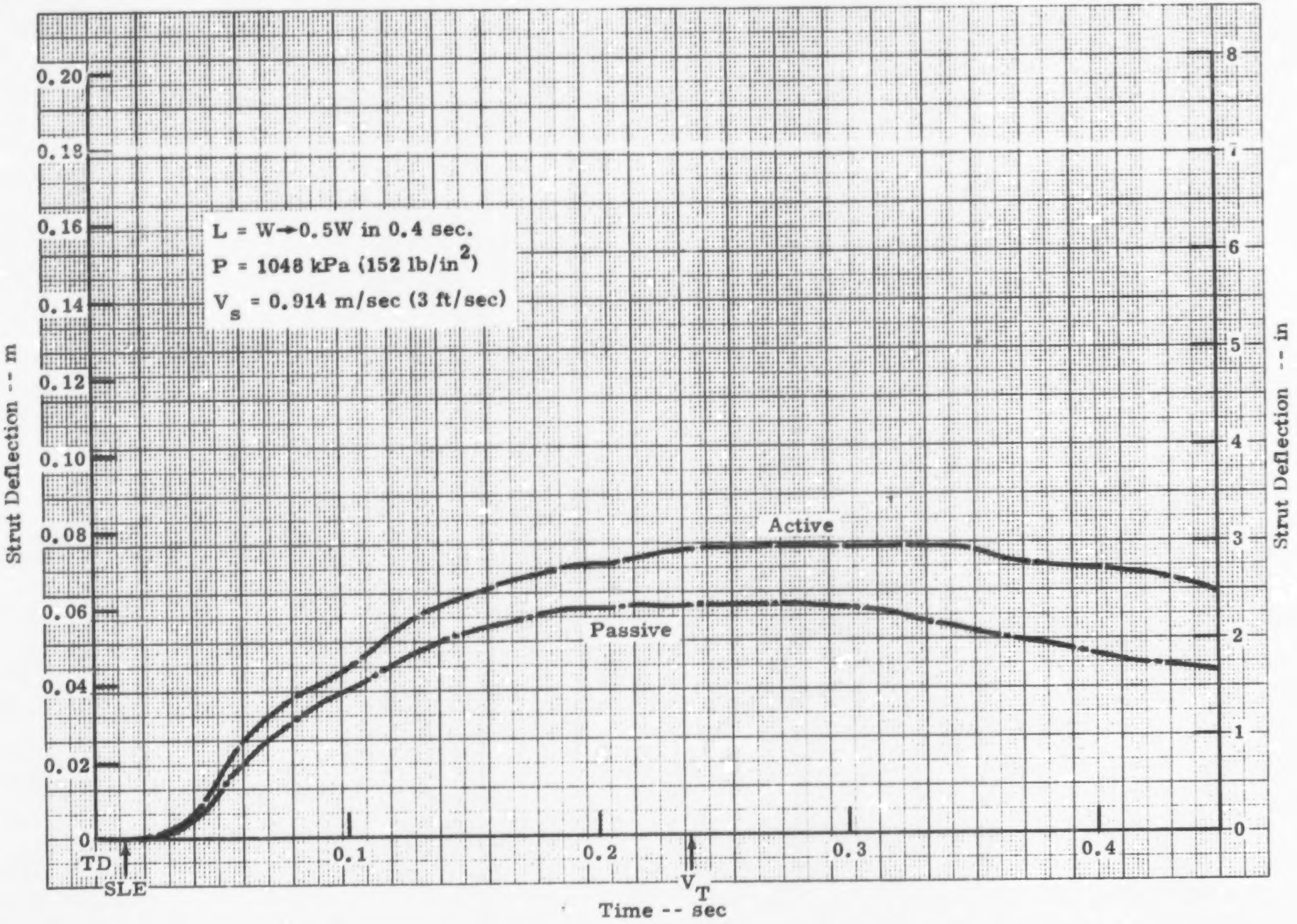

Figure 60. Strut Deflection, Conditions 2, 5

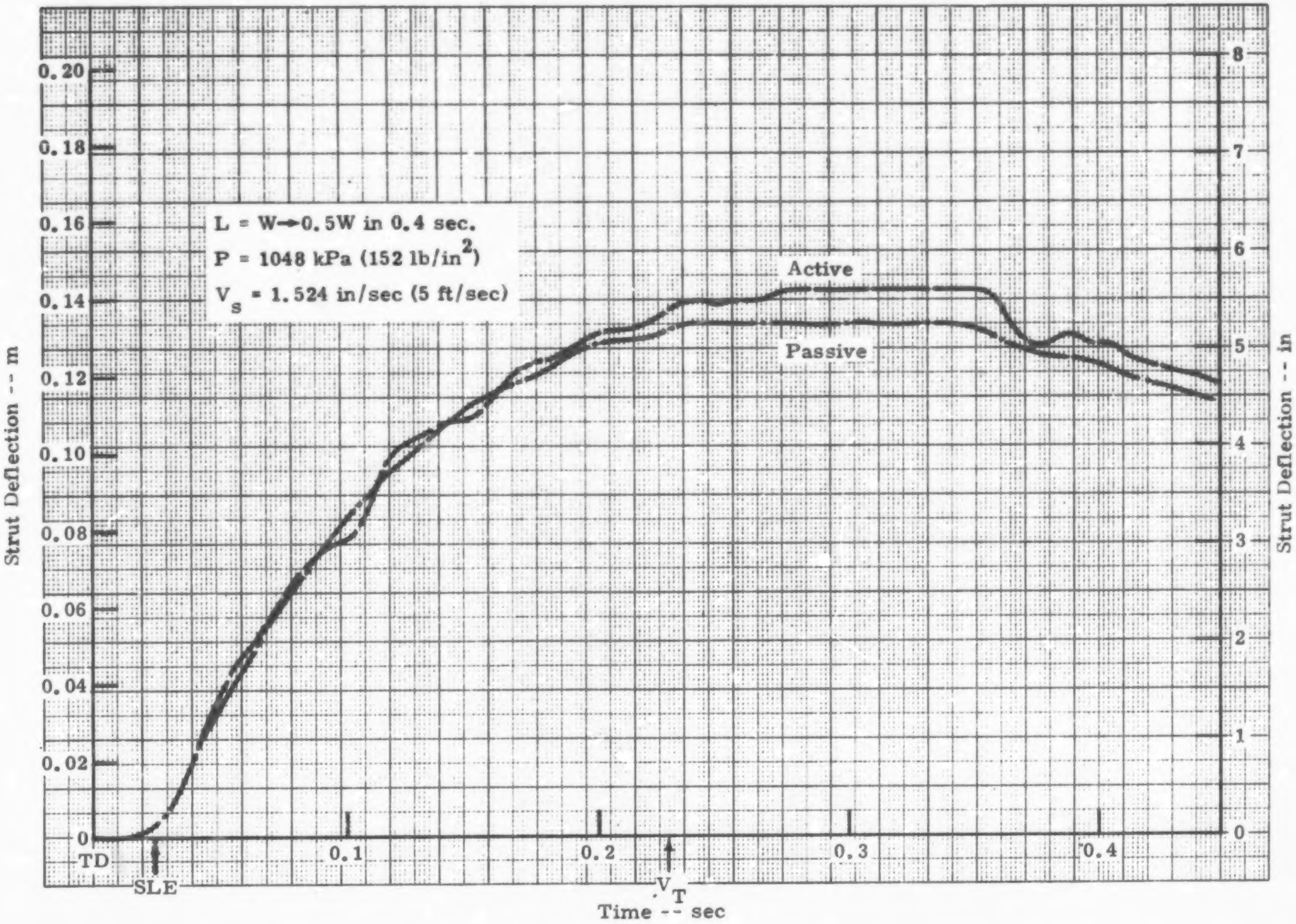

Figure 61. Strut Deflection, Conditions 3, 6

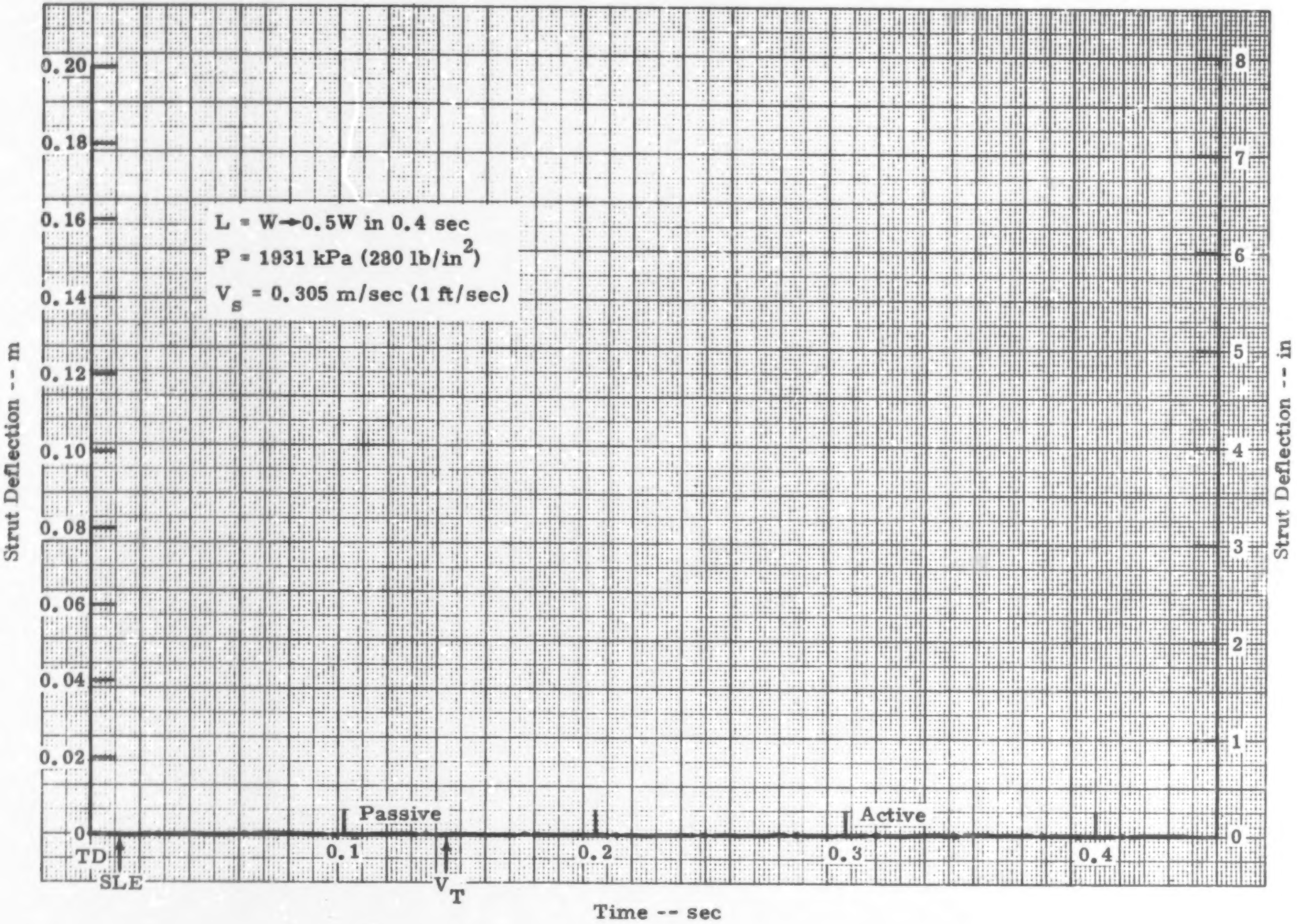

Figure 62. Strut Deflection, Conditions 7, 10

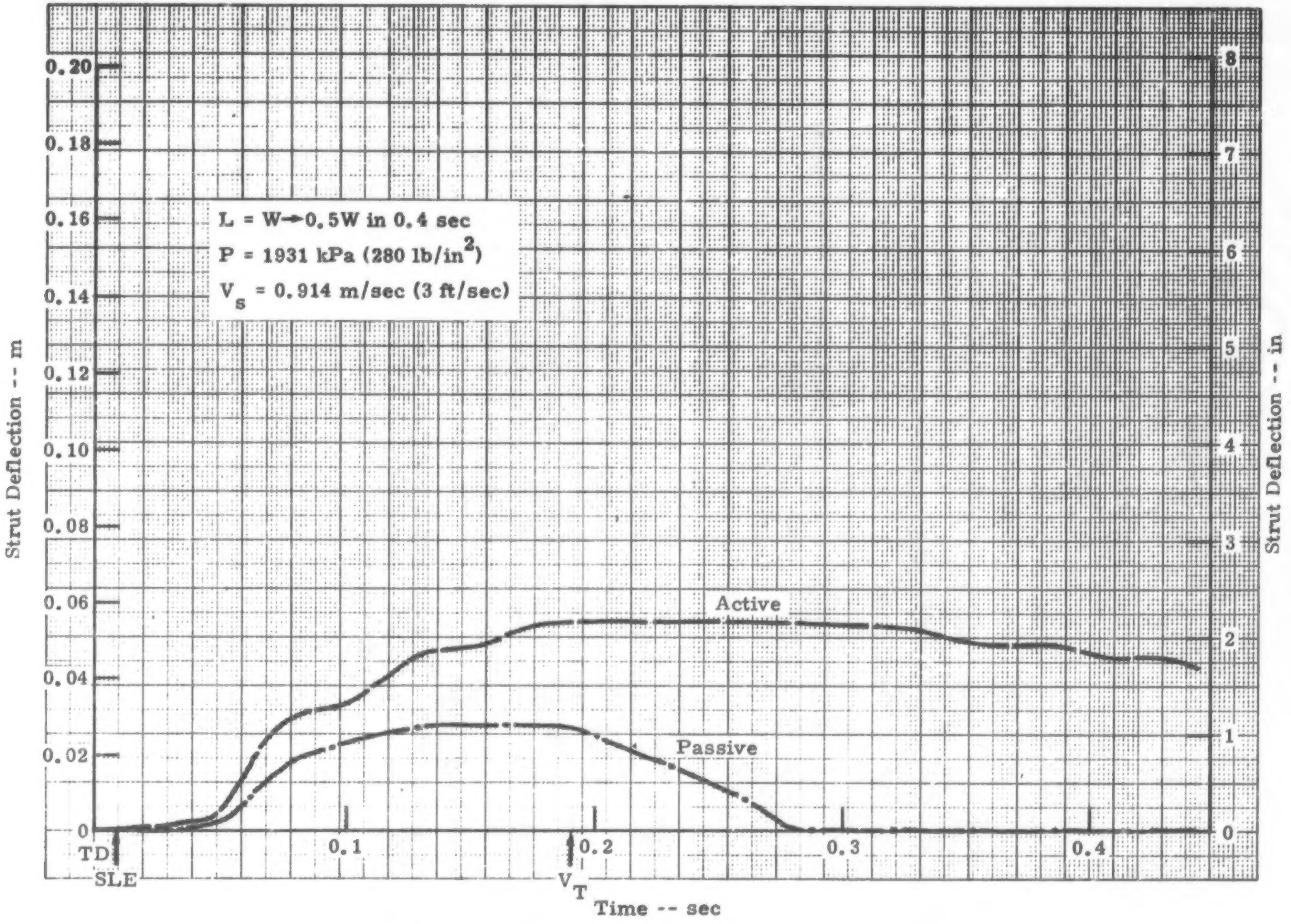

Figure 63. S.rut Deflection, Conditions 8, 11

N 5 1979

Item 830-H-14

NAS 1.26: 3113

NASA Contractor Report 3113

ORIGINAL

COMPLETED

An Electronic Control for an Electrohydraulic Active Control Aircraft Landing Gear

MICROFILMED FROM
BEST AVAILABLE COPY

Irving Ross and Ralph Edson

CONTRACT NAS1-14459
APRIL 1979

NASA

170

NASA Contractor Report 3113

An Electronic Control for an Electrohydraulic Active Control Aircraft Landing Gear

Irving Ross and Ralph Edson
Hydraulic Research Textron
Valencia, California

Prepared for
Langley Research Center
under Contract NAS1-14459

National Aeronautics
and Space Administration

Scientific and Technical
Information Office

1979

Blank Page

CONTENTS

Page

SUMMARY 1

INTRODUCTION 1

SYMBOLS. 3

ANALYSIS 8

Nonlinear Math Model for Vertical Drops 8

Equations of Motion 10

Pressure, Flow, and Volume Relationship 14

Servovalve Dynamics 16

Linear Math Model for Vertical Drops 18

Energy Considerations 27

Stability Analysis 39

ANALYTICAL RESULTS 51

Vertical Drop Cases 53

Land and Roll Cases 53

CONTROLLER FUNCTIONAL DESCRIPTION 71

Associated Equipment. 71

Interface 71

Performance Characteristics 76

Operating-Mode Determination. 76

Landing Mode 76

Takeoff Mode 77

Limit-Force Command Determination 78

Control Law Implementation 78

Controller Design 78

Functional Sections 78

CONTENTS (Contd.)

Page

TEST 89
  Test Fixture 89
  Test Conditions 93
  Test Results 93

CONCLUSIONS 114

APPENDIX

A Microprocessor Program Listing 115
B Electronic Controller Detailed Description 131
C Test Procedure 142
D Oscillograph Recordings 148

FIGURES

1 Illustration of variables used in nonlinear simulation of simplified vertical drop case 9
2 Free body diagram of airplane mass 11
3 Free body diagram of upper shock strut 11
4 Free body diagram of lower shock strut 11
5 Dynamic response of servovalve, ±10% input signal . . . 17
6 Illustration of "Equivalent" system for the linear math model 22
7 Block diagram of linear math model 26
8 Comparison of linear model and nonlinear model results, open loop, no compensation, no position feedback 28
9 Various energy terms versus time, from the simplified nonlinear vertical drop simulation 33
10 Illustration of the variation of limit force versus time and the various phases of operation following impact . . . 35
11 Block diagram of linear system without compensation . . 40

CONTENTS (Contd.)

Page

FIGURES

12 Nyquist plot of F_{wg}/F_{lim} with force loop opened, no position feedback, no compensation 41
13 Electronic compensation network and its characteristics . . 42
14 Nyquist plot of F_{wg}/F_{lim} with force loop opened, no position feedback, with compensation 43
15 Nyquist plot of F_{wg}/F_{lim} with force loop opened, position loop closed, with compensation 45
16 Nyquist plot of X_s/X_c with position loop opened, force loop closed, with compensation 46
17 Frequency response of F_{wg}/F_{lim} with force and position loops closed, with compensation 47
18 Frequency response of X_s/X_c with force and position loops closed, with compensation 48
19 Nyquist plot of F_{wg}/F_{lim} with force loop opened, position loop closed, with compensation. 49
20 Nyquist plot of F_{wg}/F_{lim} with force loop opened, position loop closed, with compensation. 50
21 Wing/gear force transient, case A 54
22 Wing/gear force transient, case B 55
23 Strut position transient, case B 56
24 Wing/gear force transient, case 1 57
25 Strut pressures, case 1 58
26 Strut position transient, case 1 59
27 Wing/gear force transient, case 2 60
28 Strut position transient, case 2 61
29 Wing/gear force transient, case 3 63
30 Wing/gear force transient, case 4 64
31 Servovalve flow rate, case A 65
32 Servovalve flow rate, case B 66

CONTENTS (Contd.)

Page

FIGURES

33 Servovalve flow rate, case 1 67
34 Servovalve flow rate, case 2 68
35 Servovalve flow rate, case 3 69
36 Servovalve flow rate, case 4 70
37 Input/Output Signal Schematic 72
38 Control Law Functional Schematic 79
39 Controller Functional Schematic 81
40 Basic Functional Requirements 82
41 Software Flow Chart 84
42 Analog Section Schematic 85
43 Analog Section - Front Panel Inputs 87
44 Analog Section - Front Panel Outputs 88
45 S-1C Test Fixture, Landing Gear Installed (View 1) 90
46 S-1C Test Fixture, Landing Gear Installed (View 2) 91
47 Net Force, Conditions 1, 4 (From W/G Accel #1) 95
48 Net Force, Conditions 2, 5 (From W/G Accel #1) 96
49 Net Force, Conditions 3, 6 (From W/G Accel #1) 97
50 Net Force, Conditions 7, 10 (From W/G Accel #1) 98
51 Net Force, Conditions 8, 11 (From W/G Accel #1) 99
52 Net Force, Conditions 9, 12 (From W/G Accel #1) 100
53 Gear Hydraulic Pressure, Conditions 1, 4 101
54 Gear Hydraulic Pressure, Conditions 2, 5 102
55 Gear Hydraulic Pressure, Conditions 3, 6 103
56 Gear Hydraulic Pressure, Conditions 7, 10 104
57 Gear Hydraulic Pressure, Conditions 8, 11 105
58 Gear Hydraulic Pressure, Conditions 9, 12 106

CONTENTS (Contd.)

Page

FIGURES

59 Strut Deflection, Conditions 1, 4 107
60 Strut Deflection, Conditions 2, 5 108
61 Strut Deflection, Conditions 3, 6 109
62 Strut Deflection, Conditions 7, 10 110
63 Strut Deflection, Conditions 8, 11 111
64 Strut Deflection, Conditions 9, 12 112

TABLES

I SUMMARY OF ACTIVE CONTROL LANDING CASES SIMULATED ON THE COMPUTER 52
II PRIMARY INPUT SIGNAL SPECIFICATIONS 73
III SECONDARY INPUT SPECIFICATIONS 74
IV OUTPUT SPECIFICATIONS 75
V CONTROL LAW TRANSFER FUNCTIONS. 80
VI PEAK FORCES AND PERCENTAGE REDUCTION. . . . 94

REFERENCES. 161

SUMMARY

The electronic controller described in this report, together with an active control landing gear, are found to provide significant reductions in forces sustained by an aircraft during takeoff, landing impact and rollout. The degree of force reduction increases with the sink rate. These results were obtained analytically and confirmed experimentally by actual drop tests of a landing gear under active control.

The electronic controller continuously compares the kinetic energy of the aircraft with the work potential of the gear until the work potential exceeds the kinetic energy. The wing/gear interface force present at this condition becomes the command force to a servo loop which maintains the wing/gear interface force at this level by providing a signal to an electro-hydraulic servovalve to port flow into or out of the landing gear.

INTRODUCTION

Hydraulic Research (HR) was retained under NASA Contract NAS 1-14459 to design, develop, fabricate and test an electronic controller for an electro-hydraulic active control landing gear, as described in Reference 1. The primary function of the active control landing gear is to minimize the force to which the aircraft is subjected as a result of landing impact and rollout, takeoffs and taxi operations. As shown in Ref. 1, the resultant decrease in applied loads could be very beneficial in reducing structural fatigue design problems and increasing ride comfort for passengers and crew. The work was divided into two major phases: Phase 1 for the analytical development and design of the controller; and, Phase 2 for the fabrication and testing. This report summarizes the effort of both phases and provides the rationale for the controller design selected.

Phase 1 included the development and use of digital computer programs which simulated the dynamics of the landing gear/controller system. A nonlinear dynamic model and a simplified linear model for vertical drops were developed by HR and used extensively in the analysis. In addition, a computer program developed by NASA, which included aerodynamic simulation and landing gear dynamics, was supplied to HR in support of the program. The computer program was modified by HR to include the dynamics of the electrohydraulic servovalve and this program was incorporated into the study. The landing gear parameters, as described in the NASA computer program, were used as the basis for all analyses described herein. During this phase, the controller design was also developed. This design included analog circuitry for the control laws, compensation, summations and the signal to the servovalve driver while a digital microprocessor was used for the nonlinear computations and decision making.

During Phase 2, the controller, as defined in Phase 1, was fabricated and tested by actual drop tests of the gear.

SYMBOLS

A_o	area of orifice in shock strut orifice plate, 0.0000786 m^2 (0.1219 in^2)
A_1	shock strut hydraulic area (piston area), 0.00317 m^2 (4.909 in^2)
A_2	shock strut pneumatic area (cylinder area), 0.00535 m^2 (8.286 in^2)
A_3	annular area in shock strut between piston and cylinder walls, 0.00151 m^2 (2.34 in^2)
C_d	discharge coefficient for active control servovalve orifice, 0.62
C_{do}	discharge coefficient for shock strut orifice, 0.90
C_o	orifice coefficient for shock strut orifice $= C_{do} A_o \sqrt{2g_c/\rho}$, 3.45 (10^{-8}) $m^4\ sec^{-1} \cdot N^{-1/2}$ (17.51 $in^3/sec/\sqrt{lb/in^2}$)
CP	linearized orifice coefficient for active control servovalve $= -\partial Q_{sv}/\partial P_1$ $= 3.16\ (10^{-11})\ m^5 \cdot N^{-1} \cdot sec^{-1}$ (0.01334 $in^3/sec/lb/in^2$)
CP_o	linearized orifice coefficient for shock strut orifice $= \partial Q_o/\partial P_1$ $= C_o/(2\sqrt{P_1-P_2})$, $m^5 \cdot N^{-1} \cdot sec^{-1}$ ($in^3/sec/lb/in^2$)
CQ	linearized orifice coefficient for active control servovalve $= \partial Q_{sv}/\partial X_{sv}$ $= C_{sv}\ \sqrt{(P_S + P_R)/2}$, 8.61 m^2/sec (13 340 $\cdot$ $in^3/sec/in$)
C_{sv}	orifice coefficient for active control servovalve $= C_d W_{sv} \sqrt{2g_c/\rho}$, 0.00268 $m^3 \cdot sec^{-1} \cdot lb^{-1/2}$ (344.4 $in^3/sec/\sqrt{lb/in^2}$)
f	Coulomb friction between shock strut piston and cylinder, N (lb)
F_a	vertical force exerted on shock strut by the runway surface, N (lb)
F_{li}	impact phase limit force, N (lb)
F_{lim}	limit force, N (lb)
F_s	shock strut force, N (lb)
F_{wg}	wing/gear interface force, N (lb)

SYMBOLS (Continued)

g	acceleration due to gravity, 9.80 m/sec^2 (386 · in/sec^2)
g_c	gravitational acceleration constant, 1 kg · m · N^{-1} · sec^{-2} (12 slug · in · lb^{-1} · sec^{-2})
i_1	input signal to electronic compensation networks, A
i_2	output signal from electronic compensation networks, or input signal to active control servovalve, A (±0.040 A maximum)
K_a	amplifier gain in active control loop, 0.000040 A/V
K_f	position feedback gain in strut position control loop, 196.9 V/m (5.0 V/in)
K_{FDGE}	fraction of total strut stroke assumed available when computing impact phase force from equation 37
K_{sv}	position gain of servovalve in active control loop, 0.0635 m/A (2.50 in/A)
K_t	effective spring rate of tire, 245 000 · N/m (1400 lb/in)
K_x	gain in strut position control loop, 1.0 m/m (1.0 in/in)
L	total life force, N (lb)
M	mass of airplane per gear, 1456 kg (99.8 slugs)
M_C	mass of upper portion of landing gear (cylinder plus orifice plate attachment, kg (slug)
M_L	mass of lower portion of landing gear (piston plus tire), 32.1 kg (2.20 slugs)
M_U	upper mass, 1456 kg (99.8 slugs)
PE_t	potential energy stored in tire due to compression, N · m (ft · lb)
P_S	hydraulic supply pressure, 2.07 (10^7) N/m^2 (3000 lb/in^2)
P_R	hydraulic return pressure, 0.0 N/m^2 (0.0 lb/in^2)

SYMBOLS (Continued)

PROM	programmable read only memory
P_1	hydraulic pressure in shock strut piston, N/m^2 (lb/in^2)
P_2	pneumatic pressure in shock strut cylinder, N/m^2 (lb/in^2)
P_3	pressure in volume between walls of shock strut piston and cylinder, N/m^2 (lb/in^2)
Q_O	flow rate through shock strut orifice from piston to cylinder, m^3/sec (in^3/sec)
Q_{sv}	flow rate from active control servovalve to shock strut piston, linear mode, m^3/sec (in^3/sec)
Q_{sv_1}	flow rate through active control servovalve from supply pressure to the shock strut piston, m^3/sec (in^3/sec)
Q_{sv_2}	flow rate through active control servovalve from shock strut piston to return pressure, m^3/sec (in^3/sec)
RAM	random access memory
R_s	the slope of the limit force with respect to time during transition phase, 137 900 N/sec (31 000 lb/sec)
s	LaPlace operator, sec^{-1}
t	time, sec
V	velocity
V_1	hydraulic volume in shock strut piston and lines up to the active control servovalve, 0.00426 m^3 (260.0 in^3) for fully extended strut
V_2	pneumatic volume, 0.000624 m^3 (38.1 in^3) for fully extended strut
V_3	volume between shock strut piston and cylinder, 0.0 m^3 (0.0 in^3) for fully extended strut
Wsv	window width of orifices on third stage spool of active control servovalve, 0.0884 m (3.48 in)

SYMBOLS (Continued)

X	displacement, m (in)
X_c	commanded position of shock strut, 0.1016 m (4.0 in)
β	bulk modulus of hydraulic fluid, 6.89 (10^8) N/m^2 $(1 \cdot 10^5\ lb/in^2)$
γ	ratio of specific heat of gas at constant pressure to that at constant volume, 1.1
ρ	mass density of hydraulic fluid, 838 kg/m^3 (0.000941 $slugs/in^3$)
τ_f	time constant in strut position feedback loop, 0.10 sec
τ_1	time constant in electronic compensation network, 0.0281 sec
τ_2	time constant in electronic compensation network, 0.0141 sec
τ_3	time constant in electronic compensation network, 0.0010 sec
τ_4	time constant in electronic compensation network, 0.0001 sec
ω_c	corner frequency in active control servovalve transfer function, 1263 sec^{-1}
ω_{sv}	natural frequency in active control servovalve transfer function, 655.5 sec^{-1}
ω_1	natural frequency in electronic compensation network, 251.3 sec^{-1}
ζ_{sv}	damping coefficient in active control servovalve transfer function, 0.436
ζ_1	damping coefficient in electronic compensation network, 5.10
ζ_2	damping coefficient in electronic compensation network, 0.10

SYMBOLS (Continued)

Subscripts:

a	lower mass of shock strut or axle
g	ground
i	initial conditions before impact
im	impact phase
L	lower mass
max	maximum value
min	minimum value
r	rollout phase
s	shock strut relative motion of the lower mass (piston) with respect to the upper mass (cylinder)
sv	servovalve
tr	transition phase
U	upper mass
wg	wing/gear interface

Miscellaneous:

d( )	indicates the differential of a variable
$\Delta(\ )$	indicates difference or change in a variable
$(\dot{\ }),(\ddot{\ }),(\dddot{\ })$	dots indicate differentiation with respect to time

ANALYSIS

Nonlinear Math Model for Vertical Drops

A simplified nonlinear dynamic model of an active control landing gear for vertical drops without aerodynamics and airplane dynamics was developed. The airplane mass is represented simply as a point mass located on top of the landing gear. This model proved to be of great value in this project for various reasons. First, it enhanced understanding of the basic equations of motion of the landing gear and the dynamic characteristics. This was very useful in the further development of an even more simplified linearized dynamic model, which was used extensively in the development of the electronic compensation networks that are required for stability. The linear model and its application are discussed in later sections. Secondly, it often was desirable to study the dynamic operation of the system without the complicating influences of the airplane dynamics, and the simplified nonlinear model provided a good tool to do this. Also, by neglecting airplane dynamics, the size of the computer simulation is greatly reduced and runs can be made in less computational time. Finally, the simplified model was used as a check with the more general computer program supplied by NASA, which required many programming changes in its application to this study.

Figure 1 shows a schematic of the simplified vertical drop case along with some of the variables used in modeling the system. The system basically consists of (1) an upper mass M_U, which is the mass M (per gear) of the airplane plus the mass M_C of the upper portion of the landing gear (i. e., the cylinder plus the orifice plate attachment), (2) a lower mass M_L, which consists of the tire mass plus the mass of the lower portion of the landing gear (i. e., the piston), (3) a three-way servovalve that ports fluid in the piston chamber to either supply or return pressure, and (4) an electronic controller. Note that the tire dynamics are simulated as a mass and linear

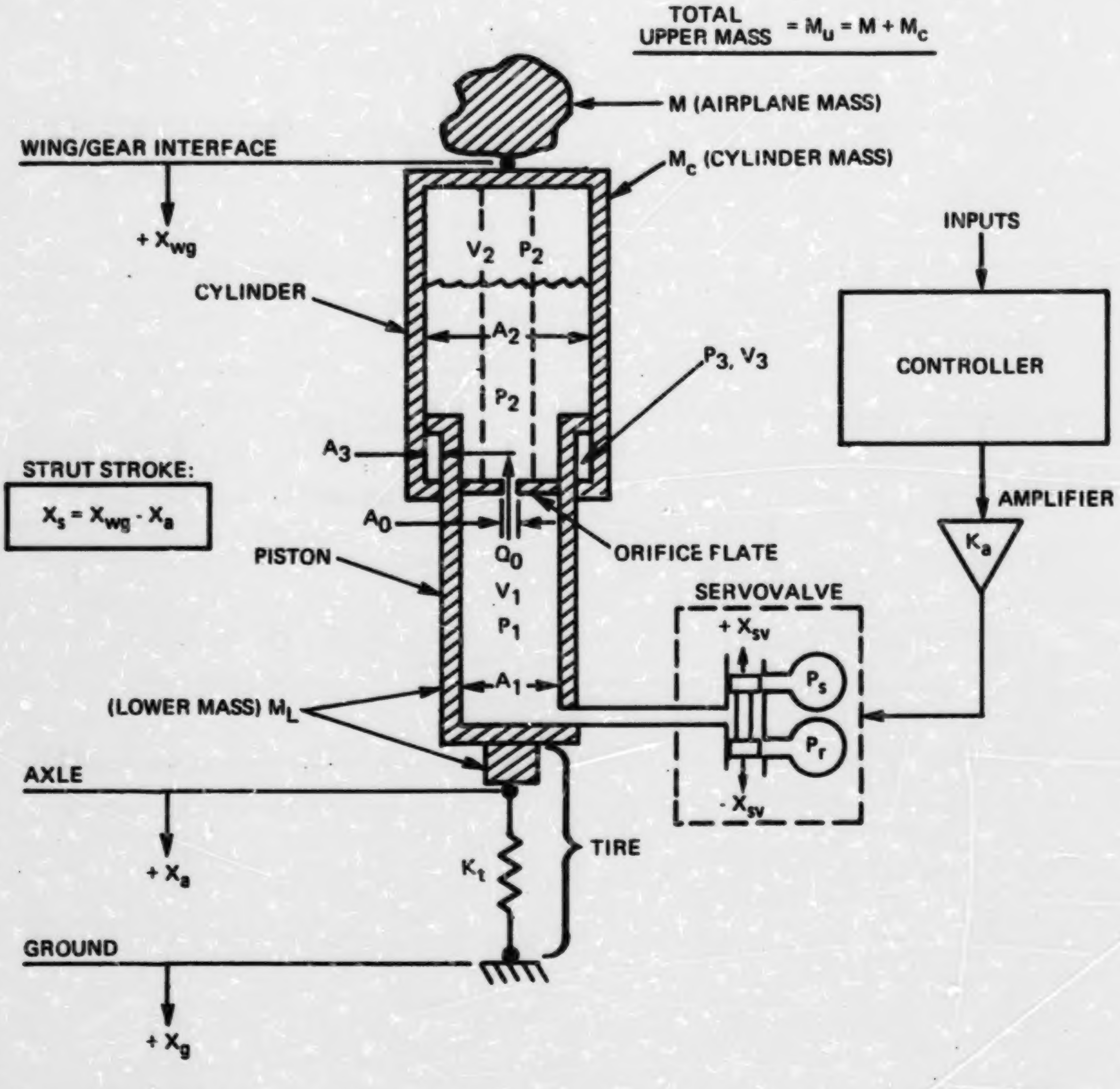
TOTAL UPPER MASS = $M_u = M + M_c$
M (AIRPLANE MASS)
WING/GEAR INTERFACE
M_c (CYLINDER MASS)
$+X_{wg}$
V_2
P_2
CYLINDER
A_2
P_3, V_3
P_2
INPUTS
CONTROLLER
A_3
STRUT STROKE:
$X_s = X_{wg} - X_a$
A_0
ORIFICE PLATE
AMPLIFIER
K_a
PISTON
Q_0
V_1
P_1
SERVOVALVE
$+X_{sv}$
P_s
A_1
P_r
(LOWER MASS) M_L
AXLE
$-X_{sv}$
$+X_a$
K_t
TIRE
GROUND
$+X_g$

Figure 1. - Illustration of variables used in nonlinear simulation of simplified vertical drop case.

spring K_t. The controller dynamics are presented later and will not be repeated here. Suffice it to say that at each instant in time the controller processes the input signals to provide a current to the servovalve.

Equations of Motion

The equations of motion of the landing gear in the vertical direction will now be derived, with down being defined as the positive direction. The two independent masses M_U and M_L give rise to two degrees of freedom, X_{wg} and X_a (See Figure 1). The final results, however, will be expressed in terms of the displacement variables X_{wg} and X_s, where X_s is the shock strut stroke, which ranges from zero for a fully extended strut to the maximum value for a fully contracted strut. The variable X_s is equal to $(X_{wg}-X_a)$.

Referring to Figure 2, a force balance on the airplane mass gives

$$M\ddot{X}_{wg} = Mg - L - F_s = -F_{wg} \qquad \ldots (1)$$

where F_s is the "shock strut force" and F_{wg} is the "wing gear interface force".

Referring to Figure 3, a force balance on the upper portion of the shock strut, which is assumed to be rigidly connected to the airplane mass, gives

$$M_c \ddot{X}_{wg} = M_c g + F_s - P_2A_2 + P_2(A_1-A_o) - P_1 (A_1-A_o) + P_3A_3 \mp f$$

or

$$F_s = M_c \ddot{X}_{wg} - M_c g + (P_1-P_2)(A_1-A_o) + P_2A_2 - P_3A_3 \pm f \qquad \ldots (2)$$

Referring to Figure 4, a force balance on the lower portion of the shock strut, which includes the wheel and tire mass, gives

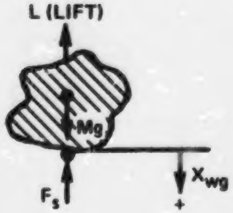
L (LIFT)
Mg
F_s
X_wg
+

Figure 2. - Free body diagram of airplane mass

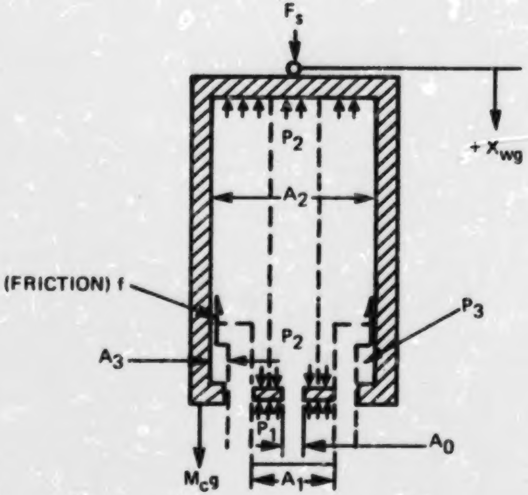
F_s
+ X_wg
P_2
A_2
(FRICTION) f
P_3
P_2
A_3
P_1
A_0
M_cg
A_1

Figure 3. - Free body diagram of upper shock strut

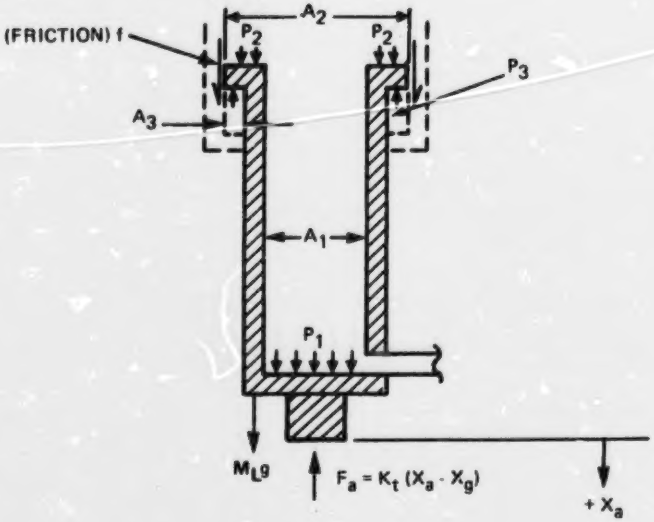
(FRICTION) f
P_2
A_2
P_2
P_3
A_3
A_1
P_1
M_Lg
F_a = K_t (X_a - X_g)
+ X_a

Figure 4. - Free body diagram of lower shock strut

$$M_L\ddot{X}_a = M_Lg + P_2(A_2-A_1) + P_1A_1 - P_3A_3 - F_a \pm f \qquad \ldots (3)$$

substituting $(X_{wg}-X_s)$ for X_a

$$\left.\begin{array}{l} M_L(\ddot{X}_{wg} - \ddot{X}_s) = M_Lg + (P_1-P_2)A_1 + P_2A_2 - P_3A_3 - F_a \pm f \\ \\ \text{where } F_a = \begin{cases} K_t(X_{wg} - X_s - X_g) & \text{for } X_{wg} - X_s > X_g \\ 0 & \text{for } X_{wg} - X_s \leq X_g \end{cases} \end{array}\right\} \qquad \ldots (4)$$

Note that the tire force F_a is zero when the tire is not in contact with the runway surface.

Equations were developed for: (1) the case where the piston is in motion relative to the cylinder, or $V_s \neq 0$; and (2) the case where the piston is not in motion relative to the cylinder due to Coulomb stiction between the two, or $V_s = 0$. For the first case, the Coulomb friction f is simply the value of running friction that exists. But for the second case, the Coulomb friction is actually a stiction force that can vary over a range of absolute values from zero up to the breakaway friction value. Transition from case 1 to case 2 will occur whenever the relative velocity is zero or passes through zero throughout the digital integration process. Transition from case 2 to case 1 will occur whenever the absolute value of the friction force f exceeds the known breakaway friction value. The following equations express these relationships.

First, for the case when $V_s \neq 0$, equations 1 and 2 are combined to eliminate F_s.

$$M_u\ddot{X}_{wg} = M_ug - L - (P_1-P_2)(A_1-A_o) - P_2A_2 + P_3A_3 \mp f \qquad \ldots (5)$$

Substituting equation 5 for $\ddot{X}_{wg}$ into equation 4

$$\frac{M_L}{M_u}[M_u g - L - (P_1 - P_2)(A_1 - A_o) - P_2A_2 + P_3A_3 \mp f] - M_L\ddot{X}_s$$

$$= M_L g + (P_1 - P_2)A_1 + P_2A_2 - P_3A_3 - F_a \pm f$$

Solving for $\ddot{X}_s$

$$M_L\ddot{X}_s = \frac{M_L}{M_u}[(M_u + M_L)g - L] + (1 + \frac{M_L}{M_u})[-M_L g - (P_1 - P_2)A_1 - P_2A_2 + P_3A_3]$$

$$+ \frac{M_L}{M_u}(P_1 - P_2)A_o + F_a \mp (1 + \frac{M_L}{M_u})f$$

or

$$M_L\ddot{X}_s = (1 + \frac{M_L}{M_u})[\text{FORCE} \mp f] \qquad \ldots(6)$$

$$\text{FORCE} = \frac{\frac{M_L}{M_u}[(M_u + M_L)g - L] + (1 + \frac{M_L}{M_u})[-M_L g - (P_1 - P_2)A_1 - P_2A_2 + P_3A_3] + \frac{M_L}{M_u}(P_1 - P_2)A_o + F_a}{1 + \frac{M_L}{M_u}}$$

Equations 5 and 6 constitute the two inertial equations of motion when $V_s \neq 0$.

Next, for the case when $V_s = 0$, equations 4 and 5 are totaled to get

$$(M_u + M_L)\ddot{X}_{wg} = (M_u + M_L)g - L + (P_1 - P_2)A_o - F_a \qquad \ldots(7)$$

$$\ddot{X}_s = 0 \qquad \ldots(8)$$

Equations 7 and 8 are the two inertial equations of motion when $V_s = 0$. However, an expression must be derived to tell when the two masses break away from one another; i.e., when the break away stiction will be overcome causing relative motion between them. This required solving for the variable friction force f. Substituting equation 5 for $\ddot{X}_{wg}$ into equation 4

$$\frac{M_L}{M_u}\left[M_u g - L - (P_1 - P_2)(A_1 - A_o) - P_2A_2 + P_3A_3 \mp f\right]$$

$$= M_L g + (P_1 - P_2)A_1 + P_2A_2 - P_3A_3 - F_a \pm f$$

Solving for f, gives

$$\pm f = \frac{\frac{M_L}{M_u}\left[(M_u + M_L)g - L\right] + \left(1 + \frac{M_L}{M_u}\right)\left[-M_L g - (P_1 - P_2)A_1 - P_2A_2 + P_3A_3\right] + \frac{M_L}{M_u}(P_1 - P_2)A_o + F_a}{1 + \frac{M_L}{M_u}} \qquad \ldots(9)$$

If the value of f as calculated by equation 9 exceeds the breakaway stiction, then relative motion will result.

Pressure, Flow, and Volume Relationship

Referring to Figure 1, conservation of mass applied to the hydraulic fluid in volume V_1 gives

$$\frac{V_1}{\beta}\dot{P}_1 = A_1\dot{X}_s - Q_o + Q_{sv1} - Q_{sv2} \qquad \ldots(10)$$

where

$$Q_o = \begin{cases} A_o C_{do} \sqrt{\dfrac{2 g_c}{\rho} (P_1 - P_2)} & \text{for } P_1 > P_2 \\ -A_o C_{do} \sqrt{\dfrac{2 g_c}{\rho} (P_2 - P_1)} & \text{for } P_2 > P_1 \end{cases}$$

$$V_1 = V_{1_i} - A_1 X_s$$

The parameters Q_{sv1} and Q_{sv2} are the servovalve flows from supply pressure to P_1 and from P_1 to return pressure, respectively, and are a function of the spool displacement and valve geometry. These flows are calculated in a subroutine titled FLOZE2 in the nonlinear simulations. Note also that equation 10 considers the effect of fluid compressibility, which gives rise to the first derivative of pressure term.

The pressure/volume relationship for the pneumatic volume V_2 is

$$P_2 = P_{2_i} \left(\frac{V_{2_i}}{V_2}\right)^{\gamma} \qquad \text{...(11)}$$

where

$$V_2 = V_{2_i} - (A_2 - A_1) X_s - V_{cum} + (V_3 - V_{3_i})$$

$V_{cum} = \Sigma (Q_o \Delta t) =$ the cumulative fluid flow through the orifice from V_1 to V_2

$$V_3 = V_{3_i} + A_3 X_s$$

The initial values of the pressure and volume variables referred to in the above equations are for the fully extended strut just prior to impact.

Servovalve Dynamics

The dynamic characteristics of the NASA-selected three-stage high response servovalve were supplied to HR by NASA. A mathematical representation of the servovalve dynamics was derived by the following procedure. The small signal frequency response characteristics obtained from NASA are shown reproduced in Figure 5 for reference. Amplitude and phase angle data at several discrete frequencies over the range of interest were taken from these curves and input to an HR-developed computer program that solves for an approximate linear transfer function by the method of least squares. The resultant transfer function is

$$\frac{X_{sv}}{i_2} = \frac{K_{sv}}{\left(\frac{s^2}{\omega^2_{sv}} + \frac{2\zeta_{sv}}{\omega_{sv}} s + 1\right)\left(\frac{s}{\omega_c} + 1\right)} \qquad \ldots(12)$$

where the values of the constants K_{sv}, ω_{sv}, ω_c, and ζ_{sv} are given in the SYMBOLS section and i_2 is input current and X_{sv} is output displacement of the third stage spool. For the nonlinear simulation this transfer function is represented in differential equation form as follows:

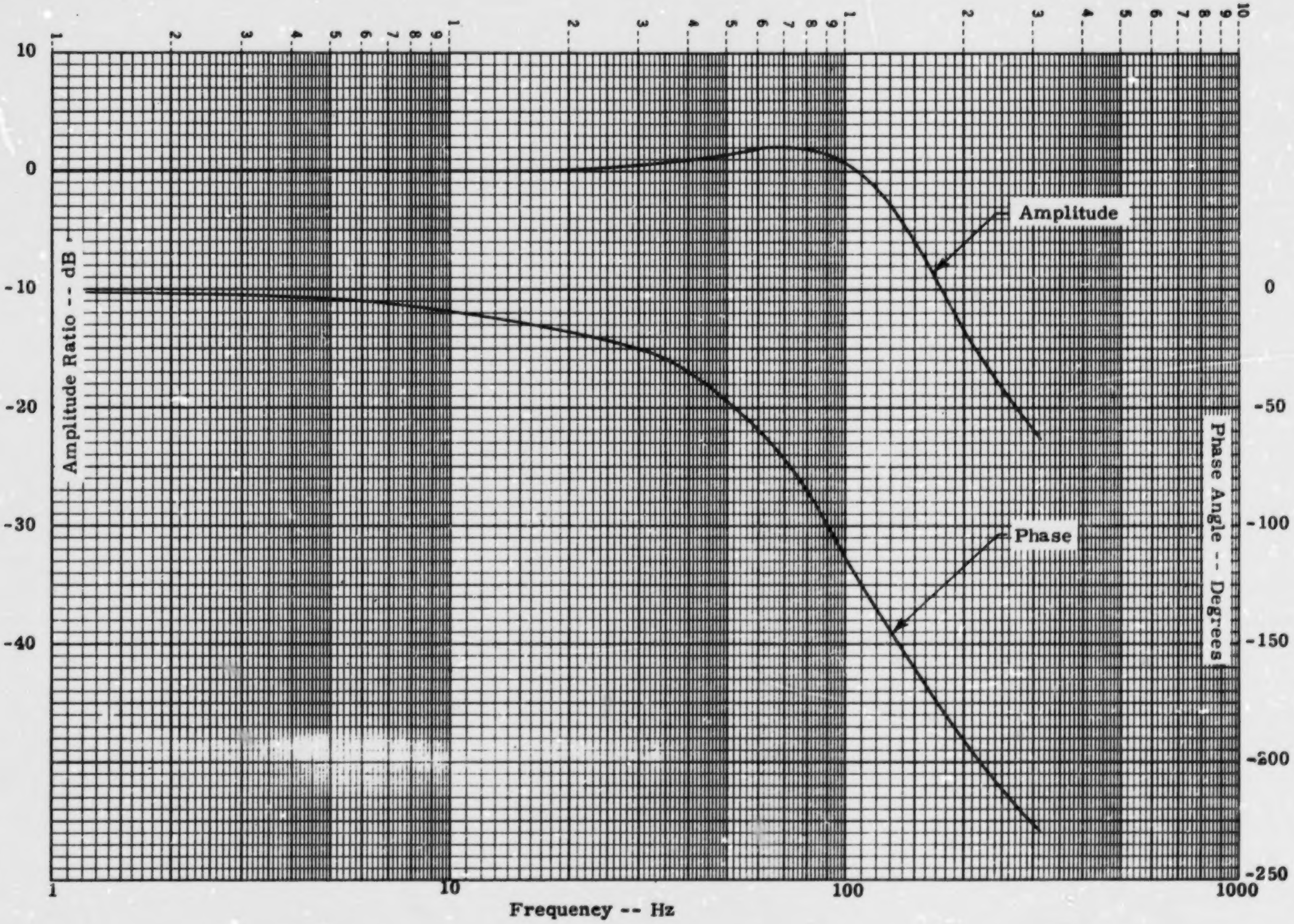

Figure 5. - Dynamic response of servovalve, ±10% input signal.

17

$$\left(\frac{1}{\omega_{sv}^2 \, \omega_c}\right)\dddot{X}_{sv} + \left(\frac{1}{\omega_{sv}^2} + \frac{2\zeta_{sv}}{\omega_{sv}\,\omega_c}\right)\ddot{X}_{sv} + \left(\frac{2\zeta_{sv}}{\omega_{sv}} + \frac{1}{\omega_c}\right)\dot{X}_{sv} + X_{sv} = K_{sv}\, i_2 \qquad \ldots(13)$$

Saturations in the various stages are treated as follows. Third stage spool saturation obviously places a limit on X_{sv} equal to $\pm X_{sv}$ max. Second stage saturation is assumed to place a limit on $d(X_{sv})/dt$ equal to $\pm$ (QSV2/ASV3), where QSV2 is the second stage saturation flow and ASV3 is the effective cross sectional area of the third stage spool connected to the lines from the second stage. First stage flapper saturation is assumed to place a limit on $d^2(X_{sv})/dt^2$ equal to $\pm$ $(QSV1 \cdot CQ_2)/(ASV2 \cdot ASV3)$, where QSV1 is the first stage saturation flow, CQ_2 is the linearized flow gain of the second stage spool (flow rate per unit displacement of spool), ASV2 is the effective cross sectional area of the second stage spool connected to the flow lines from the first stage, and ASV3 is as already described.

Linear Math Model for Vertical Drops

This section describes the development of an approximate linear model of an active control landing gear for vertical drops, exclusive of aerodynamics and airplane dynamics. The linear model is a valuable tool since the effect of system modifications can be ascertained very rapidly. The study of system stability and the development of the electronic compensation networks, discussed in the following section, relied very heavily on the linear model. The results were then supported by analysis using the complete nonlinear model.

The equations for the actual landing gear and controller are inherently nonlinear, so some assumptions and simplifications must be made. The following list summarizes the assumptions that were made in the linearization process.

(1) The coulomb friction f between the piston and the cylinder is neglected.

(2) The pneumatic pressure P_2 is assumed constant.

(3) The pressure P_3 is identical to the pressure P_2.

(4) The lift and gravitational forces are constant.

(5) The cross sectional area of the piston wall is negligible with respect to the overall piston area.

(6) The area of the fixed orifice is negligible with respect to the overall piston area.

(7) The inertia of the upper part of the shock strut mass is negligible with respect to the airplane mass.

(8) Servovalve nonlinearities are neglected (i.e., constant flow gain and pressure gain partial derivative values are assumed).

The equations given in the previous section for the nonlinear math model can now be simplified as follows. Equations 5 and 6 become

$$M_u \ddot{X}_{wg} \approx M_u g - L - P_1 A_1$$

$$M_L \ddot{X}_s \approx \frac{M_L}{M_u} \left[(M_u + M_L) g - L \right] + \left(1 + \frac{M_L}{M_u}\right) \left[- M_L g - P_1 A_1 \right] + K_t \left(X_{wg} - X_s\right)$$

If we let the variables X'_{wg}, X'_a, X'_s, and P'_1 represent the perturbation variables of X_{wg}, X_a, X_s, and P_1, (that is, they represent changes in those variables about some mean condition), then these two equations can be written

$$M_u \ddot{X}'_{wg} = -P'_1 A_1$$

$$M_L \ddot{X}'_s = \left(1 + \frac{M_L}{M_u}\right)(-P'_1 A_1) + K_t (X'_{wg} - X'_s)$$

where the lift and gravitational terms have dropped out because they are assumed constant. Making use of the identity $X_s = X_{wg} - X_a$, these two equations can be solved for X_{wg} and X_a. Dropping the primes for simplicity, the results in LaPlace transform notation are

$$X_{wg} = -\frac{A_1 P_1}{M_u s^2} \qquad \ldots(14)$$

$$X_a = \frac{A_1 P_1}{M_L s^2 + K_t} \qquad \ldots(15)$$

Also, note from equations 1 and 2 that

$$F_{wg} = F_s \approx P_1 A_1 \qquad \ldots(16)$$

It is instructive to note that equations 14 and 15 are the linearized equations of motion that would result from a mass and piston driving into a sleeve connected to ground by a spring, with an orifice in the piston connecting the internal pressure P_1 with a constant pressure P_2 on the other side. This is illustrated schematically in Figure 6, along with a servovalve for active control. A force balance on the masses M_U and M_L will result exactly in equations 14 and 15.

A linearized expression for the pressure P_1 will now be derived. Referring to Figure 6, conservation of mass applied to the hydraulic fluid in volume V_1 gives

$$dQ_{sv} - dQ_o + A_1 \dot{X}_s = \frac{V_1}{\beta} \dot{P}_1 \qquad \text{...(17)}$$

The flow from the servovalve is

$$Q_{sv} = \begin{cases} C_{sv} X_{sv} \sqrt{P_S - P_1} & \text{for } X_{sv} \geq 0 \\ C_{sv} X_{sv} \sqrt{P_1 - P_R} & \text{for } X_{sv} < 0 \end{cases}$$

Differentiating this, gives

$$dQ_{sv} = \begin{cases} C_{sv} \sqrt{P_S - P_1}\, dX_{sv} - \left(\dfrac{C_{sv} X_{sv}}{2 \sqrt{P_S - P_1}} \right) dP_1 & \text{for } X_{sv} \geq 0 \\ \\ C_{sv} \sqrt{P_1 - P_R}\, dX_{sv} + \left(\dfrac{C_{sv} X_{sv}}{2 \sqrt{P_1 - P_R}} \right) dP_1 & \text{for } X_{sv} < 0 \end{cases}$$

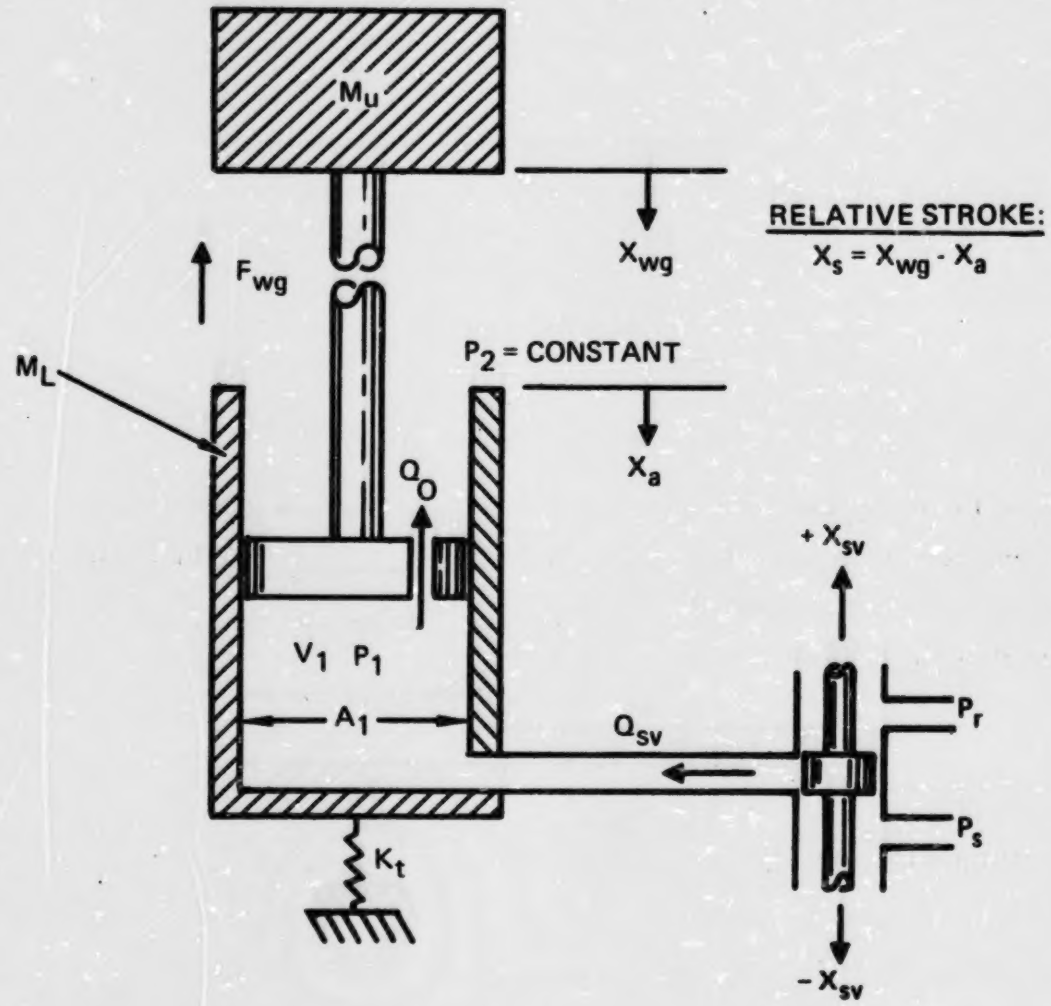
M_u
F_{wg}
X_{wg}
RELATIVE STROKE:
$X_s = X_{wg} - X_a$
M_L
P_2 = CONSTANT
X_a
Q_O
$+X_{sv}$
V_1 P_1
A_1
Q_{sv}
P_r
P_s
K_t
$-X_{sv}$

Figure 6. - Illustration of "equivalent" system for the linear math model.

Letting the mean value of the pressure P_1 equal $(P_S + P_R)/2$, and assuming small perturbations about this mean condition, the above relationships can be expressed as

$$dQ_{sv} = CQ \cdot dX_{sv} - CP \cdot dP_1 \qquad \ldots(18)$$

where

$$CQ = \frac{\partial Q_{sv}}{\partial X_{sv}} = C_{sv} \sqrt{(P_S + P_R)/2}$$

$$CP = -\frac{\partial Q_{sv}}{\partial P_1} = -CQ/PG$$

and where PG is the pressure gain of the spool in terms of pressure per spool displacement, at constant flow. In the linearized model the values of CQ and CP are assume constant.

The flow through the fixed orifice is

$$Q_o = K_o \sqrt{P_1 - P_2}$$

Differentiating this gives

$$dQ_o = \left(\frac{K_o}{2 \sqrt{P_1 - P_2}} \right) dP_1 = CP_o \, dP_1 \qquad \ldots(19)$$

However, note that at the mean condition P_1 equals P_2, so the coefficient CP_o is undefined. In actuality, CP_o is a function of excitation amplitude and frequency. It is important to keep this fact in mind when applying the linearized model. The approach taken in this study was to vary CP_o over a reasonable range to determine its influence on the dynamic response of the system, and to proceed accordingly.

Substituting equations 18 and 19 into equation 17, solving for P_1, and expressing it in LaPlace transform notation gives

$$P_1 = \frac{CQ \cdot X_{sv} + A_1 s\, X_s}{\frac{V_1}{\beta} s + (CP_o + CP)} \qquad \text{...(20)}$$

The transfer function of the servovalve dynamics in terms of output displacement of the third stage spool for input current was derived in the preceding section (equation 12) and is

$$\frac{X_{sv}}{i_2} = \frac{K_{sv}}{\left(\frac{s^2}{\omega^2_{sv}} + \frac{2\zeta_{sv}}{\omega_{sv}} s + 1\right)\left(\frac{s}{\omega_c} + 1\right)}$$

The transfer function for the electronic compensation network, which is derived in the next section, is

$$\frac{i_2}{i_1} = \left(\frac{s^2 + 2\zeta_2\, \omega_1 s + \omega_1{}^2}{s^2 + 2\zeta_1\, \omega_1 s + \omega_1{}^2}\right)\left(\frac{\tau_1 s + 1}{\tau_2 s + 1}\right)\left(\frac{\tau_3 s + 1}{\tau_4 s + 1}\right) \qquad \text{...(21)}$$

The relationship describing the force feedback and the position loop feedback is

$$i_1 = K_a (F_{lim} - F_{wg}) - K_a \left(\frac{K_f}{\tau_f s + 1}\right) (X_c - K_x X_s) \qquad \ldots (22)$$

Equations 14, 15, 16, 20, 12, 21 and 22 make up the complete linarized model, and Figure 7 is a block diagram arrangement of these equations. The algebraic solution of transfer functions from this set of equations would be very tedious, so this practice was avoided. The following approach was taken. First, working from the block diagram, the system of equations is expressed in matrix form, where each element of the matrix is in general a polynomial in "s". A computer program is then used to solve for the coefficients of the numerator and denominator of the desired transfer function using Cramer's Rule. Frequency response characteristics are then calculated from the transfer function. Also, the roots of the numerator and denominator polynominals are easily determined using standard computer techniques. The linear model gives very rapid results, and thus is ideal for evaluating the effect of varying different parameters and for developing electronic compensation networks for stability.

The validity of the linear model was evaluated by comparing the open loop frequency response with results obtained from the nonlinear vertical drop model described in the preceding section. The loop was opened at the point of wing gear force (F_{wg}) feedback, and position feedback was not included. The conditions were for zero lift with the shock strut at a mean stroke equal to that required to balance the weight of the airplane, which was 67 percent of maximum stroke for this case. Also, no electronic compensation was used.

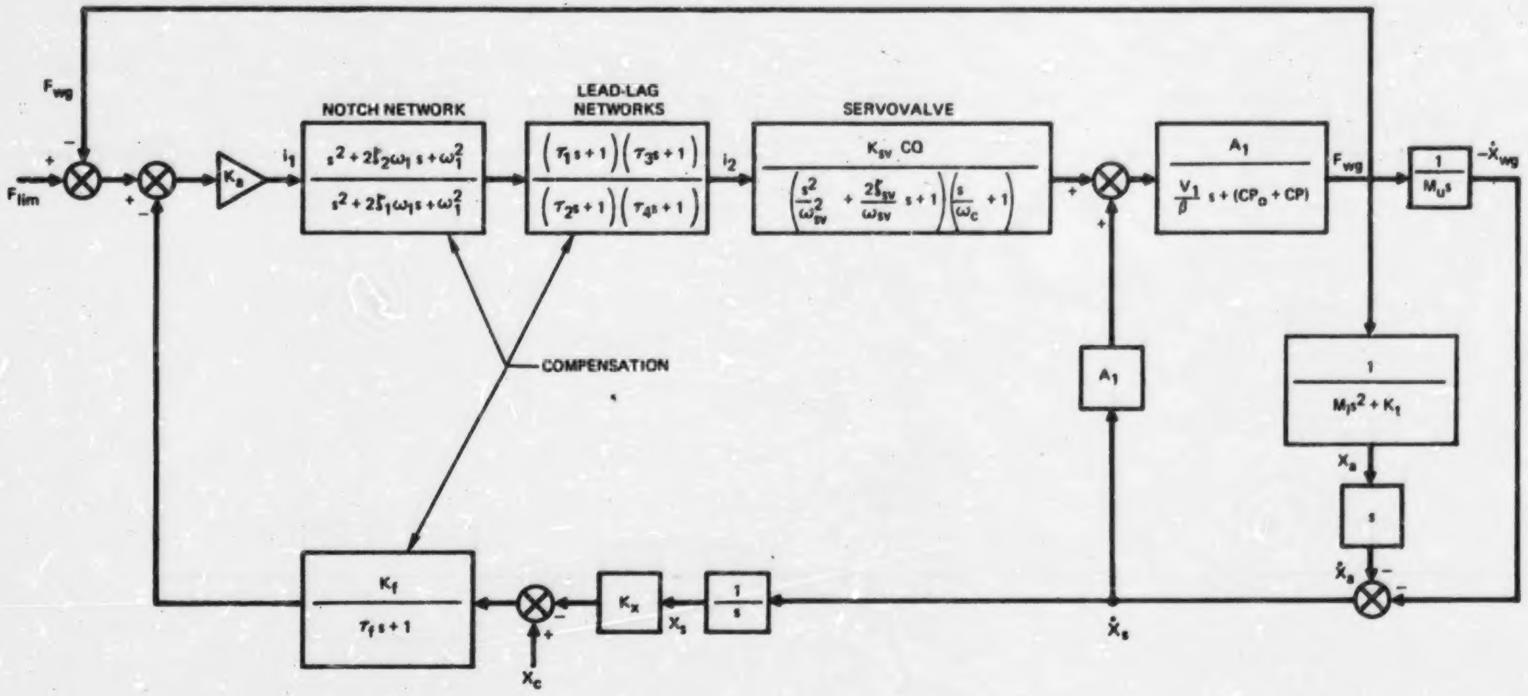
F_{wg}
F_{lim}
K_a
i_1
NOTCH NETWORK
$\frac{s^2 + 2\zeta_2\omega_1 s + \omega_1^2}{s^2 + 2\zeta_1\omega_1 s + \omega_1^2}$
LEAD-LAG NETWORKS
$\frac{(\tau_1 s + 1)(\tau_3 s + 1)}{(\tau_2 s + 1)(\tau_4 s + 1)}$
i_2
SERVOVALVE
$\frac{K_{sv}\ CO}{\left(\frac{s^2}{\omega_{sv}^2} + \frac{2\zeta_{sv}}{\omega_{sv}} s + 1\right)\left(\frac{s}{\omega_c} + 1\right)}$
$\frac{A_1}{\frac{V_1}{\beta} s + (CP_O + CP)}$
F_{wg}
$\frac{1}{M_u s}$
$-\dot{X}_{wg}$
COMPENSATION
A_1
$\frac{1}{M_i s^2 + K_t}$
X_a
s
$\dot{X}_a$
$\dot{X}_s$
$\frac{1}{s}$
X_s
K_x
X_c
$\frac{K_f}{\tau_f s + 1}$

Figure 7. - Block diagram of linear math model

The comparison of results is shown in Figure 8. Input is commanded limit force and output is wing gear force. Linear model results are shown for both a low and a high value of the fixed orifice parameter CP_o. The results for the low value of CP_o match the nonlinear results closest at low frequencies while the results for the high value of CP_o match closest at high frequencies. The basic trends are predicted reasonably well and it is concluded that the linear model is a valid tool for performing initial design and stability studies.

Energy Considerations

The primary function of the landing gear control system is to control the wing gear force at some commanded level. A secondary but necessary function of the controller is to set this commanded level such that the strut will not fully collapse, precluding structural damage. In order to do this, the controller must be able to monitor the energies present in the system during impact, and then set the limit force accordingly so that the work potential of the shock strut will be sufficient to absorb these energies. In order to study the feasibility of the controller performing this function, it is worthwhile to undergo an analytical development of the various energies present in the system and relate them to the work performed by the shock strut — the subject of this section. The equations will be developed from the equations of motion of the simplified vertical drop case, presented earlier; however, the results are almost directly applicable to the more general cases.

Equations 3 and 5 are the inertial equations of motion corresponding to the two independent masses M_U and M_L. These equations are rewritten in a form where each term represents the differential of an energy or work. This is done by multiplying equation 5 by dX_{wg} and equation 3 by dX_a, resulting in

$$M_u V_{wg} dV_{wg} = [M_u g - L - (P_1 - P_2)(A_1 - A_o) - P_2 A_2 + P_3 A_3 \mp f]\, dX_{wg} \qquad \ldots (23)$$

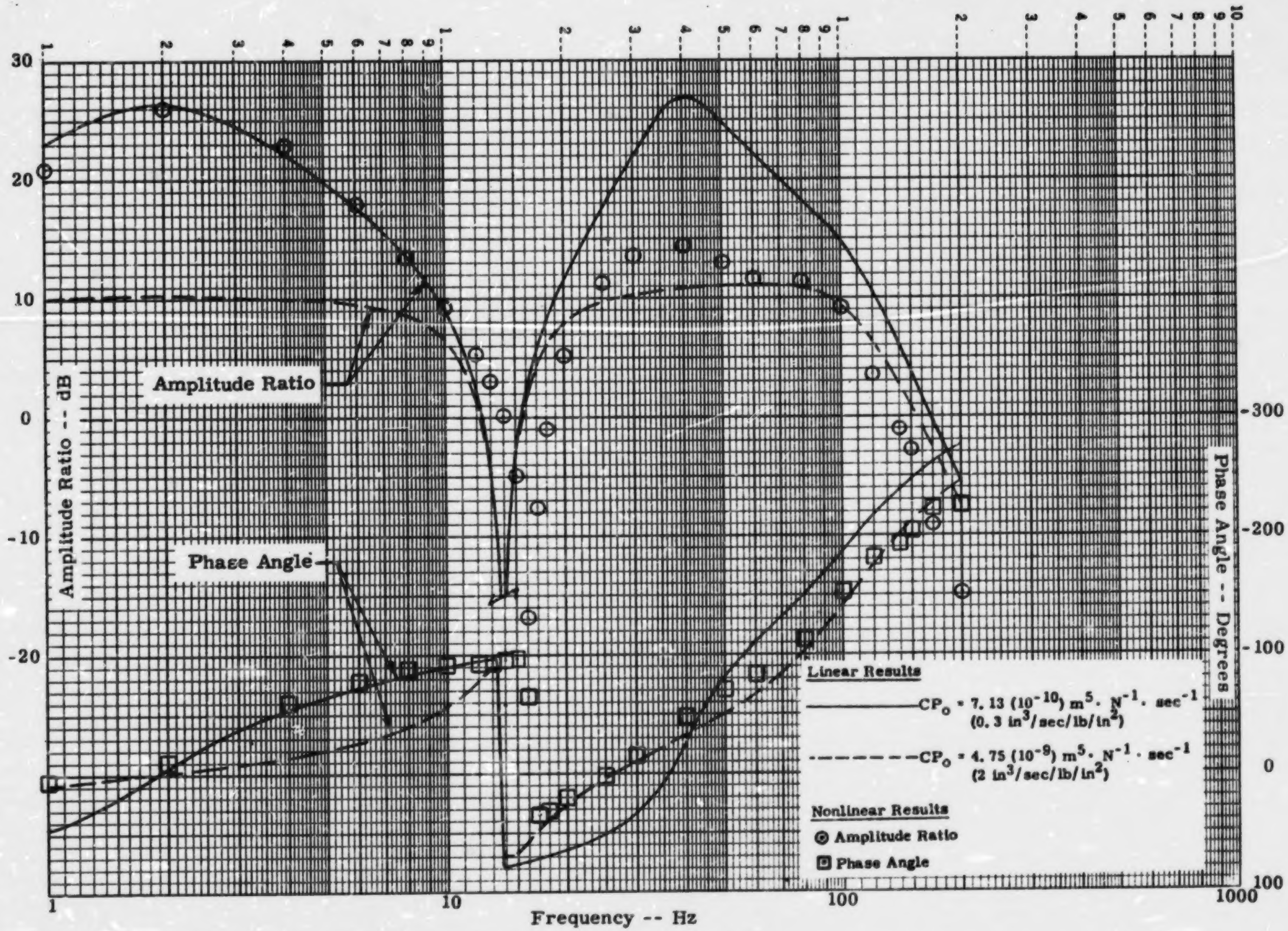

Figure 8. - Comparison of linear model and nonlinear model results, open loop, no compensation, no position feedback.

$$M_L V_a \, dV_a = [M_L g + P_2 (A_2 - A_1) + P_1 A_1 - P_3 A_3 - F_a \pm f] \, dX_a \quad \ldots(24)$$

Note that if these equations are integrated from some initial condition to a final condition they express changes in energy that occur over that time interval. For example, the integral of the terms on the left side of the equations express the total change in kinetic energy of each mass. It is desired now to write an equation expressing the total change in kinetic energy of the system, which is assumed to consist entirely of the two masses M_U and M_L, as a function of the various other energy and work terms. This is done by adding equations 23 and 24, resulting in

$$\overbrace{M_u V_{wg} \, dV_{wg}}^{1} + \overbrace{M_L V_a \, dV_a}^{2} + \overbrace{[-M_u g}^{3} + \overbrace{L}^{4} \overbrace{-(P_1 - P_2) A_o}^{5} \,] \, dX_{wg}$$

$$+ \overbrace{[-M_L g}^{6} + \overbrace{F_a}^{7}] \, dX_a + \overbrace{[(P_1 - P_2) A_1}^{8} + \overbrace{P_2 A_2 - P_3 A_3}^{9} \overbrace{\pm f}^{10}] \, dX_s = 0 \quad \ldots(25)$$

Equation 25 can be thought of as a statement of conservation of energy, since it essentially says that the sums of all changes in energy and work done in the system equals zero. Some of the terms in equation 25 are easily recognizable as to the type of energy they represent. For example, terms 1 and 2 represent changes in kinetic energy. Terms 3 and 6 represent changes in potential energy of the upper and lower masses due to height changes. Term 7 represents changes in potential energy stored in the tire spring. Term 10 represents energy dissipation due to Coulomb friction. Energy dissipation due to flow across the shock strut orifice also occurs, although this is not directly identifiable in equation 25 because of the complicating effects of fluid compressibility and flow to and from the active-control servovalve.

Equation 25 must be simplified to the point where it becomes a useful tool to the controller for monitoring the energies present in the system in terms of the available input signals; e.g., accelerometers, transducers, etc. First, term 5 was found to be negligible and can be immediately eliminated. Next, the combination of terms in the third bracket (terms 8, 9 and 10) are approximately equivalent to the shock strut force F_s. This can be seen by referring back to equation 2, neglecting the inertia and gravity forces on the shock strut portion of the upper mass, and neglecting the orifice area with respect to the piston area. With these simplifications, equation 25 is rewritten as

$$M_U V_{wg} dV_{wg} + M_L V_a dV_a + (-M_U g + L)\, dX_{wg} + (-M_L g + F_a)\, dX_a + F_s dX_s = 0 \qquad \ldots(26)$$

Note that the quantity $F_s dX_s$ represents the differential of the work performed by the shock strut. Integration of this equation over a given interval will thus yield an expression showing the net work performed by the shock strut as a function of the various other energy changes. The task of the controller is to monitor these energies and make sure that the remaining work potential of the shock strut is sufficient to dissipate them.

At this point, it is worthwhile summarizing the instrumentation that is available to the controller as originally proposed.

(1) Wing/gear acceleromters - measures $\ddot{X}_{wg}$

(2) Hub accelerometer - measures $\ddot{X}_a$

(3) LVDT on shock struct - measures X_s

(4) Upper cylinder pressure transducer - measures P_2 (pneumatic)

(5) Lower piston pressure transducer - measures P_1 (hydraulic).

With this instrumentation, it is not possible to apply equation 26 to the task at hand, because there is no way to monitor the lift L or the shock strut force F_s (note that by knowing one of these, the other may be obtained equation 1). It is therefore necessary to make further simplifications. Assuming that the total airplane weight equals the lift throughout impact, and neglecting the $M_L g$ term, then equation 26 becomes

$$M_U V_{wg} dV_{wg} + M_L V_a dV_a + F_a dX_a + F_s dX_s = 0 \qquad \text{...(27)}$$

With the weight-equals-lift assumption, all of the parameters in equation 27 may be obtained. From equation 1,

$$F_s = -M_U \ddot{X}_{wg} \qquad \text{...(28)}$$

It is possible to solve for F_a by first noting that equation 3 may be expressed as

$$M_L \ddot{X}_a \approx -F_a + F_s \qquad \text{...(29)}$$

Substituting equation 28 for F_s into equation 29,

$$F_a \approx - M_U \ddot{X}_{wg} - M_L \ddot{X}_a \qquad \text{...(30)}$$

The individual terms in equation 27 were integrated with respect to time throughout a typical vertical drop simulation using the simplified nonlinear vertical drop model described in a previous section to determine if the equation is indeed a valid representation of all the major energy changes that take place. The lift was set equal to the weight throughout the simulation, so this test case will say nothing regarding the validity of the "weight-equals-lift" simplification. The validity of that will be demonstrated later using actual land and roll simulations. The integrated variables are shown plotted in Figure 9. The sum of all the integrated variables is also shown, representing the total energy plus work done by the system. This should remain constant from the conservation of energy principle. It is indeed relatively constant, thus supporting the validity of equation 27, at least for vertical drop cases where weight equals lift. Note that the kinetic energy of the lower mass is negligible. Also, the potential energy stored in the tire, although not completely negligible, is a minor part of the total energy of the system. This raises the question whether it is worth the added complexity of including this term in the energy computations of the controller. The approach taken here is to neglect it and incorporate any errors into an empirical correction factor, if necessary. As a result, the only terms considered in the energy computations of the controller are the kinetic energy of the upper mass and the work of the shock strut.

The next step is to derive relationships that the controller can apply in setting the commanded limit force to a level such that bottoming of the strut will be prevented. There are various approximations or simplifications that can be made, some of which have already been mentioned in the preceding paragraph, which will introduce errors in the final result. In the interest of completeness and for reference, the more general derivation will be presented first, followed by the simplifications. The procedure is to integrate equation 27 from a time t_1 (controller initiation) to the end of transition; i.e., the start of rollout. The following assumptions are made.

(1) The actual wing/gear force is identical to the commanded limit force throughout the impact and transition phases.

(2) The velocity of the masses is zero at the end of transition (this also is the criterion used in calculating the wing/gear velocity at which transition begins).

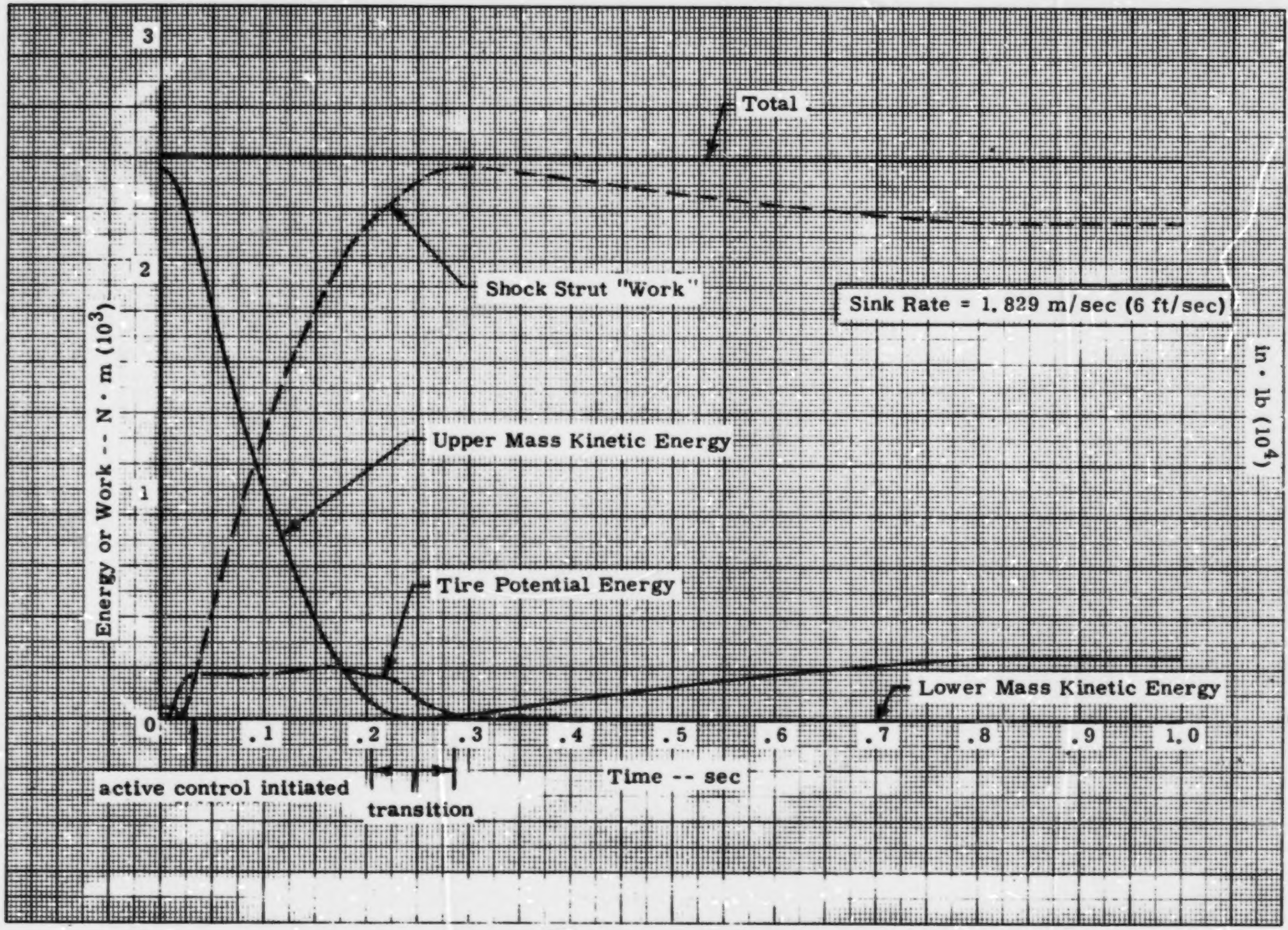

Figure 9. - Various energy terms versus time, from the simplified nonlinear vertical drop simulation.

(3) The commanded limit force is constant throughout the impact phase and linearly decreases during transition to zero limit force at the beginning of rollout. The slope in the transition phase is a known quantity.

A sketch of the variation of wing/gear force versus time for the above conditions is shown in Figure 10. Integration of equation 27 from t_1 to the start of transition t_{tr} gives

$$1/2\ M_u\,(V^2_{u_{tr}} - V^2_u) + 1/2\ M_L\,(V^2_{L_{tr}} - V^2_L) + \int_{t_1}^{t_{tr}} F_a\,dX_a + F_{li}\,\Delta X_{s_{im}} = 0$$

Integration from the start of transition t_{tr} to the end of transition t_r gives

$$1/2\ M_u\,(\cancelto{0}{V^2_{u_r}} - V^2_{u_{tr}}) + 1/2\ M_L\,(\cancelto{0}{V^2_{L_r}} - V^2_{L_{tr}}) + \int_{t_{tr}}^{t_r} F_a\,dX_a + \frac{F_{li}}{2}\,\Delta X_{s_{tr}} = 0$$

The quantities $\Delta X_{s_{im}}$ and $\Delta X_{s_{tr}}$ represent the shock strut stroke used in the impact and transition phases, respectively. The sum of these should be equal to or less than the total remaining available stroke, to prevent bottoming. Solving for ΔX_{s_i} and $\Delta X_{s_{tr}}$ in these equations and adding them together gives

$$\Delta X_s = \frac{1/2\ M_u(V^2_u - V^2_{u_{tr}}) + 1/2\ M_L\,V^2_{L_{tr}} - \int_{t_1}^{t_{tr}} F_a\,dX_a}{F_{li}} + \frac{1/2\ M_u\,V^2_{u_{tr}} + 1/2\ M_L\,V^2_{L_{tr}} - \int_{t_{tr}}^{t_r} F_a\,dX_a}{F_{li}/2} \quad \ldots(31)$$

Referring back to Figure 9, it is shown that any potential energy changes in the tire during the impact phase may be neglected. This is true because F_a and X_a remain relatively constant throughout this phase. Also, since the final

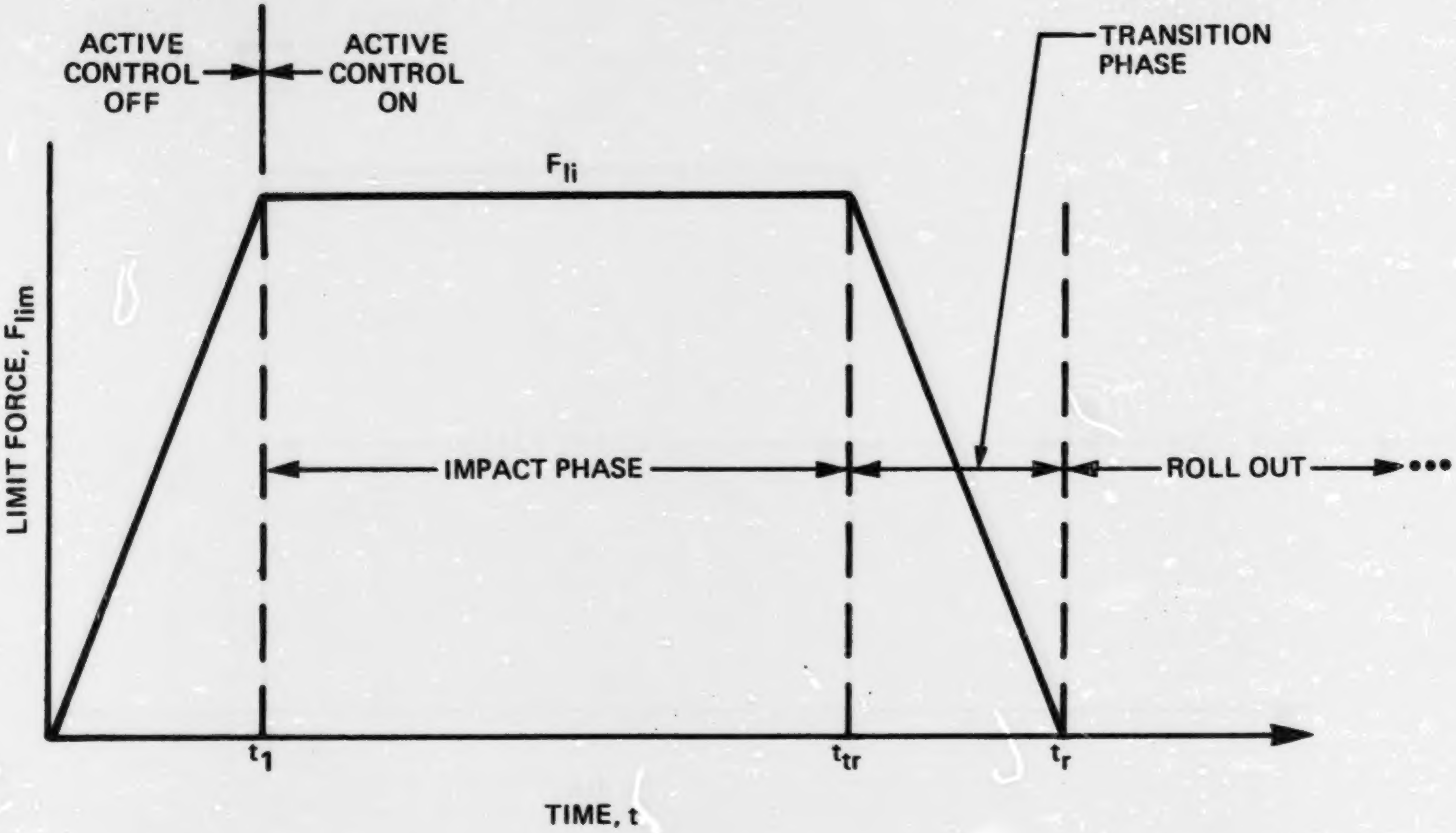

Figure 10. - Illustration of the variation of limit force versus time and the various phases of operation following impact.

rollout limit force is zero, F_a at that point will be approximately zero; and hence, roughly stated, that during transition the potential energy of the tire will go from its initial impact phase state to a zero energy state. This fact can be seen in Figure 9. Thus, in equation 31, the integral of $F_a dX_a$ over the interval t_1 to t_{tr} is approximately zero and the integral of $F_a dX_a$ over the interval t_{tr} to t_r is approximately equal to the negative of the potential energy stored in the tire at time t_1, the start of the integration interval. Signifying this energy level by the symbol PE_t, and neglecting the kinetic energy of the lower mass, equation 31 reduces to

$$F_{li}\,\Delta X_s = 1/2\, M_u V_u^2 + 1/2\, M_u\, (V_{u_{tr}})^2 + 2 \cdot PE_t \qquad \ldots(32)$$

The upper mass velocity at the start of transition can be determined by equating the impulse to the change in momentum for the transition phase, resulting in

$$V_{u_{tr}} = \frac{F_{li}^2}{2 \cdot M_u \cdot R_s} \qquad \ldots(33)$$

where R_s is the slope of the limit force with respect to time during transition.

The application of equation 32 to the controller could be as follows: when the gear first impacts the runway surface the controller is in a passive mode; that is, no command is being initiated to the servovalve. Immediately after impact, at discrete intervals, the controller will compute the strut work ($F_{li}\Delta X_s$) required to absorb the energy using equations 32 and 33. In equation 33, the transition velocity is calculated using the current value of wing/gear interface force as the impact limit force (i.e., F_{li} is set equal to F_{wg}).

This calculated value of required strut work is continually compared to a signal representing the actual strut work currently available if the controller were to go into active control at that instant. This actual strut work is simply the current value of the wing gear force times the remaining shock strut stroke. When comparison of these signals indicates that the available shock strut work exceeds the value calculated by equation 32, then active control to the servovalve is initiated and the commanded impact phase limit force is set equal to that current value of wing gear force. The velocity of transition is also then set to the value computed from equation 33.

It may be desirable to further monitor the energy situation through the remainder of the impact phase to ensure that the strut will not bottom due to additional energy inputs. If so, equations 32 and 33 could be used to compute F_{li} from the known remaining strut stroke (ΔX_s), and if the computed F_{li} ever exceeded the original F_{li} value, the controller would update F_{li} to the newly-computed value; however, this would require the solution of a quartic equation.

A simplification in equation 32 can be made by neglecting the transition region. In other words, assume that in Figure 10 the constant impact limit force is continued throughout the transition region, and at the end of transition it drops abruptly to the rollout limit force of zero. It should also be stressed that it is not being proposed that the actual limit force commanded by the controller follow this pattern; this is only for the purpose of simplifying the energy relationships. Integration of equation 27 will then result in

$$1/2\ M_u\,(V^2_{u_r} - V^2_u) + 1/2\ M_L\,(V^2_{L_r} - V^2_L) + \int_{t_1}^{t_r} F_a\,dX_a + F_{li}\,\Delta X_s = 0 \qquad \ldots(34)$$

Again, the integral of $F_a dX_a$ from t_1 to t_r is approximately equal to the negative of the potential energy stored in the tire at time t_1. Neglecting the kinetic energy of the lower mass, equation 34 becomes

$$F_{li} \Delta X_s = 1/2\, M_u V_u^2 + PE_t \qquad \ldots(35)$$

with equation 33 still applying for the velocity of transition. The use of equations 35 and 33 in the controller would be similar to that already described for equations 32 and 33.

A still further simplification, in addition to those already made, is to neglect the potential energy in the tire. Equation 35 then reduces to

$$F_{li} \Delta X_s = 1/2\, M_u V_u^2 \qquad \ldots(36)$$

with equation 33 still applying for the velocity of transition. This last approach is the one taken in the current design, and is the one programmed into the computer simulations.

To extend the use of equation 36 to actual land and roll cases, $\Delta X_s \cos \theta$ is substituted in place of ΔX_s, where θ is the angle the shock strut axis makes with the vertical (gravitational) direction. The angle θ is equal to the pitch angle of the airplane fuselage plus the angle of the wing with respect to the airplane fuselage. Also, the velocity and force in equation 36 are now the components in the vertical, or gravitational direction. The energy relationship used for land and roll cases is then

$$F_{li} \Delta X_s \cos \theta = 1/2\, M_u V^2{}_u \qquad \ldots(37)$$

For land and roll cases, the question of the validity of the "weight-equals-lift" simplication is raised. Whether or not this is valid is demonstrated by computer simulation of the actual landing roll cases provided by NASA. The simulation results are presented in the ANALYTICAL RESULTS section. Of interest to the present discussion, however, is the maximum resultant stroke that occurs in each case when the limit force is set according to equation 37 and the aforementioned procedure. Table I, presented in a later section, summarizes this information. As can be seen, the method is reasonably successful in setting the limit force so that a maximum amount of strut stroke is used in absorbing the impact energy.

Stability Analysis

The linear model discussed earlier was used to evaluate the frequency response and stability of the system. System parameters used were basically those given under SYMBOLS. The linearized orifice coefficient CP_o was given a value of 7.13 (10^{-7}) $m^3/sec/kPa$ (0.3 $in^3/sec/lb/in^2$) for frequencies less than 14 Hz and a value of 4.75 (10^{-6}) $m^3/sec/kPa$ (2.0 $in^3/sec/lb/in^2$) for frequencies greater than 14 Hz, providing a reasonable match with frequency responses generated with the nonlinear model.

Based on results from the nonlinear vertical drop model, it was determined that a force loop bandwidth of 10 Hz would be adequate to achieve desired performance. Using the uncompensated linear model shown in Figure 11, the Nyquist plot of Figure 12 was generated. The uncompensated system was unstable at a frequency (140 Hz) related to the servovalve dynamics and could not be stabilized by simply lowering loop gain without violating the 10-Hz bandwidth goal. It was evident that signal shaping was required.

Analysis of various forms of forward path electronic compensation ultimately yielded the filter configuration shown in Figure 13. It consists of a second-order notch and two lead lags. The resulting Nyquist plot is shown in Figure 14; and, it can be seen that stability margins are adequate.

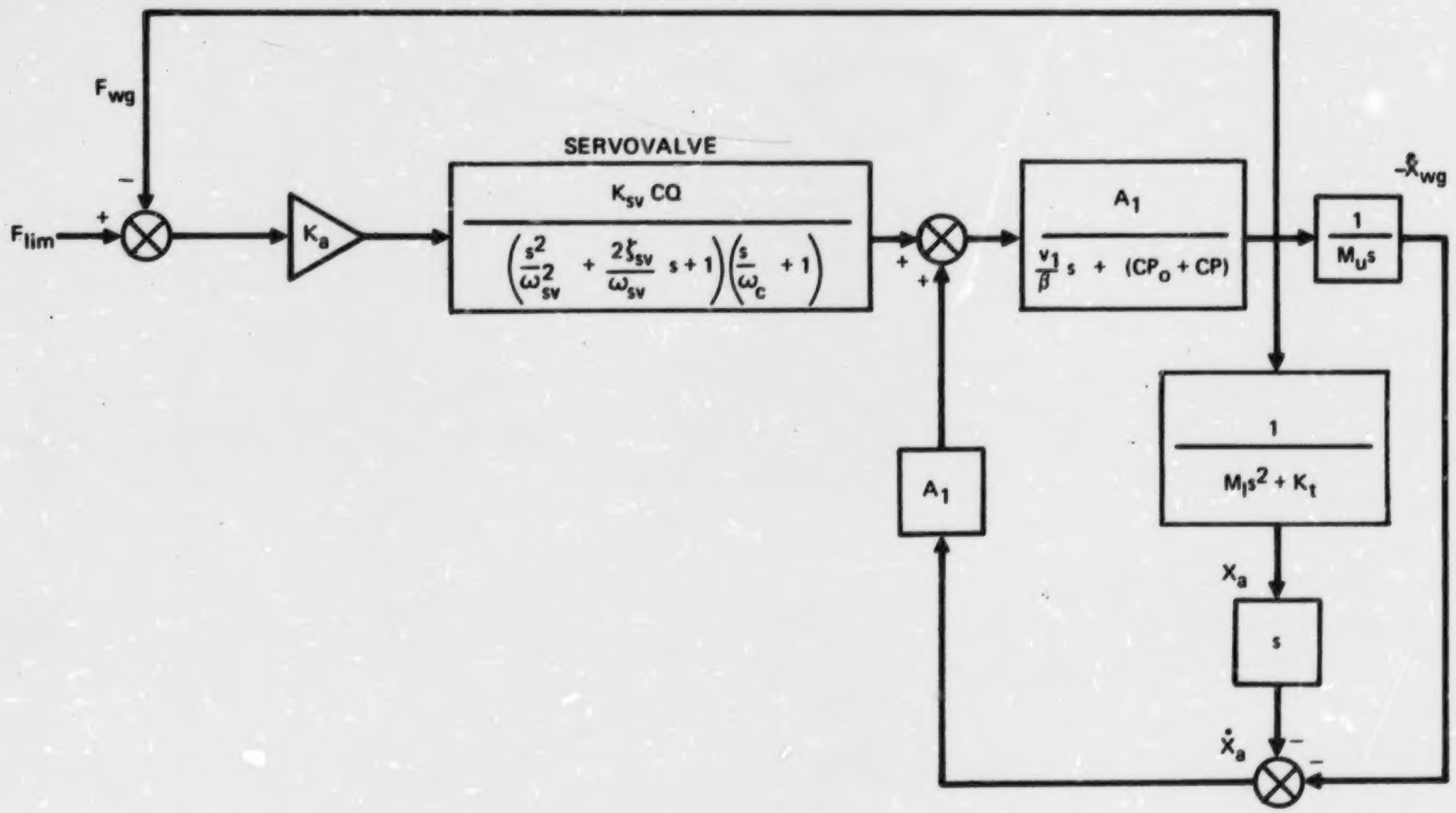

F_{wg}
−
+
F_{lim}
K_a
SERVOVALVE
$\frac{K_{sv}CQ}{\left(\frac{s^2}{\omega_{sv}^2}+\frac{2\zeta_{sv}}{\omega_{sv}}s+1\right)\left(\frac{s}{\omega_c}+1\right)}$
+
+
$\frac{A_1}{\frac{v_1}{\beta}s+(CP_o+CP)}$
$-\dot{X}_{wg}$
$\frac{1}{M_u s}$
A_1
$\frac{1}{M_l s^2+K_t}$
X_a
s
$\dot{X}_a$
−
−

Figure 11. - Block diagram of linear system without compensation.

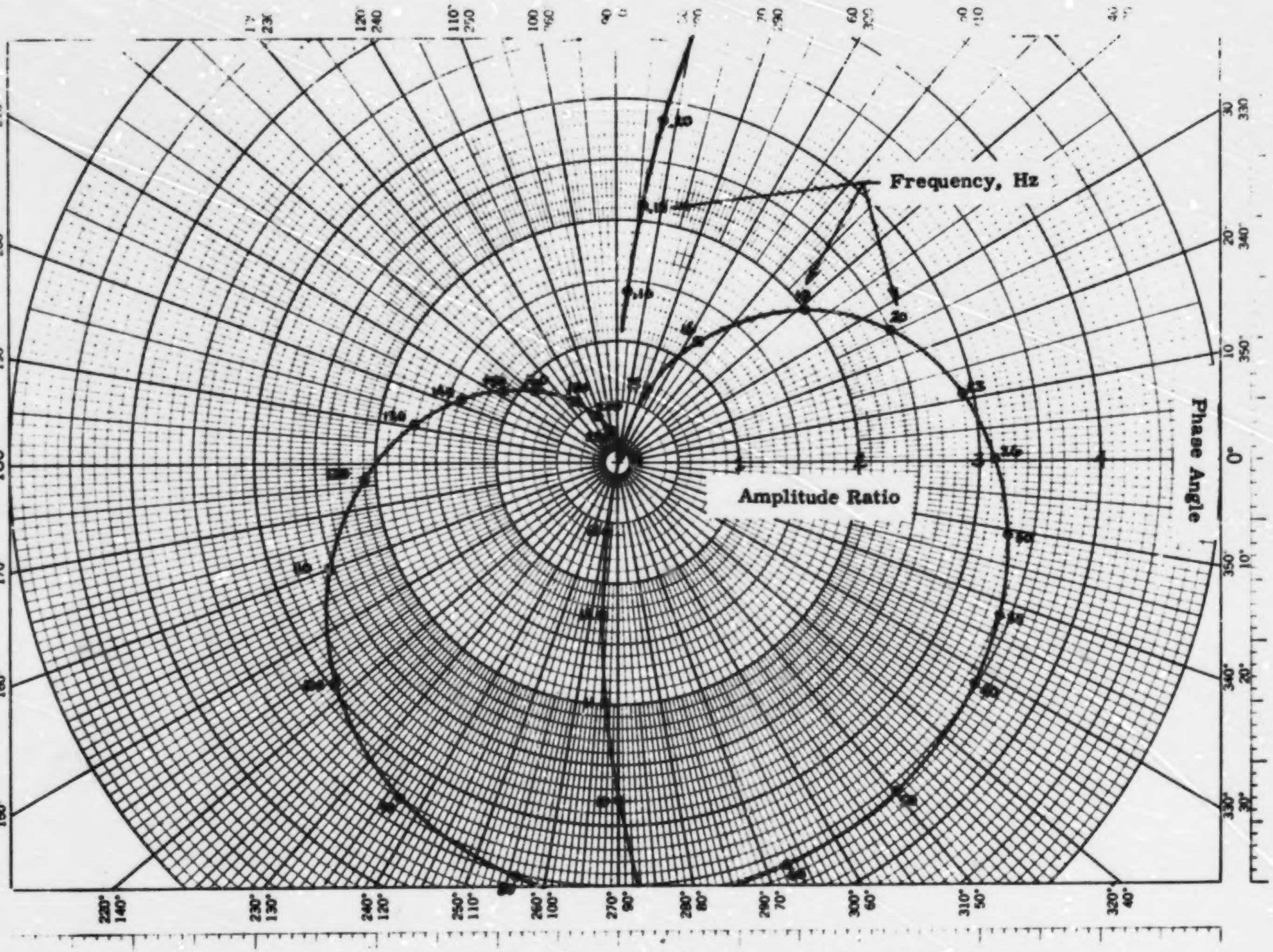

Figure 12. - Nyquist plot of F_{wg}/F_{lim} with force loop opened, no position feedback, no compensation.

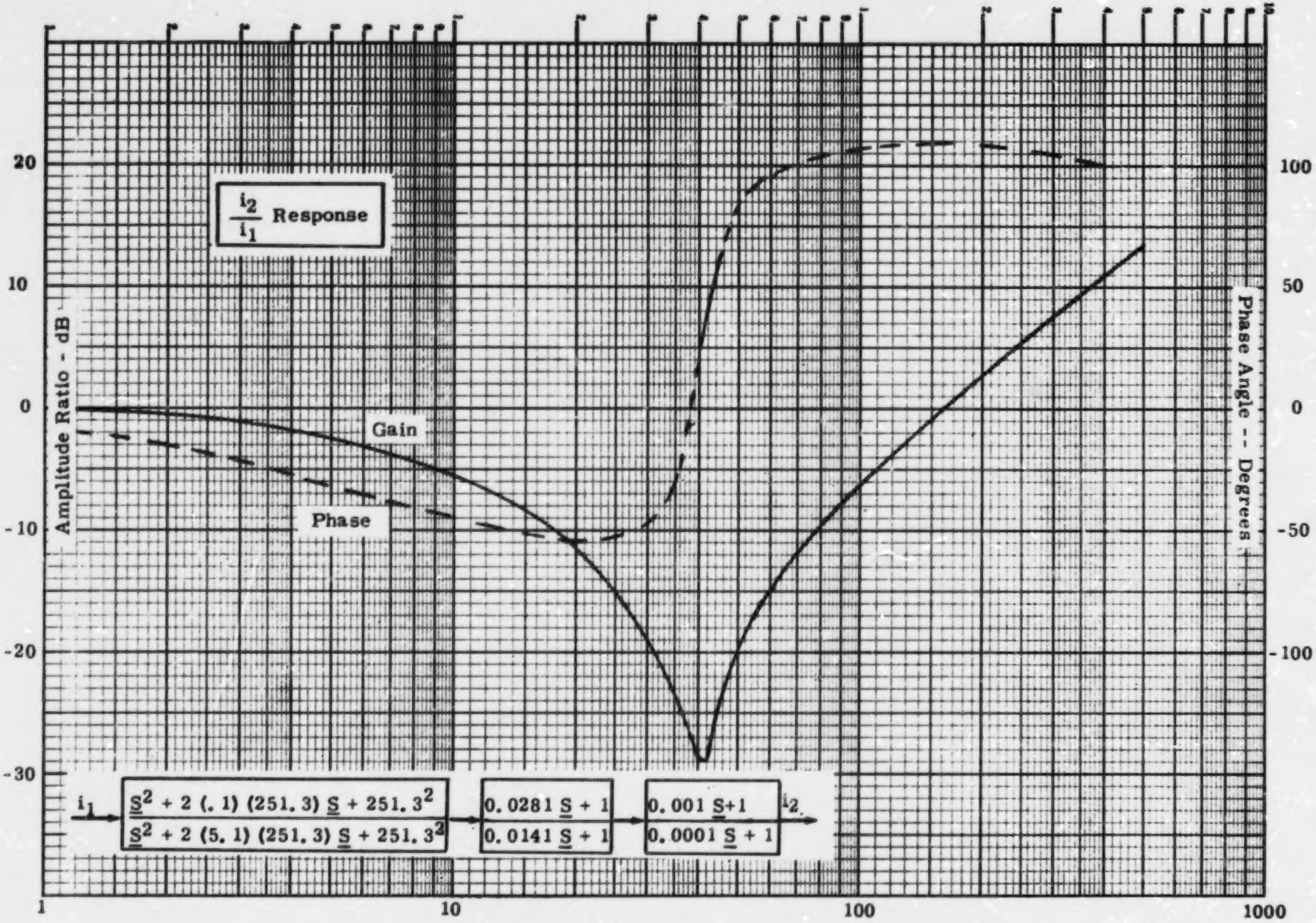

Figure 13. - Electronic compensation network and its characteristics.

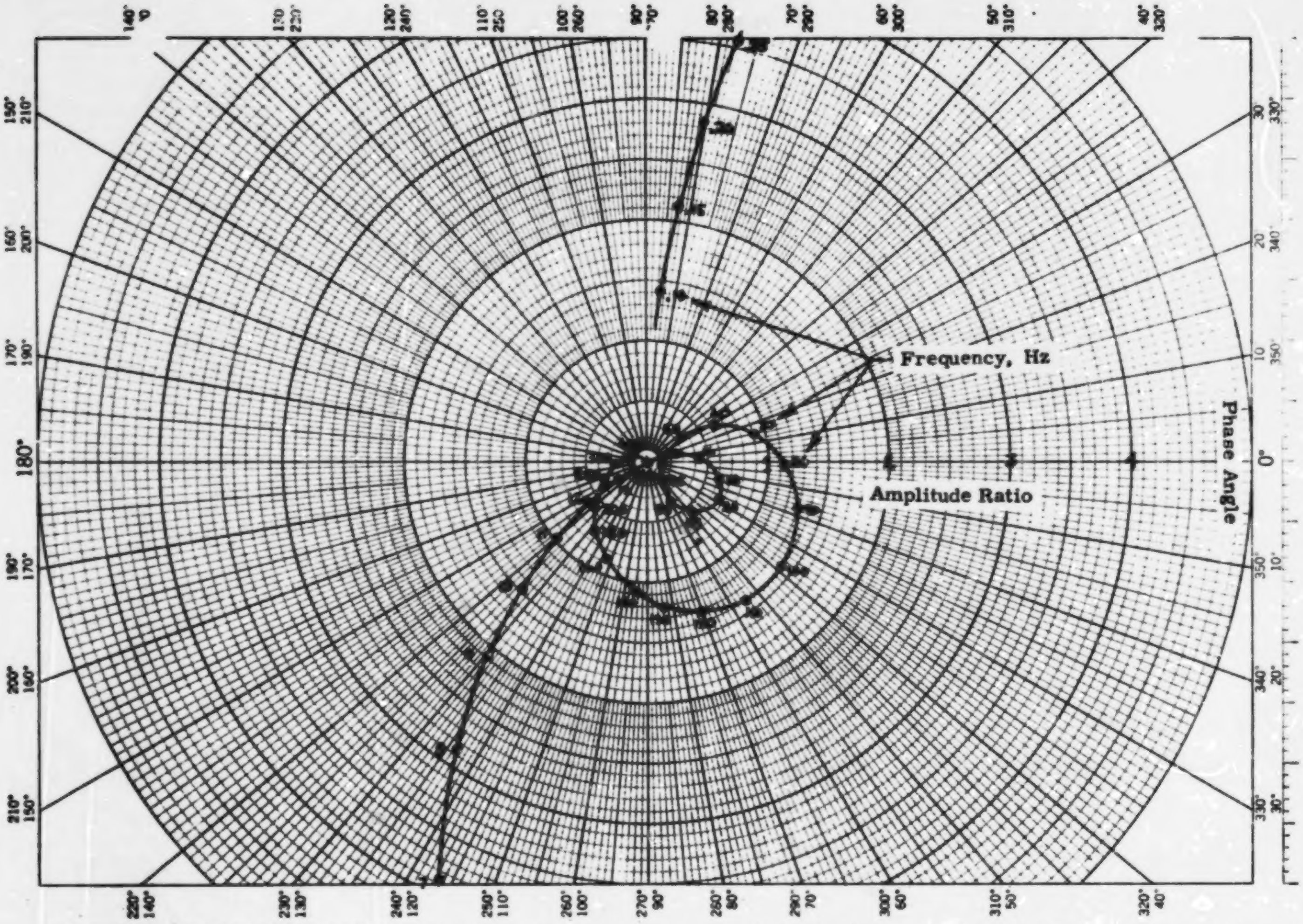

Figure 14. - Nyquist plot of F_{wg}/F_{lim} with force loop opened, no position feedback, with compensation.

The strut position feedback was next incorporated into the models. Its purpose is to ensure the return of the strut to its neutral position after landing impact. With no specific requirements on the time to return to neutral, it was assumed that a relatively gradual (approximately 10-sec) return would be acceptable. This assumption allowed a low bandwidth position loop which is essentially decoupled from the force loop. The resulting benefit is that the position loop can be continually active at all times during impact, transition, and rollout without degrading the performance of the force loop. A first-order lag in the position loop forward path yielded the desired results. The block diagram for the complete linearized system with position and force loops and compensation is shown in Figure 7.

Figure 15 shows the Nyquist plot of the F_{wg}/F_{lim} response for the complete system with the force loop opened and the position loop closed. Figure 16 shows the Nyquist plot of the X_s/X_c response with the position loop open and the force loop closed. Adequate stability margins are exhibited in these plots.

Figures 17 and 18 show the frequency response characteristics of the complete linearized system with the force and position loops closed, for F_{wg}/F_{lim} and X_s/X_c responses, respectively. Note that the bandwidth of the F_{wg}/F_{lim} response is about one hundred times greater than that for the X_s/X_c response.

The sensitivity of the system to hydraulic fluid compressibility was investigated because the effective bulk modulus of the air/oil mixture within the strut is relatively unknown. Throughout this study, a nominal bulk modulus of $6.89 (10^5)$ kPa (100 000 lb/in^2) was used based on past experience with hydraulic systems. Nyquist plots indicating system stability with bulk modulus values of $3.45 (10^5)$ kPa (50 000 lb/in^2) and $1.38 (10^6)$ kPa (200 000 lb/in^2) are shown in Figures 19 and 20. A linearized orifice coefficient of $7.13 (10^{-7})$ $m^3/sec/kPa$ (0.3 $in^3/sec/lb/in^2$) was used at all frequencies for these cases. A high bulk modulus is destabilizing in the 200-Hz range and a

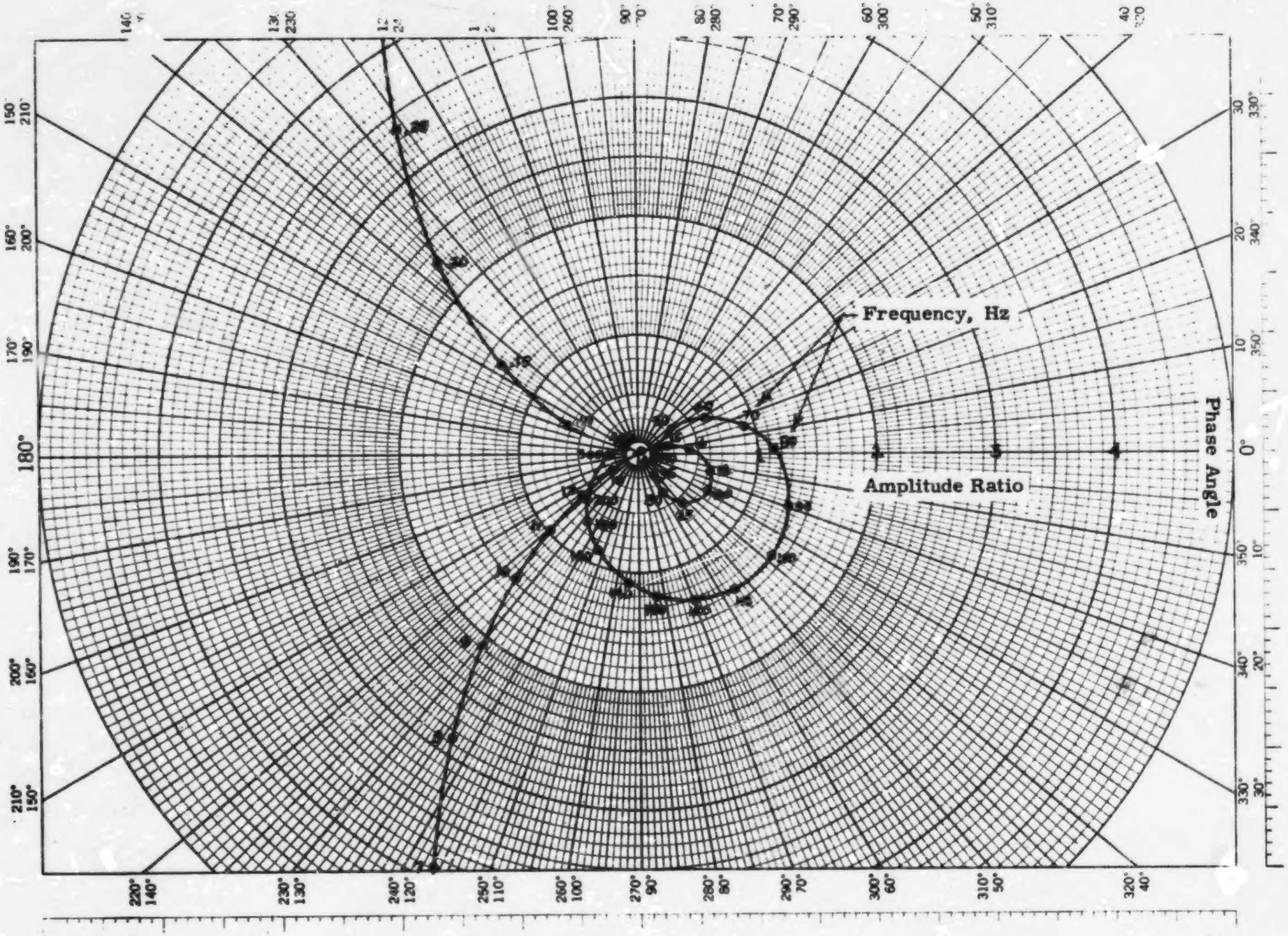

Figure 15. - Nyquist plot of F_{wg}/F_{lim} with force loop opened, position loop closed, with compensation.

BLANK PAGE

BLANK PAGE

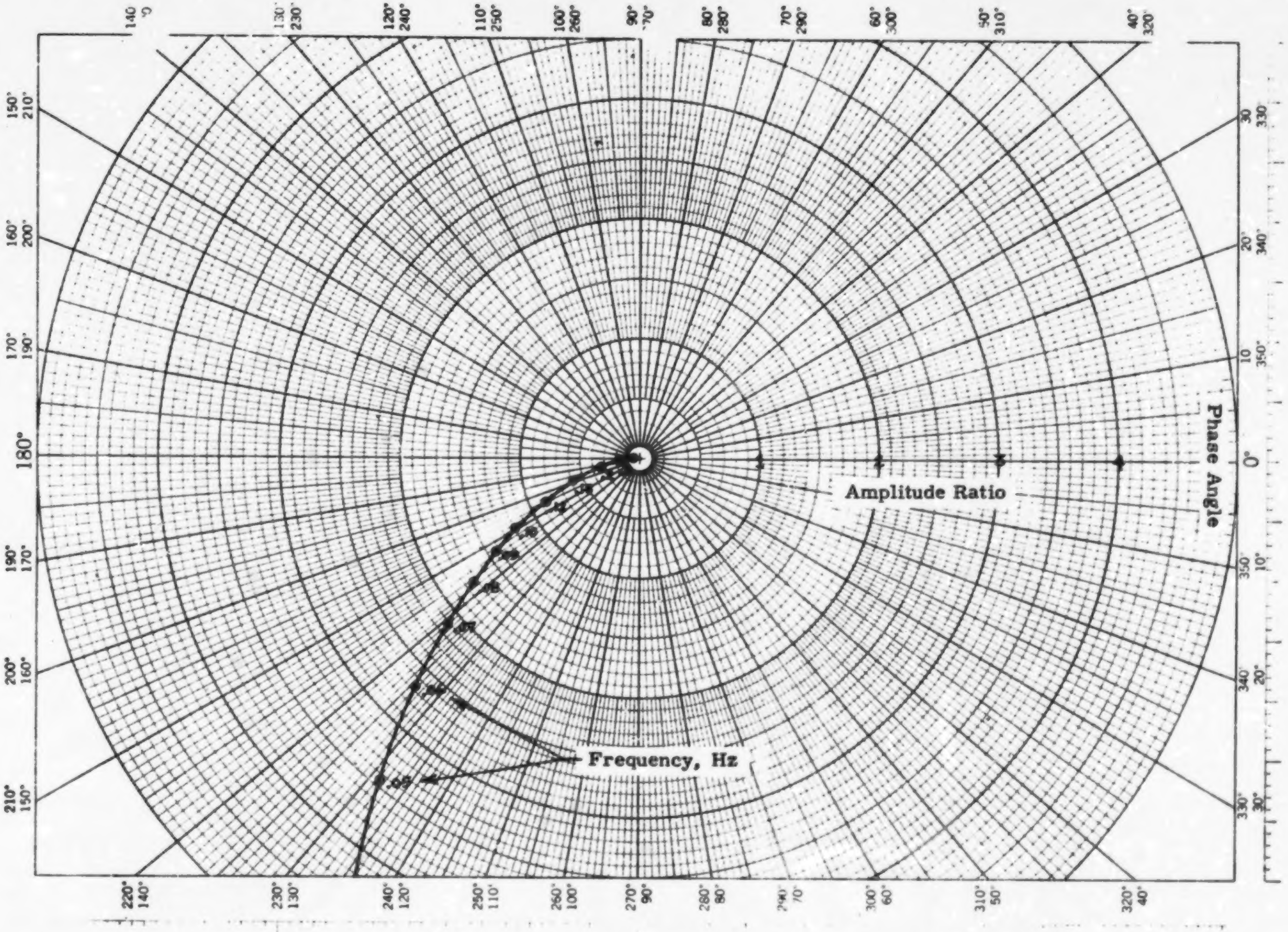

Figure 16. - Nyquist plot of X_s/X_c with position loop opened, force loop closed, with compensation.

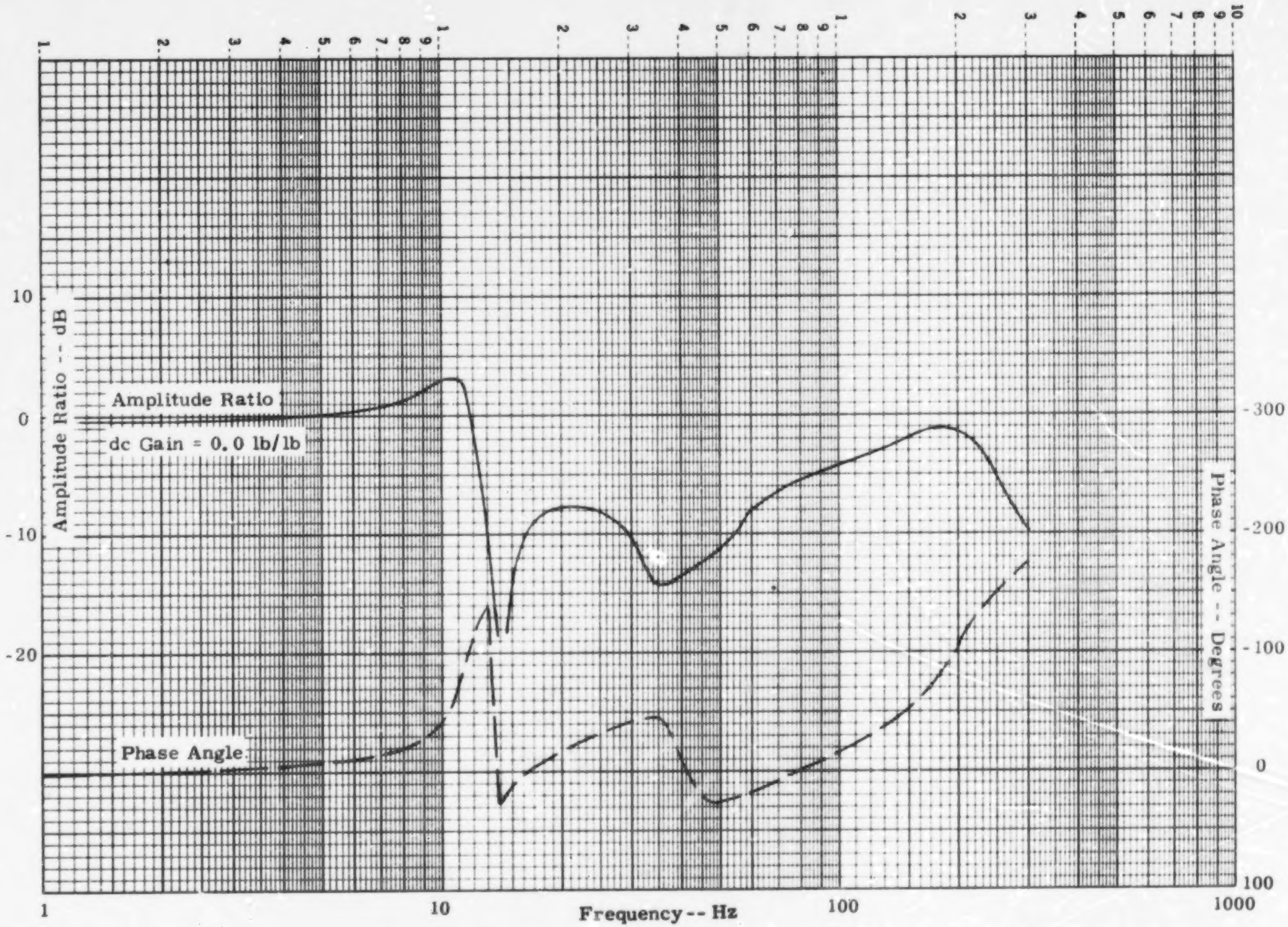

Figure 17. - Frequency response of F_{wg}/F_{lim} with force and position loops closed, with compensation.

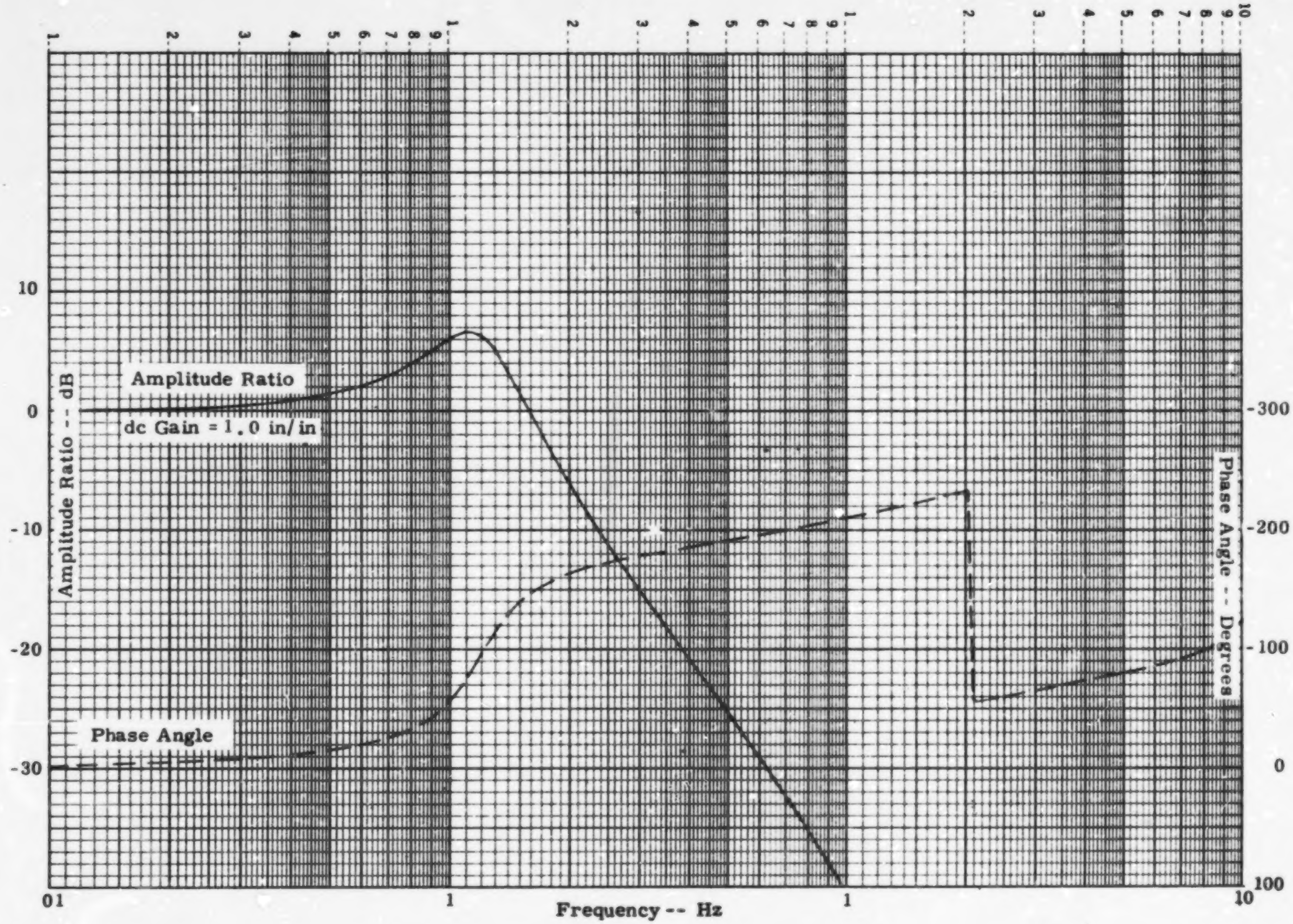

Figure 18. - Frequency response of X_s/X_c with force and position loops closed, with compensation.

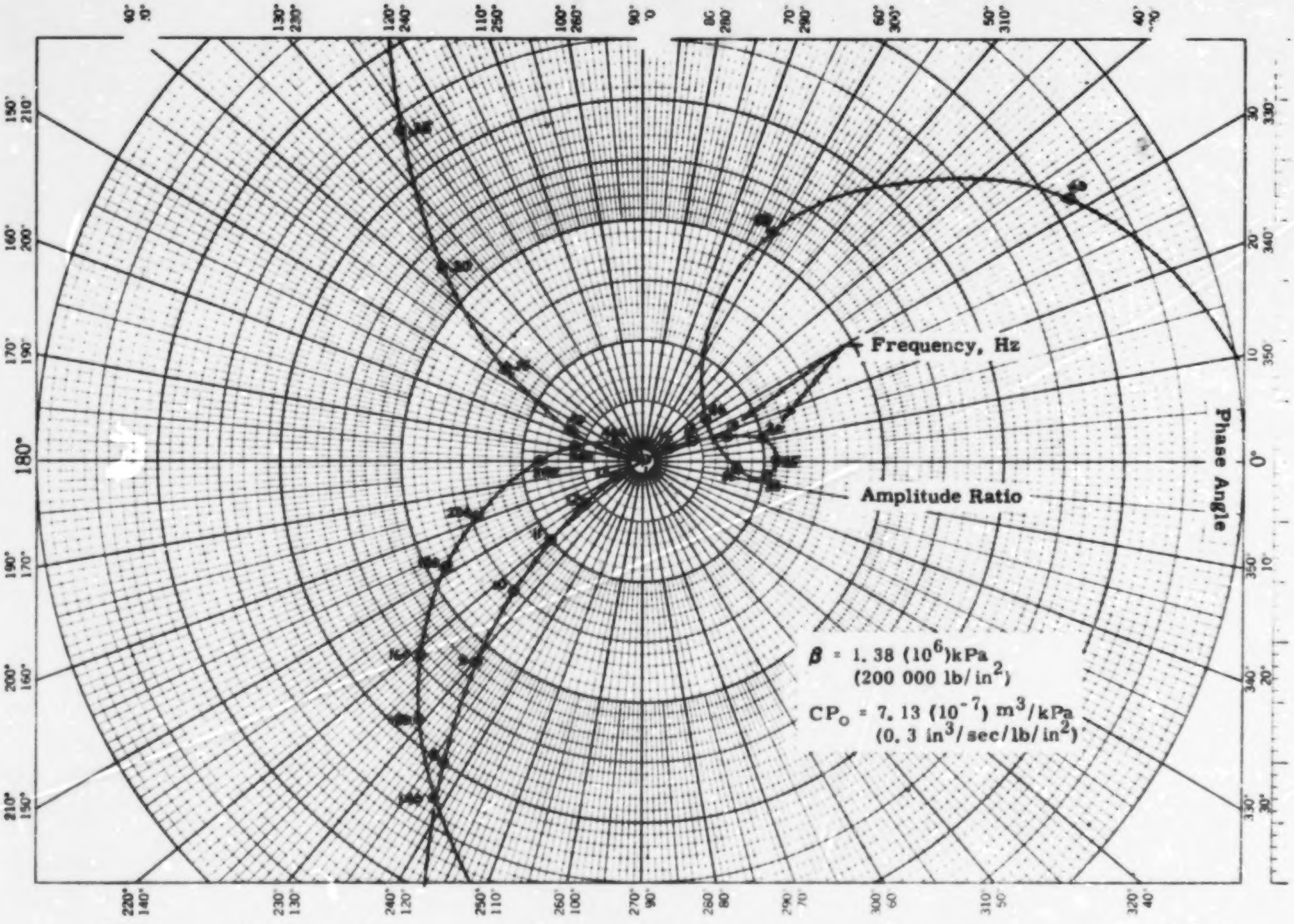

β = 1.38 (10^6)kPa
(200 000 lb/in^2)

CP_o = 7.13 (10^{-7}) m^3/kPa
(0.3 in^3/sec/lb/in^2)

Figure 19. Nyquist plot of F_{wg}/F_{lim} with force loop opened, position loop closed, with compensation.

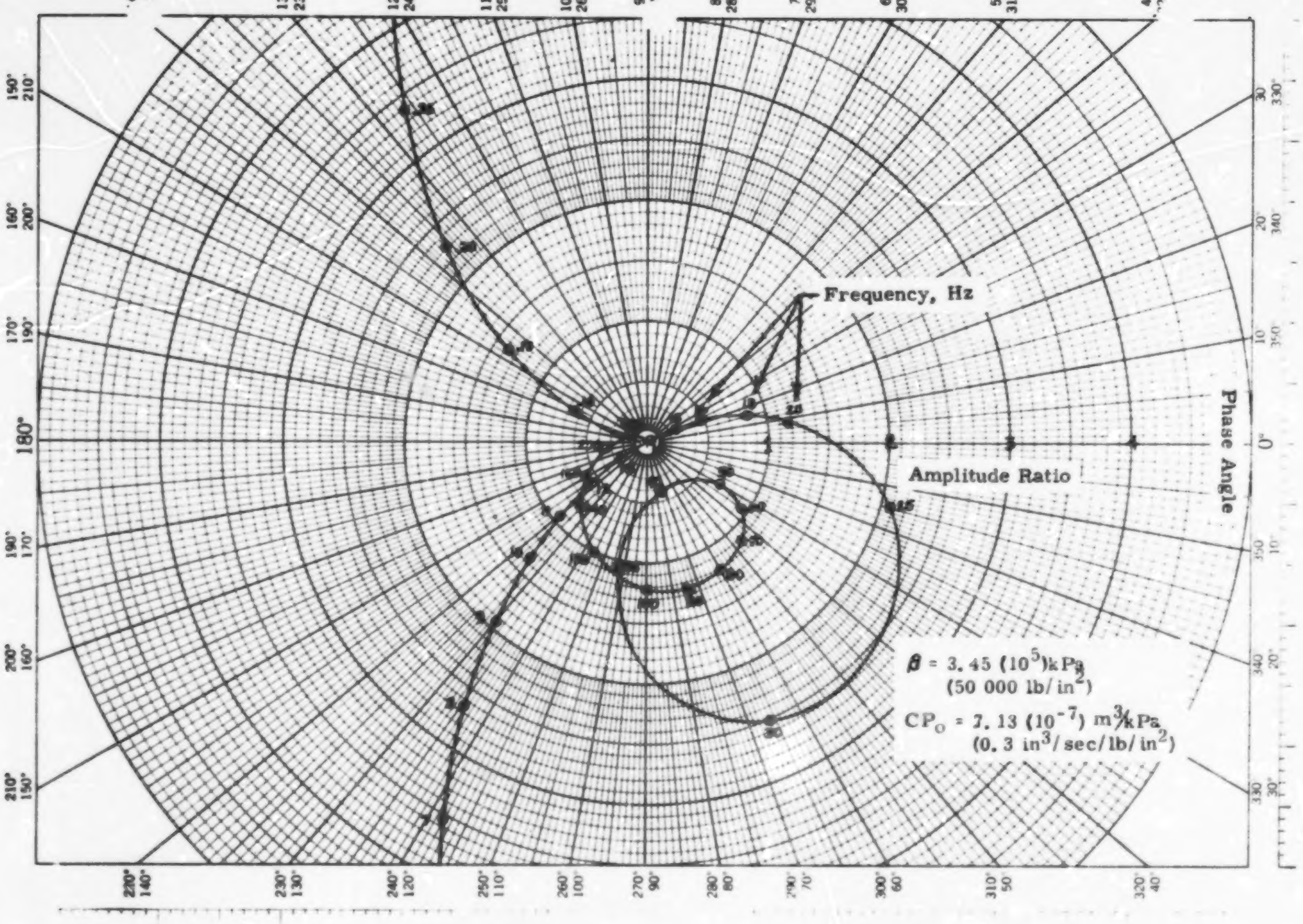

β = 3.45 (10^5)kPa
(50 000 lb/in^2)

CP_o = 7.13 (10^{-7}) m^3/kPa
(0.3 in^3/sec/lb/in^2)

Figure 20. - Nyquist plot of F_{wg}/F_{lim} with force loop opened, position loop closed, with compensation.

low bulk modulus is destabilizing in the 100-Hz range. While these results show some sensitivity to bulk modulus, they are thought to be conservative in light of the model being used. It is expected that the bulk modulus in the actual strut will lie somewhere between 3.45 (10^5) and 1.38 (10^6) m^3/sec/kPa (50 000 and 200 000 lb/in^2), and that the system, as configured, will exhibit the desired performance.

ANALYTICAL RESULTS

In this section, transient response results obtained from digital computer simulations are presented for: (1) vertical drop cases using the simplified nonlinear vertical drop model presented earlier, and (2) actual land and roll cases provided by NASA using a NASA-supplied computer program which was modified by HR for incorporation into this study. The purpose of these simulations is to demonstrate that the landing gear controller is developed and described in the previous sections performs the desired functions satisfactorily.

The NASA computer program includes detailed simulation of the aerodynamic and aircraft dynamics in two dimensions, as opposed to the one dimension for the simplified vertical drop model. However, the NASA program as supplied to HR did not contain control system and servovalve dynamics and did not include the effect of fluid compressibility. Therefore, it was modified to include all these items.

Table I lists all the cases which were simulated and reported in this section, along with a brief description of each. Cases will be referred to by the case number shown in the left column. For each case, two simulations were run — one using an active control landing gear and one using a passive gear — so that the performance of the active gear in reducing wing forces could be evaluated.

TABLE I
SUMMARY OF ACTIVE CONTROL LANDING CASES SIMULATED ON THE COMPUTER

Case No.	Type	Sink Rate m/sec(in/sec)	Forward Speed m/sec(in/sec)	Miscellaneous Comments	Peak Strut Stroke	Reduction in Peak F_{wg} due to Active Control
A*	Vertical Drop	1.83 (72)	0	Lift=Weight	95%	28%
B*		1.83 (72)	0	Lift=Weight initially, linearly decreased by 50% over 0.4 sec interval	97%	23%
1	Land and Roll	1.83 (72)	42.7 (1680)	Sinusoidal runway (3Hz, ±0.0254 m (1 in)	91%	11%
2		1.83 (72)	42.7 (1680)	Flat runway, no braking	99%	23%
3		1.22 (48)	42.7 (1680)	Sinusoidal runway (.5 Hz, ±0.0254 m (1 in)	92%	18%
4		1.22 (48)	42.7 (1680)	Flat runway	83%	17%

* K_{FDGE} = 0.9 All other Cases K_{FDGE} = 1.0

Vertical Drop Cases

Figure 21 shows the commanded and actual wing gear forces occurring during the initial impact and transition phases for Case A. The total lift force is set equal to the total weight throughout this transient; and, as a consequence, the landing gear eventually lifts off the ground (or rebounds) after 0.754 seconds. At that time, the gear is fully extended and the system has some finite upward velocity which it continues to maintain as long as the lift stays equal to the weight. Figure 21 also shows the forces for the passive gear case. A 28% reduction in peak wing/gear force is obtained when using active control.

Figure 22 shows the forces for Case B. This is the same as Case A, except that starting from the instant of impact the lift force is linearly reduced to one half of its initial value. This reduction occurs over a time interval of 0.4 seconds. The gear does not leave the ground for this case. A 23% reduction in peak wing gear force from the passive gear case is obtained. The response of the strut stroke is shown in Figure 23. As the impact transients subside, the strut approaches the value commanded by the strut positioning loop.

Land and Roll Cases

Figure 24 shows the commanded and actual wing/gear forces occurring during the initial impact and transition phases for Case 1, which uses a 3-Hz, 0.0254 m (1-inch) amplitude sinusoidal runway for the first 3.083 seconds, then a flat runway. For this case, an 11% reduction in peak wing/gear force is obtained when using active control. Figure 25 shows the pressures in the strut as a function of time. Figure 26 shows the strut stroke transient. At a time of 1.86 seconds, the strut hits the stops in the fully extended position and remains there until 2.01 seconds. Figures 27 and 28 show the wing gear force

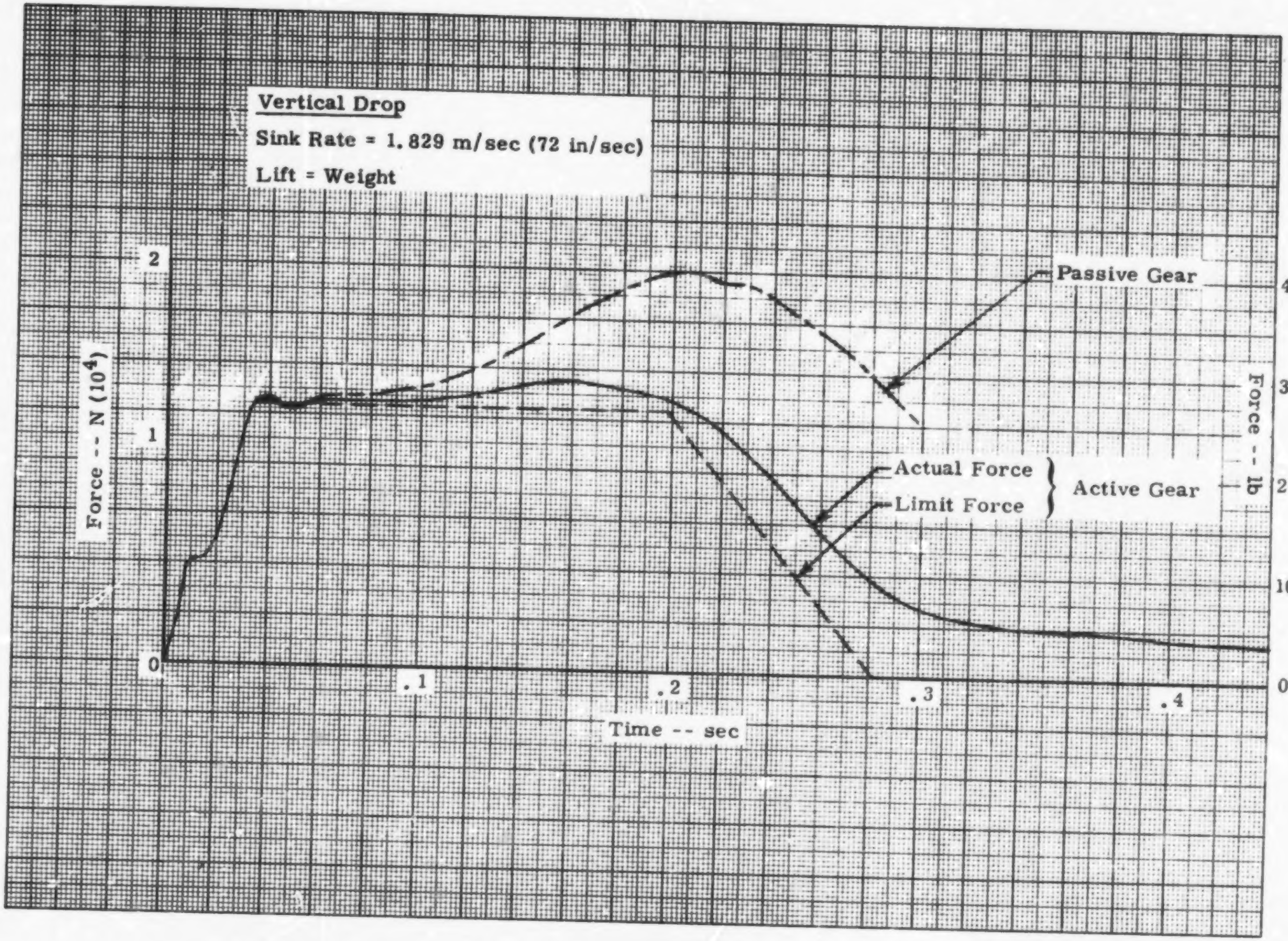

Figure 21. - Wing/gear force transient, case A.

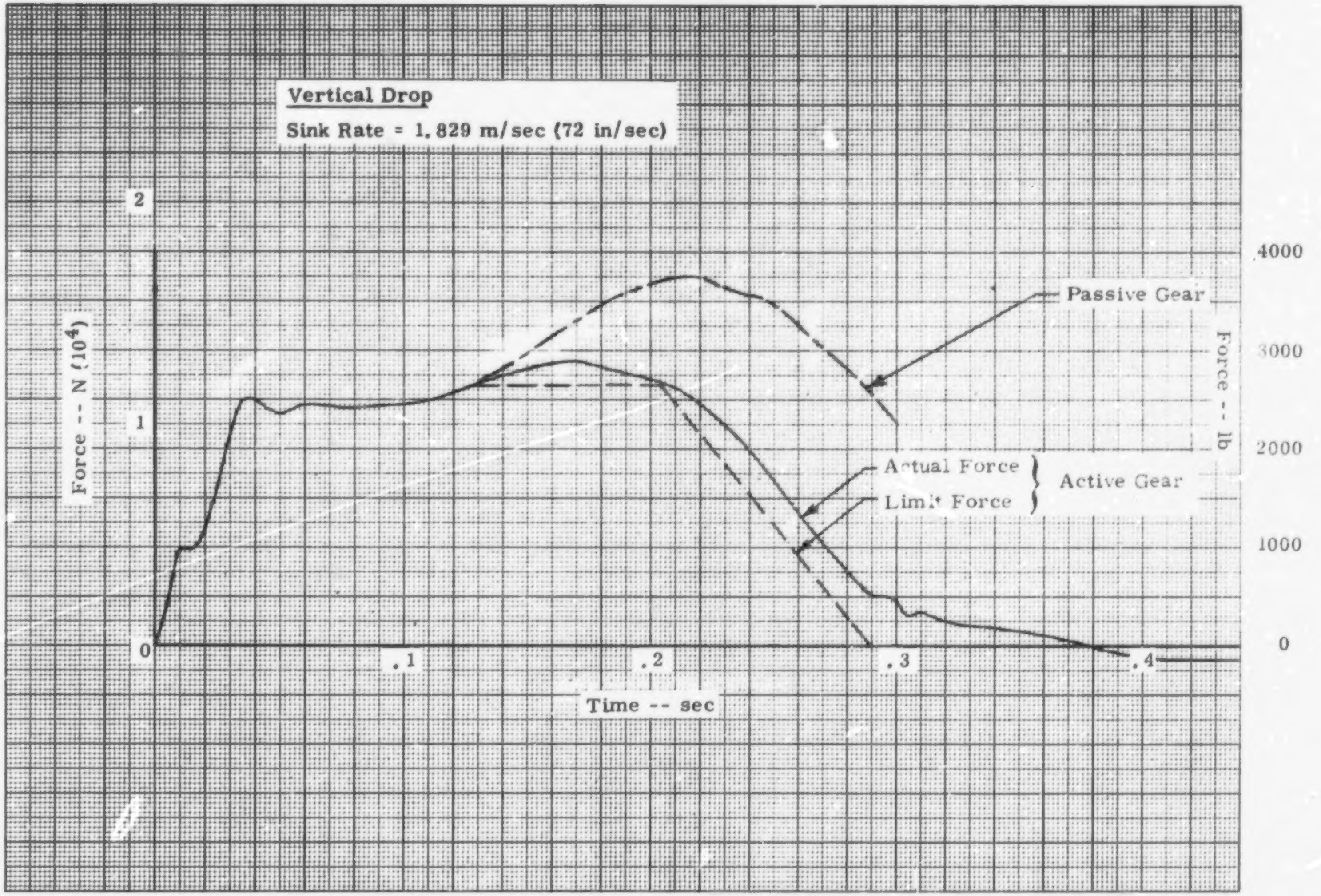

Figure 22. - Wing/gear force transient, case B.

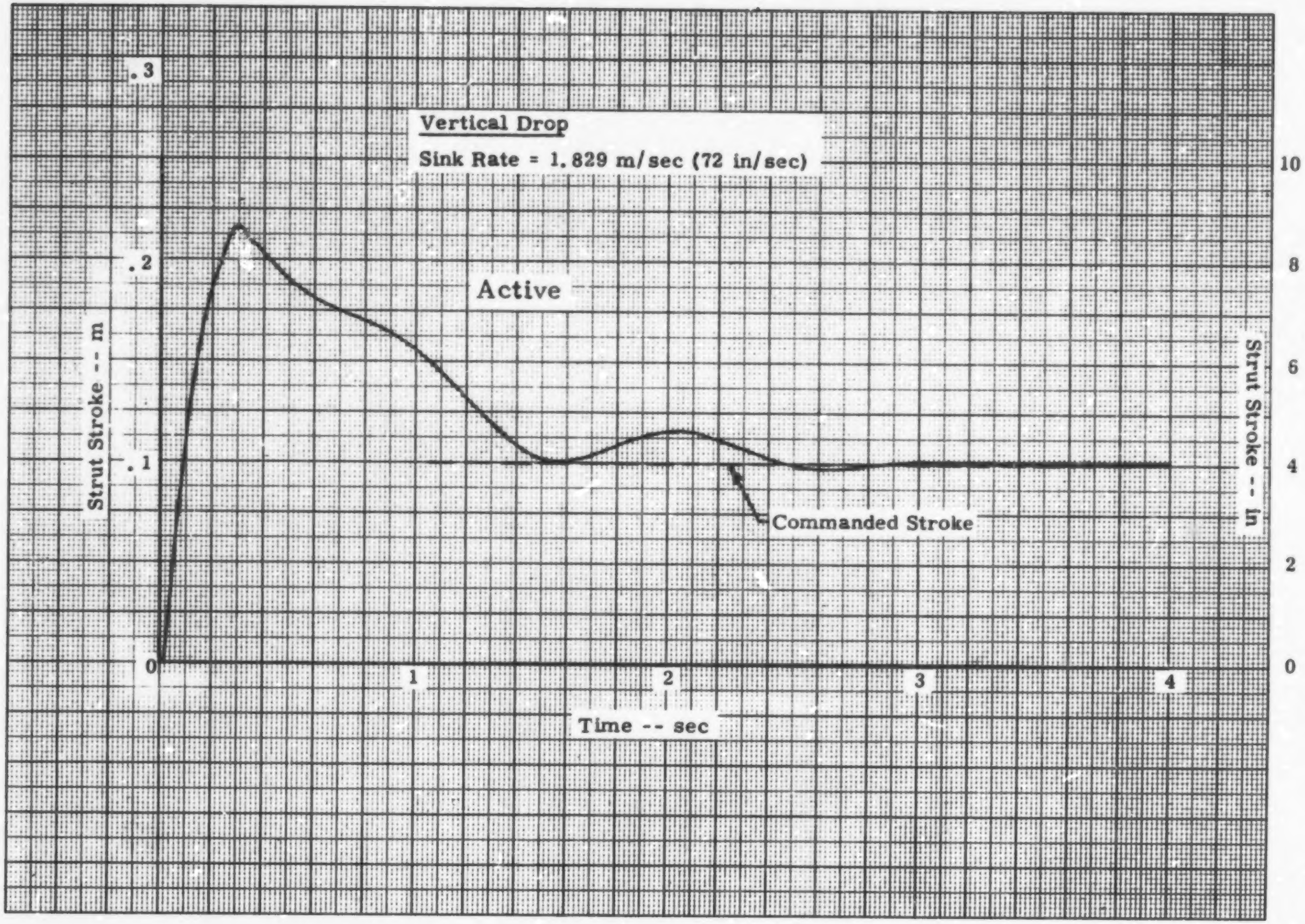

Figure 23. - Strut position transient, case B.

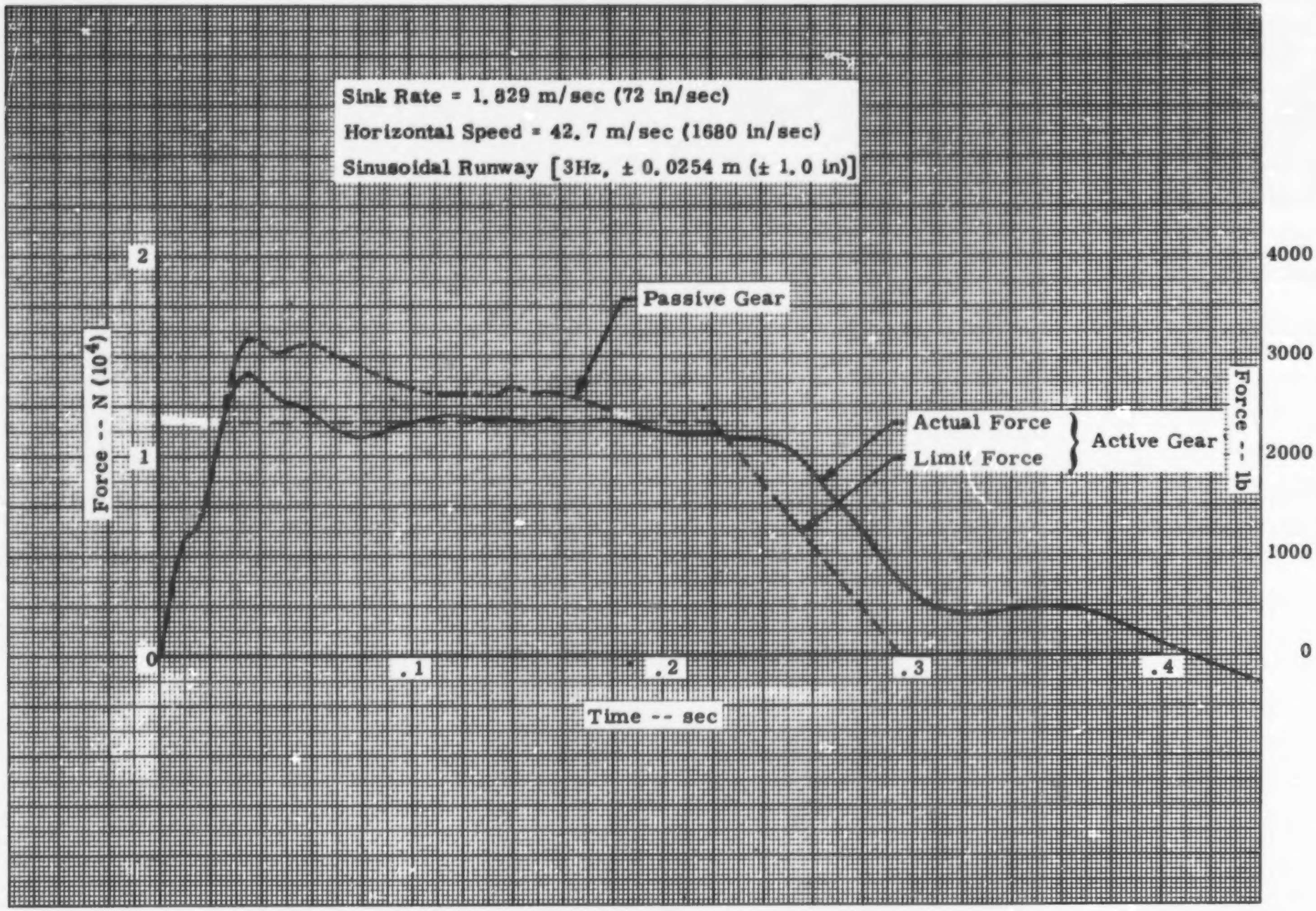

Figure 24. - Wing/gear force transient, case 1.

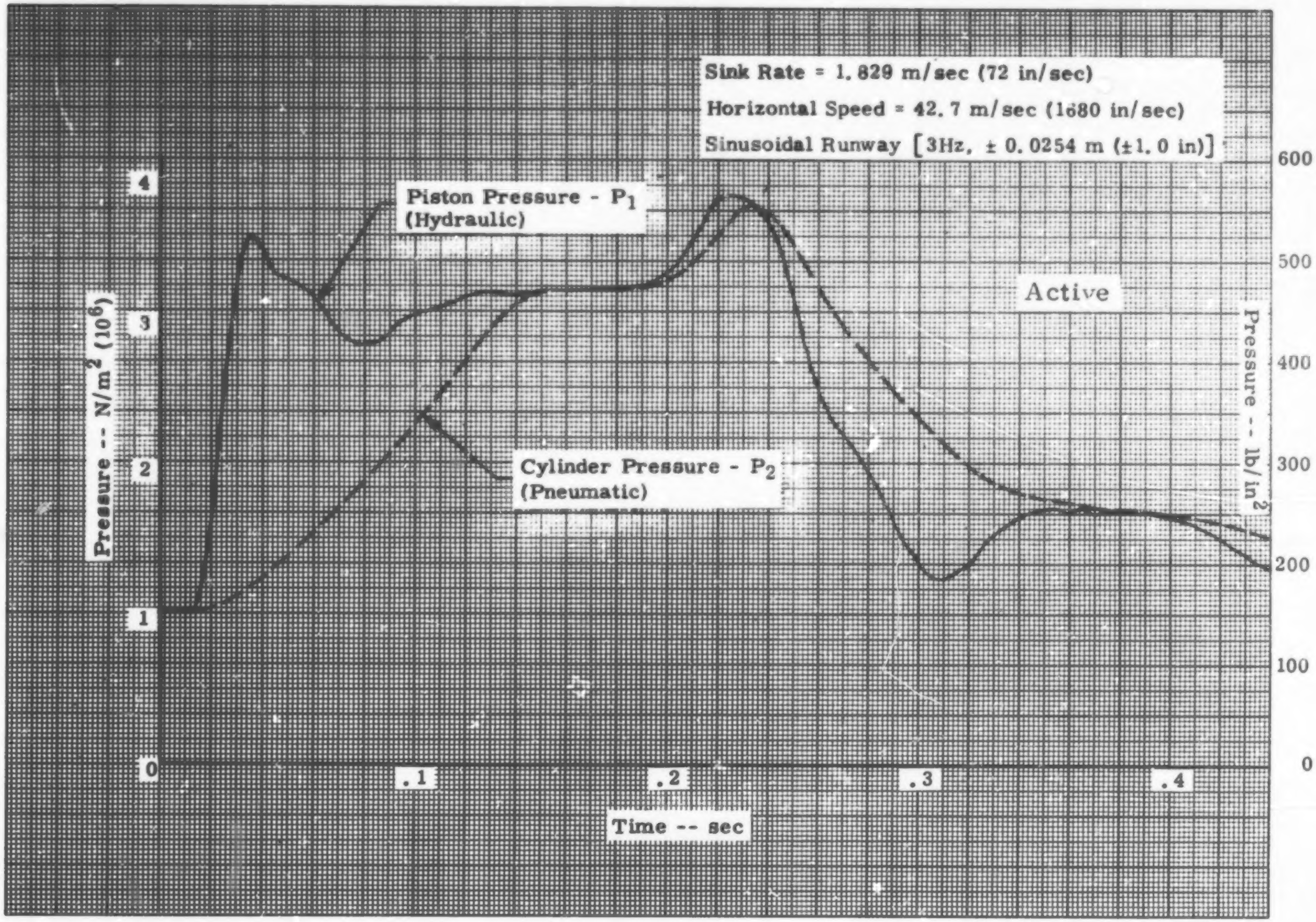

Figure 25. - Strut pressures, case 1.

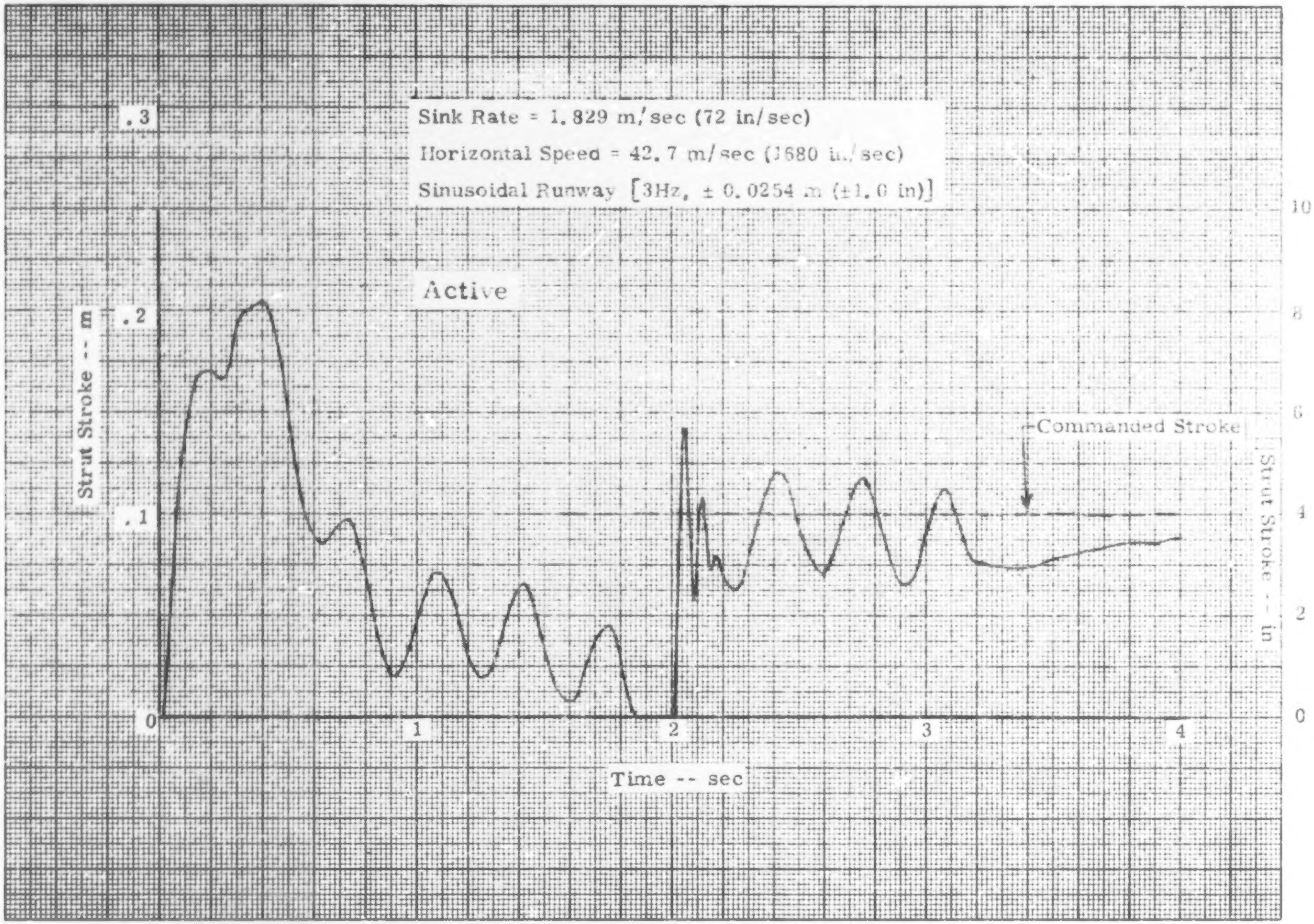

Figure 26. - Strut position transient, case 1.

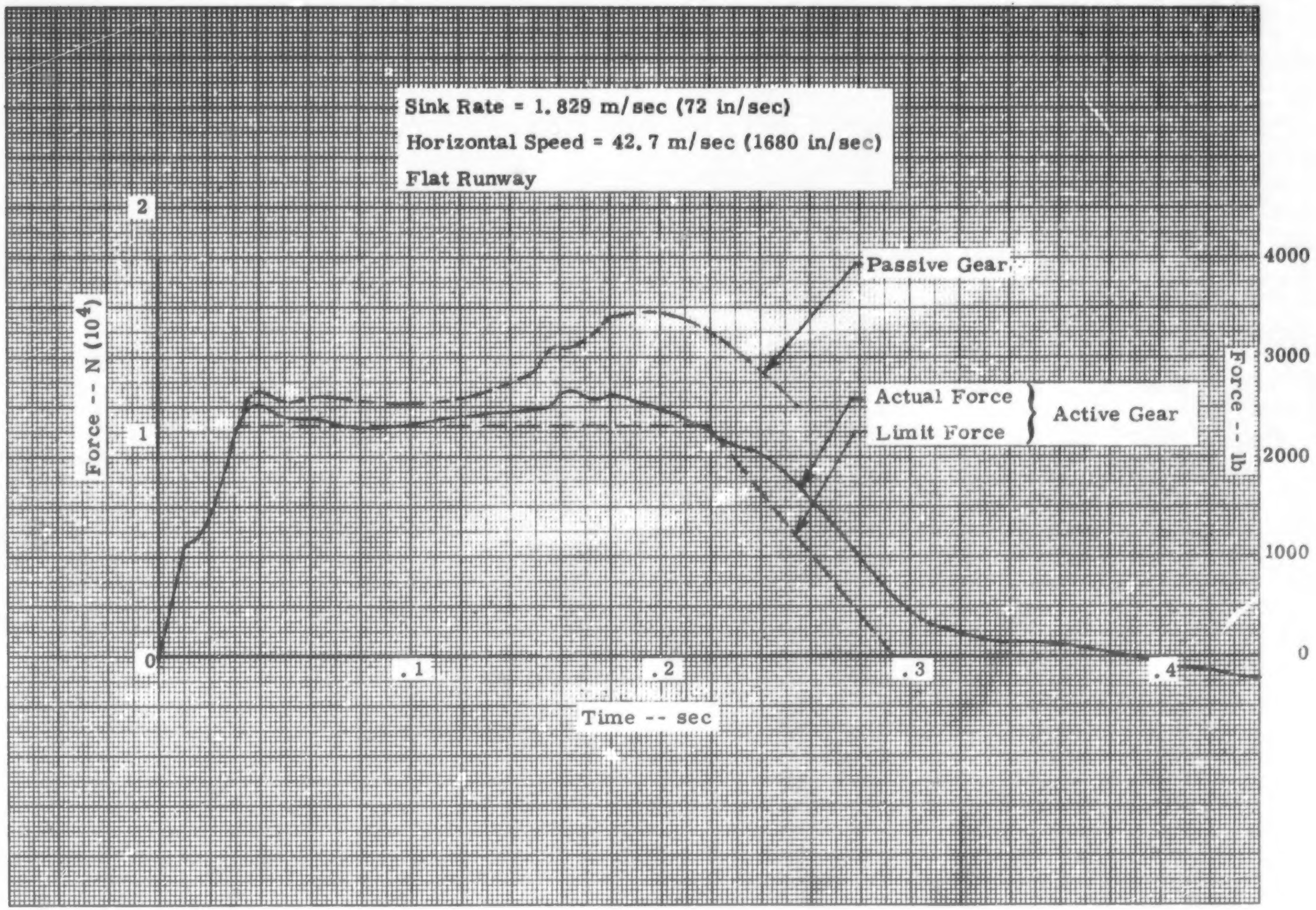

Figure 27. - Wing/gear force transient, case 2.